

# **AN ASSESSMENT OF EMPIRICAL MODELS FOR THE PREDICTION OF THE TRANSIONOSPHERIC PROPAGATION DELAY OF RADIO SIGNALS**

**S. P. NEWBY**

**August 1992**



**TECHNICAL REPORT  
NO. 160**

## PREFACE

In order to make our extensive series of technical reports more readily available, we have scanned the old master copies and produced electronic versions in Portable Document Format. The quality of the images varies depending on the quality of the originals. The images have not been converted to searchable text.

**AN ASSESSMENT OF EMPIRICAL MODELS  
FOR THE PREDICTION OF THE  
TRANSIONOSPHERIC PROPAGATION  
DELAY OF RADIO SIGNALS**

Simon P. Newby

Department of Surveying Engineering  
University of New Brunswick  
P.O. Box 4400  
Fredericton, N.B.  
Canada  
E3B 5A3

August 1992

© Simon Peter Newby, 1992

## PREFACE

This technical report is a reproduction of a thesis submitted in partial fulfillment of the requirements for the degree of Master of Science in Engineering in the Department of Surveying Engineering, August 1992. The research was supervised by Dr. Richard B. Langley, and funding was provided partially by the Natural Sciences and Engineering Research Council of Canada and by Usher Canada Ltd.

As with any copyrighted material, permission to reprint or quote extensively from this report must be received from the author. The citation to this work should appear as follows:

Newby, S.P. (1992). *An Assessment of Empirical Models for the Prediction of the Transionospheric Propagation Delay of Radio Signals*. M.Sc.E. thesis, Department of Surveying Engineering Technical Report No. 160, University of New Brunswick, Fredericton, New Brunswick, Canada, 212 pp.



## **ABSTRACT**

The objective of this thesis research was to test several empirical models of the ionosphere to see which, if any, might be a better predictor of the ionosphere's total electron content (TEC) (and therefore ionospheric delays) than the GPS single-frequency Broadcast model. A total of four models were tested, namely:

- The Bent model;
- The Ionospheric Conductivity and Electron Density (ICED) profile model;
- The 1986 International Reference Ionosphere (IRI86); and
- The GPS single-frequency Broadcast model.

Each model was adapted to enable multiple epoch/location predictions of TEC. Model testing was broken down into two distinct stages: (1) The first three models were tested against 48 station months of Faraday rotation measurements of TEC, from a total of five North American sites and one European site, recorded during three different levels of solar activity from the previous solar cycle; and (2) All four models were then compared with ionospheric delays recovered from dual-frequency GPS data recorded at two Canadian stations during a period of disturbed ionospheric behaviour in February 1991.

Comparisons with the Faraday rotation data revealed that the Bent and IRI86 models were the best. Comparisons with the GPS data showed the Broadcast and IRI86 models to be the best — the Broadcast model was able to account for approximately 70 to 90% of the daytime ionospheric delay and 60 to 70% of the night-time delay. Based upon the findings of this research some strategies for further related work are suggested.

## **TABLE OF CONTENTS**

<b>ABSTRACT.....</b>	<b>ii</b>
<b>TABLE OF CONTENTS .....</b>	<b>iii</b>
<b>LIST OF FIGURES.....</b>	<b>vii</b>
<b>LIST OF TABLES.....</b>	<b>ix</b>
<b>ACKNOWLEDGEMENTS.....</b>	<b>x</b>
<b>Chapter 1: <i>Introduction</i> .....</b>	<b>1</b>
1.1 Motivation.....	3
1.2 Contributions of the Thesis.....	5
1.3 Thesis Outline .....	5
<b>Chapter 2: <i>The Global Positioning System</i>.....</b>	<b>8</b>
2.1 The GPS Space Segment.....	8
2.2 The GPS Control Segment.....	9
2.3 The GPS Signals .....	10
2.4 Pseudorange Observations .....	10
2.5 Carrier Phase Observations.....	11
2.6 Satellite Clock Parameters .....	11
2.7 Errors and Biases .....	12
2.7.1 Ionospheric Delays .....	13
2.7.2 Selective Availability.....	14
2.8 Point Positioning Accuracy with Single-Frequency GPS .....	14
2.9 Chapter Summary.....	15
<b>Chapter 3: <i>Some Characteristics of the Ionosphere</i>.....</b>	<b>16</b>
3.1 Nomenclature of the Earth's Atmosphere.....	18
3.2 Ion Production.....	18
3.3 The Ionosphere's Total Electron Content Defined.....	19
3.4 Ionospheric Structure .....	20
3.5 Measurements of the Ionosphere.....	22

3.5.1	Ionosondes (and Ionograms) .....	22
3.5.2	Incoherent Backscatter .....	25
3.5.3	Faraday Rotation Measurements of the Ionosphere's TEC.....	27
3.6	Temporal and Geographic Variations of the Ionosphere.....	28
3.6.1	The D Region .....	29
3.6.2	The E Layer .....	31
3.6.3	The F1 Layer .....	32
3.6.4	The F2 Layer and its Anomalous Behaviour .....	32
3.7	The Earth's Magnetic Field .....	34
3.8	Ionospheric and Magnetic Storms .....	36
3.9	The Ionosphere's Major Geographic Regions.....	37
3.10	Solar and Magnetic Indices .....	39
3.10.1	Sunspot Numbers .....	39
3.10.2	The Ottawa 2800 MHz Solar Flux.....	41
3.10.3	The Kp Number and Other Magnetic Indices.....	42
3.10.4	Sources of Solar Indices.....	44
3.11	The Ionosphere in Summary .....	44
<b>Chapter 4: Empirical Modelling of the Ionosphere .....</b>		<b>46</b>
4.1	Maps of foF2 and M(3000)F2.....	47
4.2	Description of the Bent Model.....	49
4.2.1	The Ionospheric Profile of the Bent Model.....	50
4.2.2	User Input into the Bent Model .....	52
4.2.3	Output from the Bent Model .....	54
4.3	Description of ICED .....	55
4.3.1	The ICED Ionospheric Profile .....	57
4.3.2	User Input into ICED.....	58
4.3.3	Output from ICED .....	58
4.4	Description of IRI86 .....	58
4.4.1	IRI86 Ionospheric Profile .....	59
4.4.2	User Input into IRI86 .....	62
4.4.3	Output from IRI86 .....	62
4.5	The Broadcast GPS Single-Frequency Model.....	63
4.6	Model Adaptation to the Macintosh Platform .....	66
4.7	Practical Considerations for Use of the Models .....	68

4.7.1	Execution Times.....	68
4.7.2	Preparation for Use of the Models .....	69
4.8	Concluding Remarks .....	70
<b>Chapter 5: Ionospheric Refraction: Data Processing &amp; Model Testing .....</b>		<b>72</b>
5.1	Introduction to the Propagation of Radio Waves in the Ionosphere .....	72
5.1.1	Dispersion.....	75
5.1.2	Fermat's Principle.....	75
5.1.3	The Appleton–Hartree Equation, Group Delays, and Phase Advances.....	77
5.2	Faraday Rotation Database .....	79
5.3	Converting Faraday VTEC Data into Ionospheric Group Delays .....	82
5.4	Selection of the Rogue Receiver's Data Set.....	82
5.5	Preprocessing the GPS Data .....	83
5.6	Ionospheric Delays from Dual-Frequency GPS Data.....	85
5.6.1	Differential Satellite and Receiver Delays.....	91
5.6.2	Mapping Line-of-sight Ionospheric Delays to the Vertical .....	94
5.6.2.1	Sub-ionospheric Point.....	95
5.6.2.2	Obliquity Factor.....	97
5.7	Multiple Epoch/Location Computations Using the Ionospheric Models .....	102
5.8	Estimated Accuracy of Vertical Ionospheric Delays from the GPS Data.....	104
<b>Chapter 6: Analysis &amp; Results.....</b>		<b>106</b>
6.1	Comparisons with the Faraday Rotation Data.....	107
6.1.1	Conclusions Resulting from the Faraday Rotation Comparisons.....	107
6.2	Comparisons with the GPS Results .....	113
6.2.1	Conclusions Resulting from the GPS Dual-Frequency Comparisons.....	117
6.3	Recommended Strategies for Use of the Ionospheric Models .....	127
6.3.1	Recommended Latitude Limits for Use of Ionospheric Models .....	127

6.3.2	Recommended Solar Activity Limits for Use of Ionospheric Models .....	129
6.4	Summary of Results .....	129
<b>Chapter 7: Conclusions &amp; Recommendations.....</b>		<b>131</b>
7.1	Model Performances.....	131
7.2	A Synopsis of This Research & Suggestions for Future Research.....	133
7.2.1	The International Reference Ionosphere 1990.....	135
7.3	Concluding Remarks .....	136
<b>REFERENCES.....</b>		<b>137</b>
<b>APPENDIX I: Sample Solar and Geomagnetic Indices Bulletins .....</b>		<b>I.1</b>
<b>APPENDIX II: Model Errors from Comparisons with Faraday Rotation Data .....</b>		<b>II.1</b>
<b>APPENDIX III: Satellite Sky Plots for Algonquin and Yellowknife.....</b>		<b>III.1</b>
<b>APPENDIX IV: Model Errors from Comparisons with Algonquin GPS Data .....</b>		<b>IV.1</b>
<b>APPENDIX V: Model Errors from Comparisons with Yellowknife GPS Data .....</b>		<b>V.1</b>
<b>APPENDIX VI: Daily Sets of Daytime and Night-time r.m.s. Statistics for Algonquin and Yellowknife .....</b>		<b>VI.1</b>
<b>APPENDIX VII: "Whole Week" Summaries of Daytime and Night-time Mean Statistics for Algonquin and Yellowknife.....</b>		<b>VII.1</b>

## ***LIST OF FIGURES***

Figure 3.1 – Atmospheric Nomenclature .....	19
Figure 3.2 – Total Electron Content .....	20
Figure 3.3 – Sounding the Ionosphere with an Ionosonde .....	24
Figure 3.4 – The Record from an Ionogram.....	24
Figure 3.5 – A Radio Wave Passing through a Collection of Charged Particles.....	26
Figure 3.5 – Total Electron Content .....	25
Figure 3.6 – Daytime, Night-time, and Seasonal Height Variations of the Ionospheric Layers.....	29
Figure 3.7 – The earth's dip poles and geomagnetic poles do not coincide with the geographic poles. The earth's dip equator and geomagnetic equator are not coincident with the geographic equator.....	35
Figure 3.8 – Major Geographic Regions of the Ionosphere.....	38
Figure 3.9 – The 11 Year Solar Cycle .....	40
Figure 4.1 – The Bent Profile .....	51
Figure 4.2 – Sample Output from the Bent Model.....	55
Figure 4.3 – The IRI86 Electron Density Profile.....	61
Figure 4.4 – The Broadcast Model's Cosine Representation of the Ionosphere's Diurnal Variation.....	64
Figure 5.1 – The Dispersion of White Light.....	74
Figure 5.2 – An Example of a Dispersion Curve.....	75
Figure 5.3 – Propagation through the Atmosphere (Fermat's Principle).....	76
Figure 5.4 – Solar Cycles 21 and 22 .....	80
Figure 5.5 – Locations of Recording Sites of GPS Data and Faraday Rotation Data.....	81
Figure 5.6 – Daily Solar Flux and Sunspot, and Averaged Daily <i>Kp</i> Index for January and February 1991 .....	84
Figure 5.7 – Ionospheric Slant Delays Derived from Pseudorange and Carrier Phase Data to PRN#13 for February 9th 1991, Algonquin.....	90

Figure 5.8 – Carrier Smoothed Pseudorange Group Delay to PRN#13 for February 9th 1991, Algonquin.....	90
Figure 5.9 – Sub-ionospheric Point and Earth Angle.....	95
Figure 5.10 – Obliquity Factor Computed Three Different Ways .....	99
Figure 5.11 – An Example of Vertical Ionospheric Delays Determined from GPS Data .....	100
Figure 5.12 – An Example of Vertical Ionospheric Delays Determined from GPS Data .....	101
Figure 5.13 – Output Sample from the Modified Version of the Bent Model .....	102
Figure 6.1 – Daytime and Night-time r.m.s. (m) Errors (High Solar Activity).....	110
Figure 6.2 – Daytime and Night-time r.m.s. (m) Errors (Medium Solar Activity).....	111
Figure 6.3 – Daytime and Night-time r.m.s. (m) Errors (Low Solar Activity).....	112
Figure 6.4 – Satellite Visibility at Algonquin and Yellowknife for 3rd February 1991 .....	114
Figure 6.5 – Whole Week Daytime and Night-time r.m.s. Errors (m) on L1 .....	118
Figure 6.6 – Whole Week Daytime and Night-time r.m.s. Errors (%) on L1 .....	119
Figure 6.7 – Whole Week Daytime and Night-time r.m.s. Errors (m) on L1 .....	120
Figure 6.8 – Whole Week Daytime and Night-time r.m.s. Errors (%) on L1 .....	121
Figure 6.9 – The 5° Elevation Coverage Areas for Yellowknife and Algonquin .....	123
Figure 6.10 – Sub-ionospheric Point, Vertical Ionospheric Delay on L1, and Model Errors for PRN#02 at Yellowknife.....	125
Figure 6.10 – Sub-ionospheric Point, Vertical Ionospheric Delay on L1, and Model Errors for PRN#06 at Yellowknife.....	126
Figure 6.12 – Approximate Geographical Locations of the Auroral Zones and the Equatorial Region .....	128

## ***LIST OF TABLES***

Table 3.1 – Ionospheric Layers, their Subdivisions, and Heights.....	22
Table 3.2 – Summary of NGDC Solar Indices .....	43
Table 4.1 – The Ranges of the Five Sections of the Bent Profile.....	52
Table 4.2 – Errors in the Determination of the Smoothed Monthly Mean Solar Flux when Computed Using Various Techniques .....	54
Table 4.3 – Execution Times for the Bent, IRI86, ICED, and Broadcast Models.....	69
Table 4.4 – Input Data for Three Empirical Models and the Broadcast Model.....	70
Table 5.1 – Geostationary Satellites from which the Faraday Data were Recorded.....	80
Table 5.2 – Receiver Calibration Values around GPS Week # 578 for the Yellowknife Rogue GPS Receiver .....	92
Table 5.3 – Satellite and Receiver Differential Delays at Yellowknife and Algonquin for GPS Week # 578.....	94
Table 5.4 – Explanation of the Output File from the Modified Form of the Bent Model.....	103
Table 6.1 – Daytime r.m.s. (m) Errors on L1 .....	108
Table 6.2 – Night-time r.m.s. (m) Errors on L1 .....	109
Table 6.3 – Model Performances for Three Levels of Solar Activity.....	109
Table 6.4 – Daytime and Night-time r.m.s. (m) Errors on L1 to Sixteen Satellites at Algonquin .....	115
Table 6.5 – Daytime and Night-time r.m.s. (m) Errors on L1 to Sixteen Satellites at Yellowknife.....	116
Table 6.6 – Solar Indices for the Models' Test Periods.....	129



## **ACKNOWLEDGEMENTS**

World-wide the surveying community comprises a relatively small body of highly motivated scientists, engineers, and technicians. Whilst working on this research I have drawn on many sources of expertise — some close at hand, many far away. In all cases assistance has been furnished with great enthusiasm and genuine interest in the work at hand. I have found this to be most gratifying and uplifting. It is my hope that in some small way my efforts presented here will repay all those who have helped me. There can certainly be little doubt that without such assistance this research would have represented an almost impossible undertaking.

There are many people to whom I would like to extend my thanks. First and foremost I wish to thank my supervisor, Dr. Richard Langley. At times progress has been painstakingly slow, often frustrating in extremis. Richard has supported me over every hurdle and could often be heard, with his usual air of calm, to recite the words “graduate work isn’t supposed to be easy.” I extend my sincere thanks to Richard for his patience and interest in my work, and for sharing his vast wealth of knowledge so freely.

There are many others whom I should like to thank for their valuable input of data, numbers, source code, and ideas. Firstly I would like to mention Mark Caissy and Kim Lochhead of the Surveys, Mapping and Remote Sensing Division of the Canada Centre for Surveying. They have been pestered by me on numerous occasions and, despite their busy schedules, have always found time to respond to my requests for assistance. I am,

in particular, indebted to them for providing me with GPS data from their Rogue receivers.

I wish to thank Herb Kroehl and Chris Wells (National Oceanic and Atmospheric Administration) for releasing the development version of the FORTRAN source code for the Ionospheric Conductivity and Electron Density (ICED) profile model.

This acknowledgement would not be complete without giving thanks to Jack Klobuchar (Phillips Laboratory, United States Air Force), Urs Wild (University of Bern), John McKinnon (National Geophysical Data Center), Brian Wilson (Jet Propulsion Laboratory), and Jan Kouba (Geophysics Division, Geological Survey of Canada).

Finally I wish to extend my deepest thanks to Dr. Nick Christou. Nick's friendship, and contagious enthusiasm for geodesy and computing has touched many people at UNB. I owe Nick a huge debt of gratitude for the time he spent helping me get past those early hurdles when I was first facing the UNB mainframe and computing techniques which were new to me.

Funding for this research was provided by the University of New Brunswick, the Natural Sciences and Engineering Research Council of Canada, and Usher Canada Ltd.

## *Chapter 1*

### ***Introduction***

The Global Positioning System (GPS) satisfies the positioning and navigation requirements of many people from many different walks of life. Positioning using code observations is not as accurate as using carrier phase observations; it is, however, instantaneous and accurate enough for general (i.e., low accuracy) use. GPS was designed primarily for use by military organisations. In this context it also provides accurate velocity determination for use in high-dynamic environments such as weapons guidance systems and aircraft. With the design and manufacture of GPS-specific circuitry (i.e., purpose built computer chip sets) the receivers can now be packaged in hand-held units whose dimensions are not much larger than those of a walkie-talkie (e.g., the Magellan GPS NAV 1000 PRO). Such a receiver ideally suits military organisations who (one could speculate) might ultimately outfit all ground troops with their own hand-held GPS receiver. The military benefits are obvious.

Many of the same benefits apply to the civilian community. Initially the largest group of civilian users of GPS has without doubt been the surveying and geodesy community. As creatures of great patience, determination, and ingenuity this sector of GPS users has found that it is possible to determine baseline lengths and coordinates very accurately. Baselines can be **routinely** determined with an error of only 1 to 3 p.p.m. (1 to 3 mm in every kilometre of baseline length). State of the art GPS data processing can reduce this level of error by two orders of magnitude. With the advent of the purpose built chip sets

and the recuperation of research and development costs, the size and cost of future GPS receivers will certainly decrease dramatically. Within the next decade we will likely see a low cost (a few hundred dollars) GPS receiver which may be no larger than a wrist watch. When such a time comes there will probably be millions of GPS users world-wide. The usefulness of GPS will become even more apparent — we can expect to see many new vehicles (cars, buses, lorries etc.) fitted with a receiver; hikers will never again have to worry about being lost in the middle of nowhere; tractors may automatically plough fields and sow crops; even the smallest vessels will use GPS signals for positioning. And so the list goes on.

Unmodelled ionospheric delays are a major contribution to the GPS error budget. Single-frequency users of the system will commonly either ignore the effect of the ionosphere or model it using a simple half-cosine model which is commonly regarded to be of limited accuracy. In this thesis, I investigate the use of more elaborate ionospheric models which may help to improve the accuracy with which such predictions can be made.

The ensuing study shows that with the use of ionospheric models it is often possible to account for 70 to 80% of the ionospheric delay. Whilst this is not a definitive work it does show that there may be some value to the use of such models and further avenues of research are outlined as possible extensions to that which is presented here.

Other authors have investigated the use of ionospheric models and their ability to predict the ionosphere's state. *McNamara & Wilkinson* (1983) make comparisons between values of TEC recorded at 31°S and those predicted with the 1979 International Reference Ionosphere and conclude that discrepancies are usually less than 20%. *Feess & Stephens* (1986) assess the GPS single-frequency Broadcast model by making

comparisons with ionospheric time delay values determined from dual-frequency GPS data. They conclude that the Broadcast model leads to an overall reduction in r.m.s. range measurement error of 60%. *Klobuchar* (1986) describes and assesses the Broadcast model. In his assessment of the model he makes comparisons with 490 station months of Total Electron Content (TEC) data recorded at 18 sites during both solar maximum and minimum conditions. Klobuchar concludes that the Broadcast model removes approximately 55% r.m.s. of the ionosphere's effect on range measurements. The work of *Finn & Matthewman* (1989) involves the development of an entirely new algorithm (similar in form to that of the Broadcast model) to describe the ionospheric TEC. The authors state that their algorithm accounts for approximately 75% of the ionosphere in all regions of the globe for a wide range of solar activities. Finally, *Brown et al.* (1991) presents an evaluation of six ionospheric models as predictors of TEC. In the course of their testing the authors gathered TEC data from a range of geographic locations, covering a wide range of solar activity. They concluded that none of the six test models did a very good job of predicting TEC and they attributed this to (probably) poor modelling of the upper part of the ionosphere.

The thesis research presented here makes an independent assessment of four ionospheric models and does so in a way that endeavours to be pertinent to the GPS user community. As such, the results of the analysis are presented in terms of how much of the ionospheric delay was actually accounted for in metres and percent.

## **1.1 Motivation**

The role played by the ionosphere with respect to GPS has been very much a topic for hot discussion over the past two or three years. Solar activity has approached and passed through the peak of the current solar cycle and is now on its way back down towards a minimum. However, solar activity is currently still very high. There is a high

degree of correlation between the level of solar activity and the number of free electrons in the ionosphere. Also, as the number of free electrons increases so does the delay suffered by electromagnetic radiation which passes through the ionosphere. Therefore at the peak of a solar cycle GPS users can expect signals to be retarded by a relatively large amount. Such a delay can sometimes be as large as 300 ns ( $\approx$  100 metres) or so.

If a dual-frequency P-code receiver is available the dispersive nature of the ionosphere can be used to good effect by forming a linear combination of the L1 and L2 pseudorange measurements to estimate and subsequently remove the ionospheric bias from the measurements. Similarly, a linear combination of the L1 and L2 carrier phase measurements allows determination of the variation in the ionospheric delay (the so called differential delay) which is accurate to the few centimetre level. There may still however be receiver tracking problems to worry about under disturbed ionospheric conditions (Klobuchar, 1991).

If on the other hand a single-frequency receiver is used then the user is afforded no such luxury and (as previously noted) the ionosphere is either ignored or modelled using a simple representation of the ionosphere whose coefficients are included in the navigation message. Various studies have shown that this model can remove about 50% r.m.s. of the effect. Thus there can still be a residual error in the measured receiver to satellite range due to the ionosphere of the order of several tens of metres. This might be acceptable for navigating a sailboat but there are other applications where it might be regarded as an unacceptably large error. This limitation provides the *raison d'être* for this research: namely to investigate alternative ionospheric models in an attempt to improve the single-frequency GPS user's capability to combat the effects of the ionosphere.

## 1.2 Contributions of the Thesis

Three semi-global ionospheric models developed by the ionospheric research community have been obtained. In their original state these models were not in a useful form for this research. Several modifications have been made to rectify this situation and enable multiple epoch/location computations of total electron content and the delay suffered by GPS signals due to the ionosphere. This has allowed these three models **plus** the GPS Broadcast model to be compared with actual measurements of ionospheric delay so that model performances could be benchmarked against reliable data. The primary contribution made by this thesis has therefore been to acquire, adapt, implement, and test four models of the ionosphere. This work has been carried out in an attempt to find the best ionospheric model (or models) which could be used by the single-frequency GPS user.

Some of the results presented in this thesis are quite encouraging. This thesis does not however present the reader with a definitive text on the subject: a certain amount of detail has necessarily been omitted (particularly with respect to the inner workings of the models) and several avenues for continued research are suggested.

## 1.3 Thesis Outline

**Chapter 1 — *Introduction*** is a short chapter which introduces this thesis. It underlines the motivation behind the study and comments on contributions made by this work.

**Chapter 2 — *The Global Positioning System*** is a brief introduction to GPS. Its purpose is not to give a detailed understanding of GPS as such texts already exist. Instead some of the fundamental aspects of the system are introduced to give a cursory understanding of what makes the system tick.

**Chapter 3 — *Some Characteristics of the Ionosphere*** introduces the region of the earth's atmosphere which is the object of study. Its purpose is to familiarise the reader with basic concepts which pertain to the ionosphere. The chapter starts with the discovery of the ionosphere and continues by outlining the early work undertaken by scientists to investigate its properties. Some ionospheric measurement techniques are described. A somewhat more thorough account of the ionosphere and its quite distinct regions follows. Each region's characteristics are discussed as are several key solar and geomagnetic indices and the sources of index data.

**Chapter 4 — *Empirical Modelling of the Ionosphere*** introduces the three empirical ionospheric models used in this research and the GPS single-frequency Broadcast model. A brief description of each model's salient points is given. This includes details of the model profiles, required user input, and output parameters. The chapter concludes with details of adaptations of the models which were necessary in order for their use in this research. Execution times are given and comments are made with respect to the practical aspects of using such models.

**Chapter 5 — *Model Testing & Data Processing*** describes the method by which each of the four ionospheric models was tested. Processing of a dual-frequency GPS data set to obtain ionospheric delays is described in a step-by-step fashion. A description of a Faraday rotation set of ionospheric measurements is also given.

**Chapter 6 — *Analysis & Results*** outlines the statistical procedures which were adopted in order to compare modelled ionospheric delays with those obtained from the dual-frequency GPS data and the Faraday rotation data. Representative subsets of the statistical analysis are listed in tabular form and an analysis of the results is given.



Comments on model performances are made and suggested strategies for their use are proffered.

**Chapter 7 — *Conclusions & Recommendations*** is the final chapter of this thesis. This chapter comments on the successes and short-comings of this research and outlines some strategies for further related work.

## Chapter 2

# ***The Global Positioning System***

The main thrust of this thesis is to test the suitability of ionospheric models as tools to aid single-frequency users of GPS. There are many texts which detail the workings of GPS at some length; such an exposé is not the main concern in this work. Instead a brief description of some of the system's salient points is presented. There are many full accounts of the system's features (e.g., *The Institute of Navigation* (1980, 1984, and 1986); *Wells et al.* (1986)) and it is towards these that the interested reader is directed.

In 1973 the United States Department of Defense began work on the satellite-based positioning system known as Navstar GPS. Its initial goal was to design and implement a system which was capable of providing velocity, time, and positional information to military personnel. This mandate has now expanded to encompass any suitably equipped group wishing to use the signals. The information not only had to be accurate, it also had to be available at any time and from any location on earth. In line with these criteria a system composed of three segments was designed: the space segment, the ground control segment, and the users.

### **2.1 The GPS Space Segment**

When fully deployed in the mid-1990s the GPS satellite constellation will consist of 24 satellites (of which 3 will be "active spares") in 6 orbital planes. Each of the 6 orbital planes will be inclined at 55° to the equator, and each plane will contain 4 satellites. The

satellites will describe nominally circular orbits at a nominal altitude of 20 183 km with an orbital period of 12 sidereal hours.

There are currently seventeen functioning satellites in orbit (as of March 28th, 1992). Five of these are Block I (prototype) satellites, the remaining 12 are Block II and Block IIA (production) satellites. As their name suggests the Block I satellites were designed to test the concept behind positioning with GPS; they were designed to have a lifetime of about 5 years and in many cases this life expectancy has been exceeded. The most common cause of failure has been attributed to the satellite clocks. All satellites have various backup systems built into them so that should a component fail, a clock for example, a spare can be switched on in its place. Eventually these backup systems themselves fail and the satellite's operation is then terminated.

## **2.2 The GPS Control Segment**

The control segment is the ground-based part of GPS which consists of five control stations (Hawaii, Colorado Springs, Ascension, Diego Garcia, and Kwajalein) more or less evenly spaced in longitude around the world. Each of the stations operates as a monitor station: they are equipped with dual-frequency GPS receivers to monitor all GPS signals, environmental data sensors (so that tropospheric delays can be estimated), atomic frequency standards, and computers to control operations. The tracking data from each of the monitor stations is transmitted to the Master Control Station in Colorado Springs so that satellite ephemerides and clock corrections can be computed. The Master Control Station is also responsible for the control of the orbital corrections that reassign each satellite to its designated orbit should the need arise.

The Master Control Station transmits the navigation message information and other data (to the Ascension, Diego Garcia, or Kwajalein stations) ready for uploading to the GPS

satellites. Such an upload includes information on the ephemerides and clock corrections supplied by the Master Control Station as well as other broadcast message data (e.g., satellite health, coefficients for the single-frequency ionospheric model, etc.) and command telemetry.

### **2.3 The GPS Signals**

GPS satellites transmit navigation signals on two frequencies. The two carriers are called L1 and L2 and their frequencies are multiples of the GPS fundamental frequency which is 10.23 MHz. The L1 frequency is 1575.42 MHz and the L2 frequency is 1227.60 MHz. The L1 carrier is modulated by a pseudorandom noise code (PRN — binary sequences of ones and zeros) called the C/A-code, it repeats every millisecond. Both the L1 and L2 carriers are modulated by a second PRN sequence known as the P-code. The P-code repeats every 267 days, seven day segments of which are assigned to different satellites for transmission. Finally, a third modulation called the broadcast or navigation message is modulated onto the carriers. The broadcast message contains satellite clock correction coefficients, ephemeris parameters, almanac data, and health of satellite information amongst other things.

### **2.4 Pseudorange Observations**

These complex signals accommodate several quite distinct types of observation. The C/A and P-codes provide the so called pseudorange observations. Suitably equipped receivers generate (internally) replicas of one or both codes which are cross-correlated with the incoming codes from the satellites. The size of the shift (or lag) which is necessary to align the receiver generated code with the code received from the satellite provides the measure of the code's transit time from satellite to receiver. Scaling this transit time by the speed of light gives an estimate of the range between satellite and receiver. The wavelengths of the C/A and P-codes are about 300 and 30 m respectively.

As a rule of thumb GPS receivers can determine pseudoranges with a resolution of about 1% of the wavelength (*Wells et al.*, 1986), or 3 and 0.3 m for the C/A and P-codes respectively. This figure can be improved upon if carrier phase data can be used to smooth the pseudorange data thereby yielding improved “resolution.”

## 2.5 Carrier Phase Observations

Another possible observable is that of the phase,  $\phi$ , of the incoming carrier. As soon as the receiver is first switched on and has locked onto the incoming signal it will start monitoring the phase. At any time  $t$  after lock-on the total phase recorded by the receiver will be a combination of the integer number of cycles counted since lock-on and the fractional part of the cycle being measured at time  $t$ .

Clearly the receiver can only start to measure the phase of the signal from the time at which it is received. Thus the integer number of cycles between satellite and receiver (i.e., prior to lock-on) is unknown and is termed the cycle ambiguity or the unknown cycle count  $N$ . In order to use the carrier phase observations for determination of the satellite-receiver range the cycle ambiguity must be resolved during post-processing of the data.

The main advantage in using carrier phase measurements is that the wavelength of the L1 carrier is about 20 cm. Once again, by adopting the 1% rule of thumb it is clear that carrier phase observations on L1 can be made with a resolution of approximately 2 mm.

## 2.6 Satellite Clock Parameters

In a perfect world the GPS observations could be used to obtain three dimensional positions if three simultaneous observation were made to three satellites. Thus there would be three unknowns (the receiver’s Cartesian coordinates) and three observations.

This scenario assumes that the satellite and receiver internal clocks are perfectly synchronised with each other and with the system's master time scale (known as GPS time). In reality this is not the case. The United States Naval Observatory monitors each satellite's clock and determines, for each satellite, the clock offset and drift with respect to GPS time. The Master Control Station then uploads these parameters as part of the satellite's broadcast message. Thus the satellite's clock can be closely aligned with GPS time leaving only the receiver's clock offset with which to deal. For this reason simultaneous observations are made to a minimum of four satellites so that the receiver's Cartesian coordinates and clock offset can be determined.

## **2.7 Errors and Biases**

Biases and errors are not to be confused with one another: biases are systematic effects whilst errors are random errors and blunders. An attempt can be made to reduce the effect of a bias by utilising a model which is based upon known physical properties displayed (e.g., tropospheric modelling using the Hopfield model where the delay due to troposphere is a function of pressure, temperature, and relative humidity).

In a general sense the biases affecting GPS measurements fall into three groups: satellite biases, station biases, and observation dependent biases (*Wells et al.*, 1986). The observation dependent biases concern carrier phase ambiguities and signal propagation delays due to the troposphere and ionosphere. Satellite biases are concerned with biases in the satellite positions (or ephemerides) and satellite clock biases. User biases include receiver clock offsets and (in some applications of GPS) biases in reference station coordinates.

Errors can be considered to be those residual biases which remain after the main effects have been modelled (*Wells et al.*, 1986) in addition to multipath and cycle slips.

Multipath is a station bias caused by reflection of GPS signals off local (with respect to the receiver) reflective surfaces. The effect at the receiver is that two or more signals arrive by different paths and interfere with each other at the receiver. Cycle slips can occur when the path of a satellite's signal is temporarily blocked so that it can no longer be tracked by the receiver. Cycle slips can also occur in the presence of a highly disturbed ionosphere. In either case the recorded phase data then displays a discontinuity termed a cycle slip.

### **2.7.1 Ionospheric Delays**

The dual-frequency nature of GPS satellite signals is of crucial importance to successful use of GPS as a high accuracy positioning system. The ionosphere's dispersive nature dictates that the delay on an electromagnetic signal due to the ionosphere is inversely proportional to the square of the frequency. This means that as the frequency gets higher the effect due to the ionosphere will become smaller. At the GPS L1 frequency the ionosphere can retard the signal by as much as 30 m for observations made during early afternoon, at times of high solar activity, and to a satellite which is directly overhead. For satellites at low elevation angles the delay can be as large as 90 metres or more. The L1 and L2 carrier frequencies were carefully selected so that the ionosphere's dispersive nature could be exploited because by combining two well separated frequencies the ionosphere's effect can be virtually eliminated. Note that any other combination of similarly separated radio frequencies would be equally well suited to such a task.

In the absence of a GPS receiver which is capable of receiving both signals the ionosphere must either be ignored or a model can be employed to predict the ionosphere's effect. To cater for such users a simple model of the ionosphere was developed (Klobuchar, 1986) whose form is described by eight coefficients which form

part of the satellite's broadcast message. **Chapter 5** of this thesis describes in some detail both the dual and single-frequency techniques for eliminating or reducing the ionosphere's effect on the GPS signals.

### **2.7.2 Selective Availability**

Selective availability (S/A) is the intentional degradation of the positioning accuracy which can be obtained by non-authorised users of GPS (see *Georgiadou & Doucet* (1990)). It is affected by a combination of dithering of the clock frequency and modifications to the broadcast ephemeris. Dithering the clock frequency degrades the accuracy with which pseudoranges and carrier phases can be measured. The modifications to the broadcast ephemeris (i.e., the deliberate introduction of orbital errors) reduce the accuracy with which satellite positions and hence receiver coordinates can be determined. Official Department of Defense policy dictates a two-dimensional position accuracy of 100 m (at the 95 to 98% probability level) in the presence of S/A. S/A will feature on all Block II satellites but is not planned for Block I satellites (although the option to implement it is reserved by the United States Department of Defense).

## **2.8 Point Positioning Accuracy with Single-Frequency GPS**

Prior to the implementation of S/A, a single-frequency C/A-code receiver was able to determine instantaneous point positions with typical accuracies of 40 metres horizontally and 60 metres vertically at the 95% probability level (*Wells & Kleusberg*, 1990). In the presence of a severely disturbed ionosphere these figures might be significantly larger. One important factor governing this accuracy level is caused by the ionosphere and the fact that a simple model is typically used to model its effect on the observations. There are few references dealing with the effects of data processing with and without the inclusion of such ionospheric corrections. *Lachapelle & Wade* (1982) did however state that "using pseudo-range observations gathered in the P code, two frequency mode, an accuracy of the order of 10 m can routinely be achieved for quasi-instantaneous (four to



five minute period) positioning when four satellites are simultaneously available in a reasonably good geometry. The use of C/A code, one frequency, observations does not produce any apparent deterioration of the solution at the above accuracy level if the effect of the ionosphere is taken into account. Daily solutions made at irregular intervals over a five month period indicate a repeatability of about 10 m.” In the same research it was found that the accuracy from C/A code, single-frequency, observations actually improved considerably in the absence of the ionospheric correction but no explanation for this was proffered.

## 2.9 Chapter Summary

A basic understanding of GPS has been given in this chapter. The system’s components have been described as have two measurement types and the associated errors and biases which a user might expect to encounter. From the standpoint of ultimate point positioning accuracy it is obvious that carrier phase measurements are desirable. Such measurements are not without their own difficulties however and it has been mentioned that cycle slips and the resolution of integer ambiguities can sometimes present difficulties. Pseudorange measurements suffer from neither of these hindrances; they do not however offer the ideal positioning solution due to the intrinsically longer wavelengths of the C/A and P-codes which can be only be resolved roughly at the 3 and 0.3 m levels respectively. Additionally, problems due to S/A and an ionospheric model which is of limited accuracy must be dealt with.

The next chapter (**Chapter 3**) introduces the ionosphere — starting with its discovery and continuing by outlining the early work undertaken by scientists to investigate its properties — and familiarises the reader with the basic terminology, concepts, characteristics, and morphology associated with this region of the earth’s atmosphere. Some ionospheric measurement techniques are described as are several key solar and geomagnetic indices.

## *Chapter 3*

### ***Some Characteristics of the Ionosphere***

The ionosphere's existence was first postulated by Balfour Stewart in 1882 (Ratcliffe, 1970). He suggested that the regular fluctuations experienced throughout the day by a compass needle might be attributed to electric currents in the high atmosphere. Because two phenomena, the aurora and geomagnetism, were observed easily using simple equipment there were early speculations about the electrical state of the upper atmosphere.

In 1901 Marconi successfully transmitted radio signals from England to Newfoundland — a feat which, at the time, was difficult to explain. In 1902, shortly after Marconi's success, Heaviside in England and Kennelly in America suggested (almost simultaneously and quite independently) that for the radio signals to have traversed the Atlantic they must have “bounced” off an overhead reflector. They suggested that this reflector was probably formed from free electrical charges in the upper atmosphere. Subsequently, the then hypothetical layer became known as the Heaviside layer.

Following Marconi's success, the 1920s saw commercial communication links established across the Atlantic. Measurements of the strengths of the received signals revealed regular variations in the strength on a daily, seasonal, and solar cycle basis. It was further noticed that the regular daily variation was disturbed whenever a geomagnetic storm occurred.

Verification of the existence of the Heaviside layer came later when in 1925 Appleton and Hartree in England, and shortly thereafter Breit and Tuve in the United States, established both the existence and altitude of the Heaviside layer. Breit and Tuve employed short pulses of radio energy at vertical incidence and showed that a radio wave travelling nearly vertically during darkness was reflected from the Heaviside layer (*Breit & Tuve*, 1926). This result was important because it suggested that radio waves could possibly be used as a tool to explore the nature of charged particles in the ionised upper atmosphere. From the delay time between the transmitted and reflected pulses and assuming waves propagated at the speed of light, the height of reflection could be determined. Transmissions at different frequencies produced different heights of reflection. This effect is now known to be the result of an altitude variation in the density of free electrons. The work of Appleton and Barnett and Breit and Tuve provided the basis for modern day ionospheric soundings.

It is clear that the discipline of ionospheric physics finds its roots in measurements of those early trans-Atlantic radio transmissions which could only be explained by means of a reflecting layer composed of electrons and positive ions. Further investigation pointed towards the existence of reflecting layers in addition to the Heaviside layer. Indeed most of the early work attempted to explain the various layers and their variability with latitude, local time, season, etc. It did not take long to realise that the ionosphere's behaviour ranged from the very stable and reproducible electron density profiles to the rather chaotic. Periodic and aperiodic behaviour was also noticed with time scales ranging from 11 years (the average period of the solar cycle) to a few seconds. These early discoveries formed the building blocks upon which all subsequent ionospheric research has been based.

### 3.1 Nomenclature of the Earth's Atmosphere

Scientific study of the earth's upper atmosphere has necessarily led to the acceptance of suitable nomenclature to describe its various parts. This description is based upon the dominant physical processes, chemical composition, or temperature. If, for example, we consider the temperature distribution of the neutral atmosphere we talk about the mesosphere which represents a region of decreasing temperature with increasing height, and which lies approximately between the bounds of 50 and 85 km. Above 85 km we refer to the thermosphere where temperature increases with height. Sometimes the boundary locations of the atmosphere's various regions are well known and can be specified to within a few kilometres. At other times the bounds are less clear and may only be specified to within tens or hundreds of kilometres.

**Figure 3.1** illustrates some of the nomenclature associated with the earth's ionosphere and neutral atmosphere and illustrates typical electron density profiles up to altitudes of 5,000 km. In the case of the electron density profiles, the light and heavy lines represent typical mid-latitude night-time and day-time profiles respectively.

### 3.2 Ion Production

The ionosphere is defined by *Rishbeth & Garriott* (1969) as "the part of the earth's upper atmosphere where ions and electrons are present in quantities sufficient to affect the propagation of radio waves." Incident solar radiation and (to a far **lesser** extent) cosmic radiation cause the atmosphere's neutral constituents to dissociate into positive ions and negative electrons. The energy responsible for this ionisation is found in the ultraviolet and soft x-ray regions of the electromagnetic spectrum, although particle radiation also contributes during solar storm periods (*Davies*, 1966).

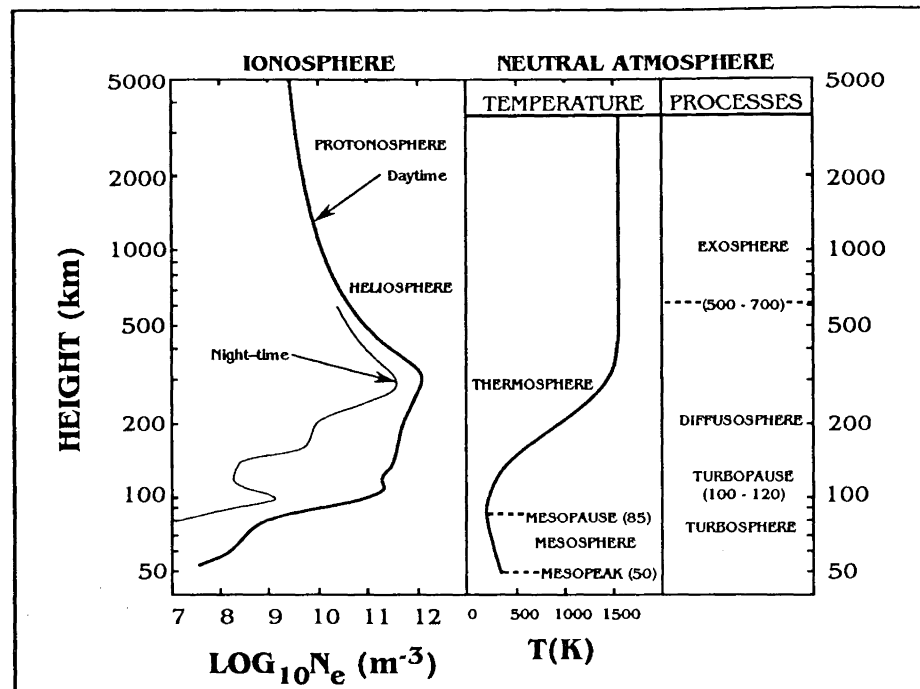


**Figure 3.1** – Atmospheric Nomenclature (after Van Zandt & Knecht (1964))

There is almost full ionisation above about 1,000 km but this part of the atmosphere is so tenuous that the concentrations of electrons and ions are very small. Below about 1,000 km there is far more gas to be ionised. Incident solar radiation is therefore more strongly absorbed and as a consequence the ion concentrations are greater. At still lower levels (below about 50 km) the radiation has been “used up” so that the degree of ionisation is again small (*Budden, 1985*). The ionosphere is generally regarded as that part of the earth’s atmosphere whose lower and upper bounds are **approximately** 50 km and 2,000 km respectively, although in reality the upper boundary should be extended until it merges with the interplanetary plasma.

### 3.3 The Ionosphere’s Total Electron Content Defined

**Figure 3.1** shows curves which represent both the night-time and daytime vertical electron density profiles through the ionosphere. Integration of this quantity (or of a slant electron density profile) leads to a quantity termed **total electron content** (TEC).

TEC can be thought of as representing the number of electrons found in a column (whose cross-sectional area is  $1 \text{ m}^2$ ) along the receiver to satellite path (see **Figure 3.2**).

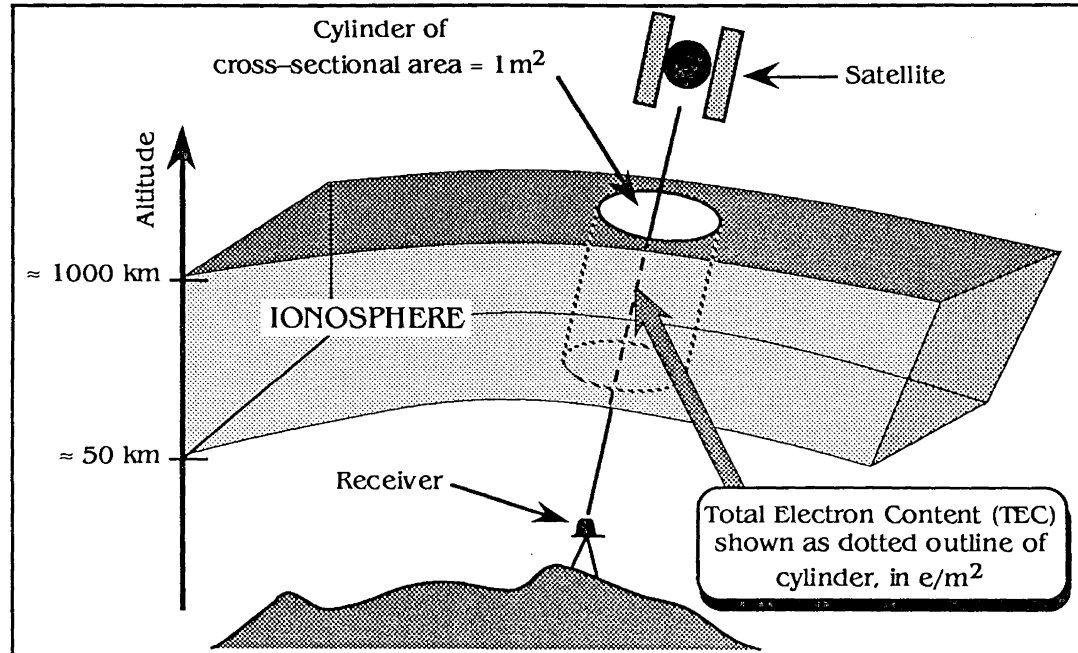


**Figure 3.2** – Total Electron Content

Throughout this thesis, if the quantity of interest is the vertical TEC (or VTEC) then this will be explicitly stated and the term VTEC will be used.

### 3.4 Ionospheric Structure

Following on from the work of Breit and Tuve it was expected that as the frequency of the transmitted wave was gradually increased the height at which the wave was reflected would also rise, and that it would continue to rise until such time as it reached a peak of the layer where the electron concentration had its maximum value. If the frequency were then to be further increased it was expected that the wave would escape into space without reflection, and that the frequency at which this occurred (the penetration frequency or critical frequency) would then provide a measure of the electron concentration at the peak. This was what was expected. However, practical experiments

revealed a quite different truth when Appleton found that once the peak of the layer had been reached, and the frequency of the transmitted wave was increased, the radio-wave did not go into outer space but was reflected off another layer at a greater height. Appleton had discovered another layer which was, naturally, known as the Appleton layer in order to distinguish it from the Heaviside layer.

Appleton observed that were additional layers to exist it would be somewhat clumsy to name each one after the name of the scientist responsible for its discovery. He therefore decided that the layer discovered by Heaviside should be termed the E layer whilst the Appleton layer would in future be termed the F layer. By so doing he left room to label any remaining (and as yet undiscovered) layers, above and below, with neighbouring letters of the alphabet. Several different ionospheric layers and regions have been discovered — the D region, E, and F layers, the heliosphere and the protonosphere — but undoubtedly the principal ones are the E and F layers. The upper boundary of the ionosphere is not well defined, but merges into (or may be extended to include) the heliosphere, where neutral and ionised helium are important constituents, and the protonosphere, which is composed principally of ionised hydrogen. Both the heliosphere and the protonosphere are poorly defined in extent (*Rishbeth & Garriot, 1969*).

For the sake of convenience the E and F layers are further sub-divided. **Table 3.1** summarises the ionospheric layers, the approximate heights at which the layers occur, the approximate heights of their respective maximum electron densities, and the magnitude of the peak electron density in each layer. Due to uncertainty and variability these heights should not be taken as definitions but merely as convenient guide-lines. **Table 3.1** refers both to regions and layers; this distinction is quite deliberate as — unlike the E and F layers — the D region displays no distinct layers or ledges.

Regions & Layers	Height Range (km)	Identified Sub-Divisions	Ht. of Max. Electron Density (km)	Peak Electron Density ( $e/m^3$ )
D region	50 – 90	D	N/A	$10^9$
E layer	90 – (120 – 140)	E, Es	90 – 140	$10^{11}$
F layer	Above (120 – 140)	F1, F2	200 – 450	$10^{12}$

**Table 3.1** – Ionospheric Layers, their Subdivisions, and Heights

### 3.5 Measurements of the Ionosphere

The next logical step toward a more complete understanding of the ionosphere was to determine the magnitude of the electron densities at the layer peaks. Much of the available information concerning the ionosphere has been gained through the study of vertical incidence ionospheric sounding — using instruments (called ionosondes) similar to those used by Breit and Tuve — and incoherent backscatter experiments. Faraday rotation measurements of TEC have also added greatly to our knowledge of the ionosphere.

#### 3.5.1 Ionosondes (and Ionograms)

An ionosonde (**Figure 3.3**) automatically sweeps a pulse transmitter through a frequency band of about 1 to 20 MHz. A typical ionosonde record (called an ionogram — **Figure 3.4**) presents a plot whose vertical coordinate gives the height of reflection of a pulse whose frequency is given by the horizontal coordinate. The critical frequencies of the ionospheric layers can then be read off the ionogram and the peak electron densities computed. In **Figure 3.4** the partial split of the F layer into the F1 layer (or ledge) and F2 layer is seen. Some ionosondes record the data on magnetic tape or as digital information, some are linked to computers for control of the frequency and aerial systems and processing of electron density profiles (*Budden, 1985*).



Such ground-based ionosondes only provide information about the electrons below the F layer peak. In September 1962 the Canadian satellite Alouette 1 was launched into a circular orbit at an altitude of about 1,000 km. On it was mounted the first satellite-based compact sweep-frequency ionosonde operating on radio frequencies of 0.5 to 11.5 MHz. The ability to explore the topside ionosphere (i.e., above the F layer peak) was introduced.

The time of travel of the reflected pulses are measured on board the satellite and the results sent to a ground receiving station by telemetry to be displayed as a topside ionogram. Because the topside ionosonde is on a satellite which repeatedly orbits the earth, it provides information about the electron distribution in the upper part of the F region over a wide area. In this way information about the ionosphere above the F layer peak is obtained which, when combined with the earth-based (or bottomside) sounder's information, makes it possible to study the ionosphere up to the height of the satellite.

The ionogram may be thought of as providing a picture of the ionosphere. Suitable techniques enable the record to be translated to yield the curve of electron density vs. height (similar to the curve shown in Figure 3.1 for example). Suitable analysis of the ionogram yields the associated electron distribution. Such an analysis is however no straightforward matter and description of the techniques is not within the scope of this thesis. The interested reader is however directed towards the clear account which is given in *McNamara* (1991) and the detailed account of *Piggott & Rawer* (1972).

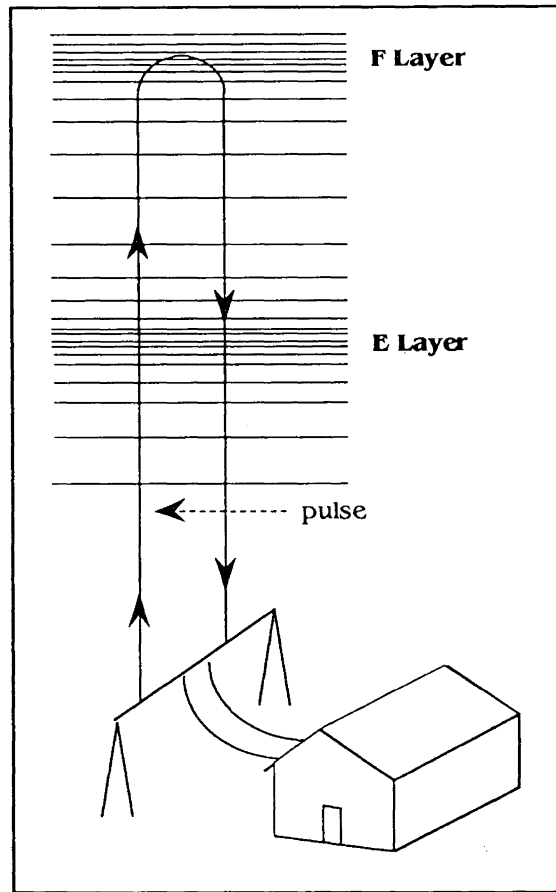


**Figure 3.3** – Sounding the Ionosphere with an Ionosonde (after *Ratcliffe* (1970))

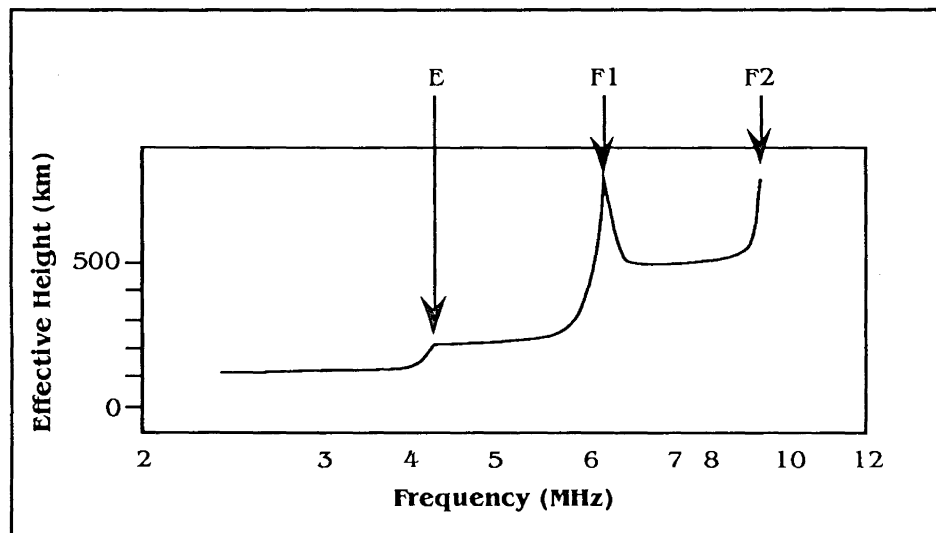


**Figure 3.4** – The Record from an Ionogram (after *Ratcliffe* (1970))

Sometimes on ionograms recorded during summer daylight hours, near the magnetic equator or auroral regions, another penetration frequency is clearly visible somewhere between the E and F layer peaks (**Figure 3.4**) at heights of about 115 km. This thin (often less than 1 km thick (*Rawer et al.*, 1981)), but intensely ionised layer is confined to relatively localised areas of radius 1,000 to 2,000 km. Its occurrence is irregular in space and time and it is therefore known as the ‘sporadic E layer,’ or Es. There are many different types of sporadic E and it is believed that they are caused by large vertical gradients of horizontal wind speed (or wind shear). Ionisation by meteorites may also have some effect, and at auroral latitudes precipitation of charged particles may contribute (*Budden*, 1985). For an Es layer that is 10 km thick (this should be regarded as a maximum layer thickness for Es) the layer’s contribution to TEC would (at most) be approximately  $10^{16}$  electrons/m<sup>2</sup> ( $\approx 0.5$  ns delay at the GPS L1 frequency) (private communication, *Jack Klobuchar*, Phillips Laboratory, United States Air Force, April 1992).

### 3.5.2 Incoherent Backscatter

The region above the F layer peak has also been explored using the technique whose name is derived from the classical Thomson scattering of waves from individual electrons (*Rishbeth & Garriott*, 1969). The technique is called incoherent backscatter, or Thomson backscatter sounding. A strong beam of radio waves is directed upwards. In order that the waves escape from earth without being reflected by the F layer they are transmitted at a frequency much greater than the F layer’s penetration frequency.

**Figure 3.5** shows a radio wave passing through a collection of charged particles. As the main wave (thick black line) passes through the ionosphere it sets the electrons into oscillations (thin black lines) so that they re-radiate wavelets in all directions. The wavelets spread radially and when received in most directions they have randomly distributed phases as the electrons from which they originate are also randomly

positioned. In a direction such as A the total phase of the direct wave (thick line) and reflected wave (thin line) is different for each particle and the combined wave is weak. Only in the forward direction B does the phase of the main wave and re-radiated wave add coherently producing a resultant wave of changed velocity. As the technique's name implies, use is made of the fact that the wavelets returned backwards towards the ground add with random phases ('incoherently') to produce a very weak signal which can be collected by a large aerial and measured using a sensitive receiver.

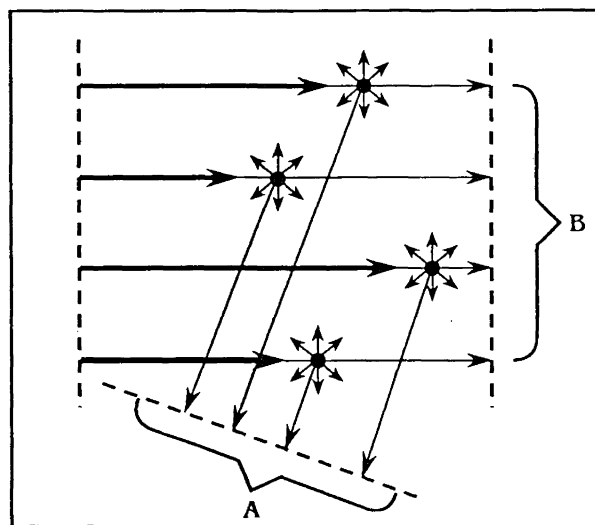


**Figure 3.5** – A Radio Wave Passing through a Collection of Charged Particles

(after Ratcliffe (1970))

As the main wave advances, each electron radiates an amount of energy which is equal to that which falls upon its cross-sectional area (which is about  $10^{-25} \text{ cm}^2$ ). Clearly the cross-sectional area of each electron is very small as is the amount of re-radiated power. In order to obtain a signal which is of sufficient size to be measured, the power radiating from a large volume of the ionosphere is collected. A large volume of the ionosphere — a cube with 100 km sides centred at a height of 700 km for example — contains about  $10^{25}$  electrons. Adding the cross-sectional areas of these electrons together results in a total radiating surface area of about  $1 \text{ cm}^2$  which, although small, now allows the re-

radiated power to be measured. By comparing the power scattered from a known volume with the power scattered from one electron, the number of electrons in the volume is determined. Two techniques for obtaining data above the F layer's peak have now been examined. Topside sounding provides information about the electron distribution at several locations and times. Incoherent backscatter on the other hand provides a continuous stream of data for one place. The two techniques are complementary.

### 3.5.3 Faraday Rotation Measurements of the Ionosphere's TEC

In 1845 Michael Faraday discovered that when plane polarised light passed through lead glass in the direction of a magnetic field, the plane of polarisation was rotated. This phenomenon became known as the **Faraday rotation**, or the **Faraday Effect**. Faraday rotation has since been observed in many media over a wide range of frequencies. In a plasma, such as the ionosphere, the free electrons contribute to this effect at radio frequencies.

In ionospheric studies the Faraday rotation technique employs ground-based measurements. A linearly polarised signal emitted by a satellite of opportunity travels right down through the ionosphere. As the plane polarised wave enters the ionosphere it can be considered to split into two characteristic waves, each of which has its own polarisation. The two waves have different phase velocities and their **phase difference** changes as they progress through the ionosphere. Thus the polarisation angle of the radio wave rotates on its way through the ionosphere by an amount which depends on the number of free electrons encountered along the ray path. Records of this Faraday rotation therefore give a direct measure of the total electron content (TEC) along a path extending through the ionosphere between the ground station and the satellite.

The equipment required to measure this effect is much simpler than the traditional ionosonde. VHF signals received from geostationary satellites provide continuous monitoring of both short and long term variations in the ionosphere. The TEC can be recorded directly, continuously and automatically, with high accuracy and resolution, and at low cost. Faraday rotation measurements to geostationary satellites should be considered to give the integrated electron content up to a fixed height of 2,000 km with an accuracy of approximately 3 to 5% (*Titheridge, 1972*). Changes of electron content as small as 0.1% are detectable (*Rishbeth & Garriott, 1969*).

### **3.6 Temporal and Geographic Variations of the Ionosphere**

Extensive measurements of the ionosphere have been made for decades, from many locations around the world, using bottomside ionospheric sounders, topside ionospheric sounders, and incoherent backscatter and Faraday rotation equipment. Interpretation of these data has enabled scientists to build an expanded understanding of the complex relationships which exist between solar conditions, geomagnetic activity, time of day, season, geographic location, and the resulting state of the ionosphere at any particular time and location.

The height and thickness of the ionospheric layers varies according to the prevailing solar and geomagnetic conditions, time of day, geographic location, and season. The resulting electron concentrations vary accordingly. **Figure 3.6** gives a cursory insight into the temporal complexities of ionospheric behaviour by illustrating the variation of the D, E, F1, and F2 layers during daytime and night-time in the summer and winter seasons.

It can be seen that the layers are subject to diurnal and seasonal variations in height and thickness — at night the layers become thinner and the D region **usually** disappears

altogether. This figure is approximate because although the layers occasionally behave in an easily predictable manner, their behaviour is often anomalous. Combining the layers together and looking at the net effect — the TEC for example — shows that its behaviour also ranges from the easily predictable to the chaotic.

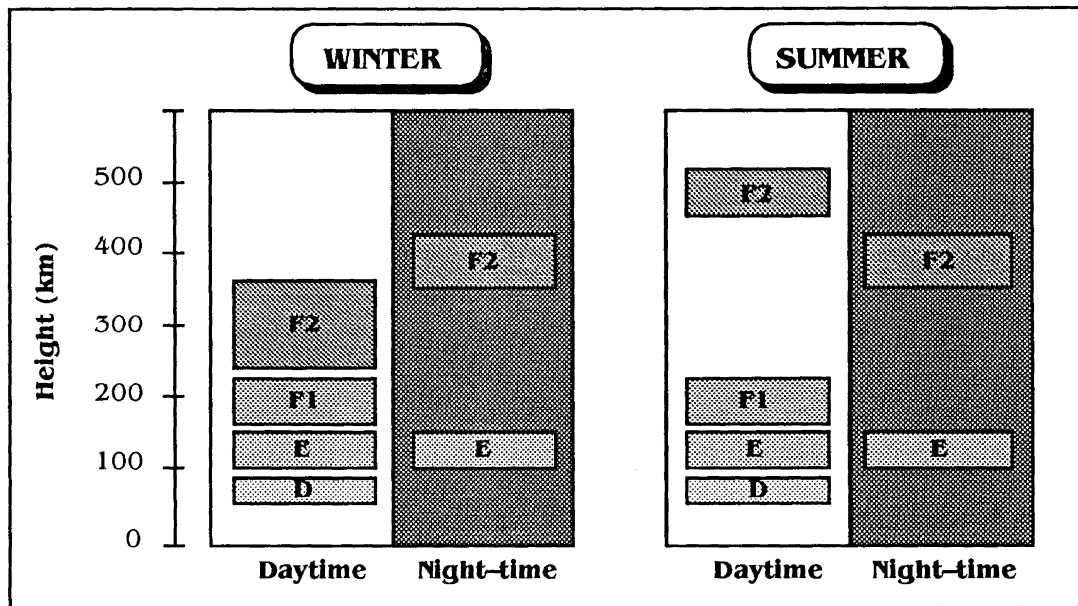


**Figure 3.6** – Daytime, Night-time, and Seasonal Height Variations  
of the Ionospheric Layers (after *Burnside* (1982))

The following paragraphs summarise a few of the salient points with respect to the behaviour of the D region and the E, F1, and F2 ionospheric layers. The description of events is based upon the particularly clear accounts which are given by *Ratcliffe* (1970) and *Van Zandt & Knecht* (1964). It will become clear that **the ionosphere's behaviour is at times far from straightforward, predictable, or easily modelled.**

### 3.6.1 The D Region

The D region is that part of the ionosphere which extends from about 50 to 90 km in height. Below heights of about 70 km cosmic radiation is an important ionising agent in

this region. Cosmic radiation consists of charged particles from outer space and the sun which move so rapidly that they can penetrate to ground level without much loss of energy. Perhaps most importantly, the amount of cosmic radiation which reaches the earth is the same by day and by night. The D region's peak electron concentration occurs at about 60 to 70 km. Because the ionisation is caused by cosmic radiation, which is deviated by the earth's magnetic field, the D region's electron concentrations are greater at the earth's poles.

Despite the fact that the cosmic radiation impinges on the earth equally strongly at all times, the related electron concentrations do not remain constant. At heights of about 60 to 70 km, and at night, the electrons collide so frequently with the molecules that most of them attach themselves to the molecules to form negative ions (*Ratcliffe, 1970*). The related number of free electrons is therefore very small. During the day, radiation from the sun causes the electrons to detach from the negative ions and a related increase in the number of free electrons ensues. Therefore the D region electrons are present by day but not by night.

At heights of 70 to 80 km the electron concentration increases gradually from sunrise to midday and then decrease towards sunset. At lower heights (where cosmic radiation is the most important ionising agent) there is a sudden increase in electron concentration at sunrise (remember that solar radiation now causes electrons to detach from the negative ions to leave many more free electrons) to a level which remains constant during daylight hours. This is followed by a sudden decrease at night when once again the electrons become attached to molecules to form negative ions.

There are interesting variations with the solar cycle also. At heights of 70 to 80 km (where solar radiation is the more important ionising agent) the electron concentrations



are greater at solar maximum than at solar minimum. In the lower part of the D region — below about 60 km, and where cosmic radiation is the more important ionising agent — this characteristic reverses itself and electron concentrations are found to be **greater** during solar minimum than they are at solar maximum. This trait is due to the fact that the flux of galactic cosmic rays reaching the earth is smaller at sunspot maximum than at minimum (*Rishbeth & Garriot*, 1969).

Clearly the D region displays quite distinct and regular patterns of behaviour both diurnally and in terms of the 11 year solar cycle. There are, however, also irregularities to its behaviour, most notably the Sudden Ionospheric Disturbance (SID). The SID is a large simultaneous increase in electron density over the entire day hemisphere. SID's are caused by a large increase in the solar x-ray flux accompanying some large solar flares. They last a few minutes to several hours (*Van Zandt & Knecht*, 1964). Also, increased radio wave absorption is observed on some winter days due to increased ionisation.

### 3.6.2 The E Layer

The daytime E layer is the best known of all the ionospheric layers, both observationally and physically. Observationally, the huge number of vertical incidence ionosonde observations of the maximum density of the E layer,  $NmE$ , have established that the daytime E layer is quite regular in its temporal and geographical variations. Not only does  $NmE$  depend almost entirely on the activity and zenith angle,  $\chi$ , of the sun, with only small corrections for beforenoon versus afternoon and for geographical location, but the E layer is almost free from the striking disturbances so characteristic of the D and F regions. Outside Arctic regions the largest daytime disturbance the E layer undergoes is at the time of an SID, during which the peak electron density of the layer may increase by as much as a factor of 2. Such a disturbance may last for several hours.

### 3.6.3 The F1 Layer

When it is present, the F1 layer is a ledge or occasionally a layer on the bottom of the F2 layer. The F1 layer partakes both of the regularity of the E layer and the variability of the F2 layer. When it is present, its mean behaviour is very much like that of the E layer. Also, like the E layer, the F1 layer disappears at night.

During the day, the shape and existence of the F1 layer are variable. When it is present, its shape usually changes rapidly in the span of fifteen minutes or so, and its onset in the morning and disappearance in the afternoon are variable from day to day. The F1 layer tends to appear when the solar zenith angle is small and is enhanced by decreases in solar activity, by solar eclipses, and especially by ionospheric storms.

The F1 layer also exhibits geomagnetic control. For a given local time the critical frequency of the F1 layer,  $foF1$ , tends to be more nearly equal at the same geomagnetic latitudes than at the same geographic latitudes (see **Figure 3.7**).

### 3.6.4 The F2 Layer and its Anomalous Behaviour

Much interest was shown in the F2 layer during the Second World War when radio communications were so important. In order that the best frequencies could be chosen for radio communications both the Germans and the Allies set up ionosondes in many parts of the globe so that penetration frequencies of the ionospheric layers could be studied. This research continued, on a much larger scale and with a greater sense of international cooperation, after the war. Studies of the ionosphere formed an important part of the International Geophysical Year in 1957–1958 and there were about 200 globally distributed ionosondes in operation. Consequently much was learnt about the F2 layer.

The F2 layer has many anomalous characteristics which do not necessarily have distinct physical causes (*Rishbeth & Garriott, 1969*). The penetration frequency of the F2 layer often reaches its maximum either just before or just after midday. Sometimes there are two maxima either side of midday. This characteristic is known as a diurnal anomaly.

Due to its height the F2 layer continues to be exposed to solar radiation for a few hours, after sunset is observed directly below at a particular spot on earth. Therefore the related F2 layer electron concentrations remain quite high for a few hours after sunset. Throughout the night the underlying trend is for the electron concentration to decrease gradually until daybreak the next day when it once again starts to rise. This gradual decrease is not very often a smooth one. Sometimes at night there is a sharp increase in electron concentration for which direct solar radiation certainly cannot be the responsible agent (*Ratcliffe, 1970*).

Behaviour of this kind is most easily seen in polar regions when, for a few weeks each year (during winter), there is no sun to illuminate the earth's poles or to impinge upon the polar ionosphere. Yet, at such times, the peak electron density of the F2 layer can be seen to behave in much the same way as it would were solar radiation to be present. That is, at "polar midday" the electron concentration is at its greatest and at "polar midnight" the electron concentration is at a minimum. Clearly, and despite the absence of direct solar radiation, there is a source of electrons that is controlled by the sun's photon radiation despite the fact that it is unable to directly impinge on the layer (*Ratcliffe, 1970*).

The mid-latitude F2 layer also displays a seasonal variation known as the seasonal or winter anomaly where the maximum electron density of the layer ( $NmF2$ ) tends to be greater in winter than in summer. The winter anomaly is a daytime characteristic (it

disappears at night) which becomes apparent as solar activity increases (it is not seen during sunspot minimum) (*Rishbeth & Garriott, 1969*).

Most importantly, examination of the wartime measurements revealed that as distance increases either side of the equator the electron concentration increases until it reaches its peak at about 20 degrees north and south of the equator, sandwiching an equatorial minimum. Moving further north and south of the 20 degree maxima, the electron concentrations decrease towards the poles. Further examinations have shown this equatorial minimum to be controlled by the earth's magnetic field.

The F2 layer displays much by way of anomalous behaviour. This anomalous behaviour not only affects the F2 layer during normal times; in fact it is often at its worse during magnetic storms. During a magnetic storm there is an associated injection of rapidly moving electrons into the auroral zones accompanied by an increased flow of electrical current in the same areas. However, the F layer is profoundly disturbed over the whole of the earth. The penetration frequency will either increase or decrease and the layer usually becomes thicker.

### 3.7 The Earth's Magnetic Field

The earth's magnetic field, or geomagnetic field, can be approximated with a simple earth-centred dipole (i.e., the best fitting dipole field to the earth's actual magnetic field). The dipole axis cuts the surface of the earth at the south and north geomagnetic poles (**Figure 3.7**) the coordinates of which are 78.3°S, 111°E and 78.3°N, 69°W respectively (*Davies, 1966*). The plane through the centre of the earth perpendicular to the dipole axis is called the dipole equatorial plane and the circle about the earth is the dipole equator (at which the lines of flux are approximately parallel to the earth's surface). The relationships between dipole coordinates ( $\varphi_m, \lambda_m$ ) and the corresponding geographic coordinates ( $\varphi_g, \lambda_g$ ) are given in the following standard equations (e.g., *Davies (1966)*)

$$\sin \varphi_m = \sin \varphi_g \sin \varphi_0 + \cos \varphi_g \cos \varphi_0 \cos(\lambda_m - \lambda_0) \quad (3.1)$$

$$\sin \lambda_m = \frac{\cos \varphi \sin(\lambda - \lambda_0)}{\cos \varphi_d} \quad (3.2)$$

where  $\varphi_0$  and  $\lambda_0$  are the geographical coordinates of the north geomagnetic pole. Scientists use slightly different nomenclature from that mentioned above when describing the earth's actual magnetic field: the poles are referred to as the dip poles (where the earth's magnetic field is vertical); the equator as the dip equator (where the earth's magnetic field is horizontal); and latitude as dip latitude.

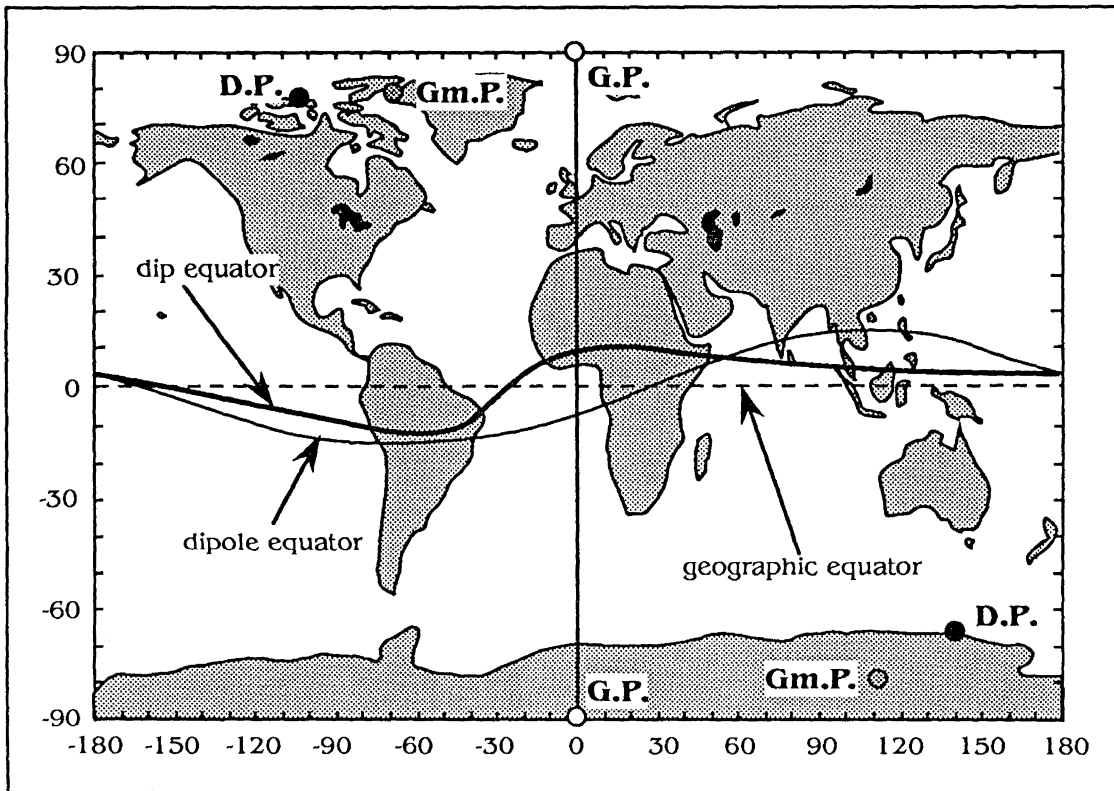


**Figure 3.7** – The earth's dip poles (D.P.) and geomagnetic poles (Gm.P.) do not coincide with the geographic poles (G.P.). The earth's dip equator and geomagnetic equator are not coincident with the geographic equator.

### 3.8 Ionospheric and Magnetic Storms

Violent eruptions on the sun's surface (known as solar flares) are responsible for the occurrence of **ionospheric storms**. The ionosphere's response to a solar flare is not instantaneous; there is typically a 2 to 4 day delay between the solar flare and the ionospheric storm which it causes. This is advantageous for the GPS user, for example, as it allows plenty of time to predict the onset of an ionospheric storm. There is a high degree of variation in terms of the size and duration of a solar flare; most of them occur at times of high solar activity and most of them are very small (as is the associated ionospheric storm). Sometimes the solar flare's effect on the ionosphere can be quite severe; the effect is seen in the ionosphere's critical frequency,  $f_oF_2$ , which can either increase or decrease. The effects of the ionospheric storm are greater in the equinoxes and in summer than in winter and are greater at higher latitudes. That is, the equatorial regions are less affected than the polar regions.

Magnetic storms occur in conjunction with ionospheric storms and have the same causes. The earth's geomagnetic field is roughly constant but high sensitivity measurements reveal constant fluctuations in magnitude and direction. Some are rapid changes with periods of minutes or even fractions of a second whilst others are longer daily variations or ones with periods of years. Most of these changes are quite small — only a fraction of 1 percent of the magnitude of the surface field. However, during a large magnetic storm there may be a field change as large as 1 or 2 percent. Such magnetic storms are often accompanied by auroral displays and ionospheric disturbances, especially in the polar regions of the earth (Cahill, 1964).

**Magnetic storms** comprise a very complicated sequence of phenomena. Theories of storms are tentative, and individual storms vary so much that exceptions may be found to almost any description of the observed phenomena. Magnetic storms are initiated by

solar disturbances and most severe storms have a sudden commencement (SC) which takes place one or two days after a solar flare, but many storms cannot be definitely attributed to any particular flare. Large flares are most common at sunspot maximum, and SC storms are most frequent then. Another type of storm, common during the declining part of the solar cycle and generally weaker than the SC type, is not associated with flares. These storms often start gradually with no SC and tend to recur at intervals of 27 days, the period of the rotation of the sun at its equator as viewed from the earth. Sometimes in a sequence of recurrent storms, some have an SC and some do not. These phenomena have been attributed to periodic immersion of the earth in particle streams emitted, more or less continuously, from active areas on the sun which have become known as (magnetic) *M* regions.

### 3.9 The Ionosphere's Major Geographic Regions

**Figure 3.8** shows the major geographic regions of the ionosphere; the boundaries of which should not be taken as fixed as they vary according to the prevailing solar and geomagnetic conditions. The auroral and polar cap regions are often the most disturbed ionospheric regions where the disturbing force can be attributed to solar particle emissions which are guided along the earth's magnetic field lines into this region. These disturbances can sometimes propagate down into the mid-latitude ionosphere also. The trough region varies in width and represents an area of dramatically depleted ionisation compared with surrounding areas of the ionosphere. Of the regions depicted here the mid-latitude ionosphere is the least disturbed and can be relatively easily modelled in a statistical sense. The elongated areas shown either side of the magnetic dip equator are referred to as **the equatorial anomaly**. These areas display a strong diurnal dependence, are significantly disturbed by various processes, and **contain the highest values of TEC in the world-wide ionosphere** (Klobuchar *et al.*, 1991).

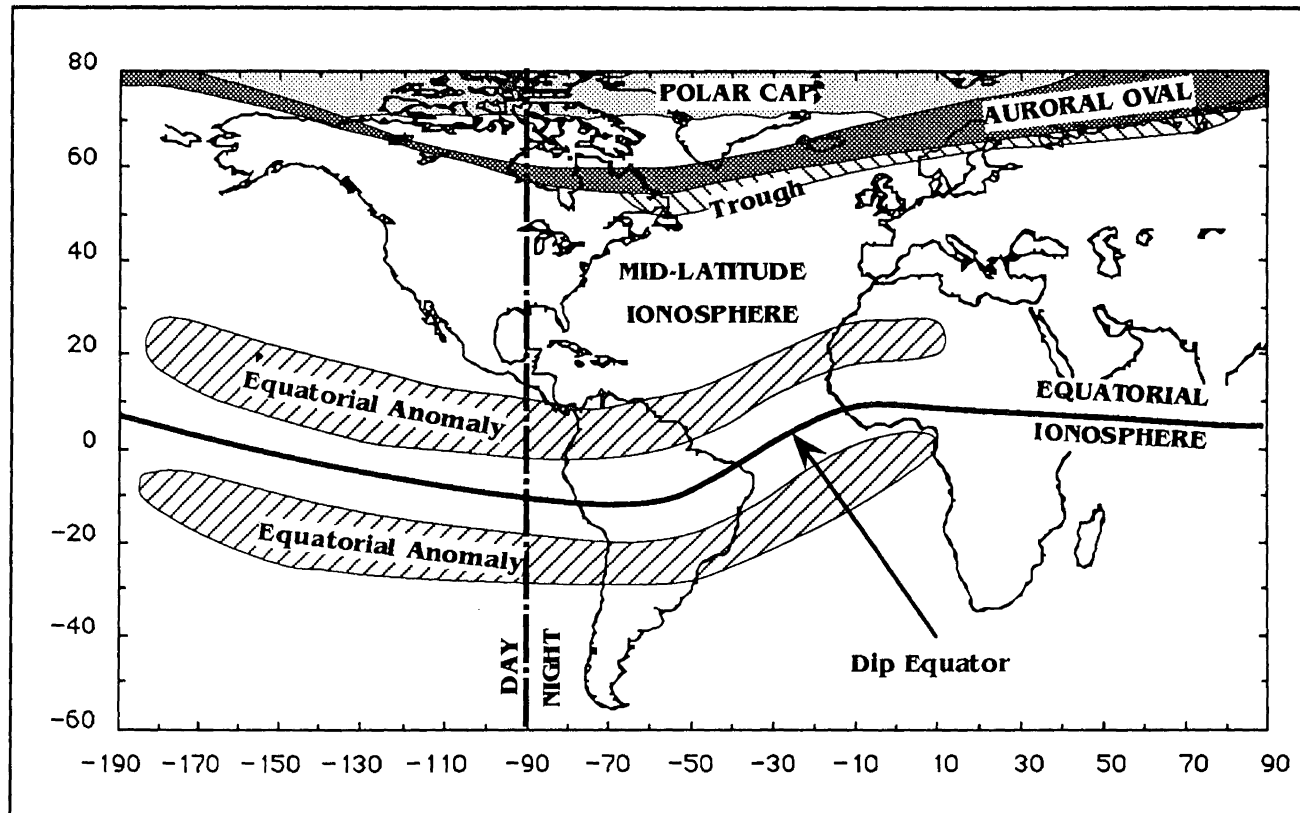


**Figure 3.8** – Major Geographic Regions of the Ionosphere (after *Bishop et al.*, (1989))



### 3.10 Solar and Magnetic Indices

Several indices of solar and magnetic activity have been developed to describe the degree of variability at any given time. Some of the work which follows in this thesis (notably the use of three semi-global empirical ionospheric models) relies on the knowledge and acquisition of sunspot numbers, solar radio flux values, and *Kp* indices. Although a number of indices have been defined only these three will be described in any detail. Data on these indices have been obtained from the National Geophysical Data Center (NGDC), Boulder, Colorado. Unless another author is specifically referenced in the following sub-sections on solar and magnetic indices, the reference material has been the notes accompanying the NGDC data sets.

#### 3.10.1 Sunspot Numbers

Dark spots (called solar sunspots) are often visible on the surface of the sun. In actuality these spots are not dark but merely appear so when seen against the brightness of the solar disc. If a sunspot could be separated from the sun and suspended in space it would be 100 times brighter than the full moon (*Ratcliffe*, 1970). Such spots were recorded as far back as 1,000 B.C. by the Chinese (*Schove*, 1983). Galileo started observing sunspots in 1611, just two years after the telescope had been invented, but records prior to 1749 are thought to be “poor” (*Hirman et al.*, 1988). Observations over the past 250 years have shown the waxing and waning of sunspots and sunspot groups to display a periodicity of approximately 11 years (**Figure 3.9**). As an interesting aside, if a spot persists for long enough it can be seen to move from one side of the solar disk to the other in 13.5 days, and then 13.5 days later it will be seen reappearing. This of course is confirmation of the sun’s period of rotation which at the equator, is about 27 days.

In 1848 the Swiss astronomer Johann Rudolph Wolf introduced a daily measurement of sunspot number. His method, which is still used today, counts both the total number of spots visible on the face of the sun and the number of groups into which they cluster, because neither quantity alone satisfactorily measures sunspot activity. In 1868 Wolf also derived sunspot numbers from data which extended back to 1700 (Schöve, 1983).

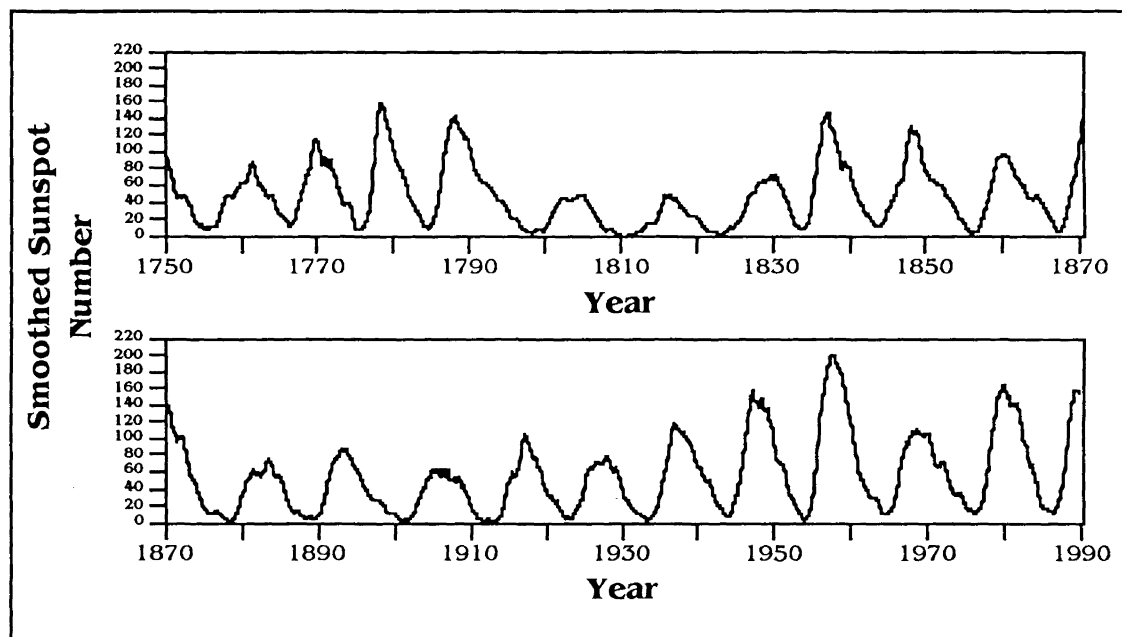


**Figure 3.9 – The 11 Year Solar Cycle**

An observer computes a daily sunspot number by multiplying the number of groups seen by ten and then adding this product to the total count of individual spots. Results, however, vary greatly, since the measurement strongly depends on observer interpretation and experience and on the stability of the earth's atmosphere above the observing site. Moreover, the use of earth as a platform from which to record these numbers contributes to their variability because the sun rotates and the evolving spot groups are distributed unevenly across solar longitudes. To compensate for these limitations, each daily international number is computed as a weighted average of measurements made from a network of cooperating observatories. The highest daily

count on record occurred December 24 and 25, 1957. On each of those days the sunspot number reached 355. In contrast, during years near the minimum of the spot cycle, the count can fall to zero.

Since 1848 the cycle duration has been 10.0 to 12.1 years. On average the cycle duration is about 11 years and is commonly referred to as the 11-year solar cycle. The average time from minimum to maximum, and then back to minimum is about 4.3 and 6.6 years respectively. Cycles with faster rise times typically have higher maxima (*Hirman et al.*, 1988). Each consecutive solar cycle has been numbered sequentially — solar cycle 21 peaked in about January 1980 and reached its minimum during August 1986. We are presently in solar cycle 22 which started in September 1986.

### **3.10.2 The Ottawa 2800 MHz Solar Flux**

The sun emits radio energy with a (mostly) slowly varying intensity — this is the so called ‘quiet sun.’ This radio flux, which originates from atmospheric layers high in the sun’s chromosphere and low in its corona, changes gradually from day-to-day, in response to the number of spot groups on the disk. Radio intensity levels consist of emissions from three sources: from the undisturbed solar surface, from developing active regions, and from short-lived enhancements above the daily level. From June 1946 to September 1948 solar flux density at 2,800 megaHertz was recorded at Ottawa. Observations were then made at South Gloucester until December 1961 at which time observations were transferred to a radio telescope at the Algonquin Radio Observatory (ARO), near Ottawa. Observations at ARO have recently ceased for the most part and are now made at the Dominion Radio Astrophysical Observatory (DRAO), Penticton, B.C., which previously had been operating in parallel with ARO. Each day, levels are determined around local noon (1900 UT) and then corrected to within a few percent for factors such as antenna gain, atmospheric absorption, bursts in progress, and background sky temperature.

The NGDC data sets contain three sets of fluxes — the observed, the adjusted, and the absolute — from the entire solar disk at a frequency of 2,800 megaHertz in units of  $10^{-22}$  Watts/square metre/Hertz. Of the three, the observed values are the least refined, since they contain fluctuations as large as 7% that arise from the changing sun–earth distance. In contrast, adjusted fluxes have this variation removed; the numbers in the data sets equal the energy flux received by a hypothetical detector located at the mean distance between sun and earth. Finally, the absolute levels carry the error reduction one step further; here each adjusted value is multiplied by 0.90 to compensate for uncertainties in antenna gain and in signals reflected from the ground.

### 3.10.3 The *Kp* Number and Other Magnetic Indices

The earth's magnetic field is seldom quiet, even when there are no storms. Several empirical magnetic indices have been developed to describe the variability at any given time. The important indices are listed in **Table 3.2**. The subscript “*p*” is affixed to some of the indices (*Kp* and *Ap* for example) and is used to indicate a planetary index. Such indices are therefore **global magnetic activity indices**. The following 13 observatories, which lie between 46 and 63 degrees north and south geomagnetic latitude, now contribute to the planetary indices published by NGDC: Lerwick (UK), Eskdalemuir (UK), Hartland (UK), Ottawa (Canada), Fredericksburg (USA), Meannook (Canada), Sitka (USA), Eyrewell (New Zealand), Canberra (Australia), Lovo (Sweden), Rude Skov (Denmark), Wingst (Germany), and Witteveen (The Netherlands).

At any observatory, for each three-hour period of every UT day, the range of variation of each of the Cartesian field components of the earth's magnetic field (*X*, *Y*, *Z*) is measured. The largest of the three components *r* (in gammas, or nanoTeslas) for a particular station is related to the *K* index. For each observatory a table is assigned, giving limits of *r* corresponding to each of ten values of *K*. The lower limit of *r* for *K* = 9

is set according to the geomagnetic latitude of the observatory. Typically the qualification for  $K = 9$  is a disturbance of 300  $\gamma$  (gammas, or nanoTeslas) for a low-latitude (but not equatorial) station, 500  $\gamma$  for a mid-latitude station, and 2,000  $\gamma$  for a station in the auroral zones. For stations of about 50° geomagnetic latitude the following logarithmic relationship between  $r$  and  $K$  applies (Davies, 1966):

Range of $r$ :	0	5	10	20	40	70	120	200	330	500
$K$ :	0	1	2	3	4	5	6	7	8	9

INDEX NAME	ZURICH & INTERNATIONAL SUNSPOT NUMBERS	OTTAWA 10.7 cm (2800 MHz) SOLAR FLUX	GEOMAGNETIC INDICES
DESCRIPTION OF DATA	<ol style="list-style-type: none"> <li>1. Daily means (1818 to present).</li> <li>2. Monthly and smoothed monthly means (1749 to present).</li> <li>3. Yearly means (1700 to present).</li> </ol>	Observed, adjusted, and absolute daily values, monthly means, and yearly means (Feb 1947 to present).	$K_p$ , $A_p$ , sunspot number (Jan 1932 to present); adjusted 10.7 cm solar flux (Feb 1947 to present) and other geomagnetic indices.
AVAILABLE FORMATS	<ol style="list-style-type: none"> <li>1. Diskettes (2).</li> <li>2. Publication, <i>Report UAG-95</i>, 112 pages.</li> <li>3. Annual subscription to monthly <i>Solar Indices Bulletin</i>, 2 pages.</li> <li>4. Sunspot number plots, publication quality graphics display entire archive of daily, monthly, and yearly mean values.</li> </ol>	<ol style="list-style-type: none"> <li>1. Booklet, 46 pages observed or adjusted or absolute values.</li> <li>2. Diskettes (2).</li> <li>3. Annual subscription to <i>Solar Indices Bulletin</i>, 2 pages.</li> </ol>	<ol style="list-style-type: none"> <li>1. Magnetic tape.</li> <li>2. Diskettes (6).</li> <li>3. Annual subscription to monthly <i>Geomagnetic Indices Bulletin</i>.</li> </ol>
ORDERING INFORMATION	National Geophysical Data Center (NGDC), 325 Broadway, Boulder, Colorado 80303 USA. Telephone: (303) 497-6346		

**Table 3.2** – Summary of NGDC Solar Indices

The arithmetic mean of the  $K$  values scaled at the 13 observatories listed on the previous page gives the planetary  $K_p$  index of which there are eight per day.  $K_p$  indices range in 28 steps from 0 (quiet) to 9 (greatly disturbed) with fractional parts expressed in thirds of

a unit. A  $Kp$  index of 27, for example, means 2 and  $2/3$  or 3–; a  $Kp$  index of 30 means 3 and  $0/3$  or 3 exactly; and a  $Kp$  index equal to 33 means 3 and  $1/3$  or 3+. A second index,  $Ap$ , is similar to  $Kp$  except that it is a daily index.

#### 3.10.4 Sources of Solar Indices

**Figure 3.9** was created from the “SMOOTHED.PLT” file of monthly sunspot numbers as obtained from NGDC. NGDC supply several indices of solar activity in a variety of formats. **Table 3.2** outlines a few of the important indices, their associated data, and the available formats.

The Herzberg Institute of Astrophysics, National Research Council Canada, has published the daily values of solar flux at 2,800 MHz in a nine-volume series of reports which can be obtained from Canada Institute for Scientific and Technical Information, National Research Council Canada, Montreal Road, Ottawa, Ontario, Canada K1A 0S2 (Phone: (613) 993-1600).

NGDC would appear to have the most complete archive of solar and geomagnetic indices. Additional services are offered; these include yearly subscriptions to the NGDC ***Solar Indices Bulletin*** and ***Geomagnetic Indices Bulletin***, examples of which can be found in **Appendix I**. Geomagnetic and solar indices can also be found in the ***Journal of Geophysical Research***, and sunspot numbers may be found in ***Sky and Telescope***.

#### 3.11 The Ionosphere in Summary

In 1882 Balfour Stewart first postulated the ionosphere's existence. Early ionospheric pioneers soon discovered roughly discreet regions, or layers, of differing electron concentrations which would either reflect radio waves or allow them to pass through.

Once the underlying physical processes responsible for the ionosphere's being were recognised, instrumentation was designed for its observation. Many years of scientific data collection have led to an increasingly more detailed understanding of the ionosphere and its constituent parts. The driving forces behind the ionosphere's state are now known with various degrees of understanding and the ionosphere's state has been found to be dependent on season, time of day, level of geomagnetic and solar activity, and geographic location. The culmination of this knowledge has enabled the development of empirical ionospheric models whose job it is (in the words of *McNamara* (1985)) "to reproduce as faithfully as possible many different observations and types of observation, and to do so in a convenient mathematical fashion."

Ionospheric science is a relatively new discipline which finds its roots some 250 or so years ago. Much has been learnt in this time, undoubtedly much more will be learnt in the next 250 years. Better understanding of the ionosphere will doubtlessly follow in years to come. This improved level of understanding will in turn lead to the development of better, more sophisticated empirical models.

## Chapter 4

# ***Empirical Modelling of the Ionosphere***

Empirical models of the ionosphere are well described by *McNamara* (1985) when he says that they are “systematised distillations of a mass of observations collected over a long period of time and from many stations. They differ from physical or theoretical models by neglecting to a large extent the physical processes involved. Their intention is to reproduce as faithfully as possible many different observations and types of observation, and to do so in a convenient mathematical fashion. Their value lies in their succinctness, their potential for use in practical applications. Validation of such models is an important pre-requisite for their use in either of the latter roles.”

For surveying with GPS the ionospheric models of interest are those which describe electron density profiles up to altitudes of 1,000 km or more. Three such models have been obtained, the salient points of which are described in the following paragraphs:

- (i) The Bent model (*Bent & Llewellyn*, 1973);
- (ii) The Ionospheric Conductivity and Electron Density (ICED) profile model (*Tascoine et al.*, 1988); and
- (iii) The 1986 International Reference Ionosphere (IRI86) (*Rawer et al.*, 1981; *Bilitza*, 1986b).



The decision to concentrate on the three models listed above was a reasonably straightforward one. The Bent model is often referred to in literature dealing with ionospheric models and appears to be regarded as the “father” of such models — the techniques used in its construction have been modified and built upon in subsequent models. IRI86 represents a model whose existence can be attributed to international cooperation amongst ionospheric scientists. In the words of *Bilitza* (1986a) “the IRI steering committee has, over the years, read like a who’s who in ionospheric physics.” ICED was considered because it is the latest all-new ionospheric model.

In addition, the GPS single-frequency **Broadcast model** (Klobuchar, 1986) is described briefly as tests will later be reported on the three empirical models listed above and the Broadcast model.

#### 4.1 Maps of *foF2* and *M(3000)F2*

Several references will be made in this chapter to the various models’ coefficient datasets. These coefficients are used to generate global maps of two crucial ionospheric quantities:

- The critical frequency of the F2 layer, or *foF2*; and
- The *M(3000)F2* factor, where  $M(3000)F2 = MUF/foF2$ , and *MUF* is defined as the maximum usable frequency that, refracted in the ionosphere, can be received at a distance of 3,000 km over the earth’s surface.

*foF2* and *M(3000)F2* are important quantities in ionospheric modelling because knowledge of them allows the peak electron density of the F2 layer (*NmF2*) and the height at which the peak occurs (*hmF2*) to be found. The Bent model for example uses

the following relationships to determine  $NmF2$  (in electrons/m<sup>3</sup>) and  $hmF2$  (in km) given  $foF2$  (in MHz) and  $M(3000)F2$  (dimensionless)

$$\left. \begin{aligned} NmF2 &= 1.24 \times 10^{10} (foF2)^2 \\ hmF2 &= 1346.92 - 526.40 [M(3000)F2] + 59.825 [M(3000)F2]^2 \end{aligned} \right\} \quad (4.1)$$

Each model considered in this research uses a different set of coefficients. The Bent model does not explicitly reference the source of its coefficients, although they are actually those to which we now refer as the International Radio Consultative Committee (CCIR) coefficients. The CCIR adopted a set of coefficients in 1966 (*Rush et al.*, 1989) that could be used to represent  $foF2$  and  $M(3000)F2$  at any point on the earth for any given universal time.

For each of two levels of solar activity ( $R = 0$  and  $R = 100$ , where  $R$  is the smoothed 12-month mean of the Zurich monthly sunspot number) CCIR uses 988 coefficients to globally represent the variation of  $foF2$  for any given month, and 441 coefficients to describe  $M(3000)F2$ . Therefore the total number of  $foF2$  and  $M(3000)F2$  coefficients for 12 months covering two levels of solar activity is 23,712 and 10,584 respectively. If evaluations are required at levels of solar activity where  $R$  is neither equal to 0 or 100 a simple linear interpolation/extrapolation is performed.

Improvement of the original set of CCIR coefficients has been an ongoing process. Most notable amongst these efforts has been that of the International Union of Radio Science (URSI) Working Group G.5. The working group's mandate is "to make improvements in the present CCIR maps of F2-layer characteristics through theory and observation and in particular to investigate the possibility of incorporating space data" (*Rush et al.*, 1989). The offshoot of this mandate has been the release of several versions of their

coefficients (e.g., the URSI-1988 coefficients). ICED utilises the URSI-1988 coefficients; IRI86 uses the CCIR-1966 coefficients. The main drawback with such coefficients is that they were derived from data gathered in a fashion which was inhomogeneous both spatially and temporally. Typically there are vast tracts of the worlds' oceans for which data does not exist. Therefore any set of coefficients such as the CCIR's or URSI's will perform relatively poorly when attempting to model  $f_oF2$  in such areas. Conversely the CCIR and URSI predictions around areas from which many data were available prove to be quite accurate. These facts are not surprising when it is borne in mind that the modelled values of  $f_oF2$  can usually only be compared with those observations from which the coefficients were originally derived (private communication, *Charles Rush*, NTIA/ITS, November 1991).

#### **4.2 Description of the Bent Model**

The Bent model was developed by Rodney Bent and Sigrid Llewellyn of the Atlantic Science Corporation of Indiatlantic, Florida (a now defunct organisation). The project was funded jointly by the Air Force Space and Missile Systems Organisation (SAMSO), the Air Force Cambridge Research Laboratory, and by NASA/Goddard Space Flight Center. The model, published in July 1972, is a FORTRAN program designed to describe the ionosphere on a world-wide basis for any past or future date. The model's FORTRAN source code, binary database of CCIR coefficients, and detailed documentation (which includes the input and expected output data for several test cases) are available from the United States Department of Commerce, National Technical Information Service, 5285 Port Royal Road, Springfield, Virginia 22161. The Bent model was designed to give refraction corrections for use in satellite to ground or satellite to satellite communications.

#### 4.2.1 The Ionospheric Profile of the Bent Model

Development of the Bent model involved fitting a theoretical electron density profile to a database of ionospheric measurements. The database entries spanned from approximately 1962 to 1969 (solar cycle number 20), and covered the minimum to the maximum of that cycle. Measurement data extended up to heights of about 1,000 km. Hourly profiles of the ionosphere up to the F layer peak from fourteen stations approximately along the American longitudes having geographic latitudes between 76° N and 12° S (magnetic latitudes of about 85° N to 0° respectively) provided the bottomside data from 1962 to 1969. Topside soundings from 1962 to 1966 provided data downwards from heights of about 1,000 km to a height just above the maximum electron density. These soundings covered magnetic latitudes of between 85° N and 75° S. Because the topside data was not available near the solar maximum, electron density probe data was obtained from the Ariel 3 satellite between May 1967 and April 1968 from 70° N to 70° S (geographic) and correlated with  $f_oF2$  values obtained from 13 stations on the ground. In total the database consisted of over 50,000 topside soundings, 6,000 satellite electron density and related  $f_oF2$  measurements, and over 400,000 bottomside soundings.

The resultant profile (**Figure 4.1**) is composed of five piece-wise sections: a bi-parabola to model the lower ionosphere; a parabola which joins together the top and bottomside ionosphere; and three exponential sections whose combined function is to model the topside ionosphere.

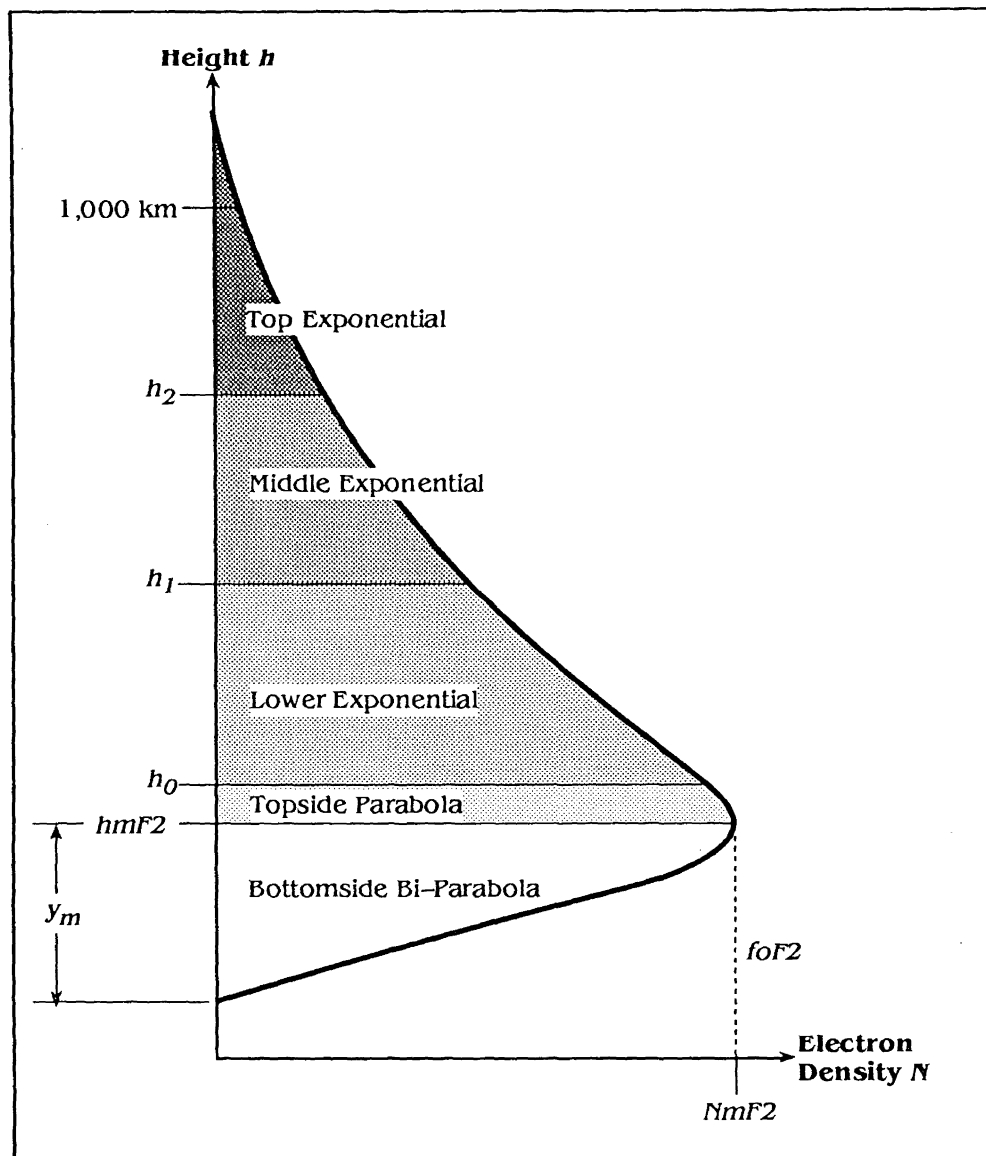


**Figure 4.1** – The Bent Profile (after *Bent & Llewellyn* (1973))

The lower parts of the ionosphere (i.e., the D region, the E layer, and the F1 layer) are not individually modelled in the Bent model. Instead their electron density values were included in the TEC below  $hmF2$  which was then used in the derivation of the lower bi-parabolic layer. **Table 4.1** shows the ranges into which each of the five sections of the Bent profile fall.

PROFILE PART	RANGE
Top Exponential	$h_2 \leq h < 2,000 \text{ km}$
Middle Exponential	$h_1 \leq h < h_2$
Lower Exponential	$h_0 \leq h < h_1$
Topside Parabola	$hmf2 \leq h < h_0$
Bottomside Bi-Parabola	$hmf2 - y_m \leq h < hmf2$ *
* $y_m$ is the half-thickness of the bottomside bi-parabola.	

**Table 4.1** – The Ranges of the Five Sections of the Bent Profile

The Bent model generates location and time dependent electron density vs. height profiles up to heights of 2,000 km from which range, range rate, and the angular refraction corrections for the wave are obtained as well as the vertical and slant total electron content. Development of the model was based upon a database of measurements that did not exceed heights of approximately 1,000 km. Despite this fact the model is allowed to generate profiles up to heights of 2,000 km by extending the exponential form of the uppermost exponential layer.

#### 4.2.2 User Input into the Bent Model

The user is required to input the satellite's transmission frequency, the elevation and azimuth to the satellite, the satellite's elevation and azimuth rates (if range-rate corrections are required), the satellite's height, the station position, time information, and a limited amount of solar data. The combination of station position and the satellite's elevation and azimuth allows line-of-sight (or slant) computations of TEC and related ionospheric delays to be performed as well as vertical evaluations at the receiver's location. To force the model to perform vertical computations, the satellite's elevation angle is entered as 90°.

The solar data required by the model is that of daily values of observed 10.7 cm solar flux, the 12-month running average of sunspot number (otherwise referred to as monthly smoothed sunspot number), and the 12-month running average of solar flux. The daily solar flux values are readily available, as are the smoothed sunspot numbers. The smoothed monthly flux  $I_{12,j}$  for month  $j$  is computed from observed monthly mean flux data (which are listed alongside the daily values) using the following expression in which  $\bar{I}_k$  is a mean flux value for month  $k$ :

$$I_{12,j} = \frac{1}{12} \left( \frac{\bar{I}_{j-6} + \bar{I}_{j+6}}{2} + \sum_{l=-5}^{+5} \bar{I}_{j+l} \right) . \quad (4.2)$$

If not enough advance data is available to form the 12-month running average, it can be approximated with a 11.5, 10.5, or 9.5-month running average

$$\text{approx. } F_{12,j} = F_{12.5-k,j} = \frac{1}{12.5-k} \left( \frac{\bar{F}_{j-6}}{2} + \sum_{l=-5}^{6-k} \bar{F}_{j+l} \right) , \quad k = 1, 2, \text{ or } 3 . \quad (4.3)$$

If there is not enough data to form even the 9.5-month running average, then the 12-month running average of solar flux can be approximated from the following expression (Stewart & Leftin, 1972) which relates the 12-month running average of solar flux to the 12-month running average of sunspot number (for which tabulated predictions are generally available, e.g., the NGDC Solar Indices Bulletin, **Appendix I**)

$$\text{approx. } F_{12,j} = 63.75 + 0.728 \times S_{12,j} + 0.00089 \times S_{12,j}^2 . \quad (4.4)$$

To test the accuracy of the 11.5, 10.5, 9.5-month running averages formed in (4.3), and of the approximate form shown in (4.4) computations have been made based on the NGDC database of monthly mean sunspot and flux values from January 1947 to

December 1989. The results (shown in **Table 4.2**) are compared with the 12-month running average of solar flux as computed from (4.2).

Approximation Used	R.M.S. Error * (S.F.U. †)	R.M.S. Error (%) *
11.5-month (eqn. 4.3)	0.978	0.72
10.5-month (eqn. 4.3)	2.785	2.06
9.5-month (eqn. 4.3)	4.519	3.34
Approximate (eqn. 4.4)	4.875	3.14
* Errors based upon comparison with the 12-month running average from (4.2).		
† 1 S.F.U. = $10^{-22} \text{ W m}^{-2} \text{ Hz}^{-1}$ .		

**Table 4.2** – Errors in the Determination of the Smoothed Monthly Mean Solar Flux when Computed Using Various Techniques

The accuracy of each computation decreases in the expected order. In the worst cases, the approximate form of (4.4) and the 9.5-month running averages from (4.3) are in error by about 3% r.m.s. If real-time predictions are required (4.4) must be adopted.

#### 4.2.3 Output from the Bent Model

There are several output options available from this model. The desired options are determined by setting flags in the model's command file equal to one (required) or zero (not required). Output parameters include VTEC, line-of-sight TEC, the ionospheric profile's parameters (and associated plot of height vs. electron density), and the associated ionospheric delay (in metres) along the line of sight to the satellite. Ray bending is not taken into account by the model and in the context of this research is of little importance anyway as only vertical delays are dealt with. **Figure 4.2** shows a sample listing of the output from a trial run using one of the test cases provided with the model (test case number 1, page 118, *Bent & Llewellyn* (1973)).



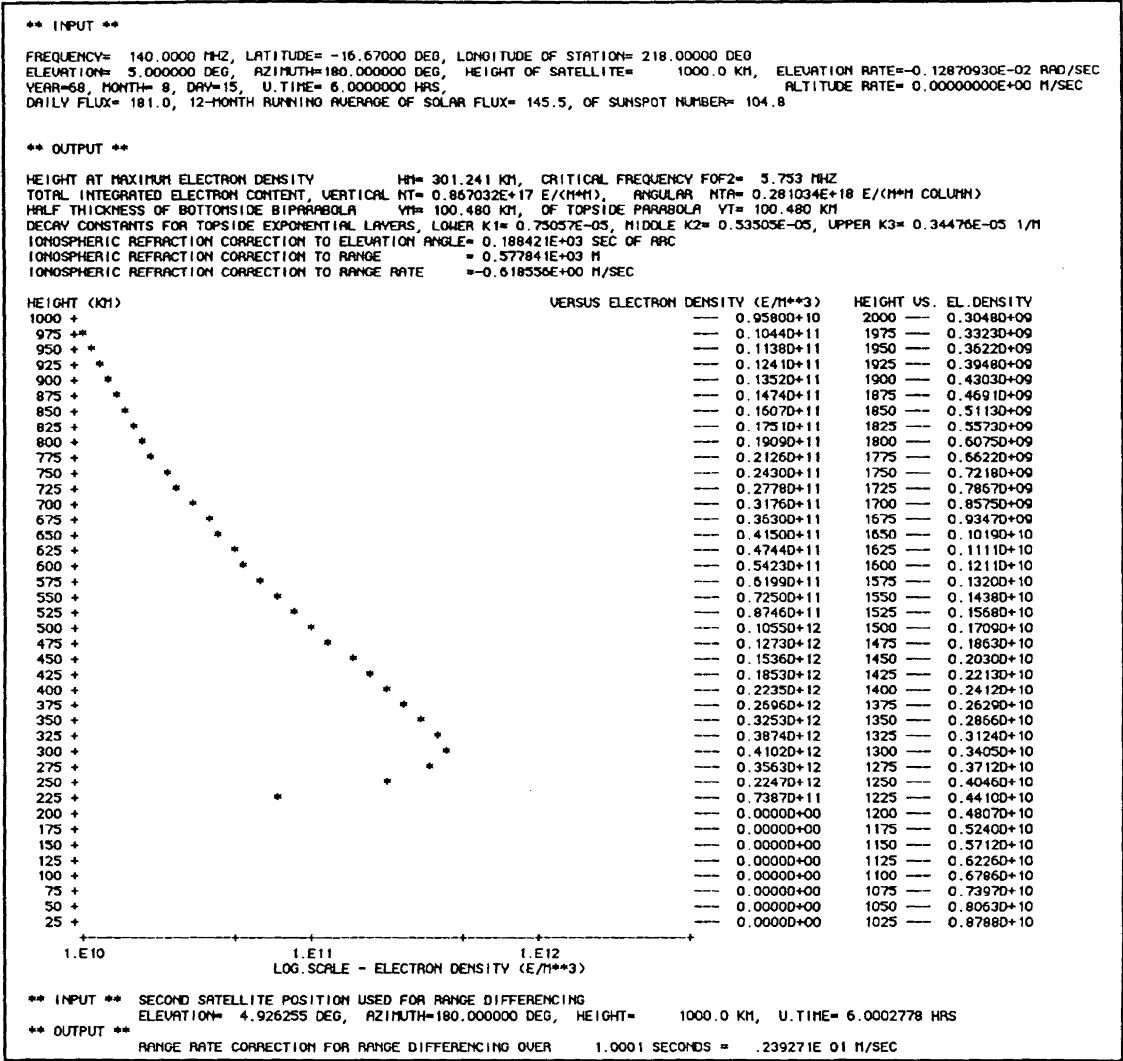


Figure 4.2 – Sample Output from the Bent Model

4.3 Description of ICED

ICED is currently under development by the National Oceanic and Atmospheric Administration (NOAA) for the United States Air Force. The research reported in this thesis used a preliminary version of the model that has not been widely released. The model's source code was obtained from Herb Kroehl, NOAA, National Geophysical Data Center, 325 Broadway, Boulder, Colorado 80303-3328. It is possible that at some stage in the future ICED might become an important benchmark against which other models will be compared.

ICED is a gridded (organised by geomagnetic coordinates) model of the northern hemisphere ionosphere. It contains distinct algorithms for low-latitudes, mid-latitudes, sub-auroral trough, equatorward portion of the auroral zone, poleward region of the auroral zone, and polar cap. Electron density profiles (from 90 km to 2,000 km) can be determined for each grid-point where the grid-point coordinates are formed from user-defined latitude and longitude boundaries and corresponding latitude and longitude increments. A semi-empirical low-latitude ionospheric model (SLIM) is currently under development by the Air Force Geophysics Laboratory. With the addition of SLIM, ICED will extend to the equator.

ICED is supplied as four separate modules (whose tasks are outlined below) which have been grouped together into one program in this implementation of the model. Modules 2 through to 4 are treated as subroutines, and module 1 as the main program. The four modules perform the following tasks:

1. **FRONT** — this module is used to construct the aforementioned grid and identify qualifier flag locations. Using both solar activity and geomagnetic activity parameters as input, the program identifies important physical boundaries within the user-specified analysis area. The boundaries include the sunrise-sunset terminators, the polar cap, the auroral zone, the sub-auroral trough, and mid-latitude and low-latitude regions. Each grid point is assigned a specific qualifier flag identifying the region into which it falls. FRONT input includes year, month, day, UT, and  $Kp$  and daily sunspot number indices. FRONT's output file serves as the input file for FIELD6;
2. **FIELD6** — the solar activity index is used to select the appropriate F region climatology which initialises  $f_oF2$  and  $h_mF2$  at all grid points. The

qualifier flags produced in FRONT are then used to select appropriate algorithms which modify the F2 region climatology to produce realistic ionospheric gradients and magnitudes appropriate for the input solar activity and magnetic field indices. The flags also dictate which algorithms are used to compute *foF1*, *hmF1*, *foE*, and *hmE* at each grid point. FIELD6's output file serves as the input file for PROFIL;

3. **PROFIL** — this module builds a complete electron density profile above each latitude and longitude grid-point, with specified boundaries, based upon the information about the E, F1, and F2 layers produced in FIELD6. The profiles specify the electron density every 10 km from 90 to 500 km and expand to a 50 km interval spacing from 500 to 2,000 km. PROFIL's output file serves as the input file for ICEDTEC, the final module;
4. **ICEDTEC** — this module integrates each grid-point's electron density profile to determine the VTEC value at each grid-point.

ICED is unique amongst the three empirical models considered here in as much as it was designed to provide ionospheric predictions for each grid-point on a user-specified grid. To fit in with the computations necessary for this research ICED's gridded facility was removed by hard coding the start/finish latitude boundaries to be the same and doing the same with the start/finish longitude boundaries.

#### 4.3.1 The ICED Ionospheric Profile

Documentation describing ICED is extremely limited. As such, details regarding its profile are necessarily sketchy. The F2 layer is divided into four distinct zones: the low-latitude and mid-latitude ionosphere, the trough, the auroral zone, and the polar cap. The model determines into which of these four regions a particular gridpoint falls. The equatorward boundary of the auroral oval has been determined from a combination of

photography from the Defense Meteorological Satellite Program polar orbiter and standard oval boundaries. The  $Kp$  indices are also used to help determine the extent of the boundary and hence whether or not the gridpoint lies inside, or outside, the auroral boundary.

#### **4.3.2 User Input into ICED**

Input to (and output from) the model is expressed in terms of geographic coordinates, but internally, the model converts geographic into geomagnetic coordinates. ICED requires input of daily solar sunspot and  $Kp$  indices (of which there are 8 per day), and date and time information.

#### **4.3.3 Output from ICED**

Due to the modular format of ICED a full representation of the model's output would involve four separate listings, each one corresponding to each of the four modules. The original form of ICED was not appropriate for the purposes of this research and, as already noted, the four modules were pieced together to form one program. Execution of this new program eliminates all of the intermediate output files and leads to one output file of VTEC values only.

#### **4.4 Description of IRI86**

The current (at the time of writing) version of the International Reference Ionosphere, IRI86, is "the standard model" for the Earth's ionosphere recommended by the Committee on Space Research (COSPAR) and URSI. COSPAR and URSI are the two organisations that represent ionospheric science in the International Council of Scientific Unions (ICSU). IRI86 was first presented at the July 1986 COSPAR meeting in Toulouse, France and is a good example of international cooperation, with contributions from scientists in the United States, Russia, India, Japan, Germany, Bulgaria, France,

Czechoslovakia, United Kingdom, Australia, Austria, Argentina, and Brazil. The model's FORTRAN source code, coefficient database, and documentation can be obtained from Dieter Bilitza, NASA Goddard Space Flight Center, Code 933, Greenbelt, MD 20771.

In a fashion similar to that of the development of the Bent model, IRI86 was also built around a vast database of ground-based and in-situ ionospheric measurements. The ground-based data include **ionosonde measurements** from more than 100 stations collected over more than 20 years and compiled in the official CCIR-1966 maps for the F region electron density peak, and **incoherent scatter** measurements from Jicamarca, Peru; Arecibo, Puerto Rico; Millstone Hill, Massachusetts; St. Santin, France; and Malvern, United Kingdom. The in-situ measurements are comprised of Alouette, Ariel, AEROS, and Atmosphere Explorer-C satellite data, and rocket measurements from the United States, the former Soviet Union, India, and United Kingdom.

IRI86 describes the global and temporal **mean** behaviour of the ionosphere at non-auroral latitudes. The intention was to produce a reliable standard model of the most important ionospheric parameters (electron density, electron and ion temperature, and ion composition). Of these four parameters only one, electron density, need concern the satellite surveying community. Thus, all subsequent tests on this model were performed with only electron densities being computed.

#### 4.4.1 IRI86 Ionospheric Profile

The 1986 version of the International Reference Ionosphere (IRI86) uses the same **basic** form for its electron density profile as that which was used in the 1979 version (IRI79). IRI79's electron density profile  $N(h)$  is described by *Rawer et al.* (1981); the same basic description is used here to describe IRI86. The ranges and designations of the profile components are shown in **Figure 4.3**. The profile consists of six height ranges — the

bottomside electron density profile consists of five height ranges (which are numbered from 2 through to 6), and the topside is numbered as region 1.

At low solar elevation angles and during the night there is a deep valley above the E region. This “valley region” (5) starts at the peak height  $hmE$  of the E region and extends to the base of the “intermediate region” (4) at a height of  $hEF$ . Characteristic  $hmE$  values were estimated from ionogram reductions combined with in-situ rocket measurements. Around noon the depth of the valley is quite small; there is even no valley at lower latitudes. The function used to describe the valley region was based on analysis of incoherent backscatter measurements.

The upper edge of the valley region is found at height  $hEF$ , which is the sum of  $hmE$  plus valley thickness  $hBR$ . Values of  $hBR$  were mainly derived from incoherent backscatter data. In the absence of a valley,  $hBR$  is set equal to zero.  $hEF$  is the lower limit of the “intermediate region” (4) which was introduced to bridge the gap between the valley and the F region above; it extends to height  $hZ$ . The F region’s profile is modelled in one of two ways depending on whether or not the F1 layer is present. In both cases the F region is still subdivided into regions; (2) for F2 and (3) for F1. If F1 is absent both of the functions which describe F1 and F2 are identical. The topside ionosphere (1) extends from  $hmF2$  to a height of 1,000 km.

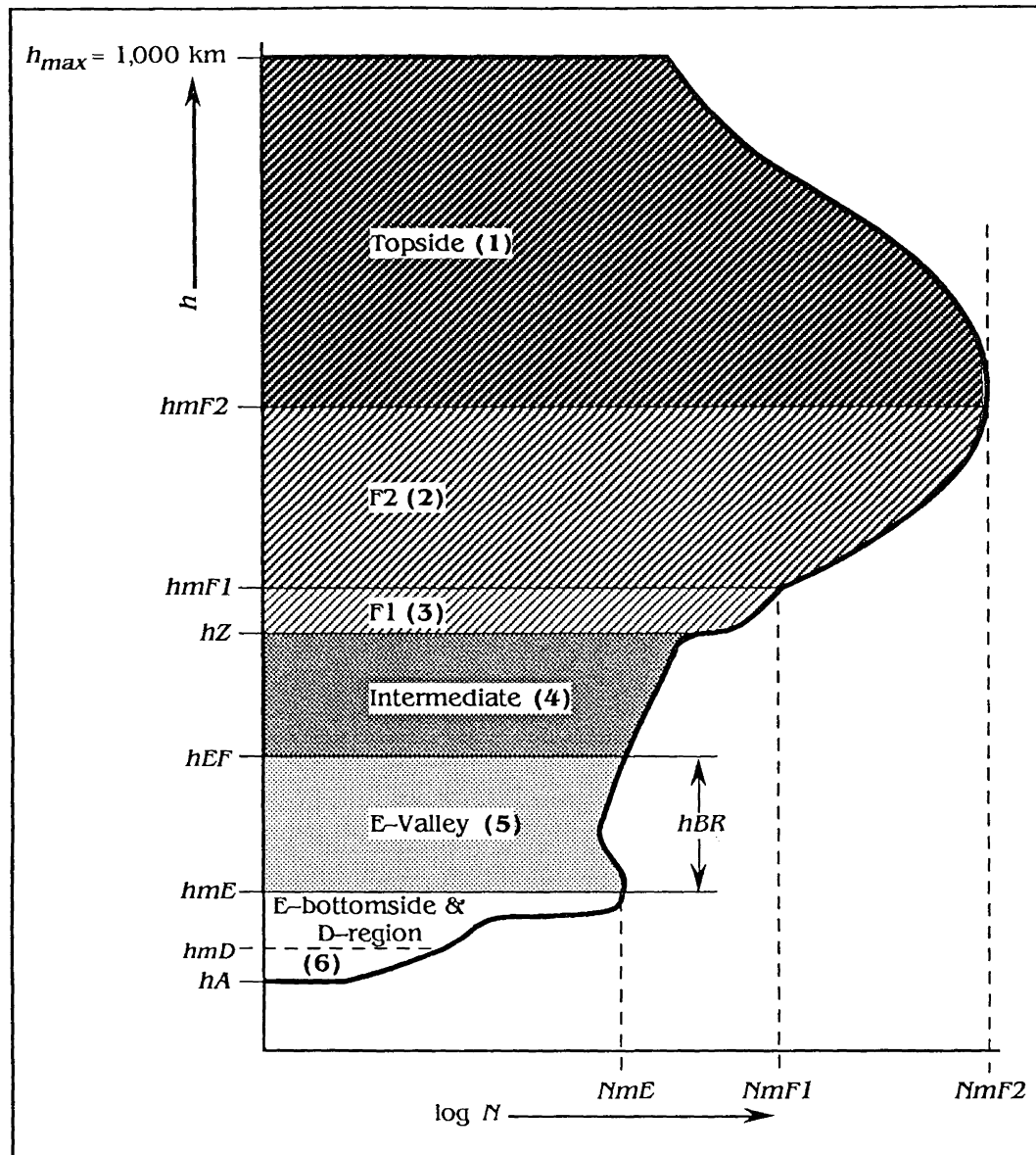


**Figure 4.3** – The IRI86 Electron Density Profile (after *Rawer et al.* (1981))

Except for the F2-peak data, derived from the CCIR coefficient method, the characteristics of the different layers — i.e., the critical frequencies (which correspond to the peak densities) and the solar zenith-angle, the solar cycle, and latitudinal dependencies — are deduced from descriptive formulas which can be found in the

model's source code. Thickness parameters were obtained mainly by ionogram reduction.

IRI86 does not attempt to include sporadic E in any of its predictions. Despite the importance of Es layers in radio wave propagation it was not realistic to include them due to their spatial and temporal irregularity. In fact this point is equally true of any ionospheric model.

#### **4.4.2 User Input into IRI86**

In comparison with the Bent model, and due to the monthly-mean nature of the model, IRI86 is a somewhat easier model to use. Daily values of solar flux are not required; instead the only solar data input into IRI86 is the monthly Zurich sunspot number (12-month-running-mean). The model also requires the month, local or UT time information, and either the geographic or geomagnetic latitude and longitude of the evaluation site. In addition (and in the rare case that this data is actually available) the user can supply F-peak density information in the form of either the critical frequency,  $f_oF2$ , of the F2 layer or the F-peak electron density,  $NmF2$ .

(4.2) to (4.4) can be used to determine the 12-month-running-mean of the Zurich sunspot number. One very important distinction to make between the Bent and IRI86 models is that IRI86 does not make non-vertical TEC predictions.

#### **4.4.3 Output from IRI86**

Careful tests were performed with IRI86 to ensure that the output from test runs exactly matched sample data-runs supplied with the model. However, due to the fact that IRI86 models not only electron density, but also electron and ion temperature, and ion composition, the original model's output is overly detailed in the context of this study.



Everything but electron density and associated VTEC computations have been skipped in the modified version of the model used in this research. As was the case with the Bent model, IRI86 has been modified to allow multiple epoch/location computations of ionospheric delay.

#### 4.5 The Broadcast GPS Single-Frequency Model

In order to improve the accuracy of positions determined using single-frequency GPS observations; a simple algorithm was developed which describes the diurnal variation of the ionosphere (*Klobuchar*, 1986). The original specification for the model detailed that it should be able to remove 50% r.m.s. of the ionospheric effect and that it was to do this using a maximum of eight coefficients for a model which was not computationally complex. Model testing (e.g., *Klobuchar* (1986) and *Feess & Stephens* (1986)) suggests that these criteria were met.

GPS satellites broadcast the eight coefficients which are necessary to drive the model; the model is commonly known as “the Broadcast model.” Individual receiver manufacturers are responsible for implementing the model’s algorithm either within their receivers or their post-processing software. The model consists of a positive half cosine representation of the diurnal variation of the ionosphere and is fully described by *Feess & Stephens* (1986), *Klobuchar* (1986), and the *GPS Interface Control Document* (ICD-200) (*Rockwell*, 1987). The model’s cosine representation is allowed to vary in amplitude and period with user latitude. **Figure 4.4** shows the main features of the model, it is clear that only four parameters are required to describe its cosine form, namely: the night-time constant, or *DC*, term; the amplitude of the cosine term; the phase of the cosine term; and the period of the cosine term. Two of the terms are held fixed — the *DC* term is set to 5 nanoseconds, and the phase is held constant with the peak of the cosine at 1400 hours local time.

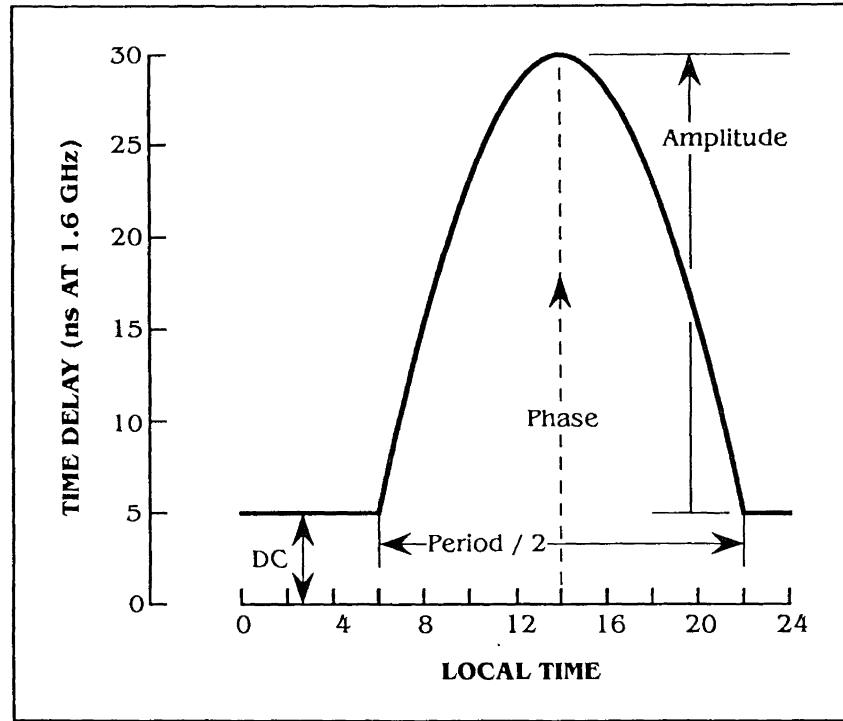


**Figure 4.4** – The Broadcast Model's Cosine Representation of the Ionosphere's Diurnal Variation (after *Klobuchar* (1986))

The cosine function is

$$T_g = DC + A \cos \frac{2\pi(t - T_p)}{P} \quad (4.5)$$

where  $T_g$  is the ionospheric delay on L1 (seconds),  $DC$  is the constant night-time offset ( $5 \times 10^{-9}$  seconds),  $A$  is the amplitude (seconds),  $P$  is the period (seconds),  $T_p$  is the phase (50400 seconds), and  $t$  is the local time at the sub-ionospheric point (seconds).

The period and amplitude are modelled as 3rd order polynomials of the form

$$A = \sum_{n=0}^3 \alpha_n \varphi_m^n \quad \text{and} \quad P = \sum_{n=0}^3 \beta_n \varphi_m^n \quad (4.6)$$

where  $\alpha_n$  and  $\beta_n$  are the broadcast model coefficients (four of each, eight in total) and  $\varphi_m$  is the geomagnetic latitude (semicircles; 1 semicircle = 180°) of the sub-ionospheric point. The  $\alpha_n$  and  $\beta_n$  coefficients are selected from 370 coefficient sets representing 10 levels of solar activity and 37 ten-day time spans which model the annual variability of the ionosphere (Greenspan *et al.*, 1991). The nominal update rate for the coefficients is once every ten days. The following expression is used for computation of  $\varphi_m$

$$\varphi_m = \frac{\sin^{-1}(\sin \varphi_I \sin 78.3^\circ + \cos \varphi_I \cos 78.3^\circ \cos(\lambda_I - 291^\circ))}{180^\circ} \quad (4.7)$$

where  $\varphi_I$ ,  $\lambda_I$  are the latitude and longitude of the sub-ionospheric point (degrees). It will be seen in Chapter 5 that modelled delays are referenced to the sub-ionospheric point which is a function of the receiver's location and the elevation and azimuth to the satellite. The necessary algorithm for the computation of sub-ionospheric point is not given here; instead the reader is directed towards section 5.6.2.1. The local time at the sub-ionospheric point  $t$  (seconds) is found from the following expression

$$t = 3600 \left( \left( \frac{\lambda_I}{15^\circ} \right) + \text{UT} \right) \quad (4.8)$$

where UT is the universal time (decimal hours) at the receiver's location. The final part of the model (which is not used in this research) involves mapping the modelled delay from the vertical to a slant delay which accounts for the elevation,  $el$  (degrees), of the satellite. A simple scale factor,  $SF$ , is applied (refer to section 5.6.2.2 for additional information)

$$SF = 1 + 2 \left[ \frac{96^\circ - el}{90^\circ} \right]^3 \quad (4.9)$$

The full cosine form of (4.5) is not used without modification in the official implementation of the model (i.e., in accordance with *Rockwell*, 1987). Instead, the following truncated cosine expansion replaces it where terms higher than  $x^6$  are dropped

$$T_g = SF \left[ DC + A \left( 1 - \frac{x^2}{2} + \frac{x^4}{24} \right) \right] \quad \text{for } |x| < \frac{\pi}{2} \quad (4.10)$$

or

$$T_g = SF [DC] \quad \text{for } |x| \geq \frac{\pi}{2} \quad (4.11)$$

where

$$x = \frac{2\pi(t - T_p)}{P} \quad (4.12)$$

Both the exact (4.5) and approximate (4.10) forms of the cosine function have been tested in this research. The use of the truncated cosine expansion has been found to introduce errors of less than 0.7% (on average). For the techniques and results reported in chapters 5 and 6 the approximate form of the cosine function was adopted.

#### 4.6 Model Adaptation to the Macintosh Platform

The three empirical ionospheric models examined in this thesis were supplied in the form of FORTRAN source code. The code for the Bent model was designed for use on a mainframe computer; the ICED and IRI86 code was suited to the IBM personal computer. Originally work was undertaken using the University of New Brunswick's IBM 3090 mainframe computer. The work was then transferred to the Apple Macintosh computer platform in order that the models could be used in a more realistic setting — that of a

personal computer type platform such as a small survey company or GPS field crew might have at their disposal. A number of changes were necessary to adapt each model to this environment.

The I/O unit numbers were changed to account for differences between the mainframe, IBM PC, and Macintosh computers. The coefficient files were supplied as binary files which were either created and understood by mainframe computers or IBM compatible personal computers. Such files cannot be directly transferred to the Macintosh platform and were converted from binary to ASCII format on the IBM 3090 mainframe computer or an IBM PC (or compatible) computer. The resulting ASCII files were then transferred to the Macintosh where they were then re-written as binary files.

At this stage each model was compiled — using *Absoft Corporation's* MacFortran 020 (version 2.4) compiler — and run on the Macintosh computer using supplied sample evaluation conditions as input. The output results were carefully checked against each model's example files to ensure that no errors had crept in during the transfer between computer platforms. Several additional modifications were then made to each of the models.

The IRI86 and Bent models were originally designed to compute ionospheric parameters for only one epoch/location. ICED was designed to estimate ionospheric parameters for each point on a user-defined grid at a single epoch. As outlined earlier in this chapter the models do not compute the same parameters. Sometimes VTEC (the quantity of primary interest in this thesis) is not one of the output options. Therefore, apart from the necessary unit number changes and binary coefficient manipulations, the models have also been adapted to output VTEC (if not already an option) at multiple epochs/locations.

These modifications represent the major, and time-consuming, changes which were necessary.

To enable multiple epoch/location computations typically requires the addition of extra loops to redirect control back to the top of the main program whilst maintaining careful control over reinitialisation of variables. Once again the predicted ionospheric results were carefully checked against the same test case I/O data sets. This part of the models' adaptations was by far the most tricky, particularly in the case of ICED which was originally designed as four stand alone programs.

#### **4.7 Practical Considerations for Use of the Models**

For the models to serve any useful purpose in the vast majority of survey environments they must not only make accurate predictions of VTEC and the associated ionospheric delay but they must also make their predictions as rapidly as possible and with as little effort as possible on the part of the user. Each of the models was adapted to the Macintosh platform with these points in mind.

##### **4.7.1 Execution Times**

Several modifications have been made to the coefficient datasets upon which the models rely. During run-time, each of the ionospheric models searches the coefficients until it finds those which pertain to the month for which calculations are being performed. The coefficients are arranged in chronological order — if the evaluation conditions are for December the model will have to read eleven twelfths of the coefficients before it reaches those coefficients which are of interest. This is a time-consuming process and is easily overcome by breaking-down the large coefficient set into twelve sets of coefficients — one per month. The source code of each model was adapted so that only one set of the new coefficients had to be read into memory. The

break-down of the coefficients into twelve one-monthly sets was performed solely on the ASCII version of the files. These ASCII files were subsequently written-out as binary files to again reduce execution times.

With a multiple epoch/location computation the models are now at the stage where (for any one month) the binary coefficients only have to be read into memory once. **Table 4.3** lists each of the four ionospheric models' execution times for single and multiple epoch computations. Note that if the multiple epoch time is divided by the total number of epochs (135 in this example) the average execution time is yielded. The result is of course always a smaller number than that of the single epoch figure due to the fact that the time taken to read-in the binary coefficients is divided between a large number of epochs. Note that the preceding comments on coefficient database I/O times **do not** apply to the Broadcast model.

MODEL	SINGLE EPOCH (s)	135 EPOCHS (s)	AVERAGE OF 135 EPOCHS (s)
BENT	1.28	123.45	0.91
IRI86	2.82	51.20	0.38
ICED	1.75	180.80	1.34
Broadcast	N/A	8.65	0.06
Note: Models run on Macintosh SE/30 computer with a math coprocessor. Computations were to PRN#2 for Feb. 9th 1991 at Yellowknife.			

**Table 4.3** – Execution Times for the Bent, IRI86, ICED,  
and Broadcast Ionospheric Models

#### 4.7.2 Preparation for Use of the Models

Another very important factor to consider is that of “user friendliness.” That is, is the model easy to set-up and run for the non-ionospheric expert? Virtually the only

requirement of the user with the three empirical models considered here is that a command file containing time, location information, and solar data be written. This in itself is a straightforward process, the difficulty may however come when trying to obtain the suitable solar and geomagnetic indices for the models. **Table 4.4** summarises the input data required by each of the models.

Required Input Data	Bent	IRI86	ICED	Broadcast
Receiver Location	✓	✓	✓	✓
Time (UT)	✓	✓	✓	✓
Day	✓	X	✓	X
Month	✓	✓	✓	X
Year	✓	X	X	X
Broadcast Satellite $\alpha_I$ and $\beta_I$ coefficients	X	X	X	✓
Daily Observed Solar Flux	✓	X	X	X
Daily Sunspot Number	X	X	✓	X
Daily $K_p$ Indices	X	X	✓	X
Monthly Mean Solar Flux *	✓	X	X	X
12-Month Running Average Sunspot	✓	✓	X	X
12-Month Running Average Solar Flux **	✓	X	X	X
* The monthly mean flux data are used to compute the 12-month running average of solar flux used by the Bent model.				
** In the absence of sufficient monthly mean data (i.e., 6 monthly values before and after the month of interest) an approximation must be made using equations (4.3) or (4.4). Note that this does not apply to the 12-month running average of sunspot as the data are published directly, with approximations already made.				

**Table 4.4** – Input Data for Three Empirical Models and the Broadcast Model

#### 4.8 Concluding Remarks

The Broadcast model is most certainly the easiest to set-up and use. In fact, its operation is virtually transparent in terms of user involvement. Of the other three



models IRI86 is the easiest to use as the only solar data required is that of the 12-month running mean of the solar sunspot number. To use the Bent model, daily solar flux, monthly mean flux, and 12-month running mean of solar sunspot must be acquired. The user must then compute the 12-month running average of solar flux from the monthly mean flux values. ICED requires  $K_p$  indices and the daily solar sunspot number. The Bent and ICED models are the most difficult to set-up and use.

With the exception of ICED, each model can produce a prediction of ionospheric delay in under 1 second. This might be an important consideration in some instances were the user to require real-time predictions of the ionosphere at 1 second intervals. A shorter update rate could probably be accommodated if the models were to be further optimised and/or if they were executed on faster machines. In a post-processing situation time constraints are not such an important issue.

## *Chapter 5*

# ***Ionospheric Refraction: Data Processing & Model Testing***

Four ionospheric models have been acquired and adapted to run on the Macintosh platform. In order to gauge the effectiveness of each model it then becomes necessary to compare modelled results against reliable measurements of ionospheric delay which can be treated as a representation of “the truth.”

To this end Faraday rotation data and dual-frequency GPS measurements (from the Jet Propulsion Laboratory’s (JPL) Rogue receivers) were obtained. The Faraday rotation data provide a direct measurement of TEC. TEC or VTEC values (and therefore slant or vertical ionospheric delays) were derived from the dual-frequency GPS data.

### **5.1 Introduction to the Propagation of Radio Waves in the Ionosphere**

Before discussing the recovery of ionospheric delays from the Faraday rotation data and GPS data it is necessary to discuss some basic principles. It was seen in section 3.4 that the highest ionospheric layer is the F2 layer; this layer also has the highest critical frequency ( $f_oF2$ ) associated with it (typically between 2 and 14 MHz). Any incoming or outgoing radio wave (striking the ionosphere vertically) whose frequency is greater than the  $f_oF2$  will not be reflected. As the angle of incidence increases the frequency which can be reflected by the ionosphere becomes greater and exceeds  $f_oF2$  — a fact that is crucial for the successful operation of shortwave radio communications. There is a

simple relationship between the angle of incidence and the maximum frequency that will be reflected (known as the maximum usable frequency, or *MUF*, and defined in section 4.1) such that

$$MUF = f_c \cdot k \cdot \sec I \quad (5.1)$$

and where  $f_c$  is the critical frequency (in MHz),  $k$  (usually equal to 1.1) is a correction factor that takes into account the curvature of the earth and the ionosphere, and  $I$  is the angle of incidence (McNamara, 1991). From (5.1) it can be shown that at no angle of incidence is the ionosphere able to reflect GPS signals. It should be noted that in reality the signal is not reflected but is continuously **refracted** (or bent) towards the ground as it passes through the ionosphere.

#### 5.1.1 Dispersion

The principle of **dispersion** is well illustrated by means of a simple example whereby the passage of white light through a glass prism is considered. Generally the index of refraction of a medium depends to some extent upon the frequency of the electromagnetic radiation involved, with the highest frequencies having the highest refractive index. In ordinary glass the index of refraction for violet light is about 1% greater than it is for red light. Since the index of refraction means a different degree of deflection when a light beam enters or leaves a medium, a beam containing one or more frequencies is split into a corresponding number of different beams when it is refracted. This effect, called dispersion, is shown in **Figure 5.1** where the initial beam of white light separates out into white light's constituent colours

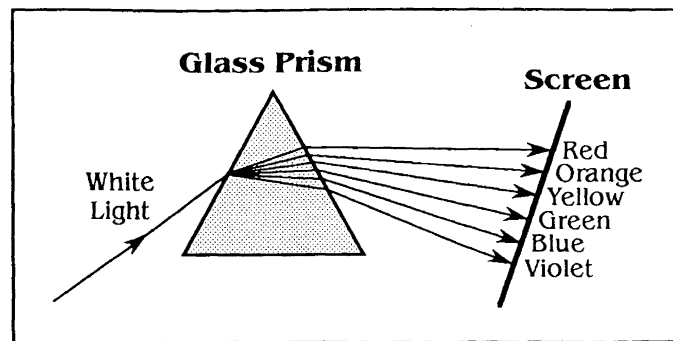


**Figure 5.1** – The Dispersion of White Light

The discussion on dispersion is now expanded to consider two different wave types:

- a pure sinusoidal wave (such as the **GPS carrier signal**); and
- waves such as the **GPS pseudorange signals** — which consist of a pure sinusoid (or carrier) modulated by the pseudorandom noise codes and the navigation message — which can be thought of as composite signals formed by the superposition of a large group of pure sinusoids of slightly different frequencies (Klobuchar, 1991).

If a pure sinusoid of radian frequency  $\omega$  and wave number  $k$  passes through a particular medium it is affected by the medium's **phase refractive index**. Conversely, a modulated signal is affected by the medium's **group refractive index**. Accordingly the terms **phase velocity** and **group velocity** are also used. A plot of  $\omega$  vs.  $k$  for a particular medium yields the so called **dispersion curve** for that medium, an example of which is shown in **Figure 5.2**.

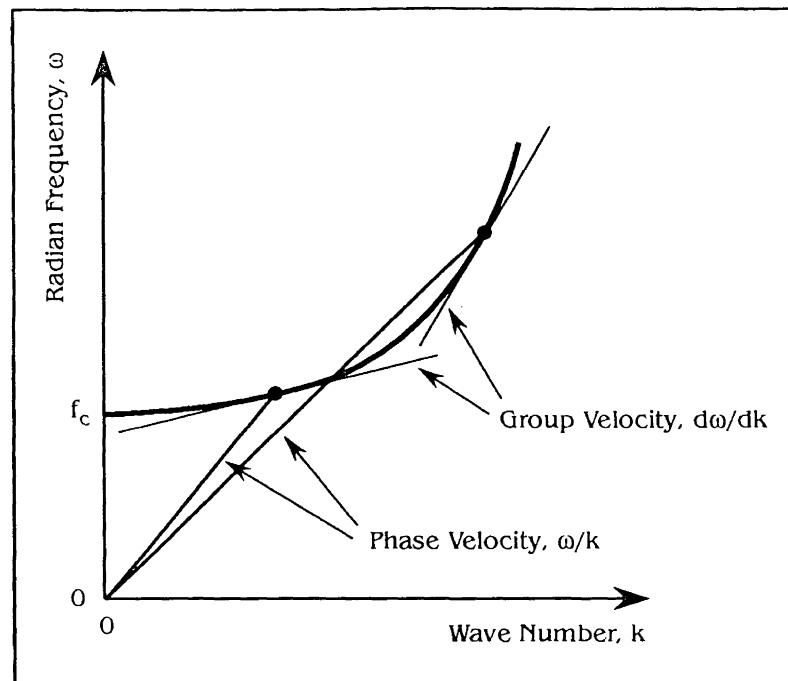


**Figure 5.2** – An Example of a Dispersion Curve

It is apparent from **Figure 5.2** that the group velocity may be either smaller or larger than the phase velocity. The same figure shows that the medium does not support wave propagation at frequencies below a critical frequency,  $f_c$ .

### 5.1.2 Fermat's Principle

**Figure 5.3** (after *Finn* (1989)) illustrates the fact that due to refraction any incoming (or outgoing) light or microwave signal passing through the earth's atmosphere is bent. The signal's velocity also differs from that of the velocity of light in a vacuo. Note that although the ray paths in **Figure 5.3** indicate a zenith angle of approximately  $35^\circ$  they are drawn like this merely to aid the readability of the figure. The ionospheric and tropospheric areas (approximately 10 m and 2.3 m respectively) indicated on the figure are of approximately the correct magnitude for the zenith case only.

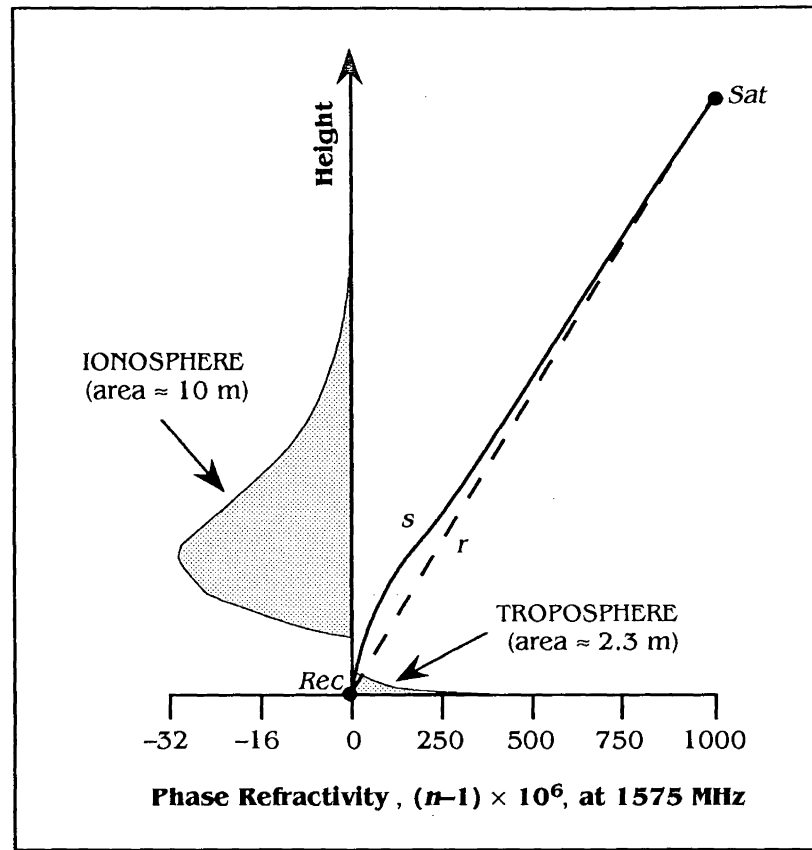


**Figure 5.3** – Propagation through the Atmosphere (Fermat's principle)

It is usually the straight line distance,  $G = \int_{Rec}^{Sat} dr$ , that is of interest but it is actually the minimum electrical path length (Fermat's principle),  $L = \int_{Rec}^{Sat} n ds$ , that is measured. The

excess path length therefore is

$$L - G = \int_{Rec}^{Sat} (n - 1) ds + (S - G) \quad (5.2)$$

where  $S = \int_{Rec}^{Sat} ds$ .

Equation (5.2) shows that the observational error is due to two components: the excess path length due to the propagation delay,  $\int_{Rec}^{Sat} (n - 1) ds$ ; and the excess path length due to bending,  $(S - G)$ .

### 5.1.3 The Appleton–Hartree Equation, Group Delays, and Phase Advances

In the 1920s Edward Appleton derived a formula which described the refractive index of the ionosphere (Davies, 1966). In 1931 D. R. Hartree amended Appleton's theory — later to have his additions discarded as they were unjustified — but in spite of this Appleton's formula became known as the **Appleton–Hartree formula**. The **phase refractive index**,  $n_p$ , of the ionosphere given as a first order approximation to the Appleton–Hartree formula is

$$n_p^2 \approx 1 - 80.56 \cdot N / f^2 \quad (5.3)$$

where  $N$  is the electron density (electrons/m<sup>3</sup>) and  $f$  is the frequency (Hz). The binomial expansion of (5.3) can be truncated to give the approximate linear form of the Appleton–Hartree formula, and therefore the phase refractive index, as

$$n_p = 1 - \left( 40.28 \frac{N}{f^2} \right) \quad (5.4)$$

where in order to retain the dimensionless property of  $n$  the constant, 40.28, is in units of m<sup>3</sup>/s<sup>2</sup>. Similarly the group refractive index,  $n_g$ , is given by

$$n_g = 1 + \left( 40.28 \frac{N}{f^2} \right) \quad (5.5)$$

Higher order terms of ionospheric effects arise because of the truncation of the series expansion of the refractive index, and because the effects of the geomagnetic field and ray bending have been ignored. The higher order terms can contribute several centimetres in path length for a low elevation satellite observed during solar conditions when high TEC values occur (*Brunner & Gu, 1991*). *Brunner & Gu (1991)* propose an improved model for the determination of  $n$  where the higher order terms are considered, and the influence of the geomagnetic field and bending effects of the ray paths at both GPS frequencies are taken into account. The authors conclude that their technique should allow determination of the true satellite–receiver range with millimetre accuracy.

Ignoring bending, the excess path length experienced at radio frequencies due to the ionosphere is given in the following equation

$$d_{ion} = \int_{Rec}^{Sat} (n - 1) ds \quad . \quad (5.6)$$

By substituting (5.4) into (5.6) the excess phase path length due to the ionosphere,  $d_{ion(\phi)}$  (metres), is given as

$$d_{ion(\phi)} = -40.28 \frac{1}{f^2} \int_{Rec}^{Sat} N ds = -\frac{40.28 \cdot TEC}{f^2} \quad (5.7)$$

where TEC is the total electron content (electrons/m<sup>2</sup>) along the satellite to receiver path. Similarly the excess group path length due to the ionosphere (e.g., for modulated signals such as the GPS code signals),  $d_{ion(g)}$  (in metres), is given as

$$d_{ion(g)} = +40.28 \frac{1}{f^2} \int_{Rec}^{Sat} N ds = +\frac{40.28 \cdot TEC}{f^2} \quad . \quad (5.8)$$



Equations (5.7) and (5.8) reveal some interesting points:

- the group and phase ionospheric biases are of equal and opposite magnitude;
- the dependence of ionospheric bias on frequency is apparent (i.e., the ionosphere is a dispersive medium at radio frequencies);
- according to (5.7) the phase velocity must exceed the speed of light in a vacuo,  $c$ , and
- according to (5.8) the group velocity — i.e., the velocity at which energy (information) is propagated — can never exceed  $c$ .

To conclude it can be stated that the ionosphere is a dispersive medium at frequencies in excess of approximately 2 to 14 MHz. This dispersive nature dictates that the ionospheric delay on a pure sinusoidal radio wave of frequency  $f$  as it propagates through the ionosphere is inversely proportional to the square of the carrier frequency. The signal that is modulating the carrier is **delayed** by the ionosphere and the delay of the modulation is termed the **group delay** (Klobuchar, 1991). Conversely if only the pure carrier is considered it undergoes a **phase advance** during which its phase is **advanced** in the presence of the ionosphere. The magnitude of the phase advance is equal to that of the group delay, but the two quantities are of opposite sign.

## 5.2 Faraday Rotation Database

A semi-global database of Faraday rotation measurements of VTEC were obtained from the National Oceanic and Atmospheric Administration (NOAA) in Boulder, Colorado. The database consists of Faraday rotation measurements of VTEC from thirteen sites for which NOAA holds data. This research used data from six of these sites covering a range

of geographic latitudes. **Figure 5.4** depicts solar cycles 21 and 22 and shows where the Faraday data used in this analysis fits in relation to solar cycle 21.

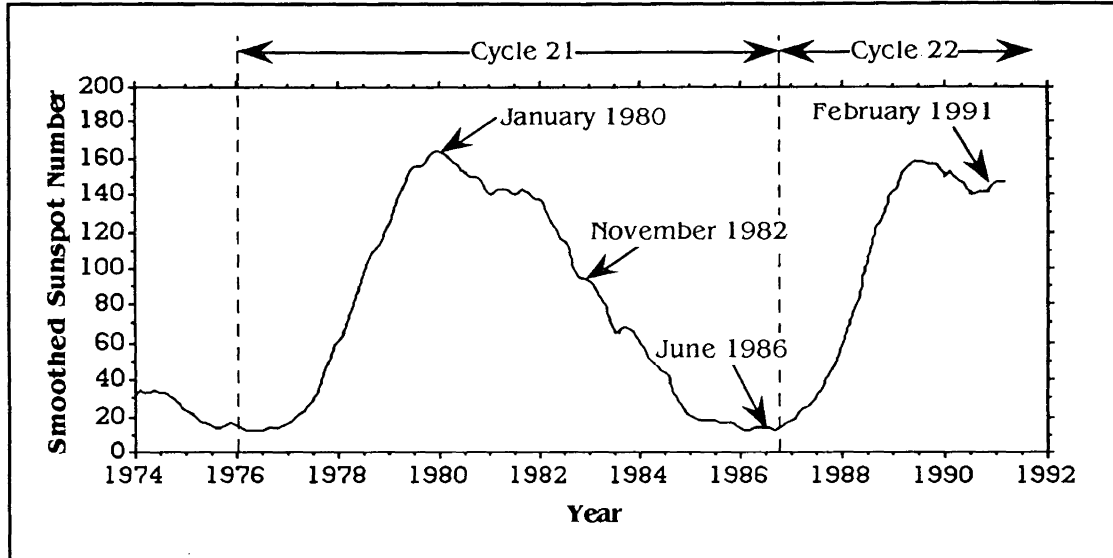


**Figure 5.4** – Solar Cycles 21 and 22

For all sites, the datasets of VTEC observations span from January 1980 to February 1988. These data were recorded at hourly intervals every day of every month and are spatially referenced by means of the sub-ionospheric point. **Table 5.1** shows from which geostationary satellites the Faraday data were recorded at each of the six test sites, at each of the three levels of solar activity which were subsequently tested.

	Jan. – Mar. 1980	Oct. – Dec. 1982	May – July 1986
<b>Anchorage</b>	N/A	GOES-3	GOES-3
<b>Goose Bay</b>	ATS-5	ATS-5	GOES-2
<b>Sagamore Hill</b>	ATS-5	ATS-5	GOES-2
<b>Athens</b>	SIRIO	SIRIO	N/A
<b>Patrick</b>	ATS-5	ATS-5	GOES-2
<b>Ramey</b>	ATS-5	ATS-5	GOES-2

**Table 5.1** – Geostationary Satellites from which the Faraday Data were Recorded

Thus, in the case of **Figure 5.5** the locations of the Faraday rotation sites reflect the sub-ionospheric points of the observations for one particular geostationary satellite. Ionospheric delays were not modelled at each of the six sites for the entire eight year period covered by the Faraday rotation data. Instead, data which coincided with three different levels of solar activity from the previous solar cycle (number 21) were chosen. January to March 1980 constituted the period of high solar activity, October to December 1982 was the period of medium activity, and May to July 1986 was the period of low activity (**Figure 5.4**). High activity VTEC data were not available for Anchorage, and low activity data were not available for Athens. Therefore a total of 9 months of data from each of 4 sites were used and 6 months of data from each of the Anchorage and Athens sites were used, for a total of 48 station months of data.

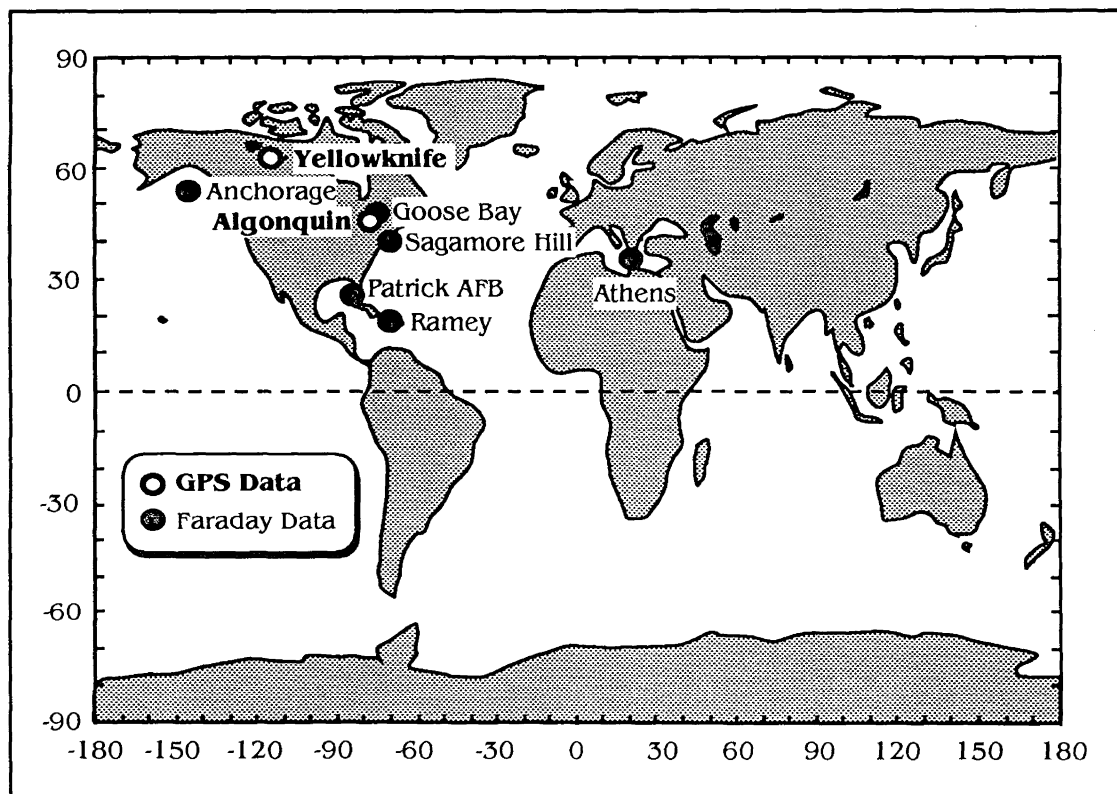


**Figure 5.5** – Locations of Recording Sites of GPS Data and Faraday Rotation Data

### **5.3 Converting Faraday VTEC Data into Ionospheric Group Delays**

The Faraday rotation data is provided in terms of TEC units. In order to maintain meaningful numbers this work opts for the idea of working with the actual (or modelled) group delay which would be experienced at the GPS L1 frequency. (5.8) is used to convert the Faraday rotation TEC data into equivalent L1 group delays. A commonly adopted convention within the ionospheric research community is that one total electron content unit (1 TECU) is equal to  $10^{16}$  electrons/m<sup>2</sup>. Therefore from (5.8) it can be seen that 1 TECU induces a delay of 0.162 m on L1 or 0.267 m on L2, thus enabling very easy conversion of TEC and VTEC values into corresponding equivalent delays at the GPS L1 frequency.

### **5.4 Selection of the Rogue Receiver's Data Set**

The Rogue receiver has been available to the GPS community for approximately three years now — prototype versions of the receiver (SNR-8) became available in August 1988 with production versions (SNR-800) following in September 1990. The data used in this analysis were obtained from the Surveys, Mapping and Remote Sensing Division of the Canada Centre for Surveying who have been operating Rogue receivers at their Yellowknife and Algonquin sites since early in 1991. The Yellowknife site was operating the SNR-8 version of the Rogue receiver whilst the Algonquin site was operating the SNR-800 version. Data was available from January 1991 onwards, but rather than arbitrarily choosing a time for which data was required, solar and geomagnetic activity indices were instead taken into account. The complete geomagnetic archive was purchased from NGDC for use in this research. This archive also contains daily values of solar sunspot number and solar flux which, in addition to the *Kp* index, were examined for January and February of 1991 (at the time the archive was acquired the indices were only available up to the end of February) to attempt to locate a period of high solar and geomagnetic activity from which to obtain Rogue data.

With reference to the sunspot and solar flux data of **Figure 5.6** it can be seen that Rogue data from GPS week # 577 or 580 would have been desirable from the standpoint of high solar activity. Analysis of the  $Kp$  indices shown in **Figure 5.6** showed that the highest average  $Kp$  index was for week # 578; and it was for this week that the GPS data were acquired. Rogue data at 120 s intervals, recorded at two sites (Yellowknife and Algonquin, see **Figure 5.5**), from the 3rd to the 9th of February 1991 (GPS week # 578, **Figure 5.4**) were provided for use in this research.

### 5.5 Preprocessing the GPS Data

The GPS data were first preprocessed using the University of New Brunswick's DIPOP 2.1 (Kleusberg *et al.*, 1989) preprocessors (PREGE and PREDD). PREGE operates on one-way (i.e., one receiver, one satellite) single or dual-frequency observations and serves several purposes: it eliminates any observations with incorrect time tags; it eliminates noisy observations; and it detects, determines, and approximately (at the few cycle level) corrects cycle slips. The output file from PREGE is also of the format which is understood by the next preprocessor, PREDD.

In this work PREDD was used primarily so that the satellite coordinates could be computed from the ephemerides file (one of PREDD's primary functions is actually to work on carrier phase double differences and remove those cycle slips which still remain after PREGE has been run). The satellite coordinates form an essential element in this work because it is from them that the elevation and azimuth to each satellite at each epoch is computed. Then from the elevation and azimuth, the sub-ionospheric point can be computed for each satellite at each epoch.

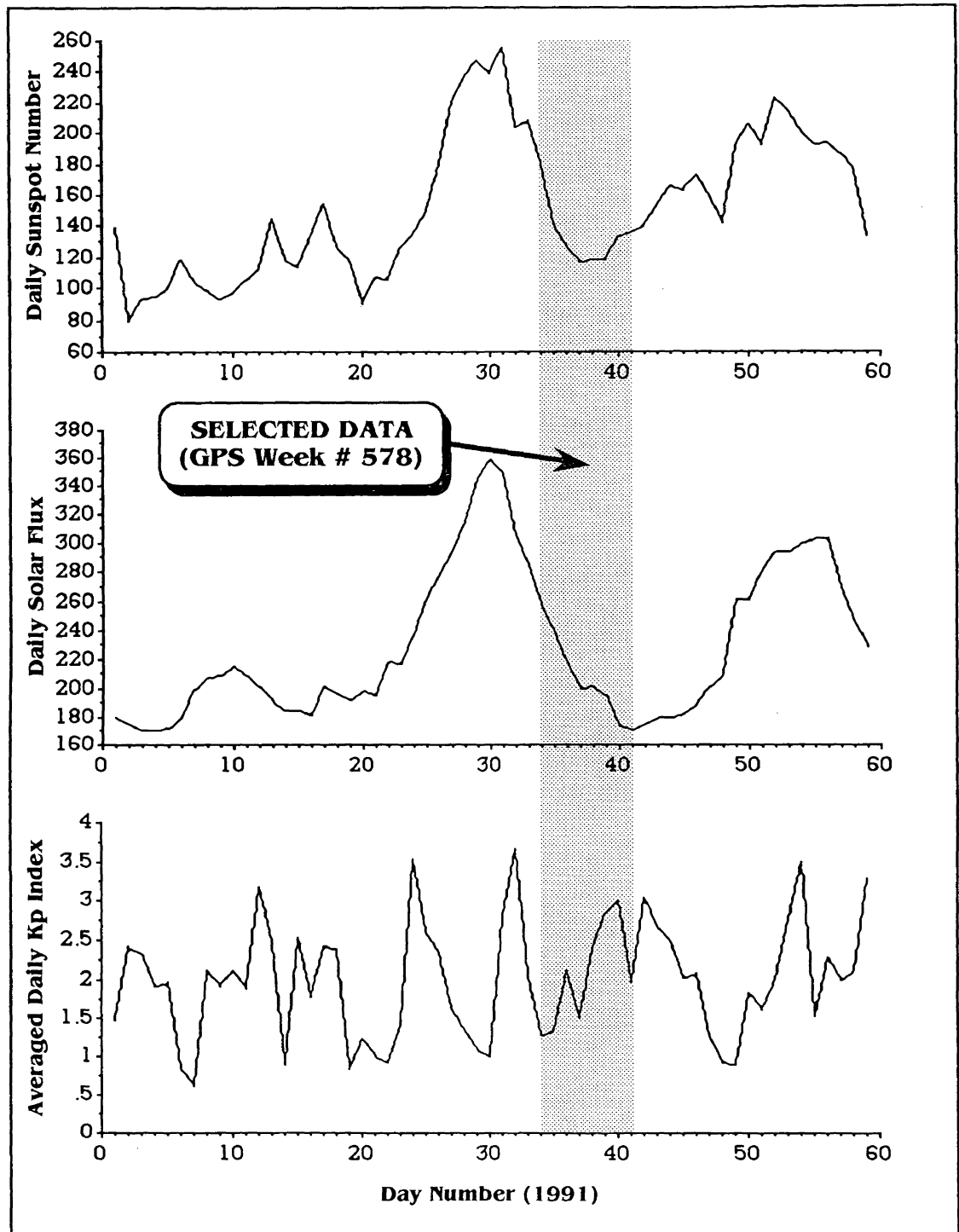


**Figure 5.6** – Daily Solar Flux and Sunspot, and Averaged Daily *Kp* Index  
for January and February 1991

It was necessary to make several modifications to both preprocessors. In their original form if dual-frequency data was processed the preprocessors automatically assumed that the data was from Texas Instruments TI 4100 receivers. The TI 4100 has a dual-frequency, single-channel four satellite multiplex design. The Rogue receiver on the other hand is capable of tracking eight satellites simultaneously. Clearly to avoid any loss of data the preprocessors had to be modified to allow processing of up to eight satellites. In fact they were modified to allow a maximum of 10 visible satellites at any one time.

### 5.6 Ionospheric Delays from Dual-Frequency GPS Data

By utilising the ionosphere's dispersive nature, dual-frequency GPS observations can be used to determine the magnitude of ionospheric delays. This dispersive nature dictates that the ionospheric group delay on a modulated signal of frequency  $f$  as it propagates through the ionosphere is inversely proportional to the square of the frequency. Therefore, the higher the frequency, the smaller the ionosphere's effect. This is expressed in the following way

$$d_{ion} \propto \frac{1}{f^2} \quad \text{or} \quad d_{ion} = \frac{k}{f^2} \quad (5.9)$$

where  $d_{ion}$  is the ionospheric delay,  $f$  is the frequency of the signal traversing the ionosphere, and  $k$  is a constant of proportionality. At the GPS frequencies where L1 is 1575.42 MHz and L2 is 1227.60 MHz it is clear that the **L2 ionospheric delays are greater than those on L1**. In terms of ionospheric delay on L1 and L2, (5.9) can be written as

$$d_{ion_1} = \frac{k}{f_1^2} \quad \text{and} \quad d_{ion_2} = \frac{k}{f_2^2}$$

which can be rearranged to eliminate the constant of proportionality

$$d_{ion_2} = d_{ion_1} \cdot \frac{f_1^2}{f_2^2} \quad (5.10)$$

The **pseudorange observation equations**, ignoring measurement and other small errors, (after *Wells et al. (1986)*) on L1 and L2 respectively are

$$P_1 = \rho + c \cdot (dt - dT) + d_{ion_1} + d_{trop} \quad (5.11)$$

$$P_2 = \rho + c \cdot (dt - dT) + d_{ion_2} + d_{trop} \quad (5.12)$$

where

$P_1, P_2$	= measured pseudoranges on L1 and L2 respectively
$\rho$	= the true range
$c$	= speed of light
$dt$	= satellite clock error
$dT$	= receiver clock error
$d_{ion_1}, d_{ion_2}$	= ionospheric delay on L1 and L2 respectively
$d_{trop}$	= tropospheric delay (independent of frequency).

Subtracting (5.12) from (5.11), and substituting (5.10) into the result gives

$$P_1 - P_2 = d_{ion_1} - d_{ion_2} = d_{ion_1} - \left( d_{ion_1} \cdot \frac{f_1^2}{f_2^2} \right) \quad (5.13)$$

which is rearranged to give the **ionospheric group delay on L1** as



$$d_{ion_1} = \frac{f_2^2}{f_2^2 - f_1^2} (P_1 - P_2) \quad . \quad (5.14)$$

Similarly, the **ionospheric group delay on L2** is

$$d_{ion_2} = \frac{f_1^2}{f_1^2 - f_2^2} (P_2 - P_1) \quad . \quad (5.15)$$

Equations (5.14) and (5.15) show that knowledge of the frequencies  $f_1$  and  $f_2$ , along with the observed pseudoranges  $P_1$  and  $P_2$ , enables the ionospheric group delay on either L1 or L2 to be determined.

The **carrier phase observation equations**, ignoring measurement and other small errors, (after *Wells et al.* (1986)) on L1 and L2 respectively are

$$\Phi_1 = \rho + c \cdot (dt - dT) + \lambda_1 \cdot N_1 - d_{ion_1} + d_{trop} \quad (5.16)$$

$$\Phi_2 = \rho + c \cdot (dt - dT) + \lambda_2 \cdot N_2 - d_{ion_2} + d_{trop} \quad (5.17)$$

where

$\Phi_1, \Phi_2$  =  $-\lambda_1 \phi_1, -\lambda_2 \phi_2$  = carrier phase observation (L1 and L2 respectively, length units)

$\phi_1, \phi_2$  = carrier phase observation on L1 and L2 respectively (in cycles)

$\lambda_1, \lambda_2$  = respective wavelengths of L1 and L2

$N_1, N_2$  = the unknown integer cycle ambiguity on L1 and L2 respectively.

Note the negative sign for the ionospheric correction term in (5.16) and (5.17) which indicates a phase advance. Subtracting (5.17) from (5.16) and substituting (5.10) into the result gives

$$\Phi_1 - \Phi_2 = \lambda_1 \cdot N_1 - \lambda_2 \cdot N_2 - d_{ion_1} + \left( d_{ion_1} \cdot \frac{f_1^2}{f_2^2} \right) \quad (5.18)$$

and rearranging leads to

$$\Phi_1 - \Phi_2 = \lambda_1 \cdot N_1 - \lambda_2 \cdot N_2 - d_{ion_1} \cdot \left( \frac{f_2^2 - f_1^2}{f_2^2} \right) . \quad (5.19)$$

Rearranging (5.19) gives the **ionospheric phase advance on L1** as

$$d_{ion_1} = \left( \frac{f_2^2}{f_2^2 - f_1^2} \right) \left[ (\lambda_1 \cdot N_1 - \lambda_2 \cdot N_2) - (\Phi_1 - \Phi_2) \right] . \quad (5.20)$$

Similarly the **ionospheric phase advance on L2** is

$$d_{ion_2} = \left( \frac{f_1^2}{f_1^2 - f_2^2} \right) \left[ (\lambda_2 \cdot N_2 - \lambda_1 \cdot N_1) - (\Phi_2 - \Phi_1) \right] . \quad (5.21)$$

The main difference between (5.20) and (5.21) and their pseudorange counterparts — (5.14) and (5.15) — is the appearance of the unknown integer cycle counts,  $N_1$  and  $N_2$ . Thus **dual-frequency carrier phase observations cannot**, by themselves, be used to determine absolute ionospheric delays as in practice  $N_1$  and  $N_2$  cannot be determined. As long as there are no cycle slips in the phase measurements (that is, they are continuous, and  $N_1$  and  $N_2$  will remain constant) such observations can be used to reveal **changes in ionospheric** delay only.

The **pseudorange** solutions of (5.14) and (5.15) do however allow computation of **absolute ionospheric delays**. The drawback to using pseudorange observations is that they contain relatively large noise levels which translate into noisy estimates of ionospheric group delay. **Figure 5.7** shows **absolute slant ionospheric delays** and **relative slant ionospheric delays** computed from dual-frequency Rogue data recorded at Algonquin on 9th February 1991; the delays are those computed to PRN 13. Note that the carrier phase delays are shifted by 6.094 metres with respect to the pseudorange delays. Note also the relative smoothness of the carrier phase delays.

A commonly adopted technique for determining ionospheric delays from dual-frequency GPS data utilises both the group delays and the phase advances to produce what is known as the **carrier smoothed pseudorange group delay** (Lanyi & Roth, 1988; Clynnch *et al.*, 1989; Coster & Gaposchkin, 1989; Srinivasan *et al.*, 1989; Coster *et al.*, 1991). The technique is very simple and merely involves finding the mean difference between the relative ionosphere as determined from the phase observations and the absolute ionosphere found from the pseudorange observations. Once this average difference is found (about 6.094 metres in the case of **Figure 5.7**) it is applied to the relative phase advance data to yield a smoother estimate of the absolute ionospheric delay, but one which is now an amalgam of both the phase and pseudorange delays. **Figure 5.8** shows the original pseudorange group delays with the new carrier smoothed pseudorange group delay superimposed over it for the first 10,000 seconds of data shown in **Figure 5.7**. Data recorded on Rogue receivers are noted for low noise levels; the addition of the Rogue's choke ring antenna reduces the effects of multipath. Analysis of the data used in this research reveals the standard deviations of the offsets for the Algonquin and Yellowknife data to be approximately 0.2 m and 0.4 m respectively which (assuming that the carrier phase determined ionospheric delays are errorless) are realistic estimates of the uncertainty of the carrier smoothed pseudorange group delays.

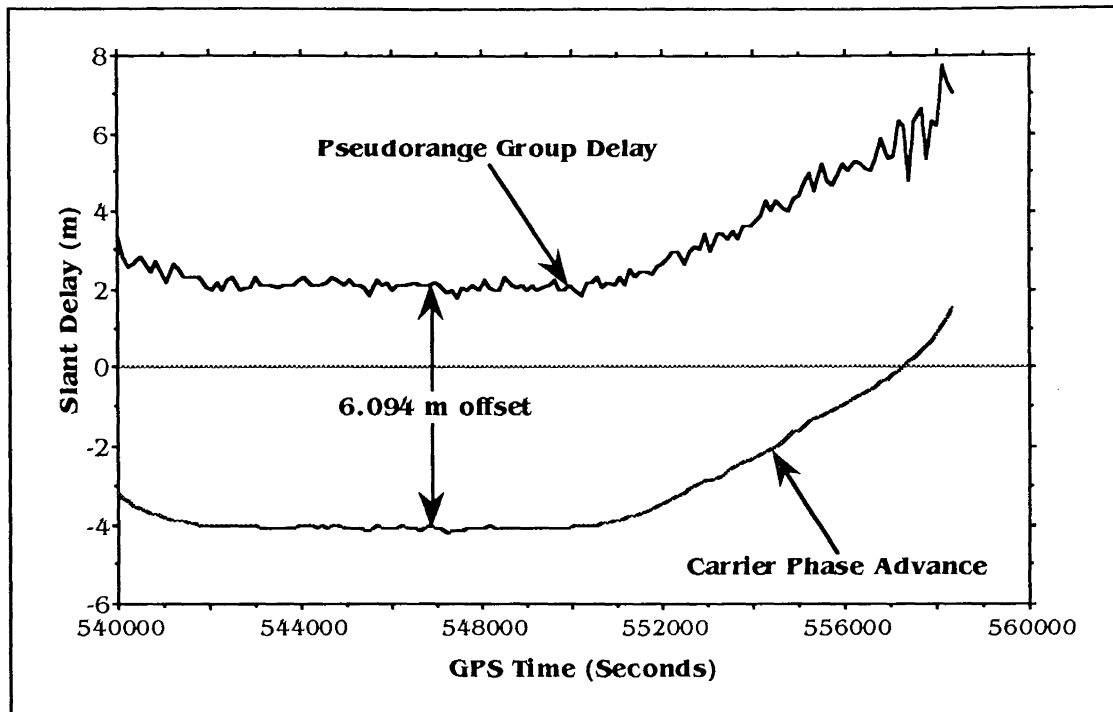


**Figure 5.7** – Ionospheric Slant Delays Derived from Pseudorange and Carrier Phase Data to PRN#13 for February 9th 1991, Algonquin

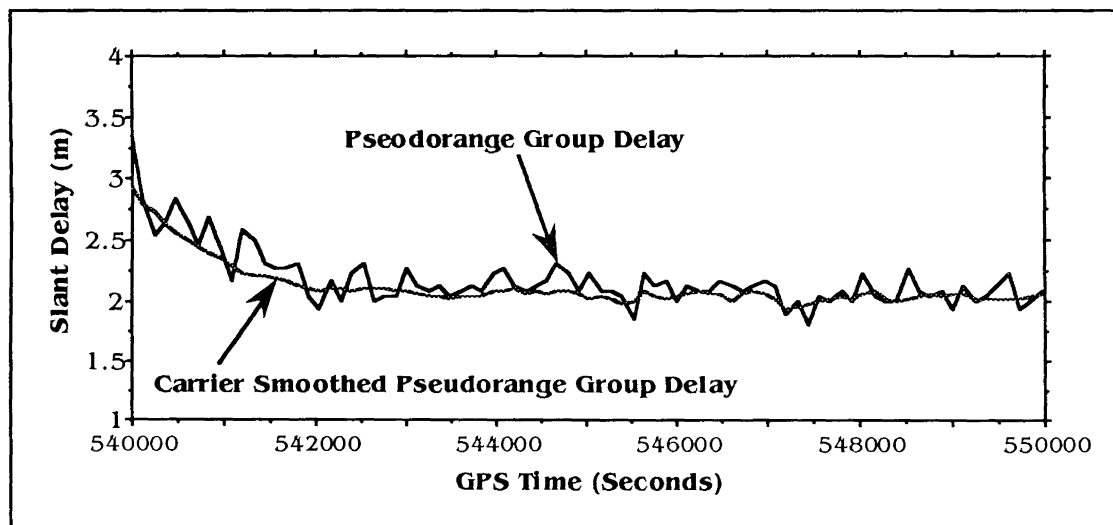


**Figure 5.8** – Carrier Smoothed Pseudorange Group Delay to PRN#13 for February 9th 1991, Algonquin

### 5.6.1 Differential Satellite and Receiver Delays

In the ideal case, group delays and the phase advances would correspond exactly with the exception of an integer cycle ambiguity and system noise errors. However, there are also internal receiver and satellite differential delays with which to contend. Differential delays, or biases, are essentially electrical delays between the L1 and L2 signals exiting the satellites and the L1 and L2 signals received in the receiver. Their net effect is that of introducing an additional differential delay between the L1 and L2 signals. Each differential satellite delay is specific to that particular satellite, as is each differential receiver delay specific to that particular receiver. As long as the differential satellite and receiver delays remain constant they have no bearing on the determination of relative ionospheric delays from phase advance data (where we can only look at ionospheric changes anyway) but in order to estimate absolute ionospheric delays from the GPS data, the satellite and receiver differential delays **must** first be obtained and then removed from the GPS dual-frequency group delay.

In the case of the Rogue receiver, the receiver's bias is easily found by looking for the "receiver calibration" term in the observation file — if the receiver has been calibrated, a correction (in nanoseconds) will be found in the file. When the Rogue receiver is calibrated a cable is used to route the L1 signal into the L2 channel so that the receiver then receives a replica of the L1 signal through its L2 channel. The receiver's "ionospheric delay" is then computed and should (for a perfect receiver with no internal differential electrical delays) be zero (private communication, *Jan Kouba*, EMR, September 1991). This is not generally the case, and the resultant "ionospheric delay" gives the magnitude of the receiver's bias.

The Rogue receiver situated in Yellowknife was calibrated three times around the period of GPS week # 578 yielding the results shown in **Table 5.2**. Although the first calibration

was performed in Ottawa (prior to the unit's shipment to Yellowknife) this and subsequent calibrations reveal a very small variation in the instrument's bias. Private communications (June 1992) with Skip Osborne (of *Allen Osborne Associates Inc.*) reveal that "the diurnal variation of a Rogue receiver's differential bias is imperceptible."

Date of Calibration	Receiver Calibration Value (ns)
January 10th, 1991	3.80 *
January 22nd, 1991	3.45
February 14th, 1991	3.68
* This calibration was performed in Ottawa prior to the receiver's shipment to Yellowknife.	

**Table 5.2** – Receiver Calibration Values around GPS Week # 578  
for the Yellowknife Rogue GPS Receiver

Differential satellite delays present a somewhat more involved problem. Although each satellite is tested prior to launch — and a pre-launch calibration figure determined and broadcast — independent assessments of the satellite differential delays have concluded that the pre-launch figures should be used with caution if accurate estimates of the absolute ionospheric delay are required (Coco *et al.*, 1991). In this research the differential satellite delays were acquired from the Jet Propulsion Laboratory (JPL).

JPL determines the differential satellite biases using the technique described in detail by Lanyi & Roth (1988). In essence night-time GPS differential group delay measurements from a mid-latitude site are input into a least squares estimation process to estimate the coefficients of a local two-dimensional quadratic model of the vertical TEC and the combined satellite and receiver biases for each satellite observed. The combined satellite plus receiver biases from different satellites can then be differenced to remove

the receiver bias contribution as the receiver bias is common to the measurements from all satellites.

The figures supplied by JPL for use in this research are the “best estimates” of the differential satellite delays for February 1991, and although the figures have formal errors which are quite small (between 0.04 and 0.1 ns) a more realistic estimate of the error would be at the 0.5 to 1 ns level ( $\approx 0.15$  and 0.3 m respectively) (private communication, *Brian Wilson*, JPL, September 1991).

By combining the receiver and satellite biases,  $diff_{receiver}$  and  $diff_{satellite}$  respectively, the total differential delay due to these two error sources is found. **Table 5.3** lists the broadcast value of the differential satellite delays, the JPL estimates of the same delays, and the combined satellite and receiver corrections which are applied to the slant ionospheric group delays,  $d_{ion}$ , as computed from the dual-frequency pseudorange data. Mathematically then the corrected ionospheric group delay,  $d_{ion_{corrected}}$ , is expressed as follows

$$d_{ion_{corrected}} = d_{ion} - diff_{receiver} - diff_{satellite} \quad . \quad (5.22)$$

Confirmation that the differential correction terms should be subtracted (rather than added) from the  $d_{ion}$  term in (5.22) was provided by JPL’s *Brian Wilson*. From **Table 5.3** it can be seen, for example, that the slant ionospheric group delay computed from data recorded at Yellowknife, using PRN#02, would be in error by +0.97 metres. Therefore 0.97 metres is subtracted from the computed group delay to yield the correct slant ionospheric group delay.

From **Table 5.3** it is also clear that the combined satellite/receiver differential delays can be quite significant (sometimes as large as –2.02 m for Algonquin). The receiver biases

for the Yellowknife and Algonquin sites are both (purely by coincidence) at the 3 ns level (which corresponds to an error of about 0.9 m), however, these figures can be larger than 15 ns ( $\approx$  4.5 m) for Rogue receivers (private communication, *Jan Kouba*, EMR, September 1991). **Figures 5.7 and 5.8** both represent slant group delays which have had the satellite/receiver corrections applied.

PRN	Broadcast Value of Diff. Sat. Delay (ns)	JPL Estimate of Diff. Sat. Delay (ns)	Yellowknife Delay (m) *	Algonquin Delay (m) *
2	0.9	-0.2	0.97	-1.06
3	-4.2	1.2	1.39	-0.64
6	-1.9	-0.1	1.00	-1.03
9	0.0	0.3	1.12	-0.91
11	0.0	3.0	1.93	-0.10
12	2.8	3.0	1.93	-0.10
13	2.8	1.6	1.51	-0.52
14	1.4	-0.5	0.88	-1.15
15	2.8	0.2	1.09	-0.94
16	5.1	0.4	1.15	-0.88
17	1.4	-1.0	0.73	-1.30
18	-1.9	-3.4	0.01	-2.02
19	4.2	-0.3	0.94	-1.09
20	3.7	-1.0	0.73	-1.30
21	6.1	1.2	1.39	-0.64
23	1.4	2.5	1.78	-0.25

\* These delays are combined receiver-satellite differential delays (computed using the JPL estimates of the satellite differential delay). Yellowknife has a receiver delay of 3.45 ns applied, Algonquin has -3.35 ns applied.

**Table 5.3** – Satellite and Receiver Differential Delays at Yellowknife and Algonquin for GPS Week # 578

### 5.6.2 Mapping Line-of-sight Ionospheric Delays to the Vertical

**Chapter 4** highlighted the fact that of the four ionospheric models considered in this research only two, the Bent model and the Broadcast model, were written to be directly capable of determining line-of-sight (or slant) ionospheric predictions. Therefore to allow comparisons between observed and modelled ionospheric delays this research looks only at vertical delays. This of course necessitates that the line-of-sight carrier smoothed pseudorange group delays be mapped to the vertical. By so doing it then



becomes an easy matter to compare the mapped GPS ionospheric delays with the vertical ionospheric predictions made by each of the models. Mapping the line-of-sight delays to the vertical is actually a two-stage process which involves computing the sub-ionospheric point and scaling by means of an obliquity factor.

#### 5.6.2.1 Sub-Ionospheric Point

*Klobuchar* (1991) describes the concept of the sub-ionospheric point (also shown in **Figure 5.9**) well when he says that it is “the point on the earth’s surface directly below where the signal ray path passes the centroid height of the ionosphere. For satellites at low elevation angles with widely different azimuths, these subionospheric points can be separated by up to 3,000 kilometers. The ionospheric behaviour at locations that far apart is generally not the same, giving different range errors along each line of sight.”

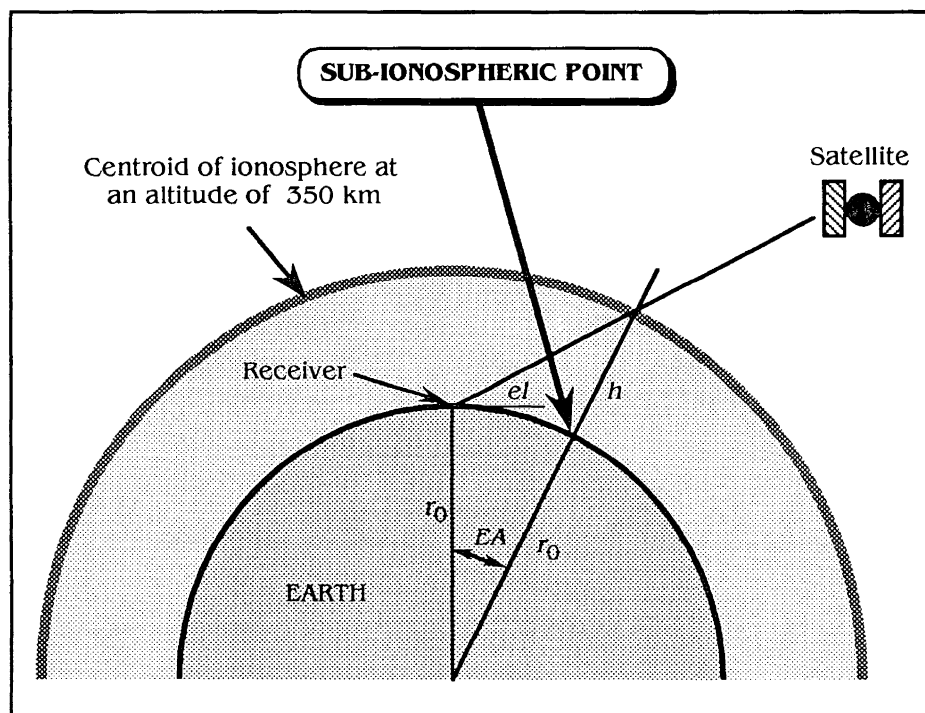


**Figure 5.9** – Sub-ionospheric Point and Earth Angle

The sub-ionospheric point is a function of the receiver's latitude and longitude,  $\varphi_r$  and  $\lambda_r$ , respectively, and the satellite's azimuth and elevation,  $az$  and  $el$  respectively, with respect to the receiver. Computation of the sub-ionospheric point's latitude and longitude is described by various authors (e.g., *Feess & Stephens*, 1986; *Klobuchar*, 1986) and is outlined below where  $r_0$  is the earth's mean radius ( $\approx 6371$  km) and  $h$  is the centroid height of the ionosphere ( $= 350$  km).

According to the ICD-200 document (*Rockwell*, 1987) the approximate forms of (5.23), (5.24), and (5.25) are to be used with the Broadcast model. Private communication with Jack Klobuchar (Phillips Laboratory, United States Air Force, May 1992) reveals that any errors introduced by use of the approximate forms are trivial when compared with the general day-to-day variability of the ionosphere with which ionospheric models cannot hope to contend. Thus the approximate forms were used in this research.

The earth angle,  $EA$ , is the angle subtended between the receiver and the satellite

$$EA = 90^\circ - el - \sin^{-1} \left[ \frac{r_0}{r_0 + h} \cos el \right] \approx \frac{445^\circ}{el + 20} - 4^\circ \quad (5.23)$$

The sub-ionospheric geocentric latitude is given by the following expression

$$\varphi_I = \sin^{-1} [\sin \varphi_r \cos EA + \cos \varphi_r \sin EA \cos az] \approx \varphi_r + EA \cos az \quad (5.24)$$

and the sub-ionospheric longitude (east) is

$$\lambda_I = \lambda_r + \sin^{-1} \left( \frac{\sin EA \sin az}{\cos \varphi_I} \right) \approx \lambda_r + \frac{EA \sin az}{\cos \varphi_I} \quad (5.25)$$

Therefore the coordinates of the sub-ionospheric point can now be found. Adopting a value of 300 or 400 km for  $h$  introduces **maximum** differences (at 5° elevation) of approximately 1.2° into the value of  $EA$  (with respect to the  $h = 350$  km values). Accordingly the sub-ionospheric latitude or longitude could be altered (from the  $h = 350$  km values) by a maximum of approximately 1.2°, depending on the satellite's azimuth. At 45° elevation the maximum effect on the sub-ionospheric latitude or longitude is only about 0.4°.

### 5.6.2.2 Obliquity Factor

Line-of-sight ionospheric delays are mapped to the vertical in order to facilitate comparisons between modelled and observed ionospheric delays. This mapping is an easy matter on a flat earth with an homogeneous ionosphere; one merely applies the cosecant of the elevation angle to yield the delay at zenith. In reality however, the situation involves a spheroidal earth and a non-uniform ionosphere. Slant delays are converted into equivalent vertical delays by dividing the slant delays by an obliquity factor,  $Q$ , which is a function of the satellite's elevation angle. The following mapping function (Clynch *et al.*, 1983; Clynch *et al.*, 1989) is adopted in this work

$$Q(eI) = \sum_{I=0}^3 a_I x^{2I} \quad \text{where} \quad x \equiv 1 - \frac{2}{\pi} eI \quad (5.26)$$

where  $a_0 = 1.0206$ ,  $a_1 = 0.4663$ ,  $a_2 = 3.5055$ ,  $a_3 = -1.8415$ , and  $eI$  is in radians.

The function's coefficients were derived from a least squares fit of (5.26) to an homogeneous spherical shell between the altitudes of 200 and 600 km. Coco *et al.* (1988) test the obliquity factor by comparing it with a more realistic one derived from ionospheric profiles generated by the Bent model (which accounts for varying geographic position and time but which assumes the local ionosphere to be free from large

horizontal gradients). Profiles were generated at 36 stations uniformly distributed around the world, using four azimuth directions and six elevation angles at each station. Analysis of the simulated results showed that at 10° elevation (5.26) was in error by 10% r.m.s. (with a maximum error of 20%), and at elevation angles above 30° the r.m.s. error was less than 3% (with a maximum error of 6%). The authors conclude that “the results of this simulation show that the obliquity factor model can be used with a wide variety of realistic ionospheric profiles without introducing a large error.”

**Figure 5.10** shows how the obliquity factor of (5.26) varies with the satellite’s elevation. For comparison’s sake the simple cosecant obliquity factor and the Broadcast model’s obliquity factor (*Klobuchar*, 1986) are also shown. There is comparatively little difference between (5.26) and the Broadcast model’s obliquity factor. The simple cosecant obliquity factor displays **severe** errors for elevation angles less than approximately 30°.

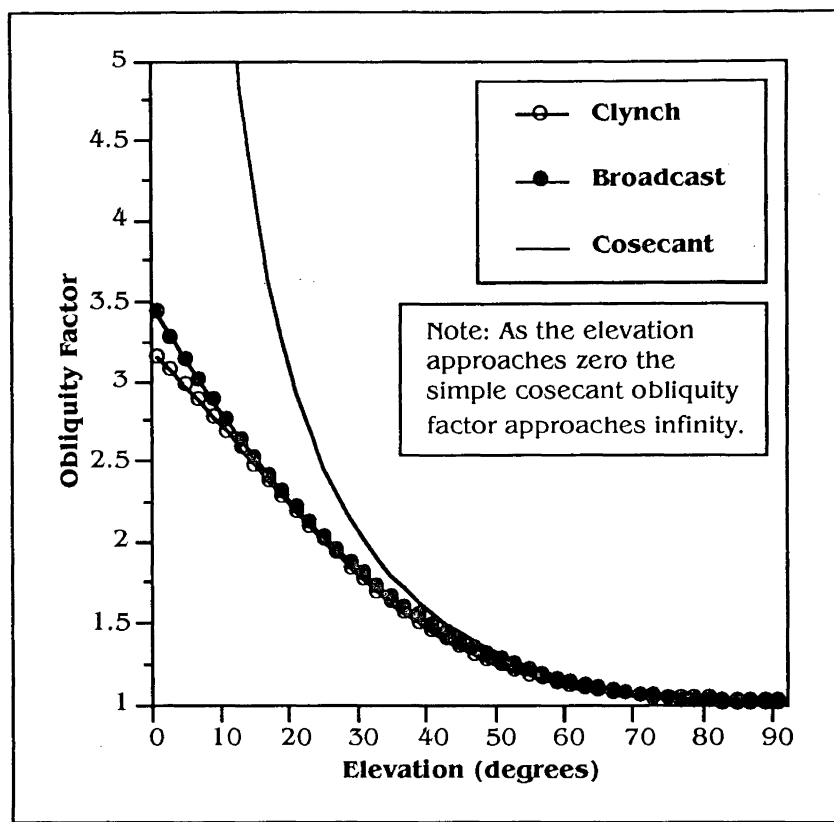


**Figure 5.10** – Obliquity Factor Computed Three Different Ways

Processing the GPS data in accordance with all of the steps listed in section 5.6 leads to smooth estimates of vertical ionospheric delays which are spatially referenced by means of the sub-ionospheric point. Of course, as the GPS satellites are never stationary the sub-ionospheric point will always be moving. **Figures 5.11** and **5.12** depict the results of such processing for one GPS day of data recorded at Algonquin and Yellowknife respectively. No attempt is made to differentiate between any of the 15 satellites whose results are plotted (PRN#09 has been omitted as it was flagged as being unhealthy) as this would lead to a very confusing plot. Neither has any attempt been made to reconcile the fact that at any particular epoch each satellite in view is located at a different sub-ionospheric point. The figures do however serve well to illustrate the diurnal behaviour of the ionosphere as determined from GPS data. Perhaps the most interesting point to note is the relatively smooth appearance of the ionosphere at Algonquin.

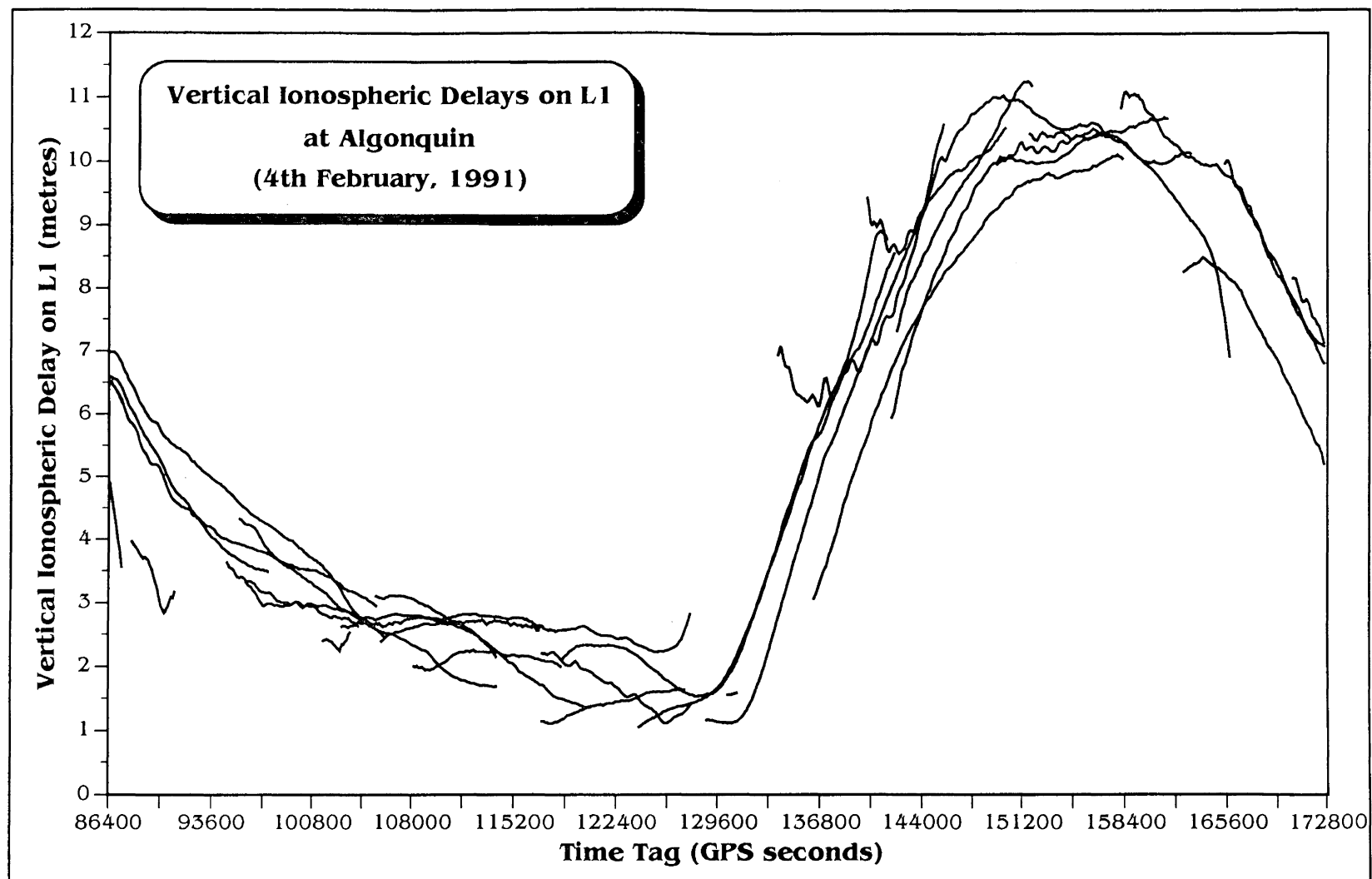


**Figure 5.11** – An Example of Vertical Ionospheric Delays Determined from GPS Data

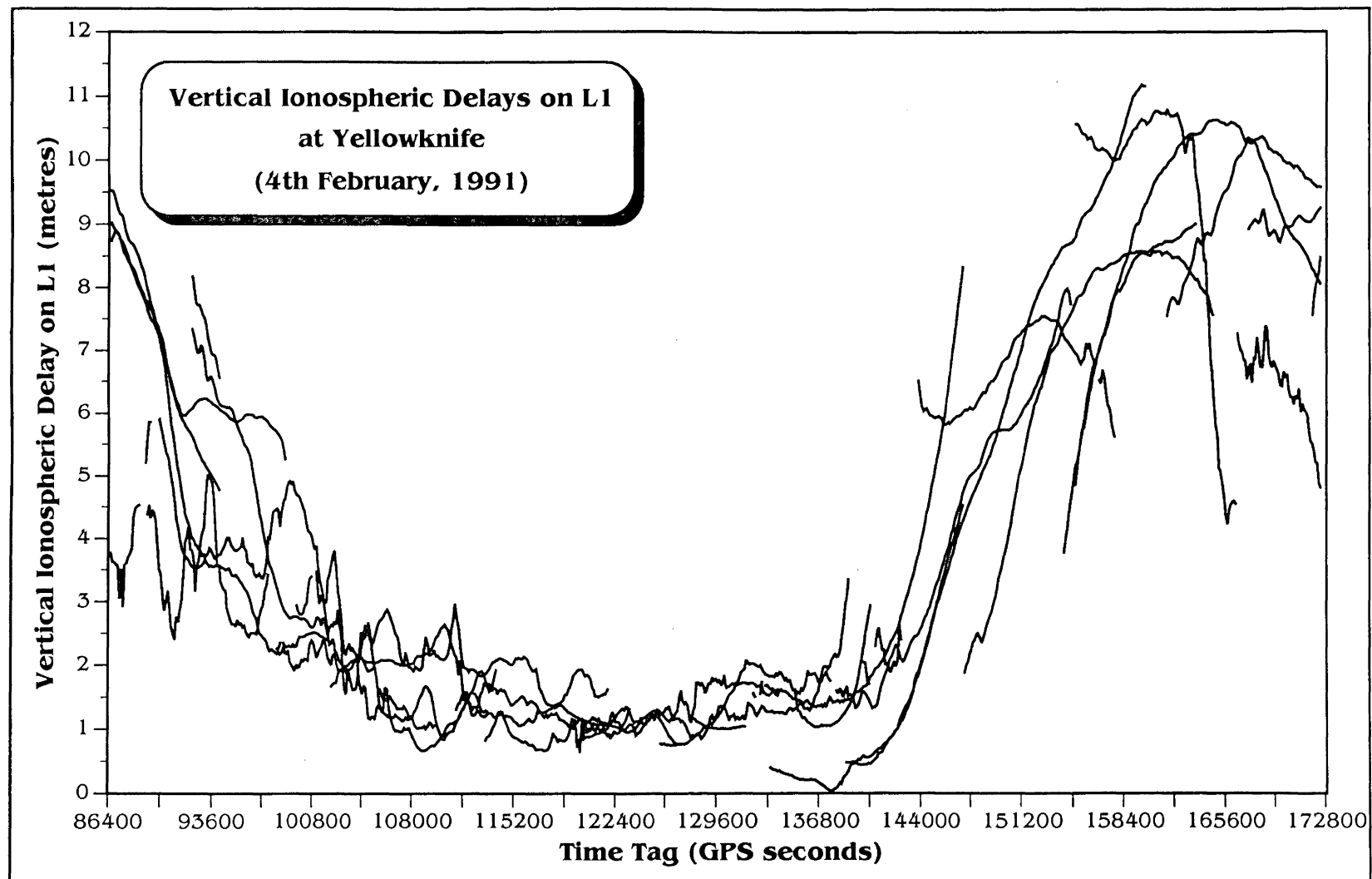


**Figure 5.12** – An Example of Vertical Ionospheric Delays Determined from GPS Data

### 5.7 Multiple Epoch/Location Computations Using the Ionospheric Models

By adopting the procedures outlined in sections 5.3 and 5.6, the Faraday rotation data and GPS Rogue data provided estimates of the vertical ionospheric delay at the GPS L1 frequency, at the sub-ionospheric point (which is different at each epoch), for each epoch that the data were recorded. For the purposes of this research modelled estimates of the vertical ionospheric delay are required for the same epochs/locations.

Each of the ionospheric models was modified to allow multiple epoch/location estimates to be computed; **Figure 5.13** is an example of the resultant output from a run of the modified version of the Bent model combined with the GPS results. Each column in the figure is explained in **Table 5.4**. Note that the "RATE" column in Figure 5.13 was computed using L1 line-of-sight carrier phase delays and **not** the vertical delays shown in the same figure. In other words the numbers in the "RATE" column **cannot** be reproduced using the data shown in Figure 5.13.

VERT DELAYS FOR : YELLOWKNIFE STATION LATITUDE : 62.481 STATION LONGITUDE : -114.480												
TIME TAG (sec)	UT (hours)	L1CODE (m)	L2CODE (m)	L1CARR (m)	L2CARR (m)	CODIFF (m)	CADIFF (m)	RATE (cm/min)	SUBLAT (deg)	SUBLON (deg)	BENTL1 (m)	BENTL2 (m)
522960.000	145.2667	8.397	14.049	8.320	13.922	5.652	5.602	-11.6	52.58	231.36	8.298	13.660
523080.000	145.3000	8.908	14.893	8.355	13.982	5.985	5.628	-14.3	53.00	231.73	8.153	13.421
523200.000	145.3333	7.806	13.082	8.372	14.014	5.276	5.642	-37.2	53.39	232.08	8.012	13.188
523320.000	145.3667	8.931	14.938	8.224	13.773	6.007	5.549	-50.3	53.75	232.42	7.874	12.961
523440.000	145.4000	7.918	13.273	7.975	13.367	5.355	5.392	-45.5	54.10	232.75	7.738	12.738
523560.000	145.4333	7.949	13.328	7.770	13.033	5.379	5.263	-40.0	54.47	233.10	7.591	12.495
523680.000	145.4667	7.700	12.922	7.584	12.731	5.222	5.147	-33.1	54.78	233.41	7.447	12.258
523800.000	145.5000	7.264	12.208	7.446	12.508	4.944	5.062	-31.1	55.07	233.70	7.314	12.040
523920.000	145.5333	7.562	12.702	7.320	12.303	5.140	4.983	-28.9	55.35	233.98	7.190	11.835
524040.000	145.5667	7.606	12.778	7.221	12.145	5.173	4.924	-21.9	55.64	234.29	7.063	11.625
524160.000	145.6000	7.296	12.272	7.160	12.049	4.977	4.889	-18.3	55.89	234.55	6.946	11.434
524280.000	145.6333	7.051	11.874	7.126	11.997	4.823	4.871	-18.9	56.13	234.81	6.832	11.246
524400.000	145.6667	7.281	12.256	7.100	11.958	4.975	4.859	-21.5	56.39	235.09	6.716	11.054
524520.000	145.7000	7.085	11.938	7.034	11.855	4.853	4.821	-25.2	56.60	235.33	6.609	10.879
524640.000	145.7333	6.916	11.665	6.947	11.717	4.749	4.769	-24.7	56.83	235.59	6.500	10.700
524760.000	145.7667	7.239	12.202	6.846	11.555	4.963	4.709	-28.6	57.03	235.82	6.399	10.533
524880.000	145.8000	6.834	11.539	6.720	11.352	4.706	4.632	-33.3	57.24	236.07	6.299	10.368
525000.000	145.8333	6.737	11.386	6.529	11.043	4.649	4.514	-39.6	57.42	236.28	6.208	10.218
525120.000	145.8667	6.586	11.142	6.284	10.645	4.556	4.361	-35.5	57.61	236.52	6.113	10.063
525240.000	145.9000	6.346	10.752	6.054	10.272	4.406	4.217	-33.3	57.78	236.71	6.027	9.921
525360.000	145.9333	5.884	9.997	5.849	9.939	4.113	4.090	-31.2	57.95	236.94	5.943	9.783
525480.000	145.9667	5.641	9.604	5.641	9.603	3.962	3.962	-27.0	58.11	237.13	5.867	9.658
525600.000	146.0000	5.658	9.637	5.480	9.343	3.979	3.863	-23.8	58.27	237.34	5.790	9.530
525720.000	146.0333	5.578	9.511	5.342	9.123	3.933	3.780	-22.7	58.42	237.55	5.713	9.404
525840.000	146.0667	5.747	9.796	5.197	8.889	4.049	3.692	-19.9	58.55	237.72	5.642	9.287
525960.000	146.1000	4.920	8.439	5.086	8.712	3.520	3.626	-20.2	58.70	237.92	5.567	9.164
526080.000	146.1333	5.015	8.603	4.964	8.519	3.588	3.555	-22.9	58.83	238.11	5.496	9.047
526200.000	146.1667	5.138	8.811	4.806	8.264	3.673	3.458	-24.2	58.97	238.30	5.440	8.955
526320.000	146.2000	4.650	8.014	4.614	7.955	3.364	3.341	-37.6	59.08	238.46	5.384	8.862
526440.000	146.2333	4.473	7.729	4.271	7.396	3.256	3.125	-32.4	59.20	238.64	5.324	8.764

**Figure 5.13** – Output Sample from the Modified Version of the Bent Model

(Evaluations for Yellowknife, Feb. 9th 1991, PRN#02)



COLUMN HEADING	DESCRIPTION
TIME TAG (sec)	Time tag taken from the GPS observations for which a modelled ionospheric delay is required.
UT (hours)	TIME TAG written in hours UT. The slight difference between the GPS and UT time scales is not taken into account.
L1CODE (m)	Vertical ionospheric delay on L1 computed from dual-frequency pseudorange observations.
L2 CODE (m)	Vertical ionospheric delay on L2 computed from dual-frequency pseudorange observations.
L1CARR (m)	Vertical ionospheric delay on L1 computed from dual-frequency carrier observations (average offset applied).
L2CARR (m)	Vertical ionospheric delay on L2 computed from dual-frequency carrier observations (average offset applied).
CODIFF (m)	L2CODE – L1CODE
CADIFF (m)	L2CARR – L1CARR
RATE (cm/min)	Rate of change of the ionosphere computed from consecutive <b>line-of-sight</b> L1CARR computations.
SUBLAT (deg)	Sub-ionospheric latitude.
SUBLON (deg)	Sub-ionospheric longitude.
BENTL1 (m)	Vertical ionospheric delay on L1 computed with the Bent model.
BENTL2 (m)	Vertical ionospheric delay on L2 computed with the Bent model.

**Table 5.4** – Explanation of the Output File from the Modified Form of the Bent Model

**Figure 5.13** shows, for each epoch of GPS time, the pseudorange and carrier smoothed pseudorange ionospheric delays on L1 and L2, the L2–L1 pseudorange and carrier smoothed pseudorange ionospheric delays (not used for anything), as well as the rate of change of the ionosphere (cm/min), the sub-ionospheric latitude and longitude, and the delays on L1 and L2 as modelled by the Bent model. Similar output files result after execution of each of the other three models under examination — each successive

models' L1 and L2 delays being added as a further 2 columns on the right-hand-side of the table. Examples of successive models' output files are not included in this text.

### 5.8 Estimated Accuracy of Vertical Ionospheric Delays from the GPS Data

There are three obvious sources of error in the vertical ionospheric delays which were determined from the dual-frequency GPS data:

- (i) Errors in the carrier smoothed pseudorange group delays;
- (ii) Errors in the differential satellite and receiver delays; and
- (iii) Errors in the obliquity factor used to map the line-of-sight delays to the vertical.

At the end of section 5.6 it was noted that the uncertainty in the carrier smoothed pseudorange group delays is approximately 0.2 m at Algonquin and 0.4 m at Yellowknife. On a **worst case basis** it was seen in section 5.6.1 that the magnitude of the second error source is approximately 1.0 ns ( $\approx 0.3$  m), this error being site independent.

It is somewhat more difficult to estimate the magnitude of the third error source. Errors introduced by the obliquity factor increase as the satellite's elevation decreases. The same errors also depend on the extent to which the assumption that the localised ionosphere is free of large horizontal gradients is true. In section 5.6.2.2 it was seen that under extreme circumstances where the satellite's elevation is low we might see errors in the obliquity factor of the order of 20% (or 10% r.m.s.). It was also seen that for satellites whose elevation is above 30° the error might be as large as 6% (or 3% r.m.s.).

For the GPS data processed in this research there were rarely any instances of line-of-sight (LOS) ionospheric delays which were in excess of 40 metres (most were far smaller than this — typically between 10 and 20 m). Also, the vast majority of observations were made to satellites whose elevations were greater than 30°. Therefore a 6% error in the mapping function evaluated for an elevation of 30° ( $Q_{30} \approx 1.76$ ) would introduce errors of approximately 1.3 m when a 40 m LOS delay is mapped to the vertical. Typically the error would probably be smaller than this as the LOS delays in this research are usually of the order of 10 to 20 m.

Combining the three error sources shows that on a **worst case basis** the total error in mapped ionospheric delays determined from a combination of P-code and carrier phase data is probably no greater than approximately 1.4 m at Algonquin and Yellowknife.

On a **more optimistic** note, if the LOS ionospheric delays are of the order of 10 m then the combined error in the mapped ionospheric delays will be of the order of 0.5 m.

## *Chapter 6*

### ***Analysis & Results***

Analysis of the results in this study are, in the first instance, treated as two quite separate cases. Firstly there are those results which are based upon the Faraday rotation data; secondly there are those which are based upon the GPS data.

Validation of the models requires that the modelled results be compared with the Faraday rotation data and the GPS-derived ionospheric delays, each of which are regarded as representing the “truth.” It was noted in **section 3.5.3** that the Faraday rotation measurements are in error by approximately 3 to 5%. Some of the larger GPS estimates of vertical ionospheric delays might be in error by as much as 1.4 m. Differences between observed and modelled VTEC are regarded as representing the model’s error. It is an easy matter to compute r.m.s. errors; and in this research daytime and night-time results are separated from one another. The reason for this separate treatment is best understood by way of the following example where we first imagine an observed night-time delay of 1 m and a corresponding modelled delay of 2 m. The modelled delay is in error by 1 m, or 100%. Now consider a daytime observed delay of 10 m and a corresponding modelled delay of 11 m. This time the modelled delay is in error by 10% although the error is still 1 metre. From this example it is clear that although the daytime and night-time results may both be in error by similar amounts (1 m in the example) the r.m.s. percentage errors can be quite different. This is entirely logical bearing in mind the relatively larger ionospheric delays which exist during daylight

hours. But of course, what is important for the single-frequency GPS user is the remaining bias (in metres) after using a model, by day or night.

Henceforth when referring to percentage r.m.s. errors, I will use the r.m.s. (%) notation. Similarly, if referring to r.m.s. errors in metres, I will use the r.m.s. (m) notation. In the following analysis any r.m.s. (m) values are based upon observed and modelled delays at the GPS L1 frequency.

## 6.1 Comparisons with the Faraday Rotation Data

**Tables 6.1** and **6.2** summarise the daytime and night-time r.m.s. errors respectively for each of the three ionospheric research models. The tables show the r.m.s. (%) and r.m.s. (m) errors. The italicised numbers in parentheses are the corresponding r.m.s. (%) values. The results are shown for three different levels of solar activity (where  $R$  is the 12-month running average of sunspot number) and for evaluations at six Faraday rotation stations. The “station” column is organised so that, reading downwards, the stations are arranged in order of decreasing geographic latitude, Anchorage being the northernmost station at 53° N. The daytime and night-time r.m.s. (m) errors are also represented for each of the three levels of solar activity in **Figures 6.1**, **6.2**, and **6.3**. Some typical examples of the models’ errors can be found in **Appendix II**. The qualification for a night-time observation is provided by (4.11) where it can be seen that according to the Broadcast model a vertical night-time ionospheric delay at the GPS L1 frequency will be equal to 5 ns, or 1.499 m.

### 6.1.1 Conclusions Resulting from the Faraday Rotation Comparisons

With respect to the daytime **r.m.s. (m)** errors listed in **Table 6.1** and depicted in **Figures 6.1** to **6.3** it can be seen that at high solar activity the high to mid-latitude (i.e., Goose Bay, Sagamore, and Athens) daytime performance of the Bent model is superior to that of IRI86 and ICED. At lower latitudes (i.e., Patrick and Ramey) IRI86’s performance is the best. Under conditions of medium solar activity IRI86 has a marginal

advantage at Anchorage, but at all other latitudes it is the Bent model which performs best. At low solar activity the Bent model performs best at Anchorage, but at all other latitudes it is ICED which performs best.

Based upon the night-time **r.m.s. (m)** results listed in **Table 6.2** and depicted in **Figures 6.1 to 6.3** it can be seen that during conditions of high solar activity at the high to medium latitude stations (i.e., Goose Bay, Sagamore, and Athens) the Bent model yields the best results. At lower latitudes (i.e., Patrick and Ramey) the favoured model is that of IRI86. During medium solar activity, and at all latitudes (with the exception of Patrick where ICED's performance is marginally better) IRI86 performs best. At low solar activity there is little to choose between any of the three models, although the Bent and IRI86 models do have a slight edge over ICED. Note that in **Tables 6.1** and **6.2** these "best performances" of the test models by day and by night, during three levels of solar activity, are highlighted by applying shading to the appropriate cell in the table.

STATION	$\phi$	LEVEL OF SOLAR ACTIVITY								
		HIGH (R = 162) (Jan. – March 1980)			MEDIUM (R = 95) (Oct. – Dec. 1982)			LOW (R = 14) (May – July 1986)		
		BENT	IRI86	ICED	BENT	IRI86	ICED	BENT	IRI86	ICED
Anchorage	53	N/A	N/A	N/A	1.39 (51)	1.25 (43)	1.71 (50)	0.22 (19)	0.31 (21)	0.29 (20)
Goose Bay	47	1.51 (42)	3.13 (84)	3.01 (58)	1.66 (35)	2.05 (35)	2.32 (38)	0.31 (31)	0.28 (23)	0.25 (21)
Sagamore	39	1.41 (24)	1.98 (41)	3.44 (51)	1.64 (28)	1.98 (29)	2.35 (38)	0.31 (24)	0.28 (18)	0.27 (18)
Athens	35	1.55 (37)	1.49 (58)	3.45 (66)	2.10 (29)	2.42 (33)	2.34 (35)	N/A	N/A	N/A
Patrick	26	1.68 (24)	1.31 (25)	3.66 (50)	1.83 (28)	2.22 (30)	2.23 (34)	0.46 (27)	0.42 (25)	0.37 (22)
Ramey	17	2.16 (28)	1.53 (26)	3.70 (47)	2.30 (33)	2.38 (31)	2.32 (34)	0.60 (31)	0.58 (39)	0.51 (28)
AVERAGE		1.66 (31)	1.89 (47)	3.45 (55)	1.82 (34)	2.05 (33)	2.21 (38)	0.38 (26)	0.37 (25)	0.34 (22)

**Table 6.1** – Daytime r.m.s. (m) Errors on L1 (the r.m.s. (%)

errors are italicised and in parentheses)

STATION	$\phi$	LEVEL OF SOLAR ACTIVITY								
		HIGH ( $R = 162$ ) (Jan. – March 1980)			MEDIUM ( $R = 95$ ) (Oct. – Dec. 1982)			LOW ( $R = 14$ ) (May – July 1986)		
		BENT	IRI86	ICED	BENT	IRI86	ICED	BENT	IRI86	ICED
Anchorage	53	N/A	N/A	N/A	0.86 (56)	0.81 (49)	0.93 (59)	0.16 (31)	0.20 (34)	0.20 (26)
Goose Bay	47	0.56 (82)	1.16 (150)	0.89 (97)	0.70 (49)	0.70 (45)	0.83 (45)	0.17 (40)	0.17 (41)	0.16 (34)
Sagamore	39	0.59 (30)	0.71 (52)	0.86 (46)	0.75 (43)	0.72 (43)	0.82 (46)	0.16 (31)	0.17 (32)	0.17 (34)
Athens	35	0.62 (47)	1.01 (83)	1.00 (60)	0.80 (37)	0.75 (35)	0.95 (41)	N/A	N/A	N/A
Patrick	26	1.02 (34)	0.61 (23)	0.94 (40)	0.83 (42)	0.69 (33)	0.67 (35)	0.24 (32)	0.21 (28)	0.28 (37)
Ramey	17	1.28 (41)	0.77 (26)	1.23 (41)	0.94 (45)	0.70 (31)	0.70 (31)	0.28 (28)	0.28 (44)	0.32 (33)
AVERAGE		0.81 (47)	0.85 (67)	0.99 (57)	0.82 (45)	0.73 (39)	0.82 (43)	0.21 (32)	0.21 (36)	0.23 (33)

**Table 6.2** – Night-time r.m.s. (m) Errors on L1 (the r.m.s. (%) errors are italicised and in parentheses)

From **Tables 6.1** and **6.2** and **Figures 6.1** to **6.3** it is clear that the model performances improve as the level of solar activity decreases. It is also clear that the night-time r.m.s. (m) errors are roughly half the magnitude of the comparable daytime errors, whereas the night-time r.m.s. (%) errors are approximately 50% larger than their daytime counterparts. **Table 6.3** summarises which model appears to perform best under each of the 3 levels of solar activity. Each models' associated average r.m.s. (%) error is listed as the italicised figure in parentheses.

	HIGH		MEDIUM		LOW	
	Day	Night	Day	Night	Day	Night
<b>BEST MODEL</b>	BENT	BENT	BENT	IRI86	ICED	BENT
<b>r.m.s. (m) error</b>	1.66	0.81	1.82	0.73	0.34	0.21
<b>r.m.s. (%) error</b>	(31)	(47)	(34)	(39)	(22)	(32)

**Table 6.3** – Model Performances for Three Levels of Solar Activity  
(based on comparisons with Faraday rotation data)

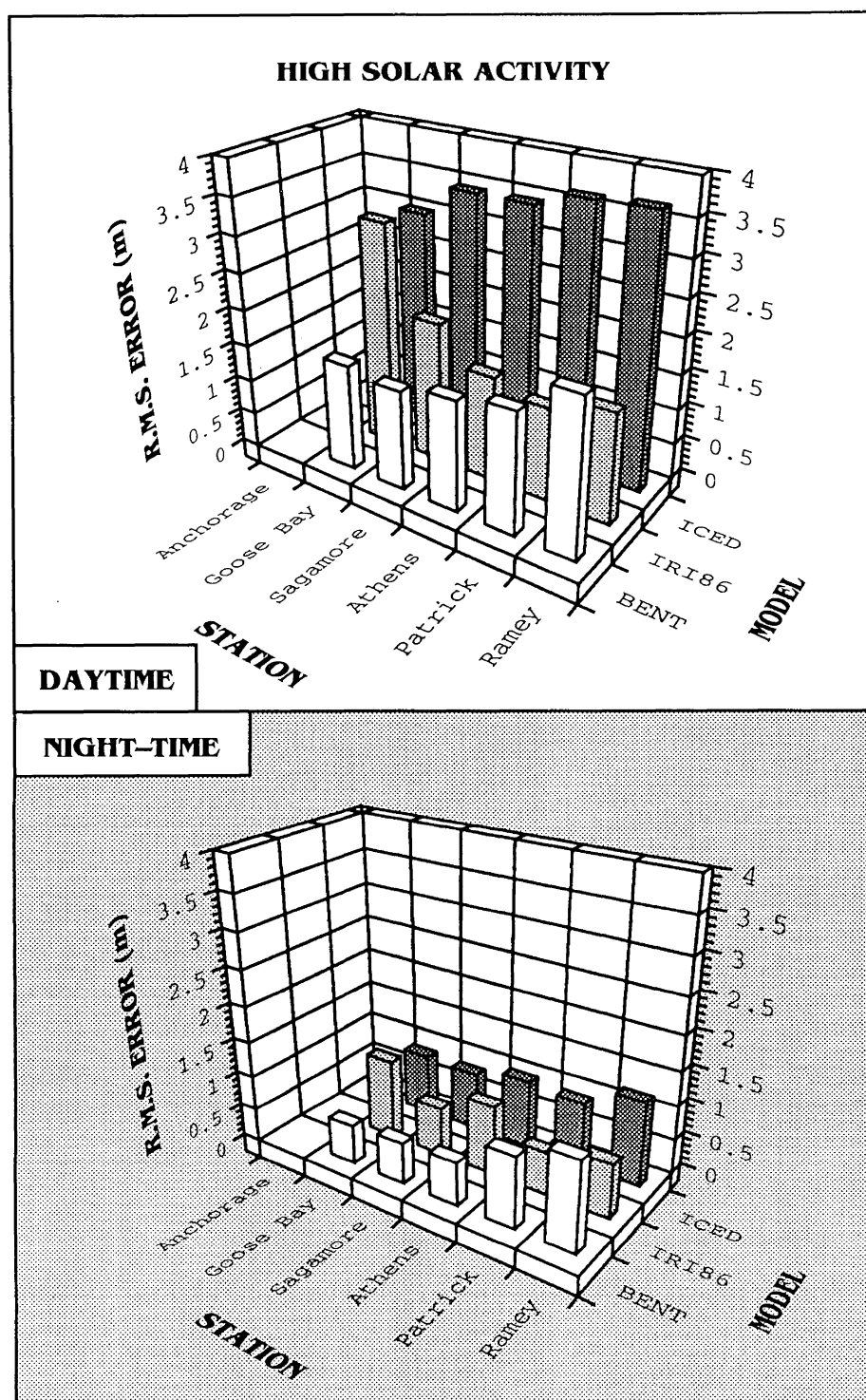


**Figure 6.1** – Daytime and Night-time r.m.s. (m) Errors (for three ionospheric models, at six sites, during high solar activity)



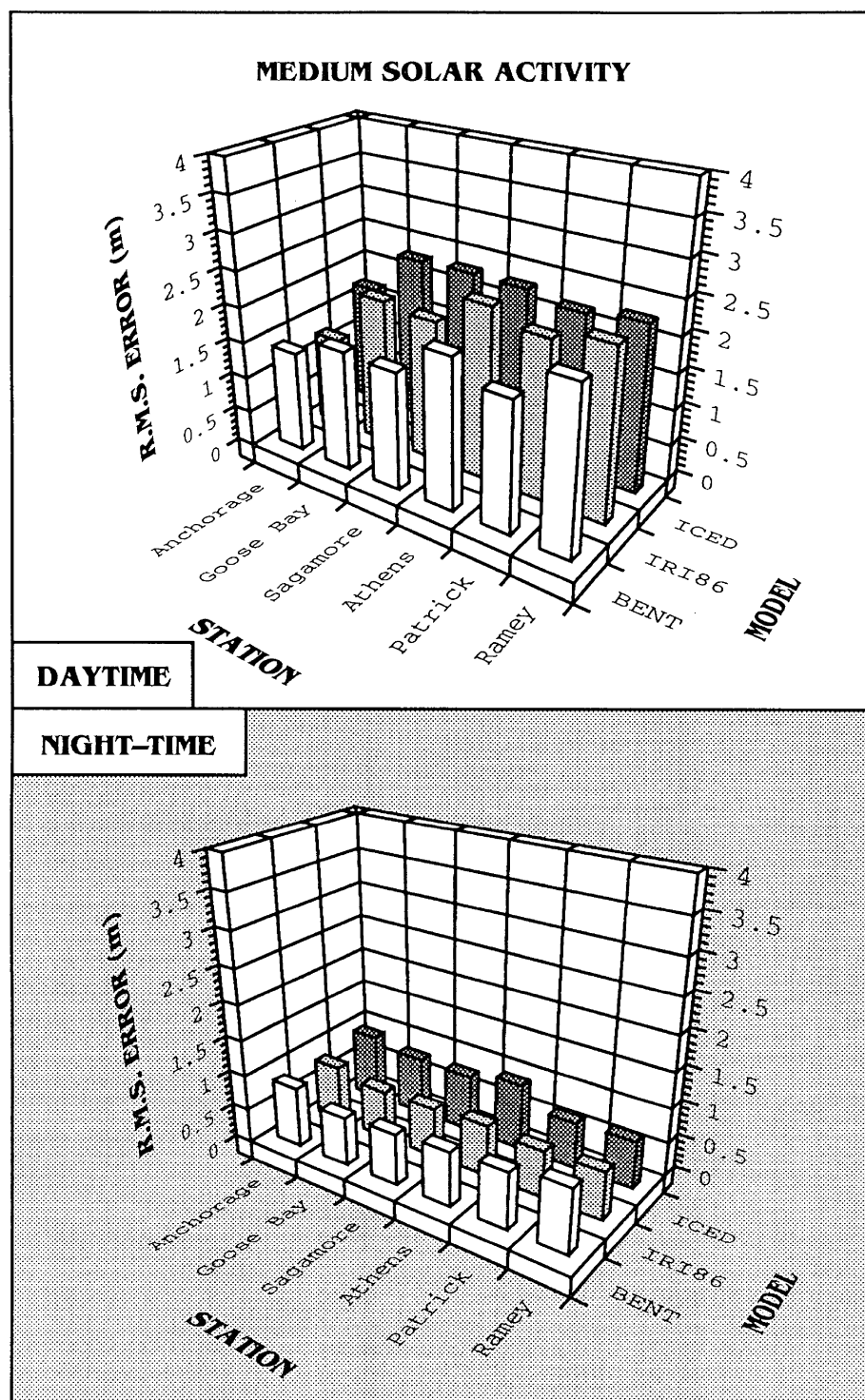


**Figure 6.2** – Daytime and Night-time r.m.s. (m) Errors (for three ionospheric models, at six sites, during medium solar activity)

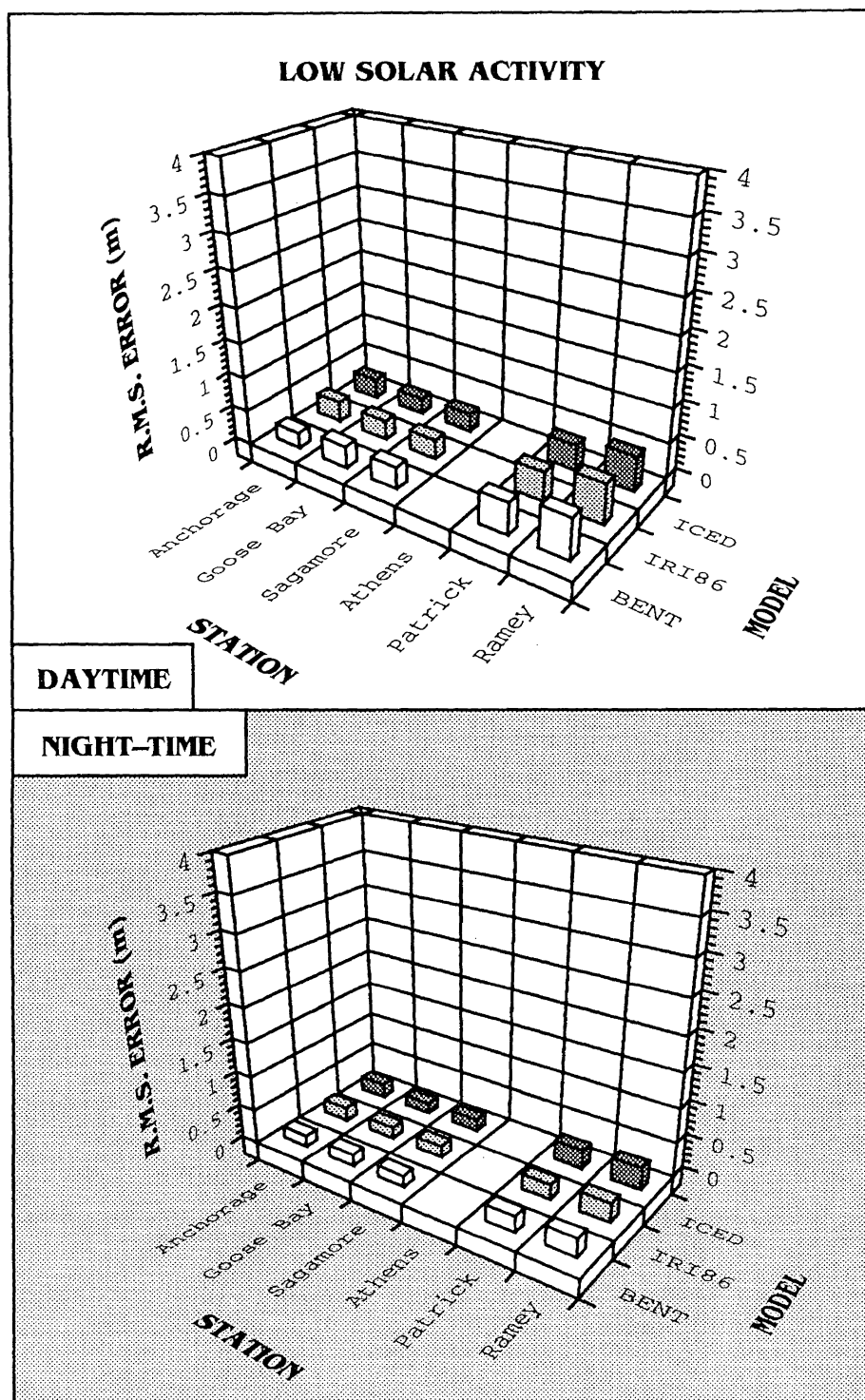


**Figure 6.3** – Daytime and Night-time r.m.s. (m) Errors (for three ionospheric models, at six sites, during low solar activity)

## 6.2 Comparisons with the GPS Results

The GPS data presents a quite different data set upon which to base any analysis. Unlike the Faraday rotation data — which covers entire 24-hour periods and whose ray path through the ionosphere is more or less constant — the GPS' dynamics mean that the epoch-by-epoch ionospheric delays refer to a constantly moving sub-ionospheric point. In essence one is presented with an ionospheric delay at a new location (albeit that this new location is only slightly different from the previous one) every time a new observation is processed. Additionally any one satellite will be in view for, at most, a little more than 6 to 7 hours (see the satellite visibility plots in **Figure 6.4**). Allied to this is the fact that 16 satellites were available at the time of the observations, the satellite sky plots for which can be found in **Appendix III**. Therefore in this analysis of the GPS-based results it is necessary to look at 16 satellites which are visible for relatively short (and different) times of the “ionospheric day” and whose sub-ionospheric points are constantly moving. These factors mean that meaningful analyses of the GPS-based comparisons are nowhere near as “clear-cut” as those of the Faraday rotation data.

Some typical differences between GPS-derived ionospheric delays and modelled ionospheric delays are presented in **Appendices IV** and **V**. Statistics are computed on a daily basis so that for the week there are seven sets of statistics for each of the two sites for each of sixteen satellites (see **Appendix VI**). A “whole week” summary is also computed. The “whole week” daytime and night-time **r.m.s. statistics** for Algonquin and Yellowknife are presented in **Tables 6.4** and **6.5** as these are representative of the daily figures shown in **Appendix VI** (in other words there was little day-to-day variation seen in the results). In both tables the best daytime and night-time results are highlighted with black-filled boxes. Two tables similar to Tables 6.4 and 6.5, only this time containing “whole week” daytime and night-time **mean statistics** for Algonquin and Yellowknife, are presented in **Appendix VII**.

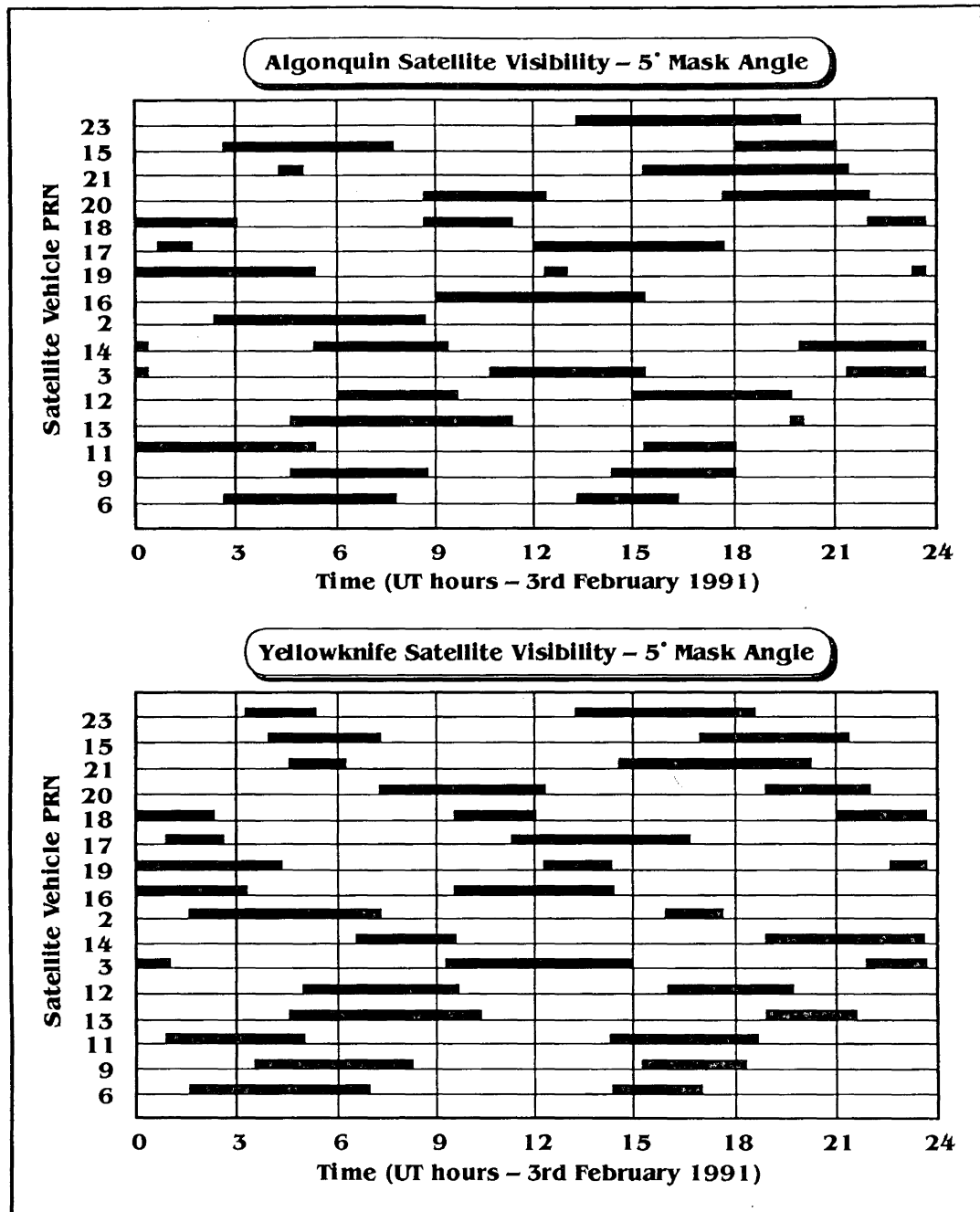


**Figure 6.4 – Satellite Visibility at Algonquin and Yellowknife for 3rd February 1991**

ALGONQUIN – WHOLE WEEK SUMMARY								
PRN	DAYTIME				NIGHT-TIME			
	BENT	IRI86	ICED	B'cast	BENT	IRI86	ICED	B'cast
2	<b>0.37</b> <i>(10)</i>	0.46 <i>(15)</i>	1.82 <i>(54)</i>	0.84 <i>(25)</i>	0.81 <i>(32)</i>	0.73 <i>(34)</i>	1.72 <i>(61)</i>	1.29 <i>(45)</i>
3	1.27 <i>(29)</i>	0.94 <i>(31)</i>	2.82 <i>(42)</i>	0.92 <i>(26)</i>	0.77 <i>(36)</i>	0.72 <i>(34)</i>	1.24 <i>(64)</i>	0.51 <i>(23)</i>
6	2.70 <i>(44)</i>	1.78 <i>(31)</i>	1.85 <i>(30)</i>	1.07 <i>(17)</i>	0.75 <i>(28)</i>	0.62 <i>(28)</i>	1.71 <i>(62)</i>	1.28 <i>(45)</i>
9	N/A	N/A	N/A	N/A	N/A	N/A	N/A	N/A
11	2.15 <i>(32)</i>	1.25 <i>(21)</i>	2.96 <i>(48)</i>	1.55 <i>(25)</i>	1.00 <i>(28)</i>	0.72 <i>(24)</i>	2.10 <i>(64)</i>	1.77 <i>(51)</i>
12	3.01 <i>(32)</i>	0.96 <i>(10)</i>	2.72 <i>(27)</i>	1.49 <i>(14)</i>	<b>0.44</b> <i>(23)</i>	0.46 <i>(25)</i>	1.30 <i>(58)</i>	0.77 <i>(32)</i>
13	0.55 <i>(21)</i>	0.49 <i>(19)</i>	1.23 <i>(47)</i>	0.38 <i>(15)</i>	0.90 <i>(36)</i>	0.87 <i>(35)</i>	1.67 <i>(66)</i>	1.06 <i>(39)</i>
14	2.22 <i>(26)</i>	1.14 <i>(14)</i>	3.41 <i>(38)</i>	1.21 <i>(13)</i>	0.67 <i>(34)</i>	0.63 <i>(35)</i>	1.46 <i>(61)</i>	1.02 <i>(38)</i>
15	4.15 <i>(48)</i>	1.75 <i>(24)</i>	2.40 <i>(32)</i>	1.37 <i>(21)</i>	0.74 <i>(40)</i>	0.63 <i>(42)</i>	1.55 <i>(59)</i>	1.18 <i>(42)</i>
16	2.24 <i>(36)</i>	1.26 <i>(29)</i>	1.33 <i>(27)</i>	0.71 <i>(16)</i>	0.88 <i>(39)</i>	0.92 <i>(41)</i>	1.37 <i>(61)</i>	0.72 <i>(31)</i>
17	2.32 <i>(33)</i>	1.04 <i>(27)</i>	1.60 <i>(27)</i>	0.98 <i>(18)</i>	0.53 <i>(33)</i>	0.64 <i>(40)</i>	0.92 <i>(46)</i>	0.87 <i>(38)</i>
18	1.16 <i>(19)</i>	0.83 <i>(14)</i>	3.31 <i>(53)</i>	1.01 <i>(18)</i>	0.59 <i>(31)</i>	0.59 <i>(34)</i>	1.07 <i>(56)</i>	0.48 <i>(28)</i>
19	0.89 <i>(17)</i>	0.54 <i>(10)</i>	3.01 <i>(56)</i>	1.06 <i>(23)</i>	1.13 <i>(34)</i>	0.88 <i>(27)</i>	2.10 <i>(64)</i>	1.82 <i>(54)</i>
20	2.46 <i>(27)</i>	0.80 <i>(15)</i>	2.95 <i>(32)</i>	1.01 <i>(14)</i>	0.54 <i>(32)</i>	0.54 <i>(31)</i>	1.00 <i>(59)</i>	0.34 <i>(23)</i>
21	3.32 <i>(40)</i>	1.32 <i>(19)</i>	2.19 <i>(23)</i>	0.96 <i>(14)</i>	0.68 <i>(44)</i>	1.01 <i>(66)</i>	0.98 <i>(35)</i>	0.96 <i>(35)</i>
23	3.74 <i>(54)</i>	1.74 <i>(33)</i>	1.45 <i>(18)</i>	1.09 <i>(23)</i>	N/A	N/A	N/A	N/A
AV.	2.17 <i>(31)</i>	1.09 <i>(21)</i>	2.34 <i>(37)</i>	1.04 <i>(19)</i>	0.74 <i>(34)</i>	0.71 <i>(35)</i>	1.44 <i>(58)</i>	1.00 <i>(37)</i>

**Table 6.4** – Daytime and Night-time r.m.s. (m) Errors on L1 to Sixteen Satellites  
at Algonquin (the r.m.s. (%) errors are italicised and in parentheses)

Note that at the time the GPS test data were recorded (3rd to the 9th of February, 1991) PRN#09 was flagged as being unhealthy — thus explaining the “N/A” notation in **Tables 6.4** and **6.5**. PRN#09 was subsequently decommissioned on the 6th of March, 1991. In **Table 6.4** the “N/A” notation for PRN#23 stems from the fact that the satellite was not in view during the night at Algonquin.

YELLOWKNIFE – WHOLE WEEK SUMMARY								
PRN	DAYTIME				NIGHT-TIME			
	BENT	IRI86	ICED	B'cast	BENT	IRI86	ICED	B'cast
2	0.75 (29)	1.18 (48)	2.60 (52)	<b>0.73 (26)</b>	0.85 (40)	0.72 (50)	1.22 (49)	0.93 (40)
3	1.90 (68)	2.65 (89)	1.94 (41)	2.26 (89)	1.38 (70)	1.34 (62)	1.57 (63)	1.16 (71)
6	0.94 (34)	1.62 (61)	2.36 (46)	1.02 (34)	0.99 (42)	0.91 (46)	1.28 (49)	1.06 (36)
9	N/A	N/A	N/A	N/A	N/A	N/A	N/A	N/A
11	1.20 (43)	1.90 (64)	2.12 (44)	1.23 (47)	0.78 (26)	1.05 (47)	1.69 (59)	1.30 (41)
12	1.94 (84)	2.16 (88)	2.21 (49)	1.57 (61)	1.33 (47)	1.26 (45)	1.57 (59)	1.12 (39)
13	2.56 (71)	2.90 (78)	1.92 (37)	2.13 (57)	1.12 (42)	1.04 (39)	1.54 (60)	1.03 (38)
14	2.16 (41)	2.05 (42)	2.90 (34)	1.46 (26)	0.85 (102)	0.97 (121)	1.45 (58)	0.97 (66)
15	3.01 (93)	2.50 (94)	2.00 (49)	1.44 (66)	0.79 (49)	1.03 (80)	1.35 (53)	0.96 (40)
16	1.56 (44)	1.54 (53)	3.68 (56)	1.42 (54)	0.90 (56)	1.00 (67)	1.10 (53)	0.79 (61)
17	0.94 (24)	1.16 (36)	2.00 (46)	1.01 (25)	1.22 (44)	1.19 (44)	1.32 (47)	1.08 (38)
18	1.89 (27)	1.67 (26)	3.63 (47)	1.37 (20)	0.91 (52)	0.93 (67)	1.67 (60)	1.10 (40)
19	1.76 (37)	1.73 (56)	3.25 (48)	1.21 (33)	<b>0.64 (49)</b>	0.89 (74)	1.44 (56)	0.98 (44)
20	1.93 (41)	2.25 (49)	3.61 (41)	2.13 (39)	0.89 (40)	0.91 (40)	1.03 (50)	0.81 (40)
21	2.10 (33)	1.62 (31)	2.22 (35)	1.09 (18)	0.96 (53)	1.21 (77)	1.32 (51)	1.02 (73)
23	1.76 (46)	1.77 (56)	1.68 (27)	1.06 (32)	0.93 (304)	1.07 (364)	1.14 (132)	0.93 (397)
AV.	1.76 (48)	1.91 (58)	2.54 (43)	1.41 (42)	0.97 (68)	1.03 (82)	1.38 (60)	1.02 (71)

**Table 6.5** – Daytime and Night-time r.m.s. (m) Errors on L1 to Sixteen Satellites at Yellowknife (the r.m.s. (%) errors are italicised and in parentheses)

The huge night-time r.m.s. (%) errors shown for PRN#23 in **Table 6.5** (depicted in **Figure 6.8**) were caused by a four hour period of data recorded on Monday 4th of February, 1991, when the night-time ionospheric delays were very small (often smaller than 0.1 m) and when none of the models were able to make sufficiently small predictions — several of the individual percentage errors were in excess of 4,000%. The important point to note from this example is the way in which a few poor results can disturb the “statistical picture” for a whole week.

### 6.2.1 Conclusions Resulting from the GPS Dual-Frequency Comparisons

**Tables 6.4** and **6.5** are graphically depicted in **Figures 6.5** to **6.8**. **Figure 6.5** shows the day and night r.m.s. (m) errors for each of the models at Algonquin. **Figure 6.6** shows the day and night r.m.s. (%) errors for each of the models at Algonquin. **Figure 6.7** and **6.8** are the Yellowknife counterparts of **Figures 6.5** and **6.6**. The same figures reveal that the model performances for Yellowknife are worse than those for Algonquin (this is especially true of the daytime results but is less evident in the night-time results). The performance of the models with respect to each other is also revealed quite clearly (especially in the daytime plots) and it can be seen that the Broadcast and IRI86 models appear to perform better than the Bent and ICED models at both sites for almost all of the 15 satellites. There is therefore some evidence to suggest that the relatively good performances of the Broadcast and IRI86 models are statistically significant. Treating the Algonquin and Yellowknife results as two separate cases reveals the following:

- (i) In **Figure 6.5** the Algonquin r.m.s. (m) errors reveal that the Broadcast model is consistently able to maintain daytime r.m.s. (m) errors to a level of about 1 metre. IRI86 also performs well but there are several cases where the r.m.s. (m) errors are as large as 2 metres. The night-time results do not show any significant improvement over the daytime results except that this time it appears to be the Bent and IRI86 models which consistently maintain r.m.s. (m) errors of the order of 1 metre. ICED is the worst performer both by day and by night.
- (ii) Referring to **Figure 6.7** the Yellowknife r.m.s. (m) errors are noticeably larger than those for Algonquin for every model — this is especially evident in the daytime values. Once again the Broadcast model's daytime performance is consistently superior to that of the other models. There are however two or three cases where its r.m.s. (m) errors are as large as 2 metres or so. The night-time results are more or less the same for the Broadcast, IRI86, and Bent models (they are approximately 1 metre r.m.s.), but ICED is once again very clearly the worst performer both by day and by night.

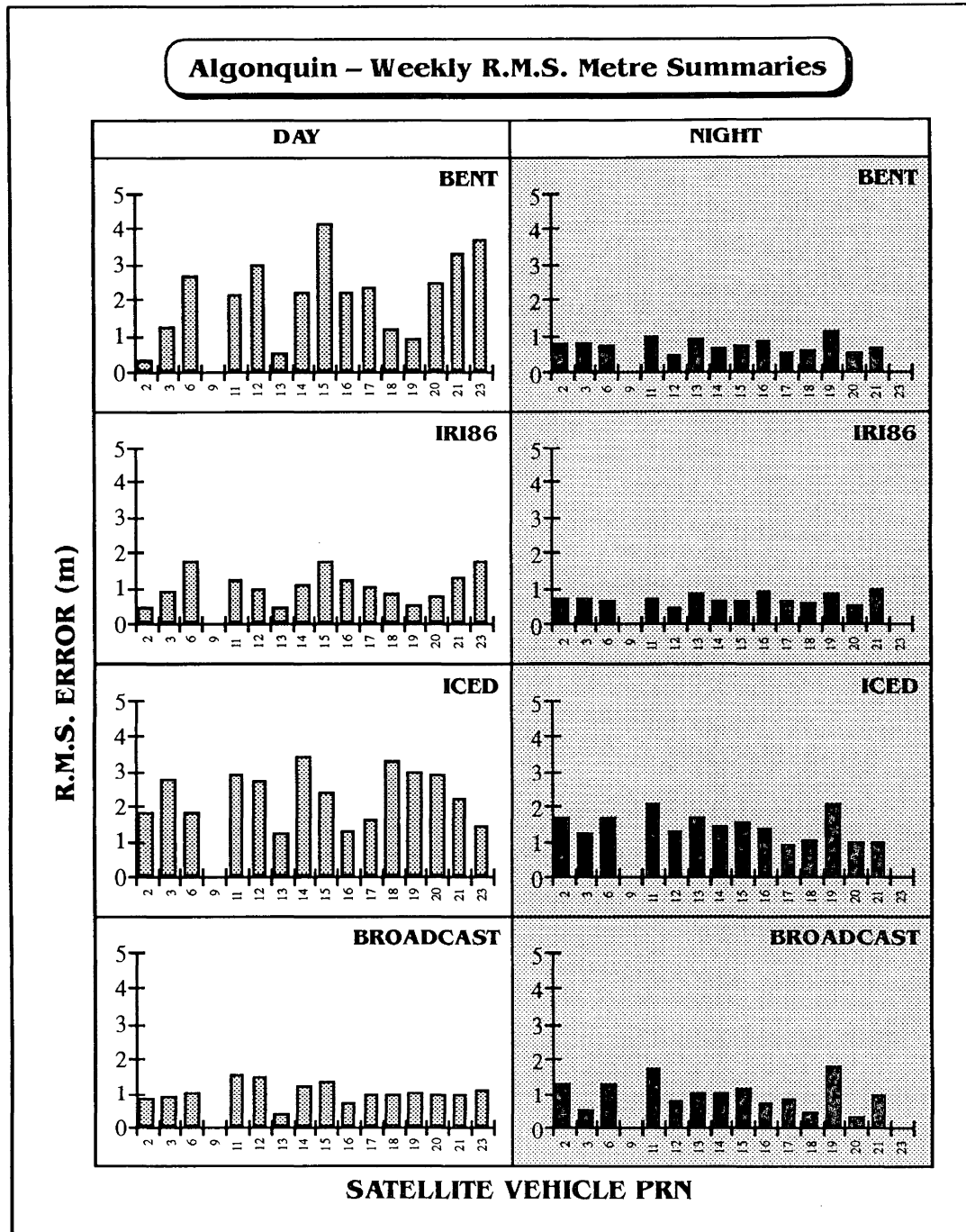


**Figure 6.5 – Whole Week Daytime and Night-time r.m.s. Errors (m) on L1**  
(to sixteen satellites for four ionospheric models at Algonquin)



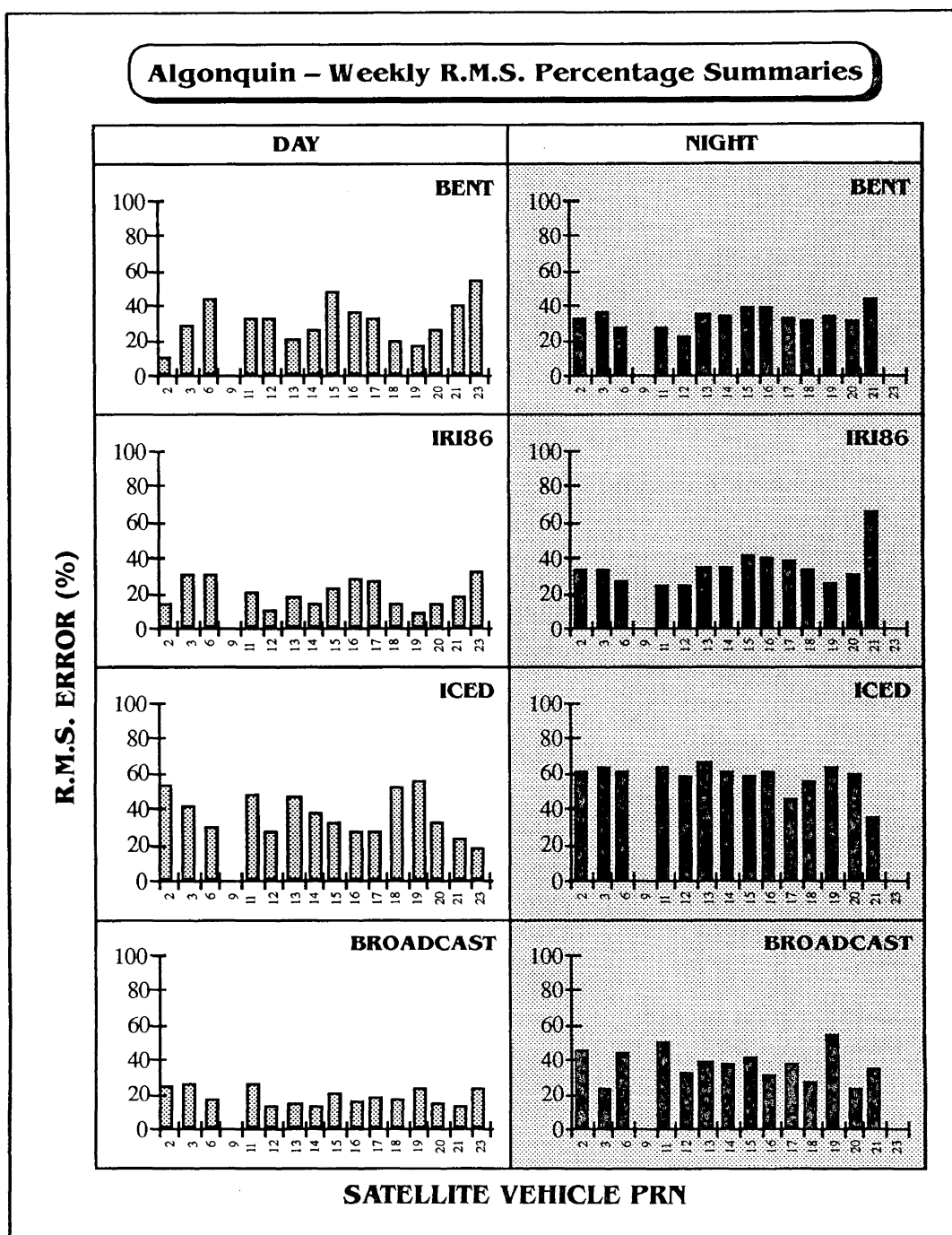


**Figure 6.6 – Whole Week Daytime and Night-time r.m.s. Errors (%) on L1**  
 (to sixteen satellites for four ionospheric models at Algonquin)

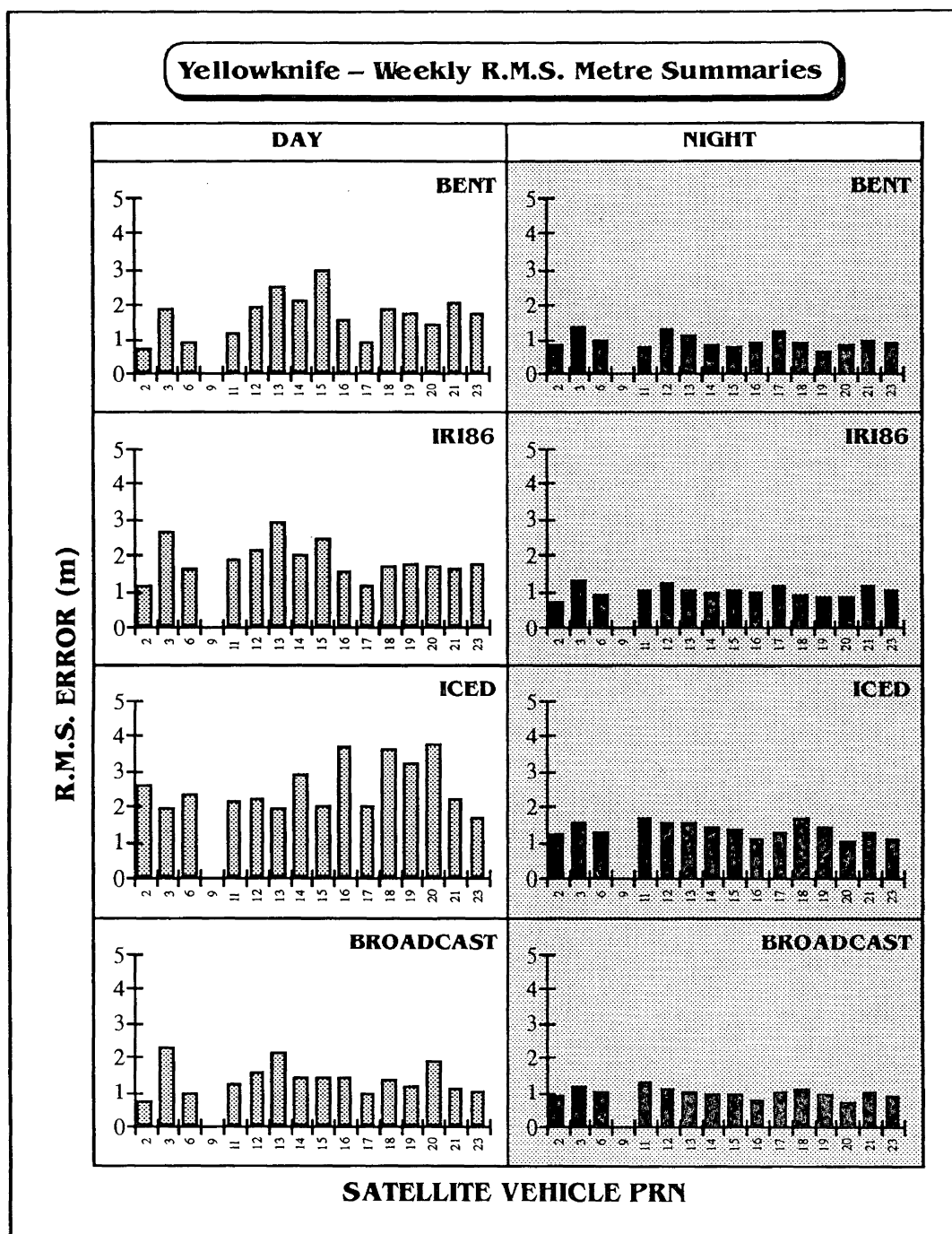


**Figure 6.7 – Whole Week Daytime and Night-time r.m.s. Errors (m) on L1**  
 (to sixteen satellites for four ionospheric models at Yellowknife)

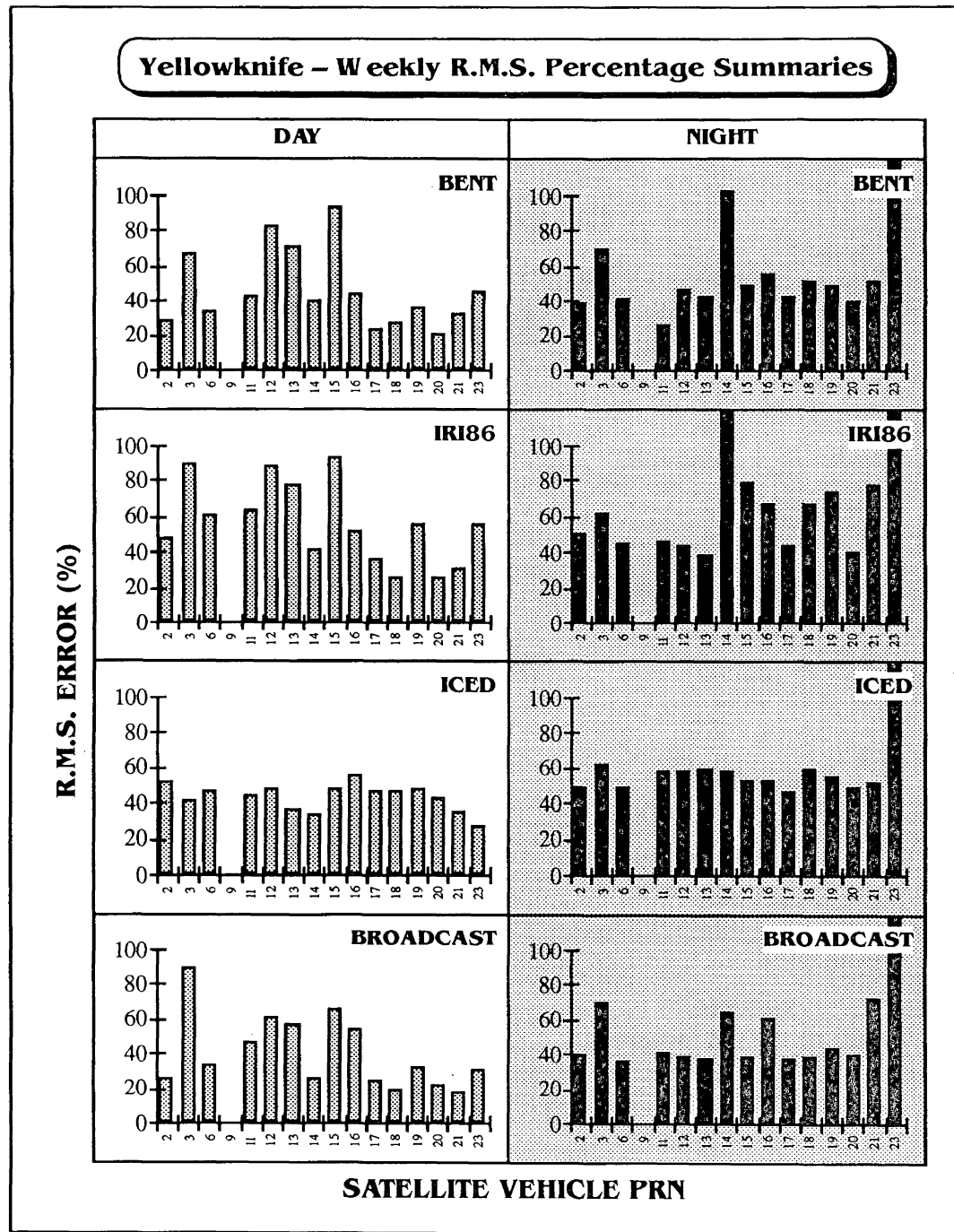


**Figure 6.8** – Whole Week Daytime and Night-time r.m.s. Errors (%) on L1  
(to sixteen satellites for four ionospheric models at Yellowknife)

Three obvious points result from the observations made in (i) and (ii):

- The models generally perform less well at Yellowknife;
- ICED's performance is consistently the worst; and
- Overall, the performance of the Broadcast model appears to be the best — this is evident by day and night at both Algonquin and Yellowknife.

The degraded model performances at Yellowknife are to be expected bearing in mind the relatively high latitude of the site. In terms of satellite geometry the day-to-day variation of the GPS satellite positions (and therefore of the sub-ionospheric point) remain more or less constant. For satellites observed at an elevation of 5° the great circle distance from the receiver to the point beneath where the 5° elevation raypath intersects the ionosphere (at a height of 350 km) will be approximately 1,600 km. Thus satellites at 5° elevation cover a circular area, the diameter of which is approximately 3,200 km. This arrangement is depicted in **Figure 6.9** where the Yellowknife and Algonquin 5° circular coverage areas have been superimposed over an enlarged extract of Figure 3.8. Also shown on the figure are the maximum sub-satellite latitudes of Block I and Block II satellites (approximately 63° N and 55° N respectively). Note that a day/night line along a meridian (as illustrated) would only exist on March or September 21st.

It should be noted that the ionospheric regions depicted in this figure are only rough indications of the true extents of these area — the auroral region is in reality quite mobile and could quite easily extend further southwards and/or further northwards. In any event it is obvious that some signals received at Yellowknife may have passed through the auroral oval (this is especially true of signals from Block I satellites) which is often highly disturbed and presents difficulties for empirical models to adequately predict TEC. Even at the lower-latitude Algonquin station there may possibly be times when signals from low elevation Block I satellites will pass through the auroral oval.

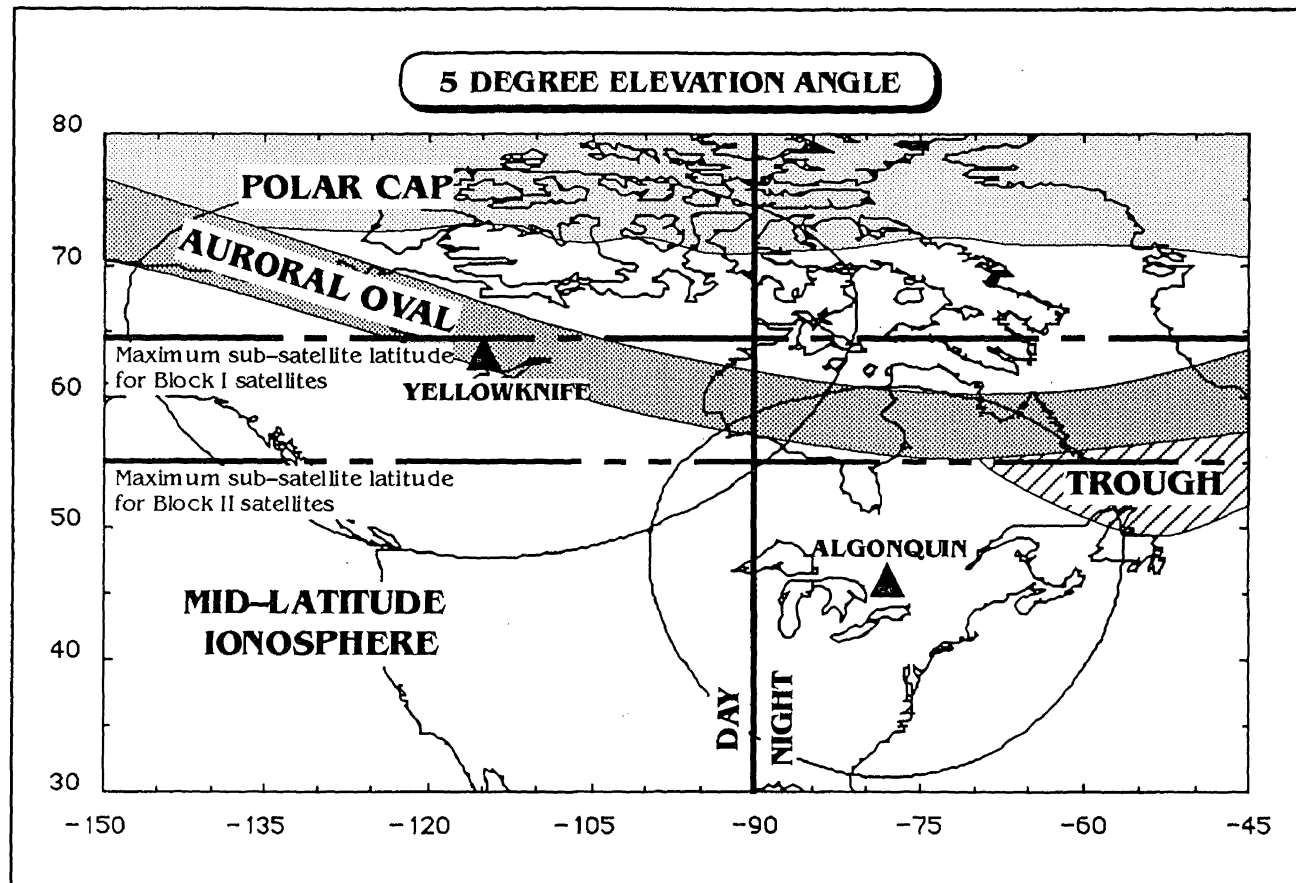


**Figure 6.9** – The 5° Elevation Coverage Areas for Yellowknife and Algonquin  
(superimposed over the major features of the area's ionosphere)

Referring to **Figure 6.5** it can be seen that at Algonquin, PRN#13's daytime ionospheric delays for the week are relatively well modelled by each model, whereas PRN#15's daytime ionospheric delays are relatively poorly modelled. Plots similar to those of Figures 6.5 to 6.8 were also produced from the daily sets of statistics found in Appendix VI. They are not included here for reasons of economy of space. However, plots representative of each of the seven days appear well correlated with each other and with the weekly sets presented here. In other words the good modelling of PRN#13 is seen on a daily basis as is the poor modelling of PRN#15. There is strong evidence for systematic effects which can only be attributed to either the models, the ray paths of the signals through the ionosphere, or (as is most likely) both.

Multiple plots of sub-ionospheric point, vertical ionospheric delay on L1, and the modelled error for each model have been formed for each satellite as viewed from Algonquin and Yellowknife. A representative set (for Sunday 3rd February, 1991) of these plots for Algonquin and Yellowknife can be found in **Appendix IV** and **Appendix V** respectively. **Figures 6.10** and **6.11** show such plots for PRN#02 and PRN#06 as observed from Yellowknife. It can be seen that both satellites were visible almost simultaneously, both satellites made the transition from daytime to night-time ionosphere almost simultaneously, the sky plots for the satellites are similar (see **Appendix III**), and the ionospheric delay on L1 and the errors in the modelled delays were similar for both satellites. This provides strong support for the previous statement that systematic effects are clearly in evidence.

One glaring fact which emerges from the figures in **Appendices IV** and **V** is that there is often a high level of correlation between the **shape** of the curve of ionospheric delays on L1 and the shape of the error curves for the models. This characteristic certainly stems from the fact that the ionospheric models present an idealised "picture" of the behaviour

of the ionosphere. The models can only hope to faithfully represent the low frequency ionospheric changes and the high-frequency changes cannot be modelled. Therefore by differencing the modelled and observed delays the dominant force behind the shape of the resulting curve can be attributed to the shape of the plot of observed delays.

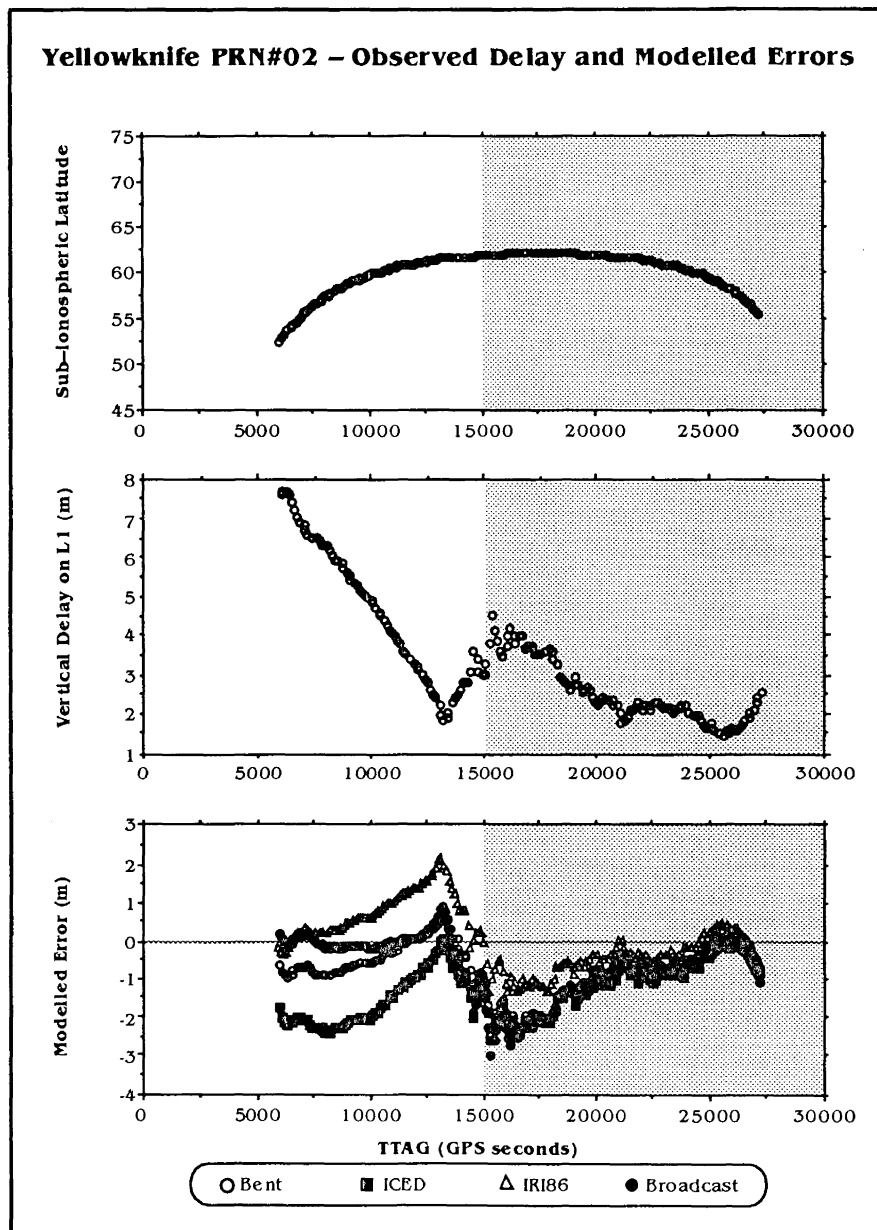


**Figure 6.10** – Sub-ionospheric Point, Vertical Ionospheric Delay on L1, and Model Errors for PRN#02 at Yellowknife

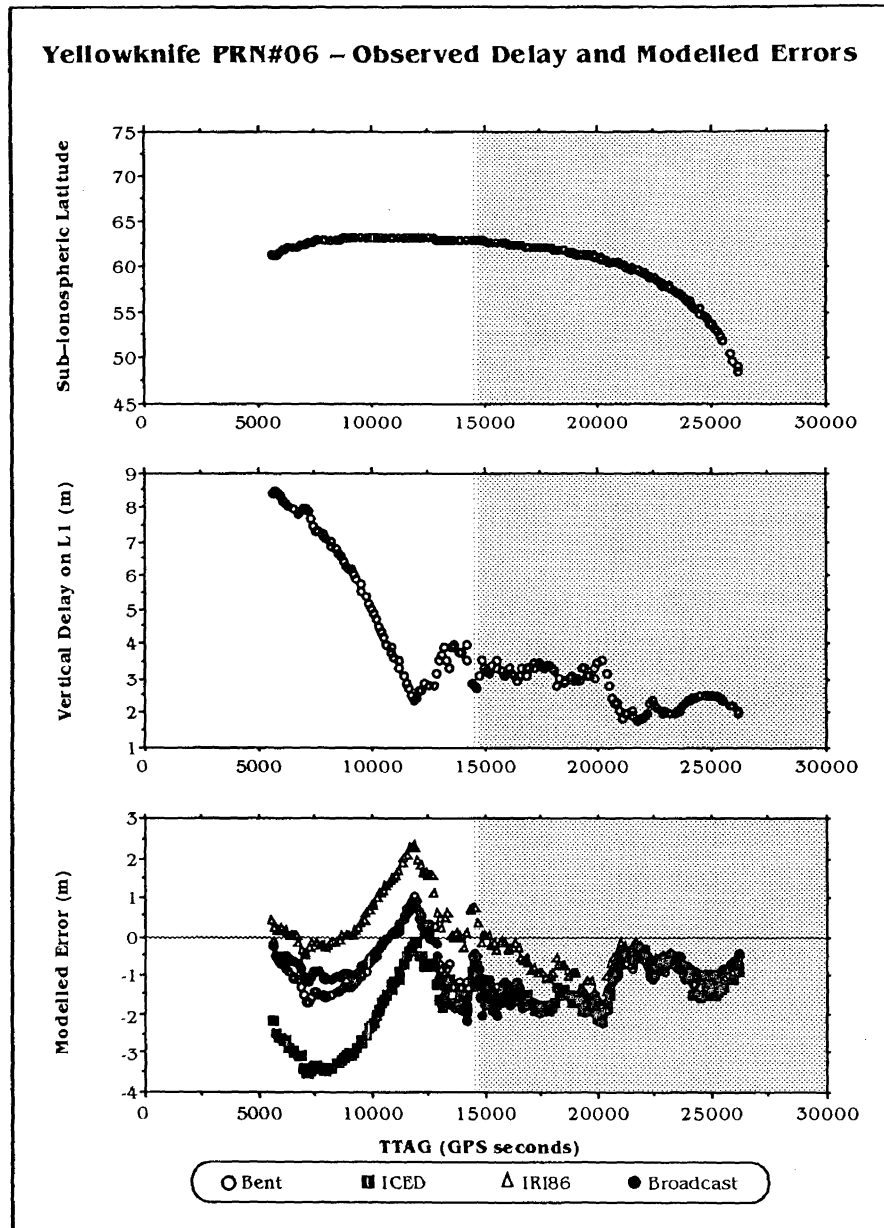


**Figure 6.11** – Sub-ionospheric Point, Vertical Ionospheric Delay on L1, and Model Errors for PRN#06 at Yellowknife



### 6.3 Recommended Strategies for Use of the Ionospheric Models

As a direct result of the tests and results outlined in this thesis there are several points which arise with respect to successful use of the ionospheric models. It has been established that the high-latitude abilities of the models generally leads to degraded accuracies. It has also been shown that levels of high solar activity generally result in similar degradation of model performance. The following paragraphs will outline some suggested limits which should be imposed on use of the models.

#### 6.3.1 Recommended Latitude Limits for Use of Ionospheric Models

The models tested in this research vary in the ways in which they make allowance for the fact that high-latitude regions of the ionosphere cannot (in general) be satisfactorily modelled: the Broadcast model sets any **geographic** latitude which is greater than 75° equal to 75°; IRI86 warns the user if **geomagnetic** latitudes greater than 60° are used; and the Bent and ICED models do not impose latitudinal limits on their computations. Despite the fact that the Bent model and ICED apparently allow predictions of the high-latitude ionosphere, it is also an indisputable fact that this region is highly unpredictable and cannot be modelled too successfully. Therefore it would appear to be expedient for users of any ionospheric model to limit the latitudinal extent of their predictions.

It is difficult to issue a firm recommendation regarding a suitable cut-off latitude at which to cease modelling the ionosphere due to the very mobile nature of the auroral zone. Several authors (e.g., *Rishbeth & Garriott* (1969); *Ratcliffe* (1970); *Kelley* (1989)) indicate that the extent of the auroral zones is approximately removed from the geomagnetic poles by about 20 degrees. Clearly the consensus of opinion places the limits of the auroral zones (northern and southern hemisphere) at approximately 70° geomagnetic latitude. **Figure 6.12** illustrates the  $\pm 70^\circ$  geomagnetic latitude,  $\phi_m$ , contours converted into equivalent geographic latitude,  $\phi_g$ . It might also be wise to avoid the equatorial region (approximately  $\pm 20^\circ$  either side of the earth's geomagnetic equator) at least between the hours of 1900 to 2400 local time whenever possible to minimise the effects of equatorial scintillation (*Klobuchar*, 1991).

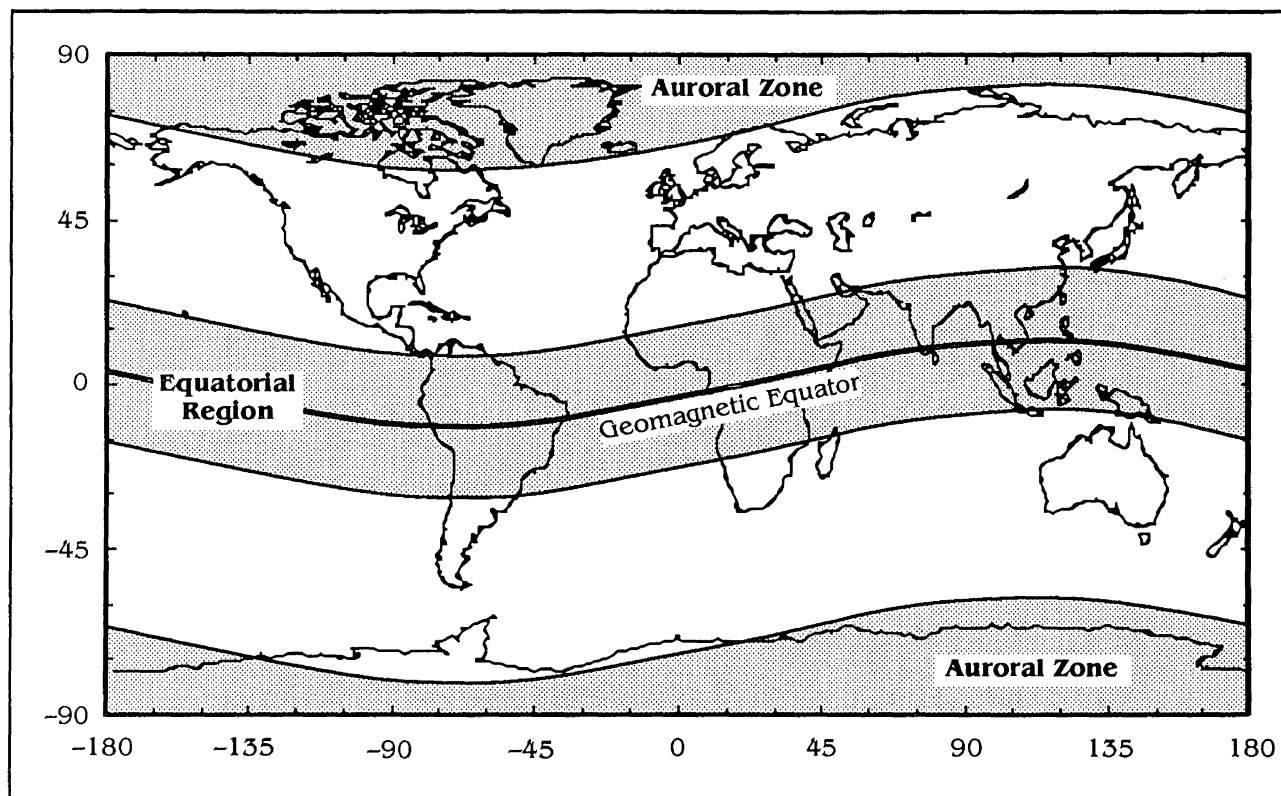


**Figure 6.12** – Approximate Geographical Locations of the Auroral Zones  
and the Equatorial Region

### 6.3.2 Recommended Solar Activity Limits for Use of Ionospheric Models

**Table 6.6** lists the 12-month running averages of solar sunspot number and solar flux for the periods of the high, medium, and low activity Faraday comparisons and for the period from which the GPS data were taken.

	DATE									
	1980			1982			1986			1991
	Jan.	Feb.	Mar.	Oct.	Nov.	Dec.	May	June	July	Feb.
<b><i>R</i></b>	163.9	162.6	160.9	95.7	94.7	94.6	14.3	13.8	13.7	141.0
<b><i>F</i></b>	200.1	200.6	199.6	155.2	153.1	151.4	74.2	74.2	74.1	184.1
<b>&gt; 130</b>	✓	✓	✓	✓	✓	✓	X	X	X	✓
<b>Note:</b> <i>R</i> is the 12-month running average of solar sunspot number and <i>F</i> is the 12-month running average of solar flux. The > 130 category shows whether or not any daily values of solar flux for the period in question were greater than 130.										

**Table 6.6** – Solar Indices for the Models' Test Periods

In much the same way as some of the models limit the geographical extent of their predictions there are also limitations with respect to the level of solar activity which can be accommodated. The Bent model does not allow daily solar flux values to exceed 130, a value which was exceeded in all but the May to July 1986 data. If a value greater than 130 is encountered the programme sets the daily solar flux value to 130. IRI86 uses *R* as its input solar data and limits *R* to a maximum value of 150. From January to March 1980 the values of *R* did exceed 150. Likewise, if a value greater than 150 is encountered IRI86 sets *R* equal to 150. ICED places no limitations on the magnitude of the solar indices that it uses.

## 6.4 Summary of Results

This chapter has produced a "mixed bag" of results. Some of the findings were easily predictable well in advance of any testing — e.g., the relatively poor performance of an

ionospheric model at high latitudes and/or under conditions of high solar activity. What wasn't known was to what extent the models would be affected by such conditions, or which model would produce the best results.

As a very general remark it can now be stated that based upon comparisons with the dual-frequency GPS data set, the Broadcast model's ability to predict ionospheric delay was on average superior to the other models tested here — its r.m.s. daytime errors were frequently 20% or less at Algonquin. The Broadcast model was followed by IRI86, then the Bent model, and finally the worst performer which was ICED.

Similarly, in comparisons with the Faraday rotation data, and in terms of consistency at all levels of solar activity, for all locations, by day and night, the Bent model appears to have been best. It was consistently able to model the ionosphere with r.m.s. errors of the order of 25 to 35% by day, and 30 to 50% by night. ICED only performed best during low solar activity, and even then its margin of superiority was slim.

The biggest surprise by far was the performance of the Broadcast model. Every indication was that this model would turn in the worst results of any as several authors have noted previously that it only accounts for approximately 50% r.m.s. of the ionosphere's effect. The results presented here show that during a period of high solar activity, the Broadcast model was able to predict daytime ionospheric delays for Algonquin with r.m.s. errors of only 20%. By night this figure becomes less consistent and can be between 20 and 40% r.m.s.

## *Chapter 7*

# ***Conclusions & Recommendations***

---

The previous chapters have introduced the Global Positioning System, the ionosphere, empirical modelling of the ionosphere, testing of four ionospheric models, and finally, some results and a discussion of the results obtained from the model testing. It was noted in Chapter 1 that this research by no means constitutes a definitive work on empirical modelling of the ionosphere as the disciplines of ionospheric physics and ionospheric modelling are indeed vast, and extraordinarily complex. It is clear that the ionosphere represents a dynamic medium whose behaviour can be erratic and consequently difficult to model successfully. That said, the research reported in this thesis has shown that there are often times when an empirical model of the ionosphere is quite capable of modelling the low frequency variations of this dynamic medium. It is the high-frequency element of the ionosphere's behaviour which poses the most difficult challenge for an empirical model.

This chapter forms the conclusion of this thesis; it starts with a discussion of the main issues which arose as a direct result of the study and ends with some recommended strategies for further work.

### **7.1 Model Performances**

Rather than recapitulating the results given in Chapter 6, a brief note is made of those results upon which the most important conclusions hinge. Comparisons of modelled

---

delays with the Faraday rotation data for the Bent, IRI86, and ICED models showed that the performance of the Bent model was generally superior to that of the others. The performance of IRI86 was generally not much worse than that of Bent. The ICED model was however a poor performer and only marginally better than the other two test models during low solar activity daytime testing.

In model comparisons with the GPS data, the Broadcast model was also tested (in addition to the three models mentioned above) and was found (on average) to produce the best results; of the remaining three test models, the IRI86 was the best, and once again the ICED model was by far the worst performer.

In a statistical sense the findings outlined above can be summarised by stating that there was little difference between the results of the high and medium activity Faraday rotation data testing. In both instances the best model's r.m.s. error was approximately 1.7 m by day and 0.8 m by night. Model testing against the low activity Faraday rotation data resulted in modelled r.m.s. errors of the order of 0.3 m by day and 0.2 m by night.

Similarly, the model testing against the Algonquin GPS data revealed that the best daytime model's r.m.s. error was approximately 1.0 m by day and 0.7 m by night. At Yellowknife the best model's r.m.s. error was approximately 1.4 m by day and 1.0 m by night.

In addition to the findings reported above, several general traits were apparent:

- Irrespective of the test model in question it was noted that model performances improved as the level of solar activity decreased;

- At night the model performances (in metres, but not %) were superior to their daytime counterparts; they also showed the same trend towards improved results at lower levels of solar activity; and
- The performances of the test models were generally degraded at higher latitudes.

The above findings were not unexpected — as was stated in section 6.4 — but what was not known was to what extent the models would be affected by such conditions, or which model would produce the best results.

## **7.2 A Synopsis of This Research & Suggestions for Future Research**

It was clear from almost every test performed that the ICED model was inferior to the others in predicting VTEC. In fact ICED only showed any improvement over the other test models during comparisons with the low activity Faraday rotation data. Even then, the margin of superiority was so slim as to be almost negligible. ICED was also the most tricky model to adapt to predictions of VTEC and it had significantly slower execution times than the other two test models. The conclusion to make therefore is that the version of ICED used in this research is not recommended for future studies of this type.

The relatively good performance of the Broadcast model was something of a surprise bearing in mind that other authors (e.g., *Klobuchar, 1986; Feess & Stephens, 1986*) found in their testing that the Broadcast model removed approximately 50 to 60% r.m.s. of the ionosphere's effect on GPS signals. One must question therefore whether or not the remarkably good performance of this model can be regarded as somewhat fortuitous — it is possible that during the week in question the satellites were broadcasting unusually “good” coefficients. It is suggested therefore that it might be a worthwhile strategy to archive the broadcast coefficients for this model so that future tests under

many differing conditions of solar activity, and for many different test sites, can be undertaken.

In a recent private communication, David Coco (Applied Research Laboratories, University of Texas at Austin, April 1992) suggested that due to the finite number of broadcast model coefficients from which to choose, and the simple rules used for selecting which coefficients to broadcast, it is probably not necessary to record and archive the coefficients in the manner suggested above. However, early on in the model testing, Jack Klobuchar was approached for estimates of what the broadcast coefficients would have been for GPS week # 578. Later on the coefficients which were actually broadcast were obtained. There was disagreement between what should have been broadcast according to the coefficient selection rules and those which were broadcast. The point to make here is that it is definitely preferable to record those coefficients which are actually broadcast by the GPS satellites. For the record it should also be pointed out that in this research all testing of the Broadcast model was carried out using the coefficients which were actually broadcast.

Based upon the results of this research it appears prudent to conclude that any future studies of the type described should (quite apart from those comments already made about the Broadcast model) concentrate upon the Bent and IRI90 (*Bilitza*, 1990) models.

The research described in this thesis limits its comments to the abilities of four ionospheric models for countering the effect of the transionospheric propagation delay experienced by radio signals. The comments are made solely in terms of the effect on the satellite-receiver vector — no GPS positioning results have entered into the analysis. In future it would probably be useful to study the ionospheric models with respect to the positioning aspect of GPS when using single-frequency observations.



Finally, *Georgiadou & Kleusberg* (1988) used estimates of vertical ionospheric biases derived from a dual-frequency GPS receiver to drive a simple ionospheric model. The model was then used to provide ionospheric corrections for the carrier phase measurements from a local (to the dual-frequency receiver) network of single-frequency GPS receivers. *Webster & Kleusberg* (1992) have expanded upon this work and used it to correct an airborne single-frequency GPS receiver's observations by using ionospheric corrections derived from three locally situated ground-based dual-frequency GPS receivers. It may be possible to supplement and improve upon these techniques by adopting the use of one of the ionospheric models tested in this research.

#### **7.2.1 The International Reference Ionosphere 1990**

IRI86 was the outcome of a joint working group of the COSPAR and URSI organisations and consists of 20 or so ionospheric scientists from around the globe. The IRI's development is an ongoing process and recently the latest version of IRI was released (*Bilitza*, 1991). The International Reference Ionosphere 1990 (IRI90) source code and documentation (*Bilitza*, 1990) are available from NSSDC, NASA/GSFC, Code 933, Greenbelt, MD 20771. The software is available on tape, IBM PC diskette, or it can be downloaded directly from NSSDC's Online Data and Information Service (NODIS).

IRI90 features several improvements over IRI86: it utilises an improved set of coefficients for the determination of  $f_oF2$  using the URSI-1989  $f_oF2$  model coefficients but gives the user a choice of either the URSI-1989 or the CCIR-1967 coefficients. There are also several improvements to the E and F region electron density profiles and other technical corrections and enhancements. Of course, independent validation of these improvements would form a useful extension to the work reported in this thesis.

### **7.3 Concluding Remarks**

Chapter 1 stated that the primary goals of this research were to acquire, adapt, implement, and test four models of the ionosphere with the aim of determining which model might be best suited to single-frequency GPS users, and to what extent the models would be able to remove the effect of the ionosphere from such measurements. The stated research goals have been met — subject to those caveats outlined above — and the findings have allowed recommendations regarding further related studies to be made.

## **REFERENCES**

- Bent, R. B., and S. K. Llewellyn (1973). *Documentation and Description of the Bent Ionospheric Model*. Space & Missiles Organization, Los Angeles, California. AFCRL-TR-73-0657.
- Bilitza, D. (1986a). "Newest ionospheric model available." *National Space Science Data Center (NSSDC) News*, Volume 2, Number 3.
- Bilitza, D. (1986b). "International Reference Ionosphere: Recent developments." *Radio Science*, Volume 21, Number 3, pp. 343-346.
- Bilitza, D. (ed.) (1990). *International Reference Ionosphere 1990*. National Space Science Center/World Data Center A for Rockets and Satellites, Lanham, Maryland 20706. Report Number NSSDC/WDC-A-R&S 90-22.
- Bilitza, D. (1991). "International Reference Ionosphere update." *EOS Transactions of the American Geophysical Union*, Volume 72, Number 30, p. 317.
- Bilitza, D., K. Rawer, and S. Pallaschke (1988). "Study of ionospheric models for satellite orbit determination." *Radio Science*, Volume 23, Number 3, pp. 223-232.
- Bishop, G. J., J. A. Klobuchar, A. E. Ronn, and M. G. Bedard (1989). "A modern trans-ionospheric propagation sensing system." Operational Decision Aids for Exploiting or Mitigating Electromagnetic Propagation Effects, NATO AGARD Electromagnetic Wave Propagation Panel Symposium, San Diego, Paper 31, AGARD Conference Proceedings Number 453.
- Breit, Q., and M. A. Tuve (1926). "A test of the existence of the conducting layer." *Physical Review*, Volume 28, Number 3, pp. 554-573.
- Brown, L. D., R. E. Daniell, M. W. Fox, J. A. Klobuchar, and P. H. Doherty (1991). "Evaluation of six ionospheric models as predictors of total electron content." *Radio Science*, Volume 26, Number 4, pp. 1007-1015.

- Brunner, F. K., and M. Gu (1991). "An improved model for the dual frequency ionospheric correction of GPS observations." *Manuscripta Geodaetica*, Volume 16, pp. 205–214.
- Budden, K. G. (1985). *The Propagation of Radio Waves*. Cambridge University Press, Cambridge.
- Burnside, C. D. (1982). *Electromagnetic Distance Measurement*. Second edition, Collins, London.
- Cahill, L. J. (1964). "The geomagnetic field." In *Space Physics*, ed. D. P. LeGalley and A. Rosen, John Wiley & Sons, Inc., New York.
- CCIR (1967). *CCIR Atlas of Ionospheric Characteristics*. Union Internationale des Télécommunications, CCIR Report 340–2, Geneva.
- Clynch, J. R., D. S. Coco, and C. Coker (1989). "A versatile GPS ionospheric monitor: High latitude measurements of TEC and scintillation." *Proceedings of ION GPS-89*, Colorado Springs, Colorado, pp. 445–450.
- Clynch, J. R., D. S. Coco, and B. A. Renfro (1983). "Differential Doppler measurements of the ionosphere during a solar eclipse." *Journal of Atmospheric Physics*, Volume 45, Number 7, pp. 527–535.
- Coco, D. S., S. R. Dahlke, and C. Coker (1988). *Effect of GPS System Biases on Differential Group Delay Measurements*. Air Force Geophysics Laboratory, Report Number ARL-TR-88-32, Hanscom AFB, Massachusetts.
- Coco, D. S., C. Coker, S. Dahlke, and J. Clynch (1991). "Variability of GPS satellite differential group delay biases." Preprint of paper accepted for publication in *I.E.E.E. Transactions on Aerospace and Electronic Systems*.
- Coster, A. J., and E. M. Gaposchkin (1989). "Use of GPS pseudo-range and phase data for measurement of ionospheric and tropospheric refraction." *Proceedings of ION GPS-89*, Colorado Springs, Colorado, pp. 439–443.

- Coster, A. J., E. M. Gaposchkin, and L. E. Thornton (1991). "Real-time ionospheric monitoring system using the GPS." *Proceedings of ION GPS-91*, Albuquerque, New Mexico, pp. 299–307.
- Davies, Kenneth (1966). *Ionospheric Radio Propagation*. Dover Publications, Inc., New York.
- Feess, W. A., and S. G. Stephens (1986). "Evaluation of GPS ionospheric time delay algorithm for single-frequency users." *Proceedings of the PLANS-86 conference*, Las Vegas, Nevada, pp. 206–213.
- Finn, R. A. (1989). *The effect of the ionosphere on satellite position fixing*. Ph.D. Dissertation, Jesus College, Cambridge.
- Finn, A., and J. Matthewman (1989). "A single frequency ionospheric refraction correction algorithm for Transit and GPS." *Proceedings of the 5th International Geodetic Symposium on Satellite Positioning*, Las Cruces, New Mexico, pp. 737–756.
- Georgiadou, Y., and K. Doucet (1990). "The issue of selective availability." *GPS World*, Volume 1, Number 5, pp. 53–56.
- Georgiadou, Y., and A. Kleusberg (1988). "On the effect of ionospheric delay on geodetic relative GPS positioning." *Manuscripta Geodaetica*, Volume 13, pp. 1–8.
- Greenspan, R. L., A. K. Tetwsky, J. I. Donna, and J. A. Klobuchar (1991). "The effects of ionospheric errors on single-frequency GPS users." *Proceedings of ION GPS-91*, Albuquerque, New Mexico, pp. 291–297.
- Hirman, J. W., G. R. Heckman, M. S. Greer, and J. B. Smith (1988). "Solar and geomagnetic activity during cycle 21 and implications for cycle 22." *EOS Transactions of the American Geophysical Union*, Volume 69, Number 42, pp. 962 and 972.
- Institute of Navigation (1980, 1984, 1986). *Global Positioning System*. Papers published in Navigation, Volumes I, II, and III.

- Kelly, M. C. (1989). *The Earth's Ionosphere. Plasma Physics and Electrodynamics*. International Geophysics Series, Volume 43, Academic Press, New York.
- Kleusberg, A., Y. Georgiadou, F. van den Heuvel, and P. Héroux (1989). *Single and Dual-Frequency GPS Data Processing with DIPOP 2.1*. Department of Surveying Engineering Technical Memorandum TM-21, University of New Brunswick, Fredericton, Canada.
- Klobuchar, J. A. (1986). "Design and characteristics of the GPS ionospheric time delay algorithm for single frequency users." *Proceedings of the PLANS-86 conference*, Las Vegas, Nevada, pp. 280-286.
- Klobuchar, J. A. (1991). "Ionospheric effects on GPS." *GPS World*, Volume 2, Number 4, pp. 48-51.
- Klobuchar, J. A., D. N. Anderson, and P. H. Doherty (1991). "Model studies of the latitudinal extent of the equatorial anomaly during equinoctial conditions." *Radio Science*, Volume 26, Number 4, pp. 1025-1047.
- Lachapelle, G., and R. L. Wade (1982). "NAVSTAR/GPS single point positioning." *Technical Papers of the American Congress on Surveying and Mapping*, Denver, Colorado, pp. 603-609.
- Lanyi, G. E., and T. Roth (1988). "A comparison of mapped and measured total ionospheric electron content using Global Positioning System and beacon satellite observations." *Radio Science*, Volume 23, Number 4, pp. 483-493.
- McNamara, L. F. (1985). "The use of total electron content measurements to validate empirical models of the ionosphere." *Advances in Space Research*, Volume 5, Number 7, pp. 81-90.
- McNamara, L. F. (1991). *The Ionosphere: Communications, Surveillance, and Direction Finding*. Kreiger Publishing Company, Malabar, Florida.

- McNamara, L. F., and P. J. Wilkinson (1983). "Prediction of total electron content using the International Reference Ionosphere." *Journal of Atmospheric and Terrestrial Physics*, Volume 45, Number 2/3, pp. 169–174.
- Piggot, W. R., and K. Rawer (1972). *U.R.S.I. Handbook of Ionogram Interpretation and Reduction*. Second edition, World Data Centre A for Solar–Terrestrial Physics, NOAA, Boulder, Colorado. Report UAG–23A.
- Ratcliffe, J. A. (1970). *Sun, Earth and Radio*. McGraw–Hill, New York.
- Rawer, K., J. V. Lincoln, R. O. Conkright, D. Bilitza, B. S. N. Prasad, S. Mohanty, and F. Arnold (1981). *International Reference Ionosphere*. World Data Centre A for Solar–Terrestrial Physics, NOAA, Boulder, Colorado. Report UAG–82.
- Rishbeth, H., and O. K. Garriott (1969). *Introduction to Ionospheric Physics*. International Geophysics Series, Volume 14, Academic Press, New York.
- Rockwell (1987). *Navstar GPS Space Segment/Navigation User Interfaces*. Interface Control Document, Revision B, ICD–200, Rockwell International Corporation, pp. 106–108.
- Rush, C., M. Fox, D. Bilitza, K. Davies, L. McNamara, F. Stewart, and M. PoKempner (1989). "Ionospheric mapping: An update of foF2 coefficients." *Telecommunication Journal*, Volume 56, pp. 179–182.
- Schove, D. J. (1983). *Sunspot Cycles*. Hutchinson Ross Publishing Company, Stroudsburg, Pennsylvania.
- Srinivasan, J. M., T. K. Meehan, and L. E. Young (1989). "Code and codeless ionospheric measurements with NASA's Rogue GPS receiver." *Proceedings of ION GPS–90*, Colorado Springs, Colorado, pp. 451–453.
- Stewart, F. G., and M. Leftin (1972). "Relationship between Ottawa 10.7 cm solar radio noise flux and Zurich sunspot number." *Telecommunication Journal*, Volume 39, III/1972, pp. 159–169.

- Tascoine, T. F., H. W. Kroehl, R. Creiger, J. W. Freeman, R. A. Wolf, R. W. Spiro, R. V. Hilmer, J. W. Shade, and B. A. Hausman (1988). "New ionospheric and magnetospheric specification models." *Radio Science*, Volume 23, Number 3, pp. 211–222.
- Titheridge, J. E. (1972). "Determination of ionospheric electron content from the Faraday rotation of geostationary satellite signals." *Planetary Space Science*, Volume 20, pp. 353–369.
- Van Zandt, T. E., and R. W. Knecht (1964). "The structure and physics of the upper atmosphere." In *Space Physics*, ed. D. P. LeGalley and A. Rosen, John Wiley & Sons, Inc., New York.
- Webster, I., and A. Kleusberg (1992). "Regional modelling of the ionosphere for single frequency users of the Global Positioning System." *Proceedings of the 6th International Geodetic Symposium on Satellite Positioning*, Columbus, Ohio, 17–20 March (in press).
- Wells, D. E., N. Beck, D. Delikaraoglou, A. Kleusberg, E. J. Krakiwsky, G. Lapachelle, R. B. Langley, M. Nakiboglu, K. P. Schwarz, J. M. Tranquilla, and P. Vaníček (1986). *Guide to GPS Positioning*. Canadian GPS Associates, Fredericton, New Brunswick, Canada.
- Wells, D., and A. Kleusberg (1990). "GPS: A multipurpose system." *GPS World*, Volume 1, Number 1, pp. 60–63.



## ***APPENDIX I***

Sample of the ***Solar Indices Bulletin*** and the ***Geomagnetic Indices Bulletin*** as  
Supplied by the National Geophysical Data Centre, Boulder, Colorado.

# SOLAR INDICES BULLETIN

APRIL 1989

NATIONAL GEOPHYSICAL DATA CENTER  
Solar-Terrestrial Physics Division (E/GC2)

325 Broadway  
Boulder, Colorado 80303 USA

Telephone (303) 497-6136

## ■ SOLAR RADIO EMISSIONS

The quiet sun emits radio energy with a slowly varying intensity. These radio fluxes, which stem from atmospheric layers high in the chromosphere and low in the corona, change gradually from day-to-day, in response to the number and size of spot groups on the solar disk. The table below gives daily measurements of this slowly varying emission at selected wavelengths between about 1 and 100 centimeters. Many observatories record quiet-sun radio fluxes at the same local time each day and correct them to within a few percent for factors such as antenna gain, bursts in progress, atmospheric absorption, and sky background temperature. At 2800 megahertz (10.7 centimeters) flux observations summed over the sun's disk have been made continuously since February 1947.

## ■ SOLAR FLUX TABLE

Numbers in parentheses in the column headings below denote frequencies in megahertz. Each entry is given in solar flux units--a measure of energy received per unit time, per unit area, per unit frequency interval. One solar flux unit equals 10 to the power -22 Joules/second/square meter/hertz.

The observed and the adjusted Ottawa fluxes tabulated here are the "Series C" values reported by the Algonquin Radio Observatory in Ottawa, Ontario, Canada. The observed numbers are less refined, since they contain fluctuations as large as  $\pm 7\%$  from the continuously changing sun-earth distance. Adjusted fluxes have this variation removed; they show the energy received at the mean distance between the sun and earth. Gaps in the Sagamore Hill (SGMR) data taken at South Hamilton, Massachusetts, reflect equipment problems. Fluxes measured either at Learmonth, Australia, or at Palehua, Hawaii, will be substituted for frequencies at which nearly all Sagamore Hill values are missing.

APRIL 1989 SUNSPOT NUMBERS AND SOLAR RADIO FLUX

	Sunspot Number	Obs Flux Ottawa (2800)	—— SGMR (15400)	Solar SGMR (8800)	Flux Adjusted to 1 Astronomical Unit SGMR (4995)	SGMR (2800)	SGMR (2695)	SGMR (1415)	SGMR (610)	SGMR (410)	SGMR (245)
Day	Int1										
01	104	174.0*	524	298	211	173.8*	158	130	81	54	55
02	122	183.6	529	306	222	183.5	164	137	79	45	36
03	140	196.5*	501	309	231	196.5*	173	147	--	50	50
04	126	188.8	453	301	223	188.9	174	152	69	47	68
05	94	190.8	511	310	228	191.1	181	158	72	43	25
06	139	196.1	502	294	215	196.5	178	164	--	78	--
07	170	199.3	534	314	228	199.8	184	161	84	49	28
08	185	206.5	522	313	231	207.1	185	166	89	46	21
09	153	193.3	523	300	223	194.0	174	159	85	47	44
10	122	181.5	512	297	210	182.3	166	152	86	44	20
11	106	179.8	526	295	207	180.7	166	151	93	45	20
12	96	180.3	521	295	204	181.3	164	151	85	46	22
13	92	184.2*	534	311	219	185.3*	171	153	82	52	79
14	98	196.8	532	320	228	198.1	177	152	94	45	59
15	120	198.1	524	314	230	199.5	181	151	89	49	--
16	130	202.3	465	269	206	203.9	179	152	91	66	--
17	144	208.9*	537	322	242	210.6*	188	155	91	--	--
18	137	202.3	528	314	232	204.1	187	151	88	50	52
19	151	207.8	449	315	232	209.7	185	152	82	46	82
20	155	190.6	531	312	226	192.5	176	145	83	44	86
21	161	194.1	535	315	231	196.1	178	143	78	38	24
22	167	191.5*	530	311	224	193.6*	172	142	73	42	33
23	128	181.0*	534	315	231	183.1*	179	148	87	42	42
24	135	186.8	534	312	222	189.0	169	139	79	45	34
25	132	177.5	531	305	218	179.7	160	126	69	35	25
26	116	174.6	528	293	211	176.9	159	124	74	35	28
27	126	174.5	528	302	219	176.9	168	124	64	34	25
28	109	180.7	522	303	218	183.2	162	129	72	35	16
29	107	186.8	523	303	220	189.5	170	133	80	35	19
30	114	177.9	476	297	209	180.6	161	131	--	15	15
Mean	129.3	189.6	517	306	222	190.9	173	146	81	45	39

\* = corrected for burst in progress

#### • SUNSPOT COUNTS

In 1848 the Swiss astronomer Johann Rudolph Wolf introduced a daily measurement of sunspot number. His method, which is still used today, counts the total number of spots visible on the face of the sun and the number of groups into which they cluster, because neither quantity alone satisfactorily measures the level of sunspot activity.

An observer computes a daily sunspot number by multiplying his estimated number of groups by ten and then adding this product to his total count of individual spots. Results, however, vary greatly, since the measurement strongly depends on observer interpretation and experience and on the stability of the earth's atmosphere above the observing site. Moreover, the use of earth as a platform from which to record these numbers contributes to their variability, too, because the sun rotates and the evolving spot groups are distributed unevenly across solar longitudes. To compensate for these limitations, each daily international number is

computed as a weighted average of measurements made from a network of cooperating observatories. The international sunspot numbers tabulated on page 1 are provisional values taken from a bulletin prepared monthly by Dr. Andre Koeckelenbergh of the SUNSPOT INDEX DATA CENTER, 3 avenue Circulaire, B-1180 BRUXELLES, BELGIUM. The April 1989 data combine observations from 33 stations.

#### • HISTORICAL SUNSPOT COUNTS

How do sunspot numbers in the table on page 1 compare to the largest values ever recorded? The highest daily count on record occurred December 24-25, 1957. On each of those days the sunspot number totaled 355. In contrast, during years near the spot cycle minimum, the count can fall to zero. Today, much more sophisticated measurements of solar activity are made routinely, but none has the link with the past that sunspot numbers have. Our archives, for example, include reconstructed daily values from January 8, 1818; monthly means from January 1749; and yearly means beginning in 1700.

SMOOTHED (OBSERVED AND PREDICTED) SUNSPOT NUMBERS: CYCLES 21 AND 22

Year	Jan	Feb	Mar	Apr	May	Jun	Jul	Aug	Sep	Oct	Nov	Dec	Mean
1978	61	64	70	77	83	89	97	104	108	111	113	118	91
1979	124	131	136	141	147	153	155	155	156	158	162	164*	148
1980	164	163	161	159	156	155	153	150	150	150	148	143	154
1981	140	142	143	143	143	142	140	141	143	142	139	138	141
1982	137	133	129	124	120	117	115	109	101	96	95	95	114
1983	93	90	86	82	77	70	66	66	68	68	67	64	75
1984	60	56	53	50	48	46	44	40	34	29	25	22	42
1985	20	20	19	18	18	18	17	17	17	17	17	15	18
1986	14	13	13	14	14	14	14	13	12*	13	15	16	14
1987	18	20	22	24	26	28	31	35	39	44	47	51	32
1988	58	65	71	78	84	94	104	114	121	125	132 ( 4 )	137 ( 8 )	99 ( 6 )
1989	140 ( 9 )	144 ( 9 )	151 ( 10 )	158 ( 13 )	163 ( 15 )	169 ( 20 )	171 ( 25 )	174 ( 30 )	180 ( 34 )	185 ( 36 )	187 ( 39 )	188 ( 40 )	168 ( 26 )
1990	189 ( 41 )	190 ( 42 )	189 ( 43 )	184 ( 42 )	178 ( 39 )	174 ( 35 )	172 ( 33 )	170 ( 34 )	163 ( 33 )	155 ( 33 )	147 ( 30 )	143 ( 27 )	171 ( 36 )

\*Dec 1979 marks the maximum of Sunspot Cycle 21; Sep 1986 marks its minimum and the onset of Cycle 22.

#### • SUNSPOT NUMBER PREDICTIONS

For the end of Solar Cycle 21, and the beginning of Cycle 22, the table gives smoothed sunspot numbers up to the one calculated that first uses the most recently measured monthly mean. These smoothed, observed values are based on final, unsmoothed monthly means through December 1988 and on provisional ones thereafter. We compute a smoothed monthly mean by forming the arithmetic average of two sequential 12-month running means of monthly means.

Table entries with numbers in parentheses below them denote predictions by the McNish-Lincoln method. This method estimates future numbers by adding a correction to the mean of all cycles that is proportional to the departure of earlier values of the current cycle from the mean cycle. (See page 9 in the July 1987 supplement to *Solar-Geophysical Data*.) We use and predict only smoothed monthly means, because we believe the er-

rors are too great to estimate any values more precise. In the table above, adding the number in parentheses to the predicted value generates the upper limit of the 90% confidence interval; subtracting the number from the predicted value generates the lower limit. Consider, for example the October 1989 prediction. There exists a 90% chance that in October 1989 the actual smoothed sunspot number will fall somewhere between 149 and 221.

The McNish-Lincoln prediction method generates useful estimates of smoothed, monthly mean sunspot numbers for no more than 12 months ahead. Beyond a year these predictions regress rapidly toward the mean of all 13 cycles used in the computation. Moreover, the method is very sensitive to the date defined as the beginning of the current sunspot cycle, that is, to the date of the most recent sunspot minimum. The new cycle predictions tabulated above are based on the minimum value of 12.3 that occurred in September 1986.

Although every effort has been made to ensure that these data are correct, we can assume no liability for any damages their inaccuracies might cause. The charge for a 1-year subscription to this monthly bulletin is \$21. To become a subscriber you may either call (303) 497-6346 or write the NATIONAL GEOPHYSICAL DATA CENTER, Solar-Terrestrial Physics Division (E/GC2), 325 Broadway, Boulder, Colorado 80303 USA. Please include with your written order a check or money order payable in U.S. currency to the Department of Commerce, NOAA/NGDC. Payment may be made, too, through one of three credit cards: VISA, MasterCard, or American Express.

# GEOMAGNETIC INDICES BULLETIN AUG 1989

NATIONAL GEOPHYSICAL DATA CENTER  
Solar-Terrestrial Physics Division (E/GC2)  
Telephone (303) 497-6346

325 Broadway  
Boulder, Colorado 80303 USA

**THE GEOMAGNETIC FIELD.** The geomagnetic field measured at any point on the Earth's surface at any time is a combination of the **MAIN** field internal to the planet, of fields arising from electrical currents flowing in the ionized upper atmosphere, and of fields induced by currents flowing within the Earth's crust. The main field component varies slowly in time and can be grossly described as that of a bar magnet with north and south poles deep inside the Earth and magnetic field lines that extend well out into space.

The main field creates a cavity in interplanetary space called the magnetosphere, where the Earth's magnetic field dominates the magnetic field of the solar wind. The magnetosphere is shaped somewhat like a comet in response to the dynamic pressure of the solar wind. It is compressed on the side toward the sun to about 10 Earth radii and is extended tail-like on the side away from the sun to more than 100 Earth radii. The magnetosphere deflects the flow of most solar wind particles around the Earth, while the geomagnetic field lines guide charged particle motion within the magnetosphere.

The differential flow of ions and electrons inside the magnetosphere and in the ionosphere form current systems, which cause variations in the intensity of the Earth's magnetic field. These **EXTERNAL** currents in the ionized upper atmosphere and magnetosphere vary on a much shorter time scale than the **INTERNAL** main field and may create magnetic fields as large as 10% of the main field.

Daily regular magnetic field variations arise from current systems caused by regular solar radiation changes. Other irregular current systems produce magnetic field changes caused by the interaction of the solar wind with the magnetosphere, by the magnetosphere itself, by the interactions between the magnetosphere and ionosphere, and by the ionosphere itself. Magnetic activity indices, including those below, are designed to describe variations in the geomagnetic field caused by these irregular current systems.

MONTHLY SUMMARY OF GEOMAGNETIC ACTIVITY FOR AUGUST 1989

Day			Rank Q/D	Kp Three-Hour Indices												Kp Sum	sc		Afr	aa				Provisional			
Cal	#	Bart		1	2	3	4	5	6	7	8	9	10	Ap	Cp		{UT}	An		As	Am	N	S	M1	M2		
1	213	9	Q4	2-	1+	1-	1	1+	2-	2-	2+	12-	6	0.2			5	12	9	10	10	8	7	11	CC		
2	214	10	Q6	3-	2-	2+	1	1-	1-	1	2-	12-	6	0.3			7	14	11	12	12	9	15	6	CC		
3	215	11	Q3	2	2	2-	2+	1	1	1	0+	11	5	0.2			7	12	9	10	12	7	10	9	CC		
4	216	12		1-	1	2-	2+	3-	3+	2	2+	16	8	0.5			5	17	12	15	18	16	13	21	K		
5	217	13	Q1	1	1	0-	0+	0+	0+	0+	1	4	2	0.0			2	5	3	4	4	2	3	4	CK		
6	218	14	Q10A	1	1+	1	1	2-	2+	3+	3-	14+	8	0.4			7	16	10	13	16	9	8	18	KK		
7	219	15		2	2+	2	2	2	3-	3+	2	18+	9	0.5			10	20	14	17	24	13	17	20			
8	220	16	Q9A	2	2+	2+	3-	1+	1	2-	2-	15	7	0.4			11	17	13	15	16	12	18	10			
9	221	17		2-	1+	1-	1	2-	2-	4+	3+	16-	10	0.6	1832		11	21	14	17	21	13	9	25			
10	222	18	D4	4-	4-	6	6-	4+	4+	4	5	37-	41	1.5	0727		29	65	54	59	47	58	60	46			
11	223	19		5+	5-	3	4	4+	3+	2	2+	29	25	1.2			24	41	39	40	38	43	54	27			
12	224	20		3	2+	2	2+	1+	1-	1+	2+	16-	8	0.4			9	18	16	17	17	14	18	13			
13	225	21		3	3-	2+	2	3-	1+	2	2	18	9	0.5			10	18	16	17	19	16	18	17			
14	226	22	Q2	3+	4	7-	6	7	3+	4	5	39	55	1.6	0613		54	90	62	76	73	58	82	49			
15	227	23	D1	7-	7-	6	4+	6+	4	5	7-	46-	77	1.8			61	101	90	95	93	72	83	84			
16	228	24	Q2	6-	5	3	2+	3+	3-	3+	4	29	26	1.2			28	47	44	46	32	31	39	25			
17	229	25	D5	3+	3-	3+	3-	5+	6-	5-	5	33-	34	1.3			24	51	41	46	52	44	30	66			
18	230	26		5	4	4-	5	3-	3-	4+	4+	32-	29	1.3			25	48	39	43	50	32	51	32			
19	231	27		4	5-	2+	1	1	2-	3	1	19-	14	0.8			12	21	19	20	22	10	20	12			
20	232	1		2+	3-	5	5	5	4	2-	2-	27+	26	1.2			20	45	36	41	40	38	44	35			
21	233	2		2	1+	1	1	3+	4	5+	5	23	21	1.1	1415		12	28	31	30	33	33	10	57			
22	234	3		4+	3+	3+	3-	1+	1+	1+	1+	19	12	0.7			12	22	21	21	23	15	29	9			
23	235	4		3	3+	3-	3	5	5-	4-	4-	31-	28	1.2	0047		16	43	41	42	52	41	31	63			
24	236	5	Q5K	3	1	1	1-	2-	1+	1	2-	11+	6	0.3			5	13	10	11	15	8	11	11	C		
25	237	6	Q2	1-	1	1+	1-	1+	1	1+	2+	10-	5	0.2			5	12	7	10	11	8	7	12	CC		
26	238	7	Q8	1-	2+	2	3-	2	2-	1-	1-	13-	6	0.3			8	14	11	12	15	9	16	8	K		
27	239	8		2	4+	3	3-	4	3+	6-	4+	29+	26	1.2	1337		24	50	39	45	48	38	28	58			
28	240	9		3-	1	1	2	2	2+	4	7-	21+	22	1.1			12	32	31	32	40	30	11	59			
29	241	10	D3	7	7+	6-	4	4-	4	4-	2+	38-	58	1.7			43	79	78	79	68	63	91	39			
30	242	11		2	4+	2	3	3+	4	3	3-	24+	17	0.9			16	28	27	28	34	24	25	33			
31	243	12	Q7	2	1+	1	0+	1	3-	2-	2+	12+	6	0.3			6	12	11	12	16	8	7	16	C		
Mean																20	0.8		17	33	28	30	31	25	28		

Column headings defined on back side.

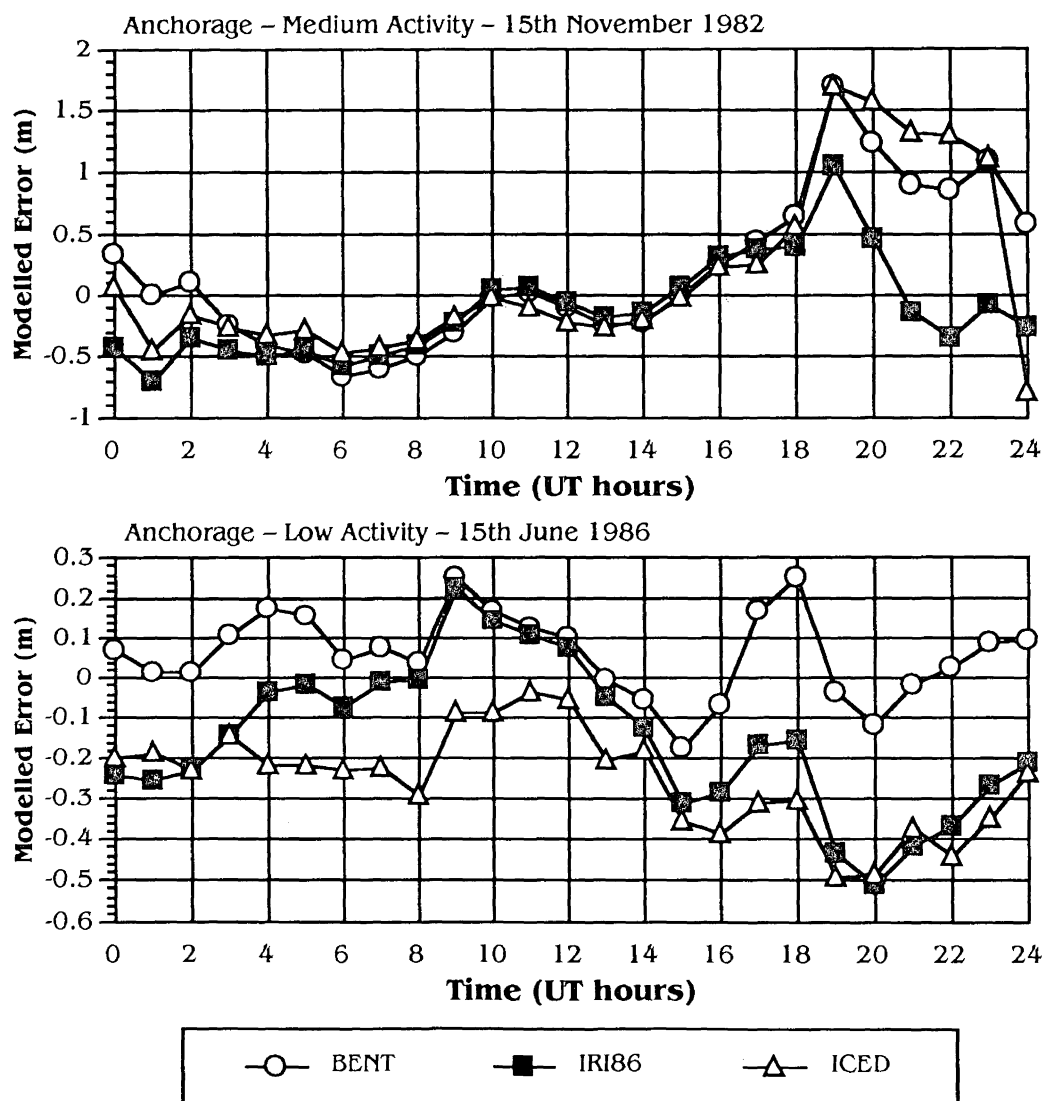
## ***APPENDIX II***

---

Some Typical Plots Showing Modelled Errors from Each of Three Ionospheric Models.  
These Plots resulted from Comparisons with the Faraday Rotation Data.

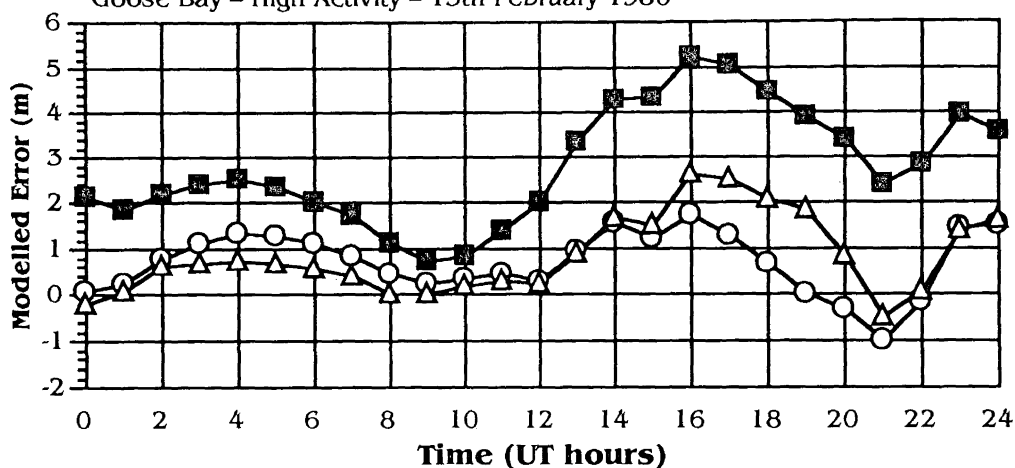
**IMPORTANT NOTE : The scales of the Y-axes in the plots are not equal.**

## ANCHORAGE

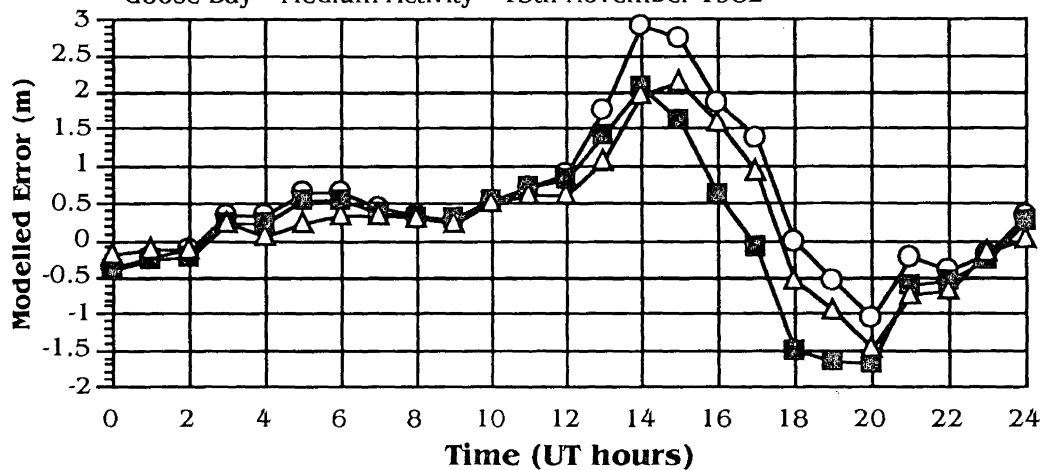


## GOOSE BAY

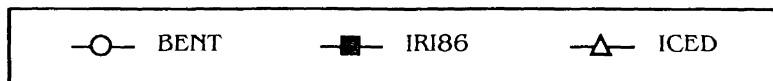
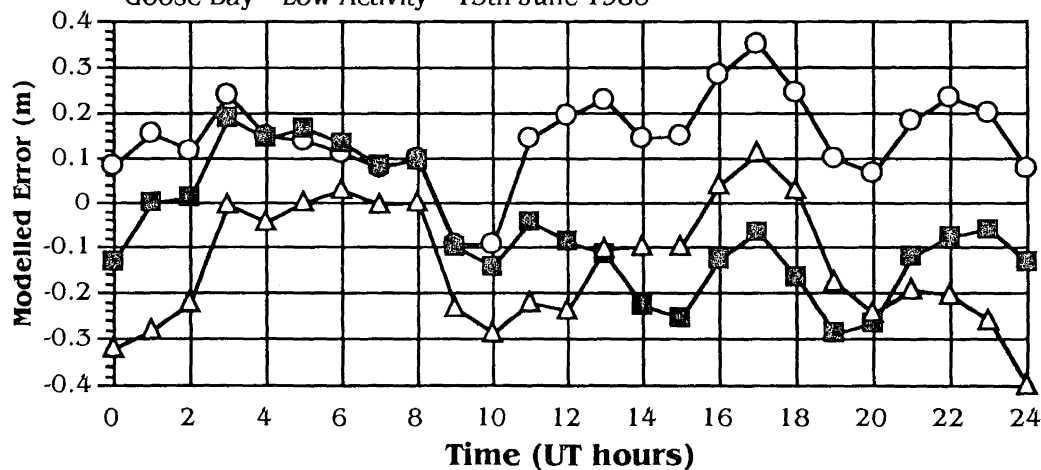
Goose Bay – High Activity – 15th February 1980



Goose Bay – Medium Activity – 15th November 1982

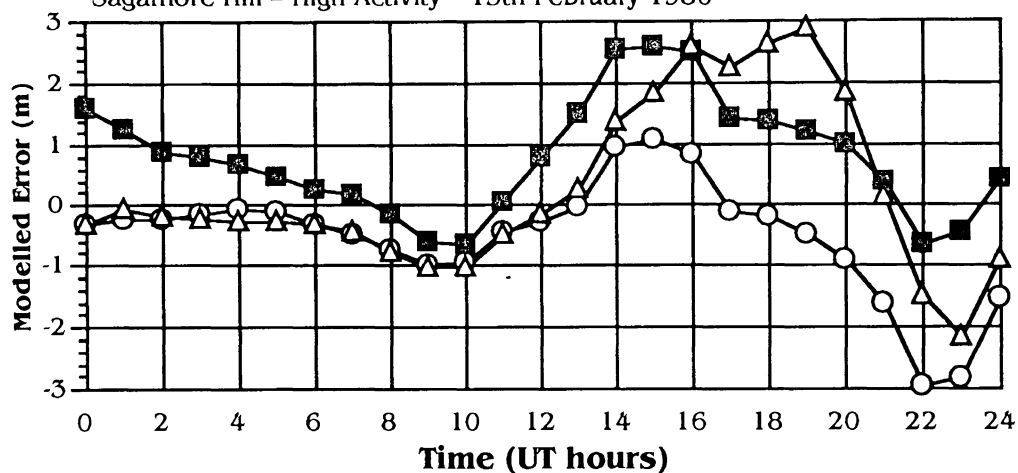


Goose Bay – Low Activity – 15th June 1986

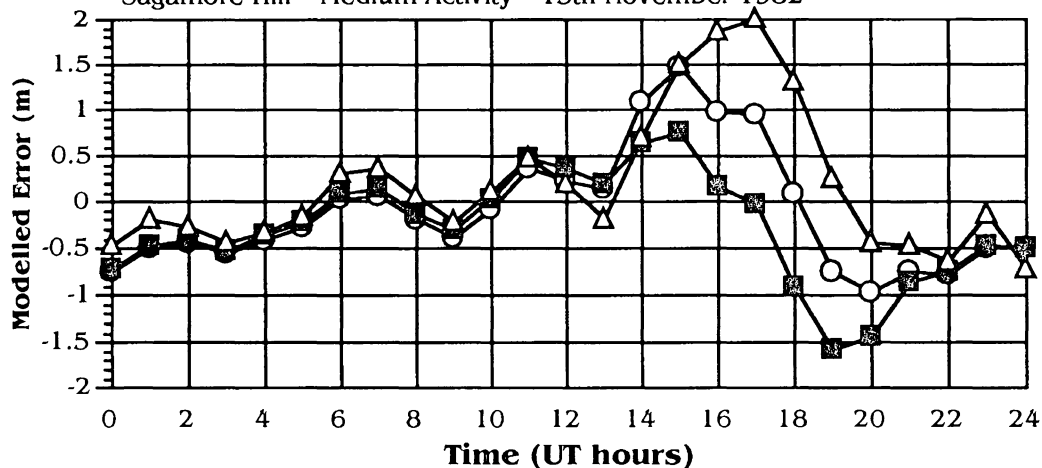


## SAGAMORE HILL

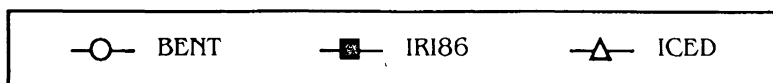
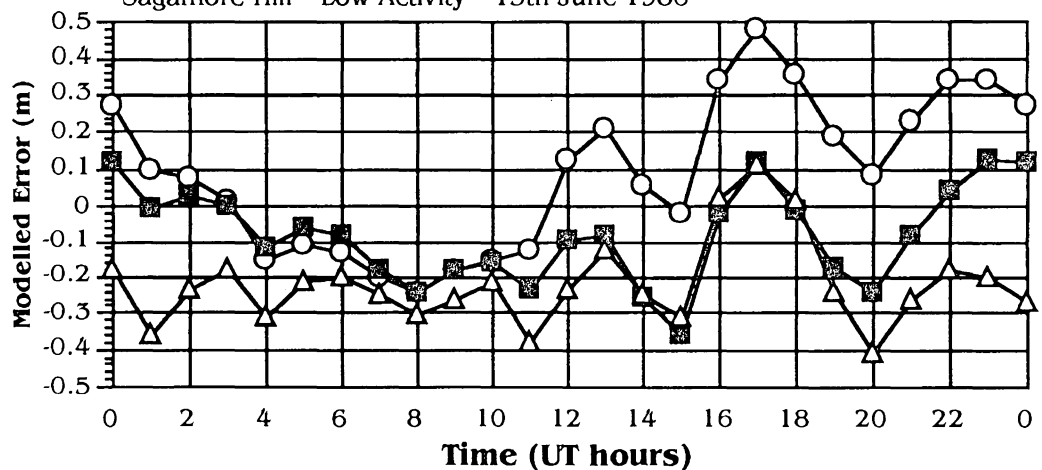
Sagamore Hill – High Activity – 15th February 1980



Sagamore Hill – Medium Activity – 15th November 1982



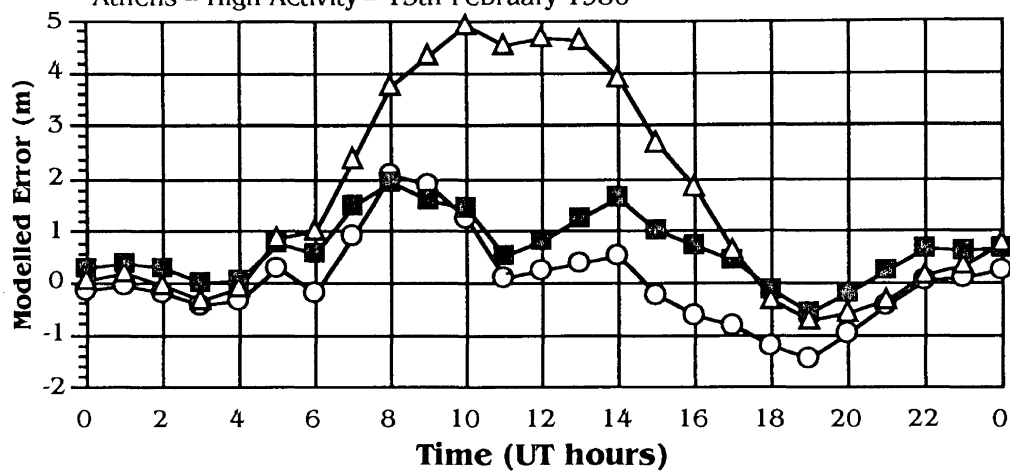
Sagamore Hill – Low Activity – 15th June 1986



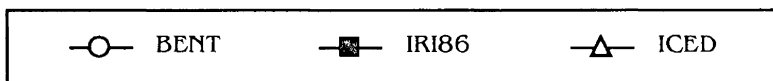
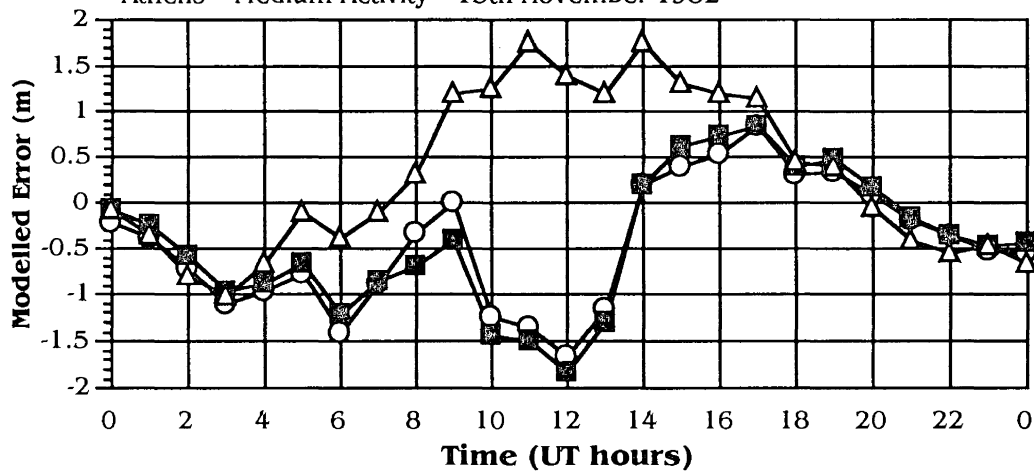


**ATHENS**

Athens – High Activity – 15th February 1980

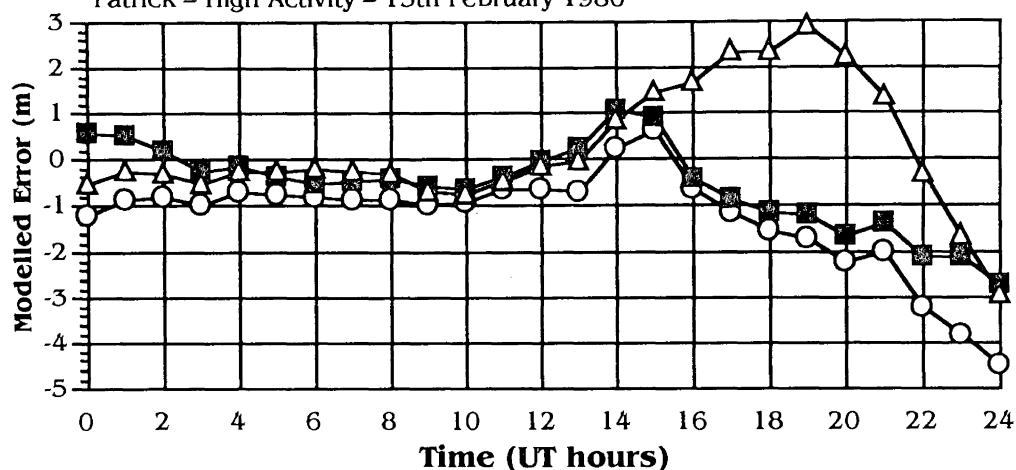


Athens – Medium Activity – 15th November 1982

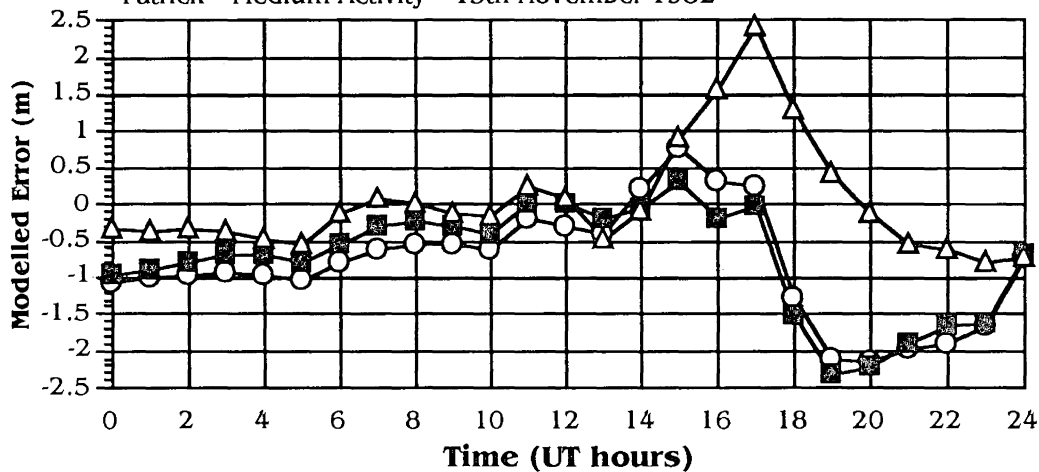


# PATRICK

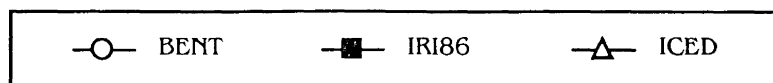
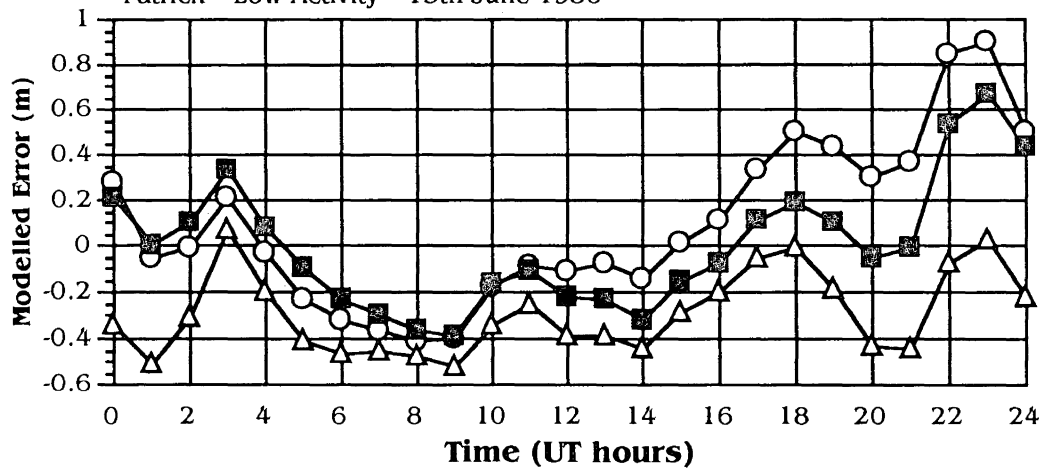
Patrick - High Activity - 15th February 1980



Patrick - Medium Activity - 15th November 1982

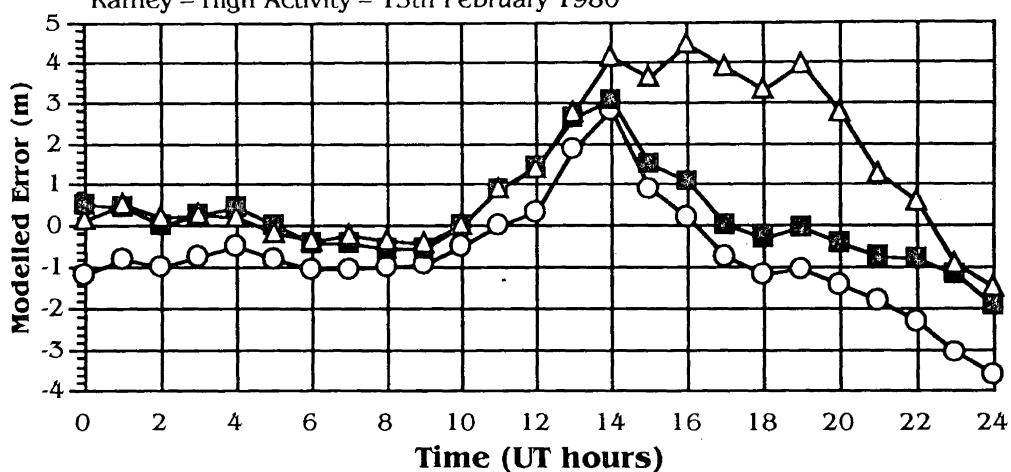


Patrick - Low Activity - 15th June 1986

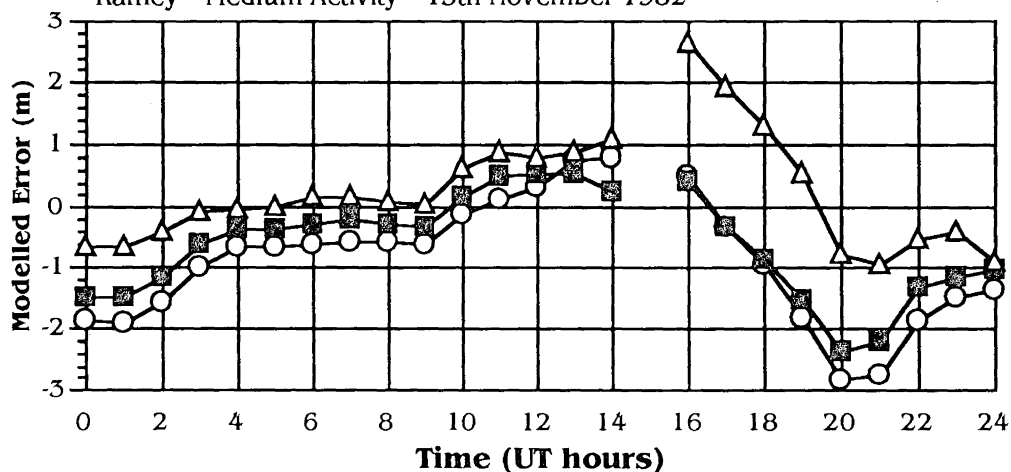


# RAMEY

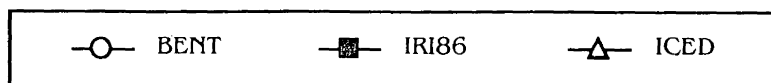
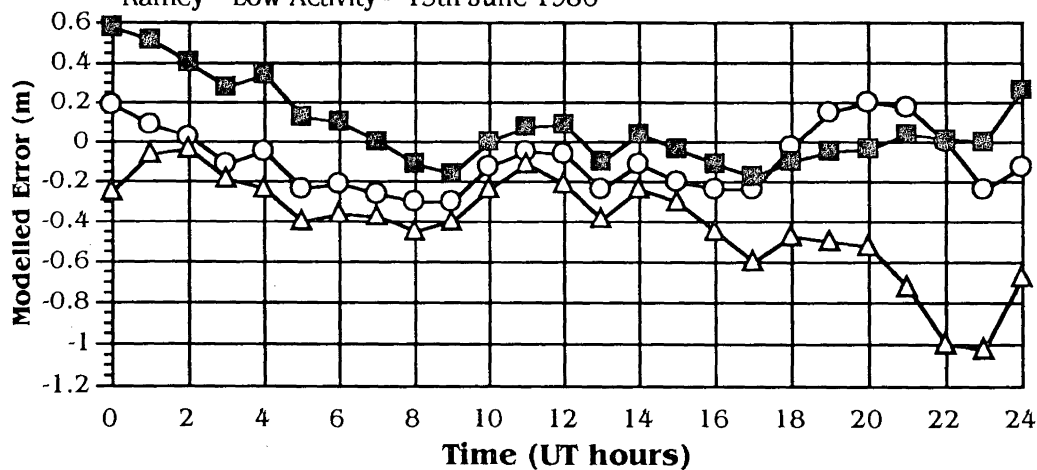
Ramey – High Activity – 15th February 1980



Ramey – Medium Activity – 15th November 1982



Ramey – Low Activity – 15th June 1986

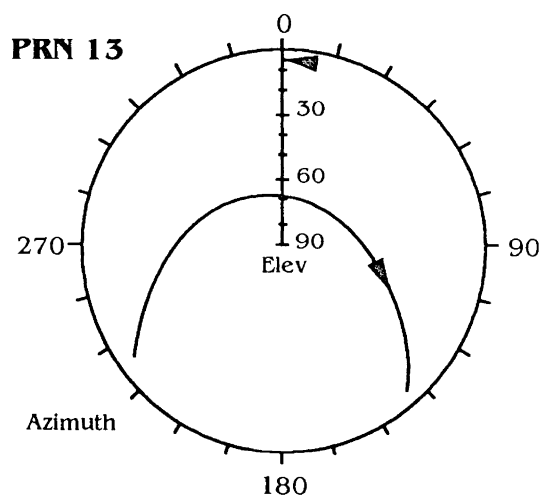
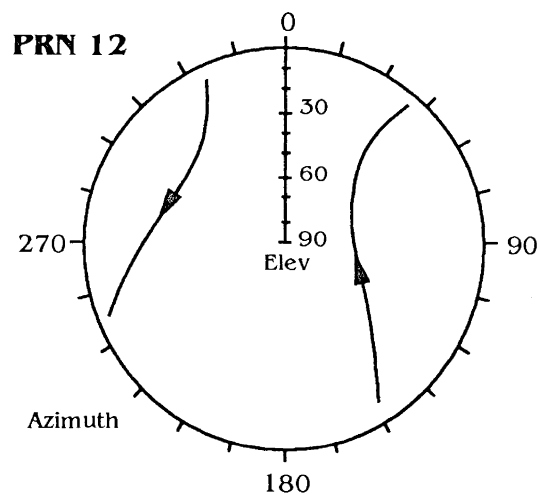
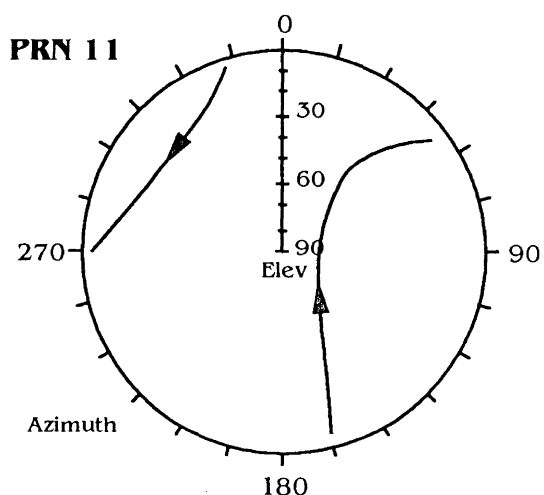
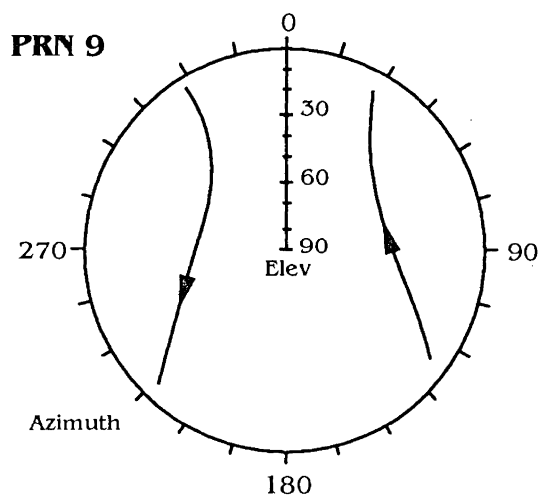
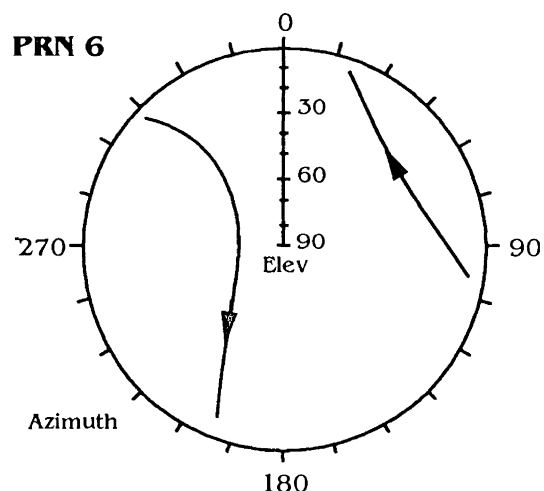
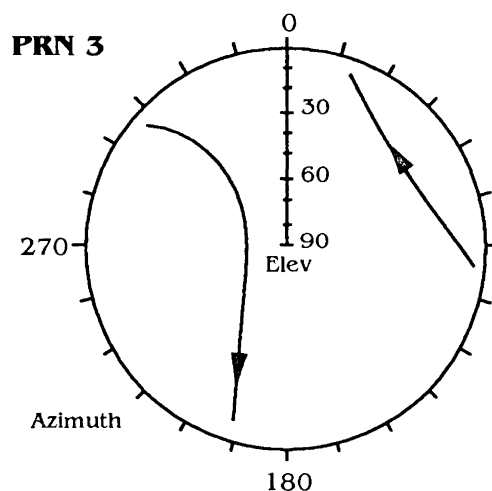


## ***APPENDIX III***

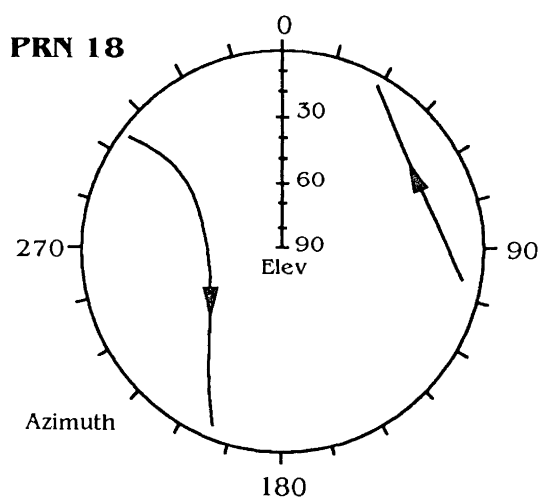
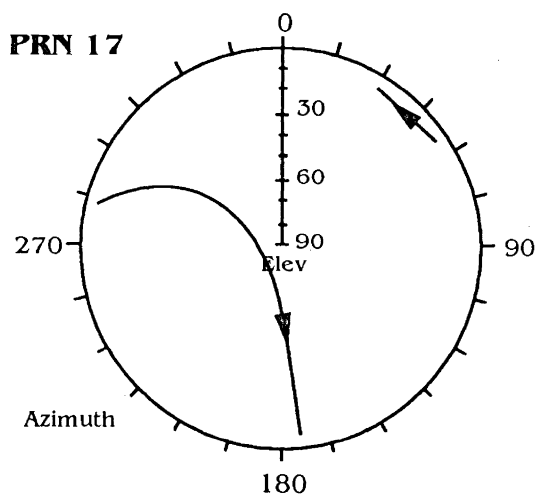
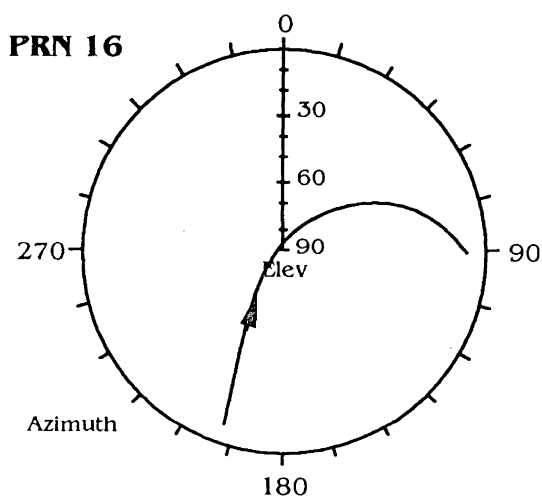
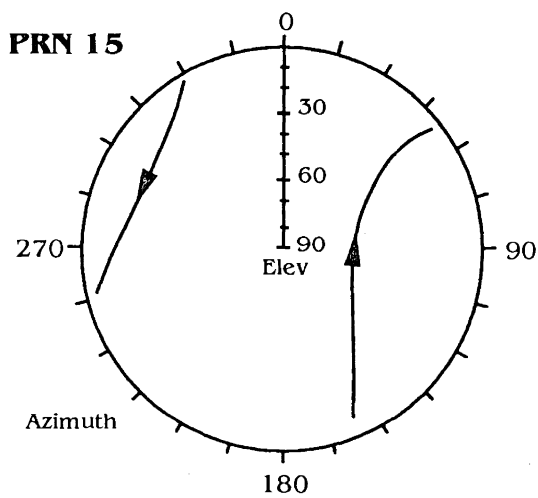
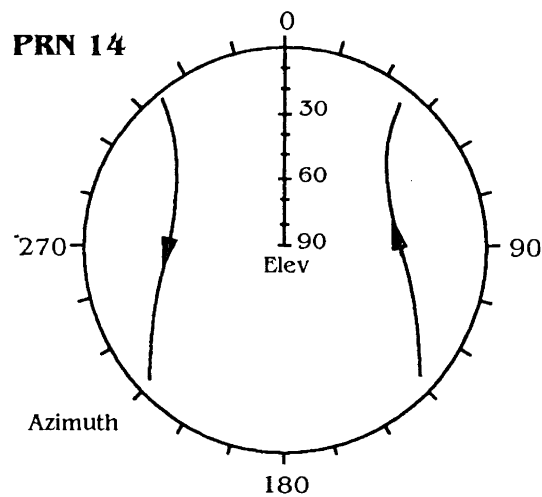
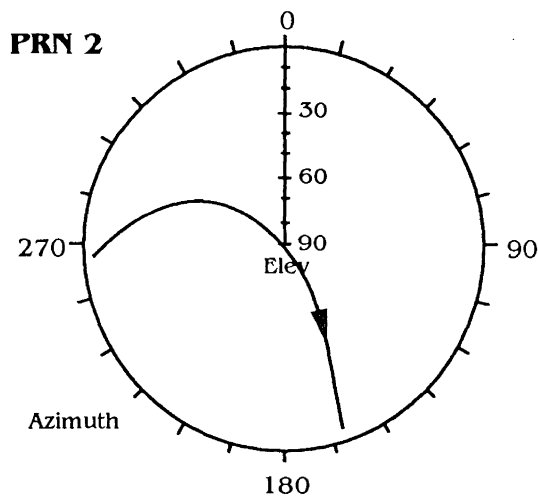
---

Satellite Sky Plots for Algonquin and Yellowknife on February 3rd, 1991.

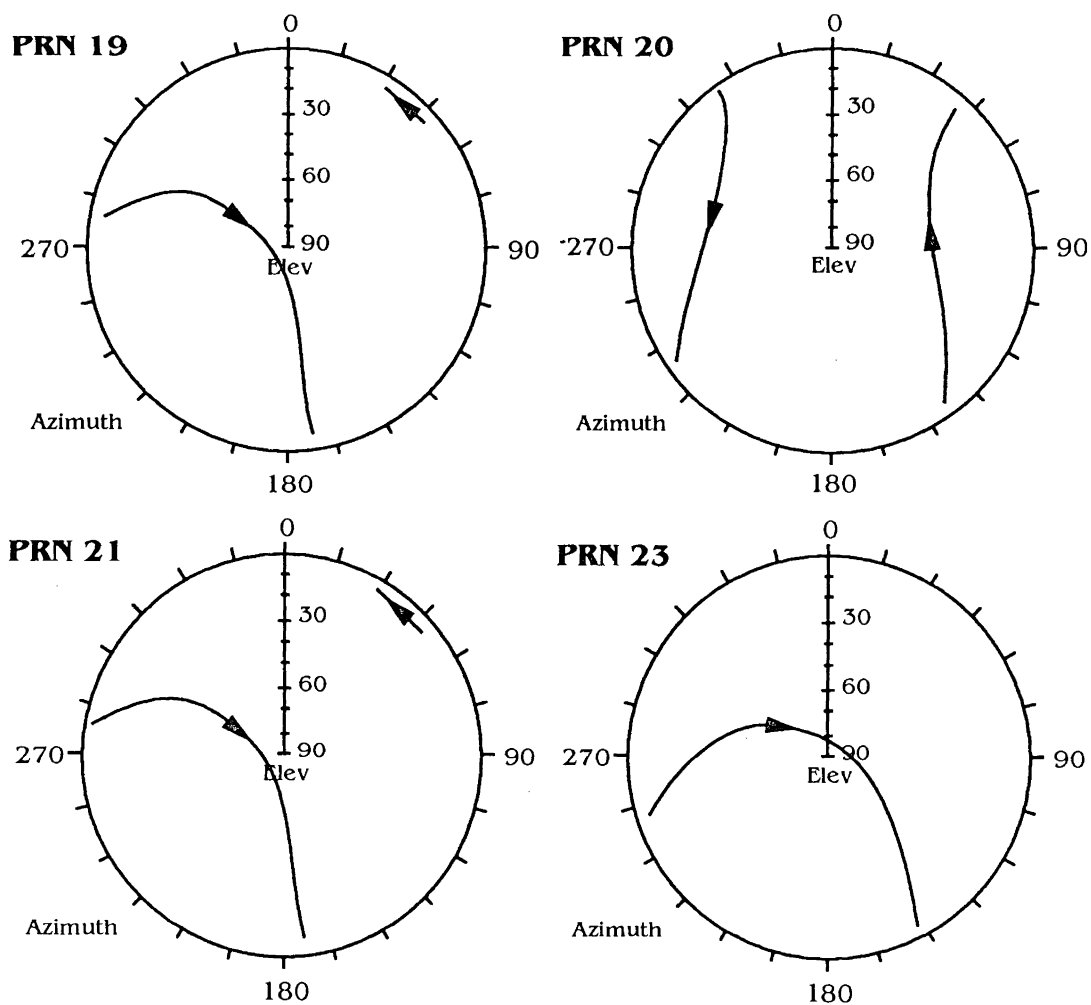
**Algonquin Satellite Sky Plots (Block I)**  
(3rd February 1991)



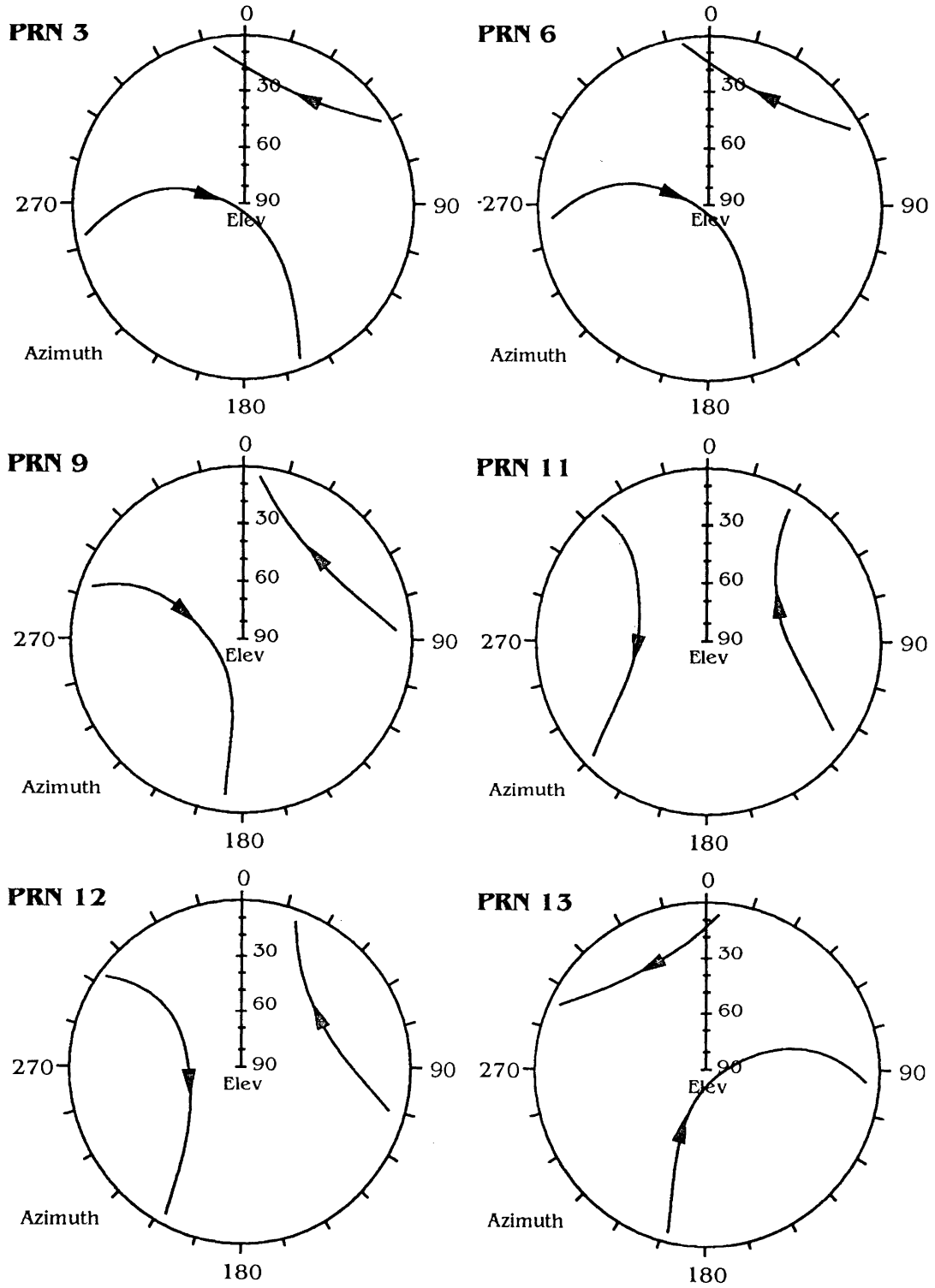
**Algonquin Satellite Sky Plots (Block II)**  
(3rd February 1991)



**Algonquin Satellite Sky Plots (Block II) Continued**  
(3rd February 1991)

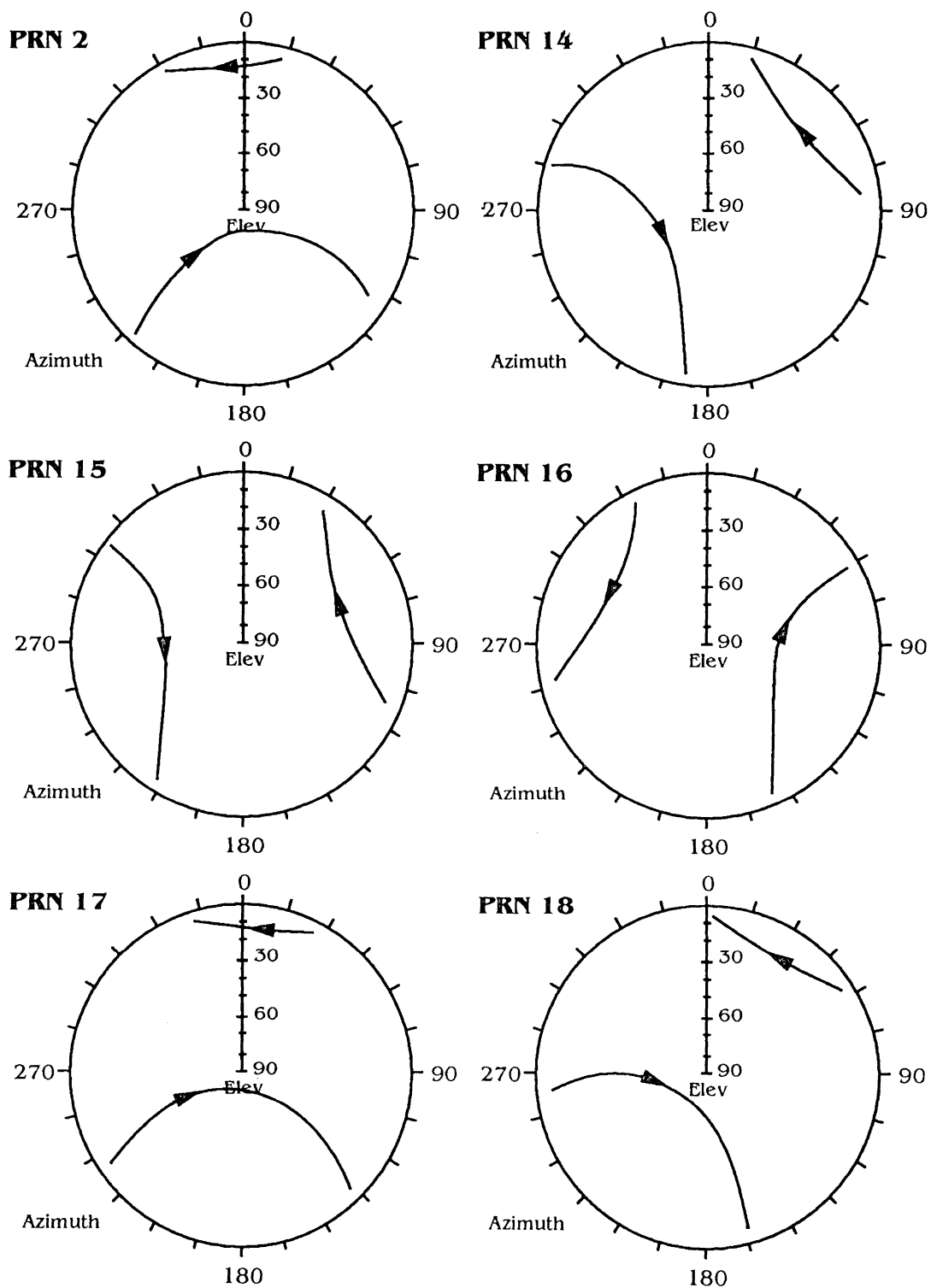


**Yellowknife Satellite Sky Plots (Block I)**  
(3rd February 1991)

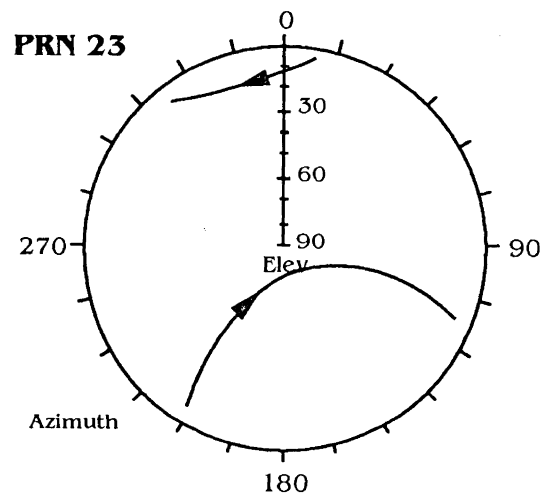
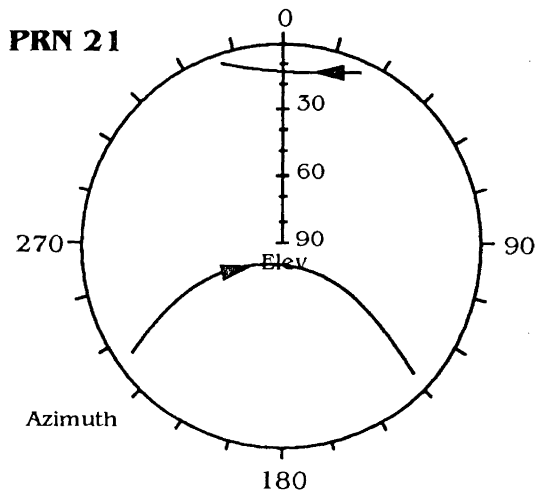
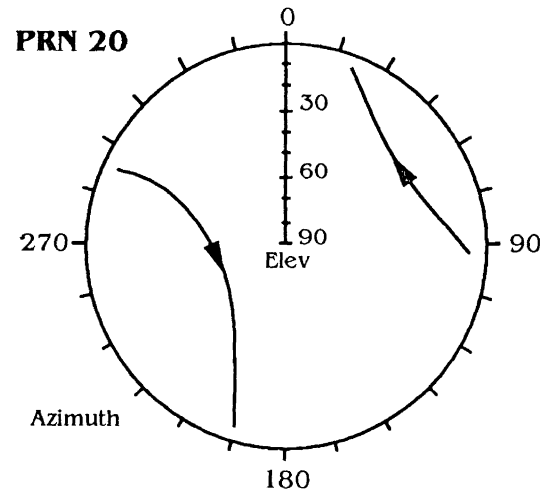
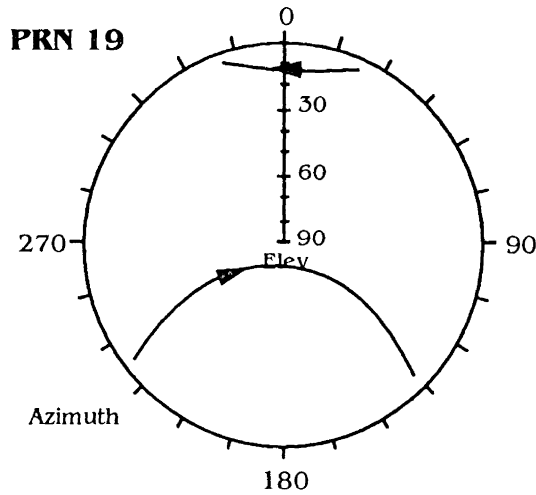




**Yellowknife Satellite Sky Plots (Block II)**  
(3rd February 1991)



**Yellowknife Satellite Sky Plots (Block II) Continued**  
(3rd February 1991)



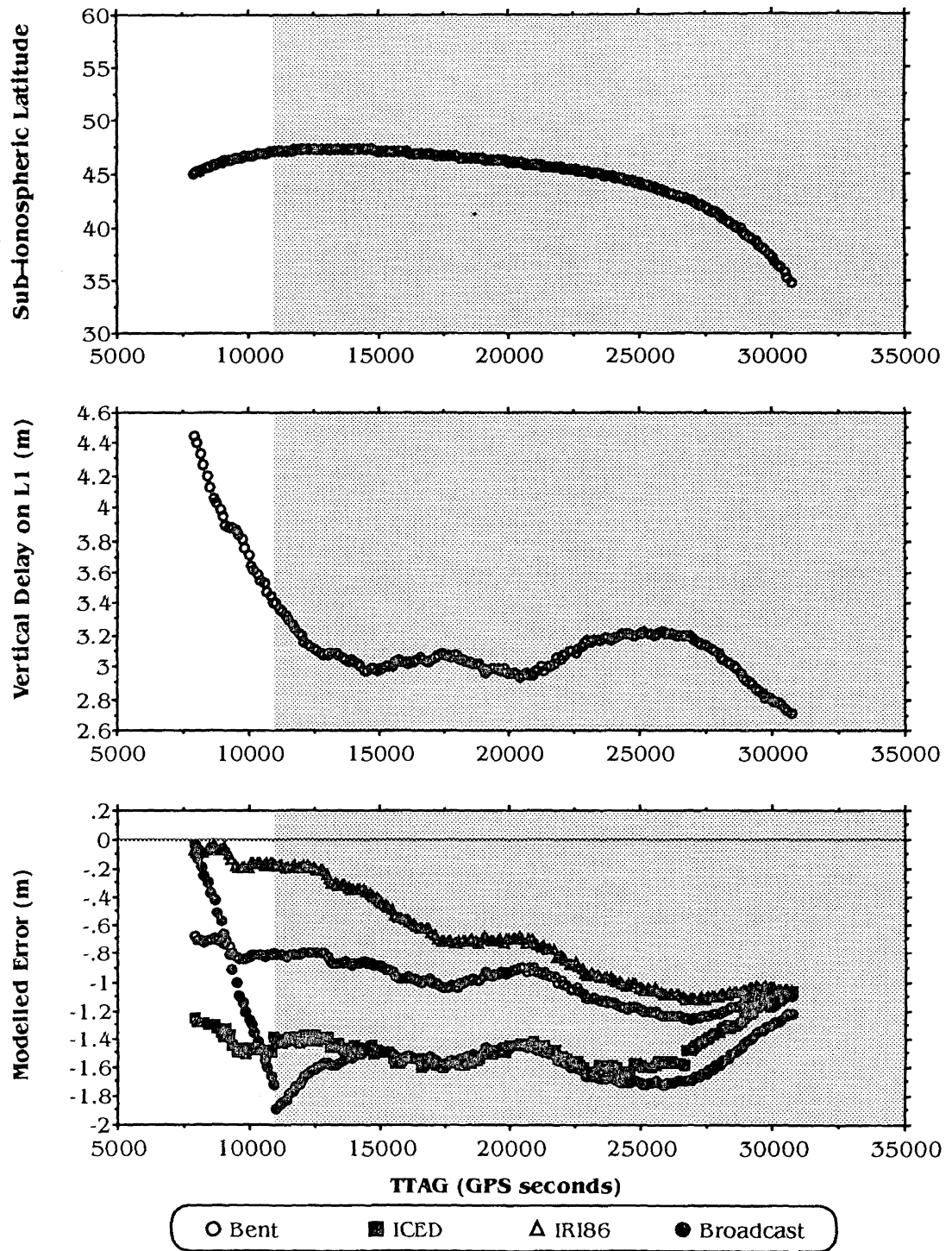
## ***APPENDIX IV***

---

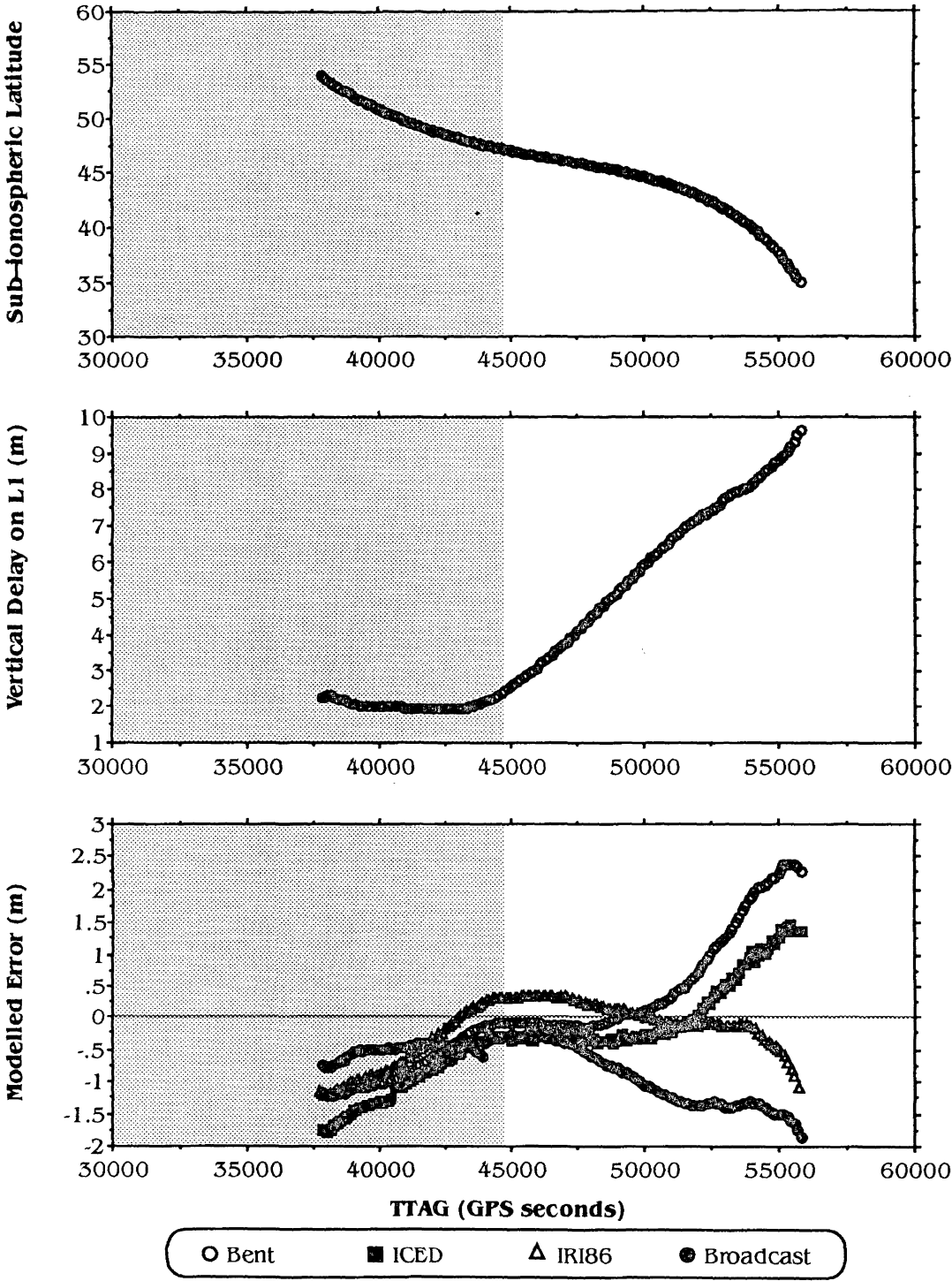
**Algonquin** Plots Showing the Latitude of the Sub-Ionospheric Point, the Vertical Ionospheric Delay on L1, and the Modelled Errors from Each of Four Ionospheric Models.

**IMPORTANT NOTES** : The scales of the Y-axes in the plots of the L1 ionospheric delay and of the modelled errors are not equal. Also note that the apparent discontinuities which are occasionally evident in ICED's modelled errors are caused by sudden changes in the *Kp* index which is used by ICED.

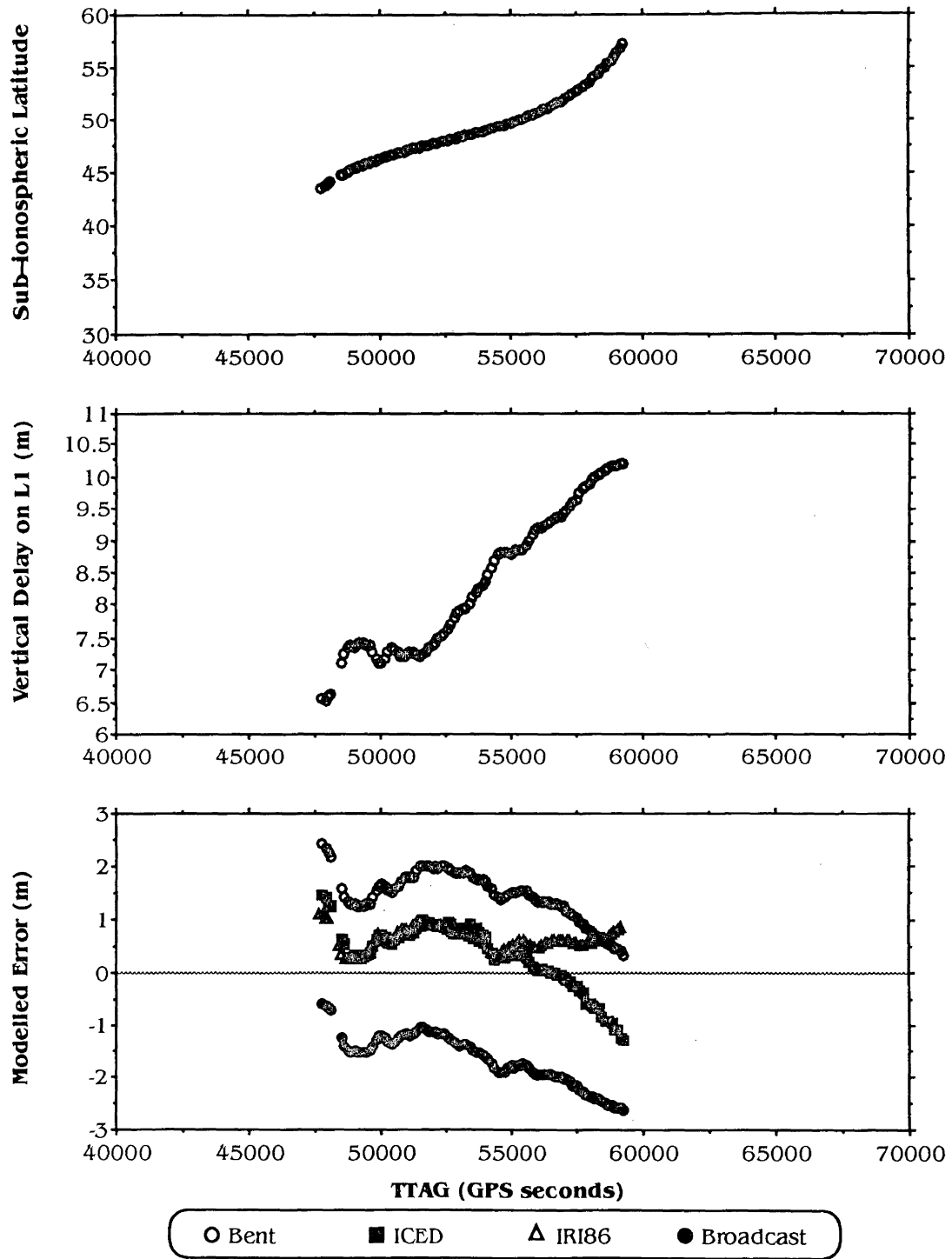
# **Algonquin PRN#02** **– Observed Delay and Modelled Errors**



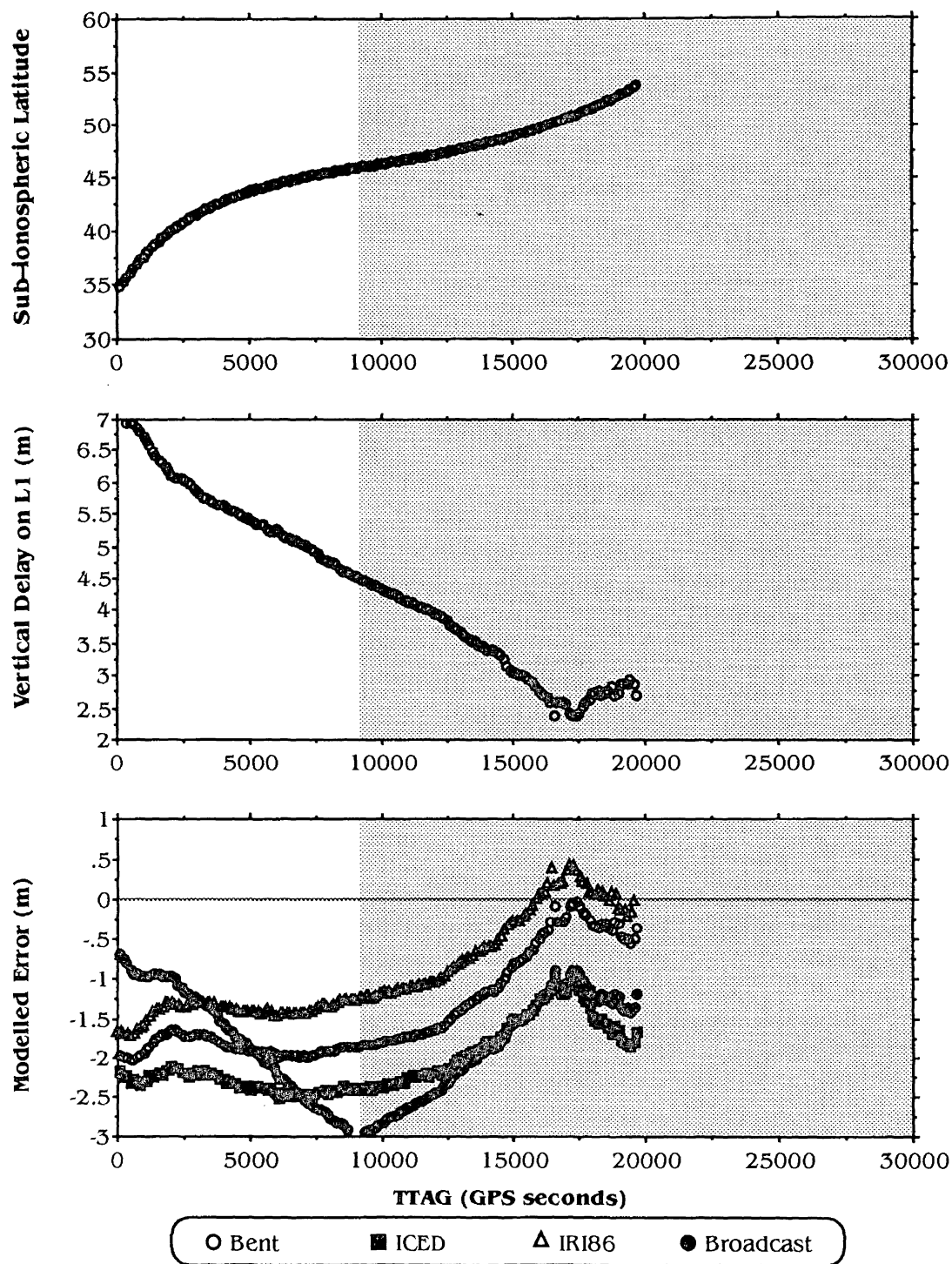
**Algonquin PRN# 03**  
**- Observed Delay and Modelled Errors**



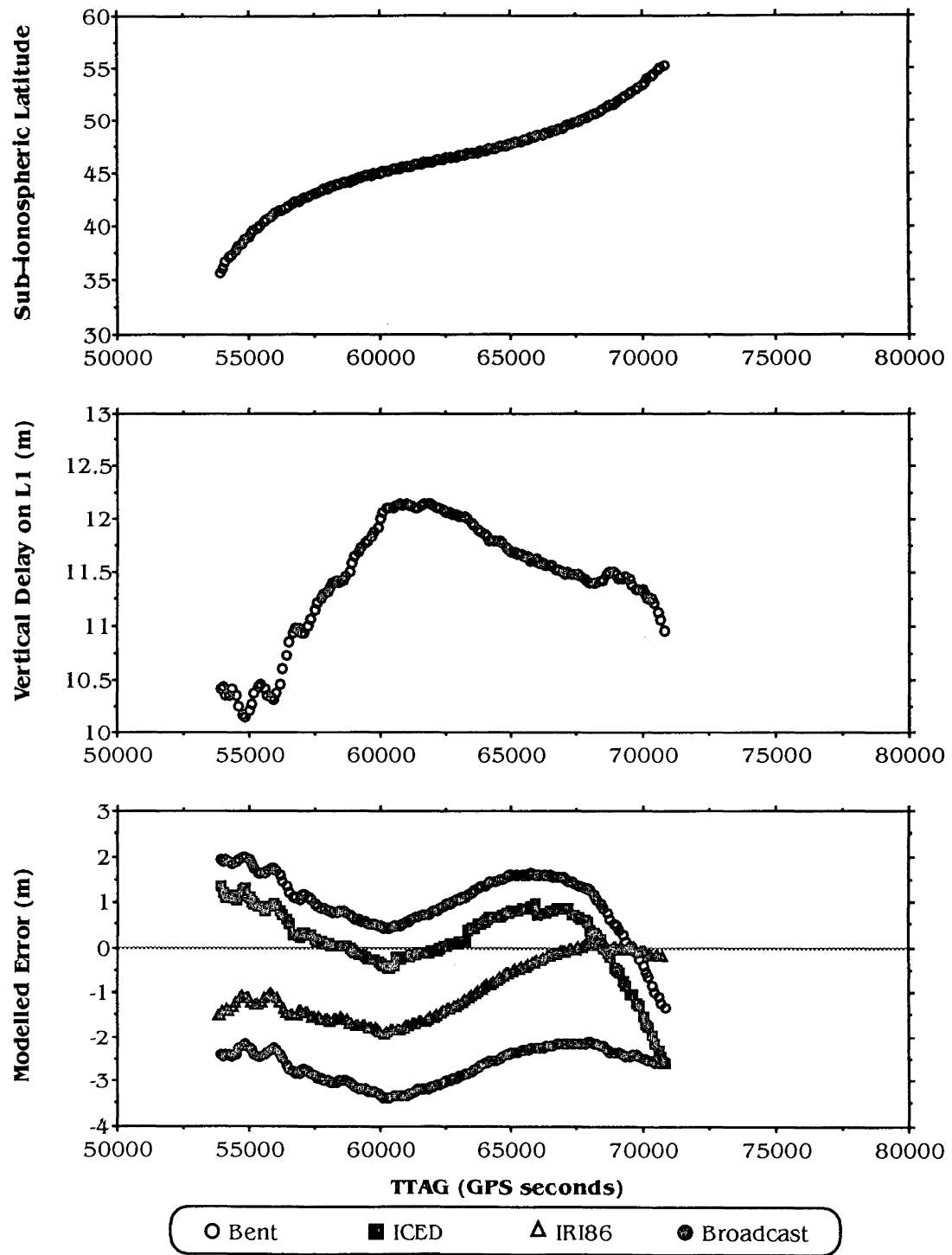
**Algonquin PRN# 06**  
**- Observed Delay and Modelled Errors**



**Algonquin PRN# 11**  
**- Observed Delay and Modelled Errors**

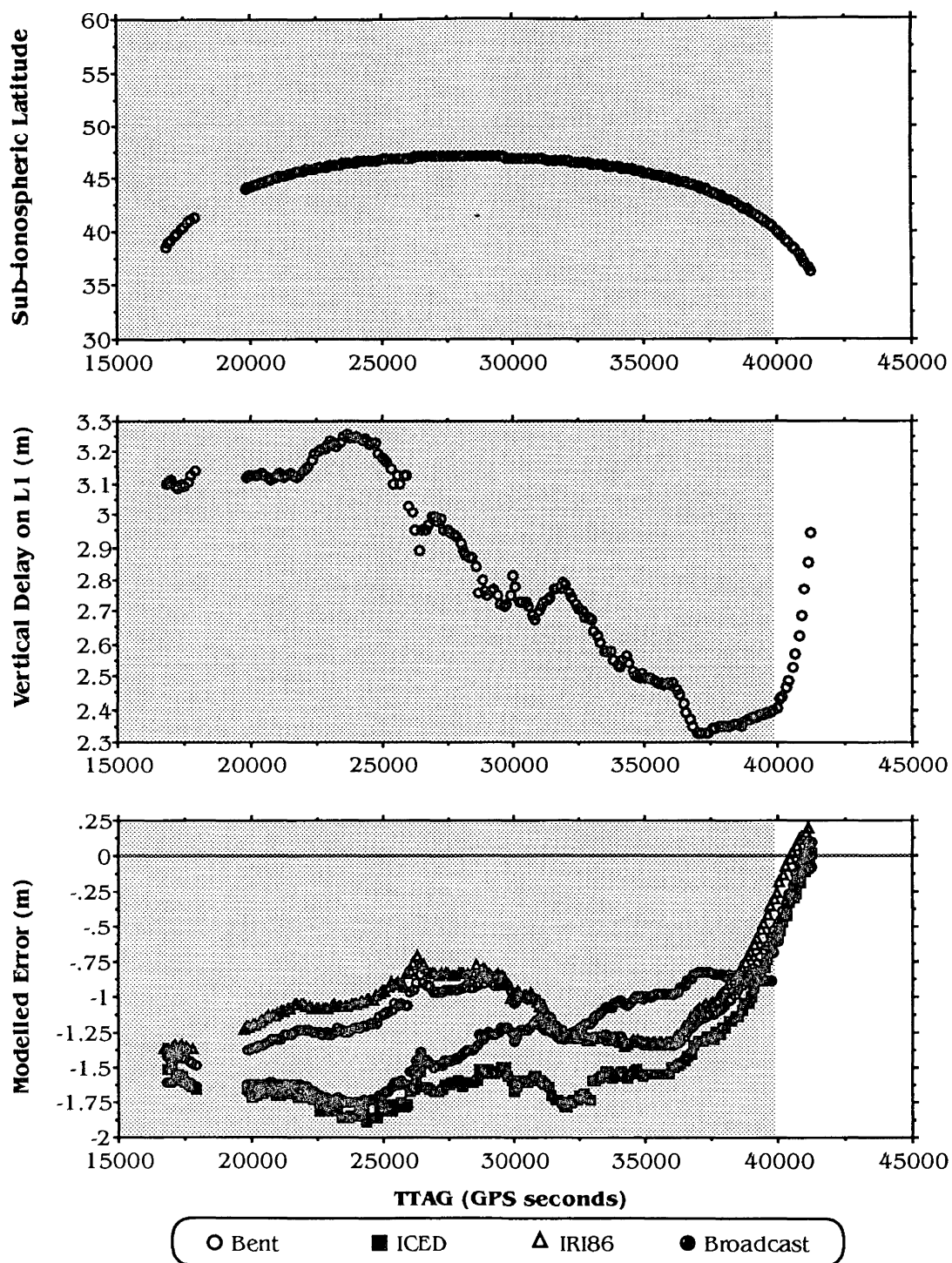


# **Algonquin PRN# 12** **– Observed Delay and Modelled Errors**

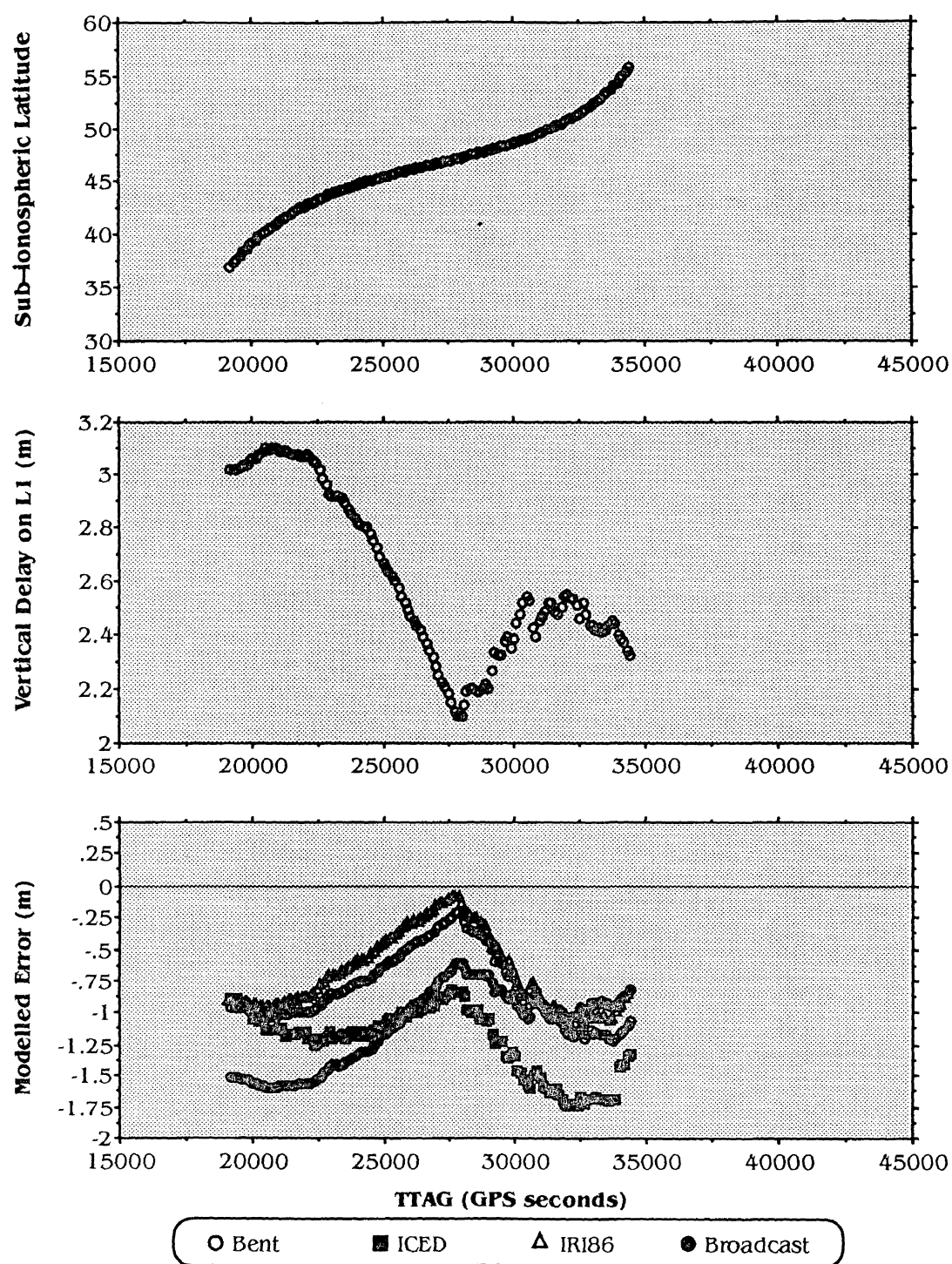




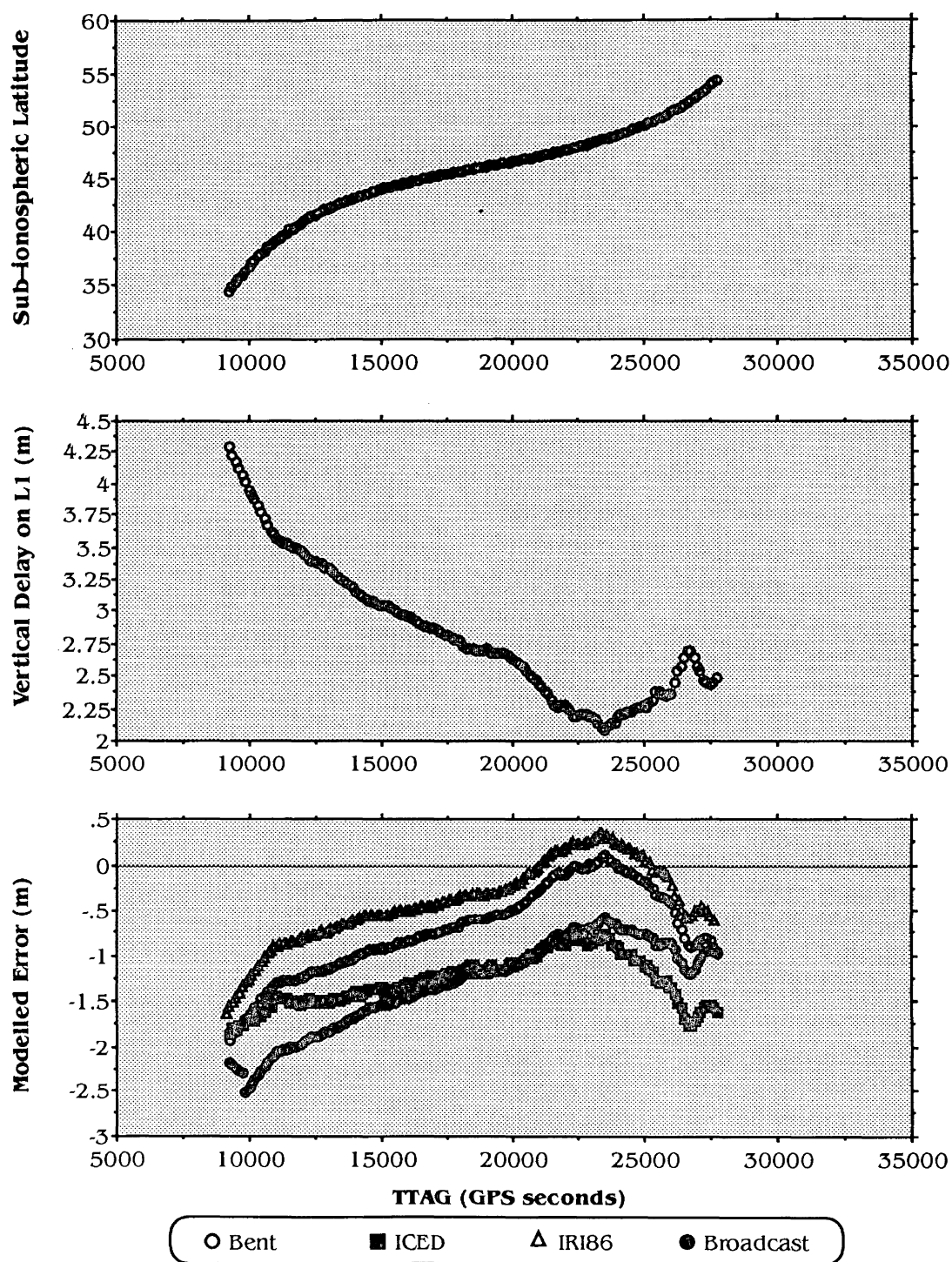
### Algonquin PRN# 13 – Observed Delay and Modelled Errors



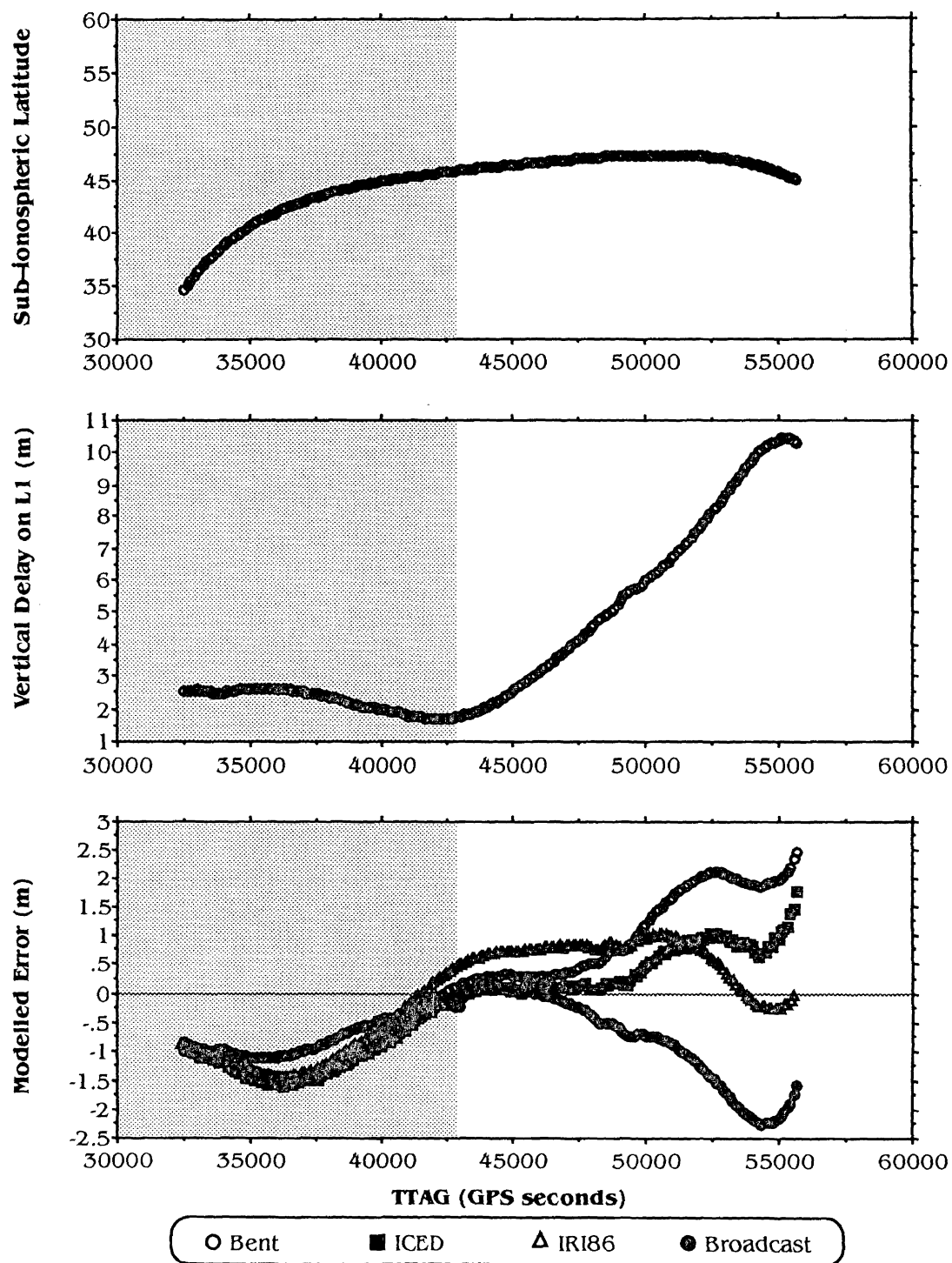
**Algonquin PRN# 14**  
**- Observed Delay and Modelled Errors**



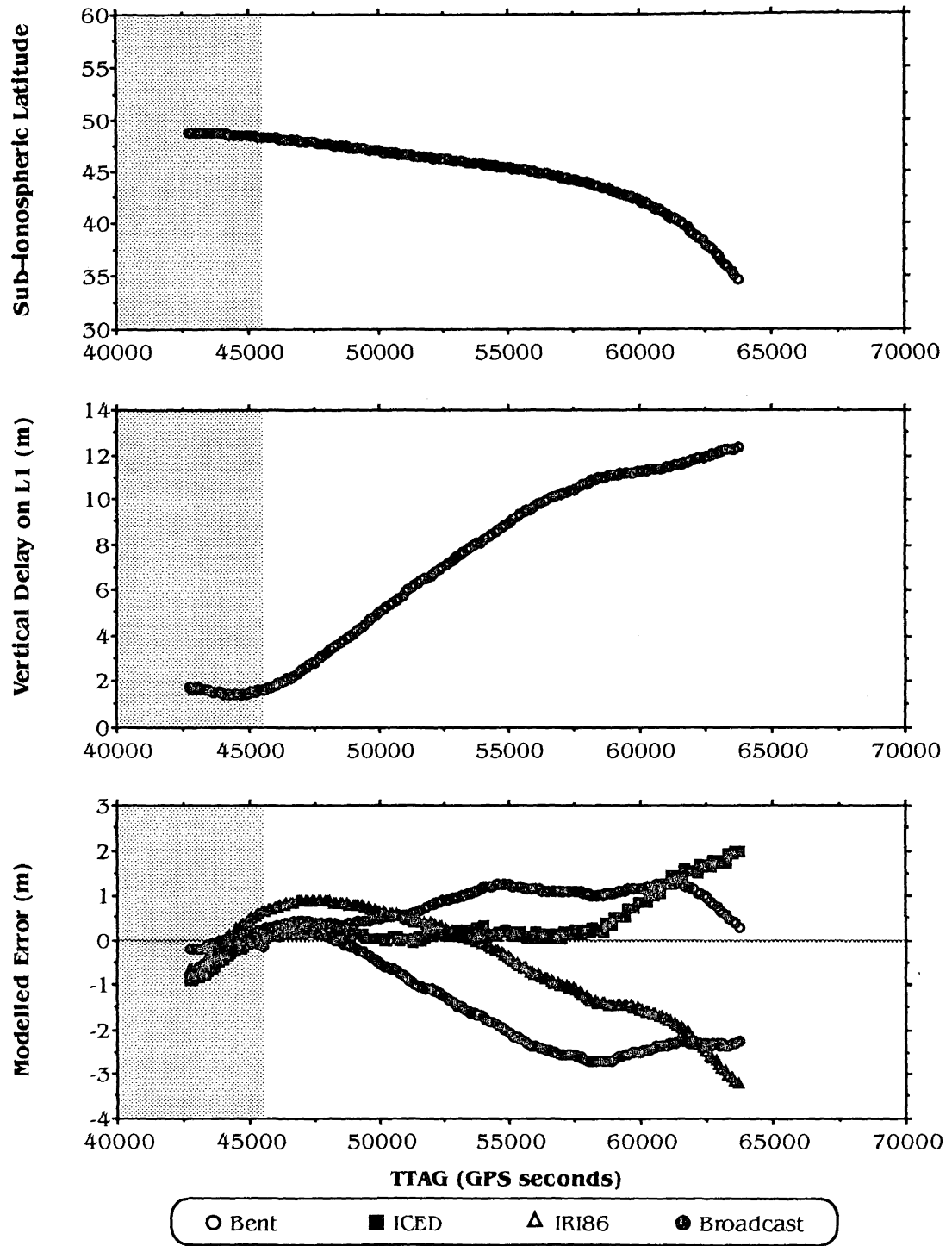
### Algonquin PRN# 15 – Observed Delay and Modelled Errors



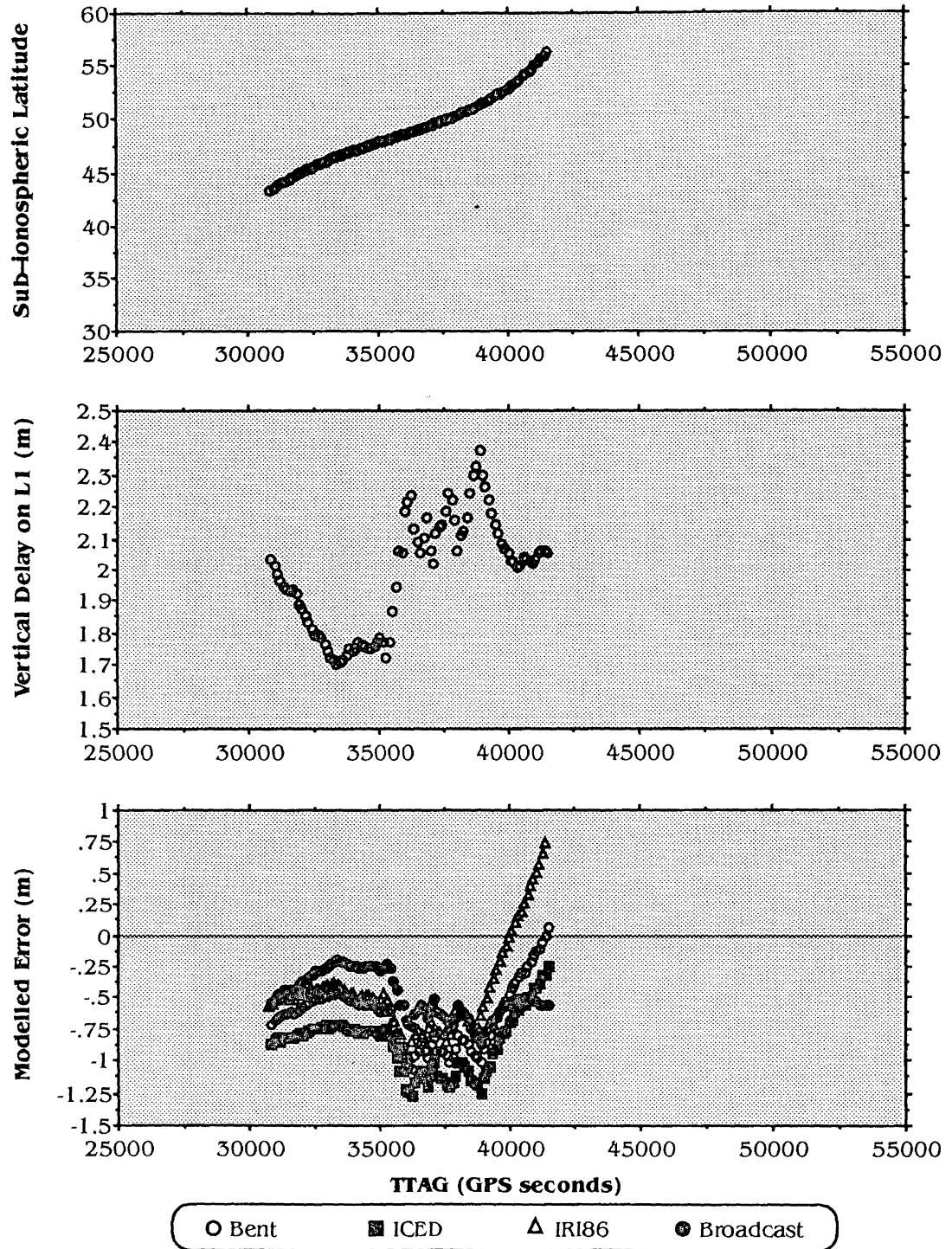
**Algonquin PRN# 16**  
**– Observed Delay and Modelled Errors**



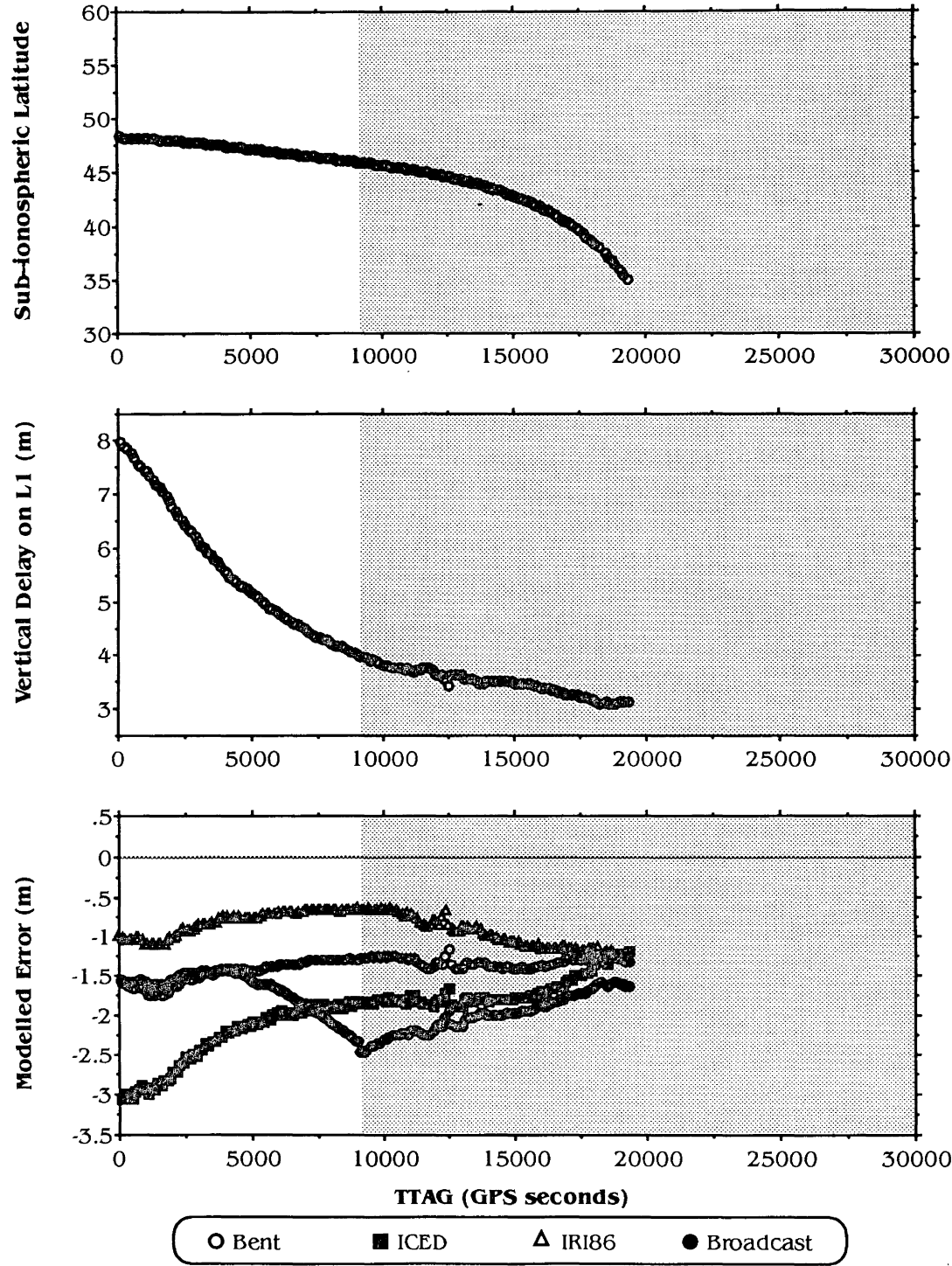
**Algonquin PRN# 17**  
**– Observed Delay and Modelled Errors**



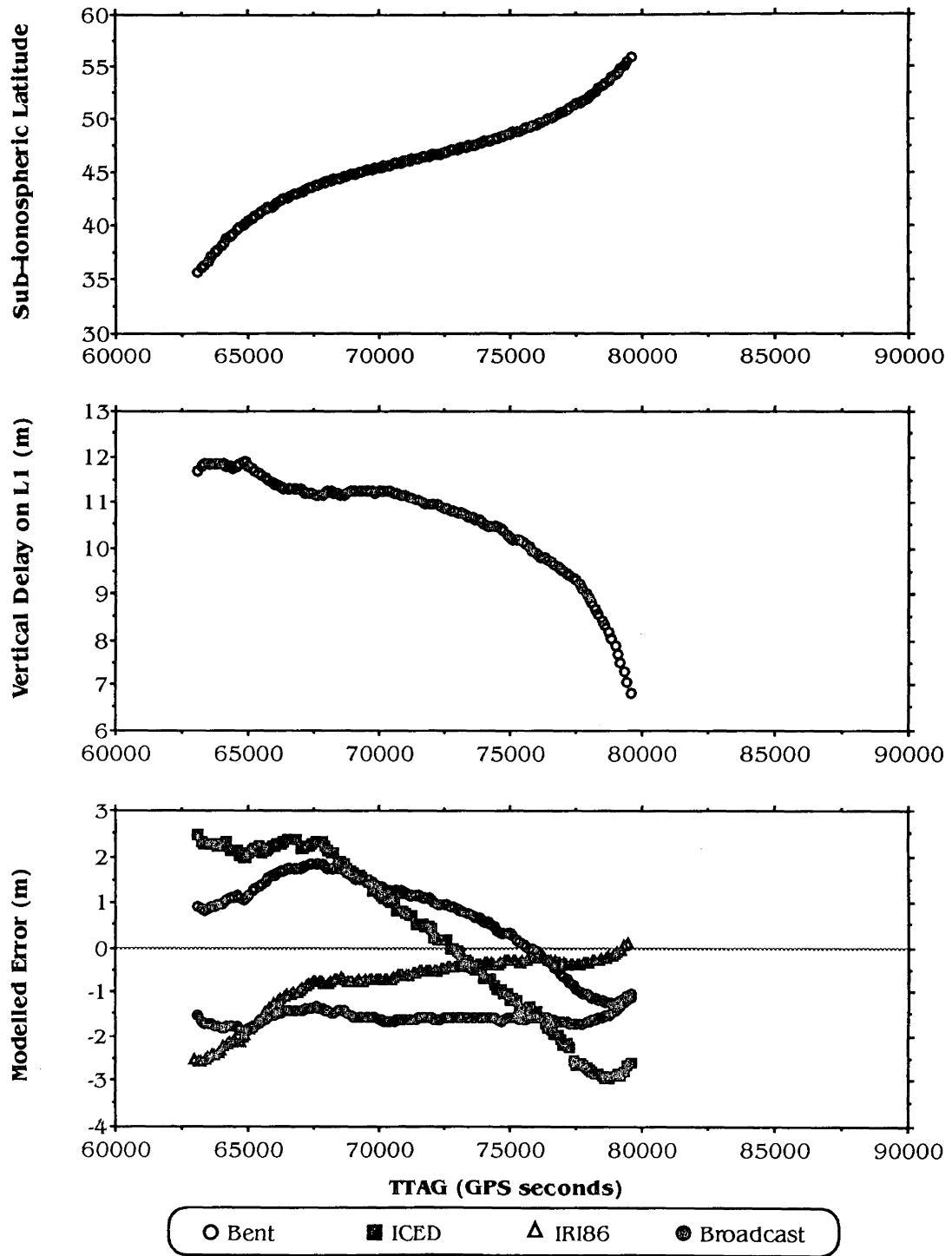
**Algonquin PRN# 18**  
**– Observed Delay and Modelled Errors**



# **Algonquin PRN# 19** **– Observed Delay and Modelled Errors**

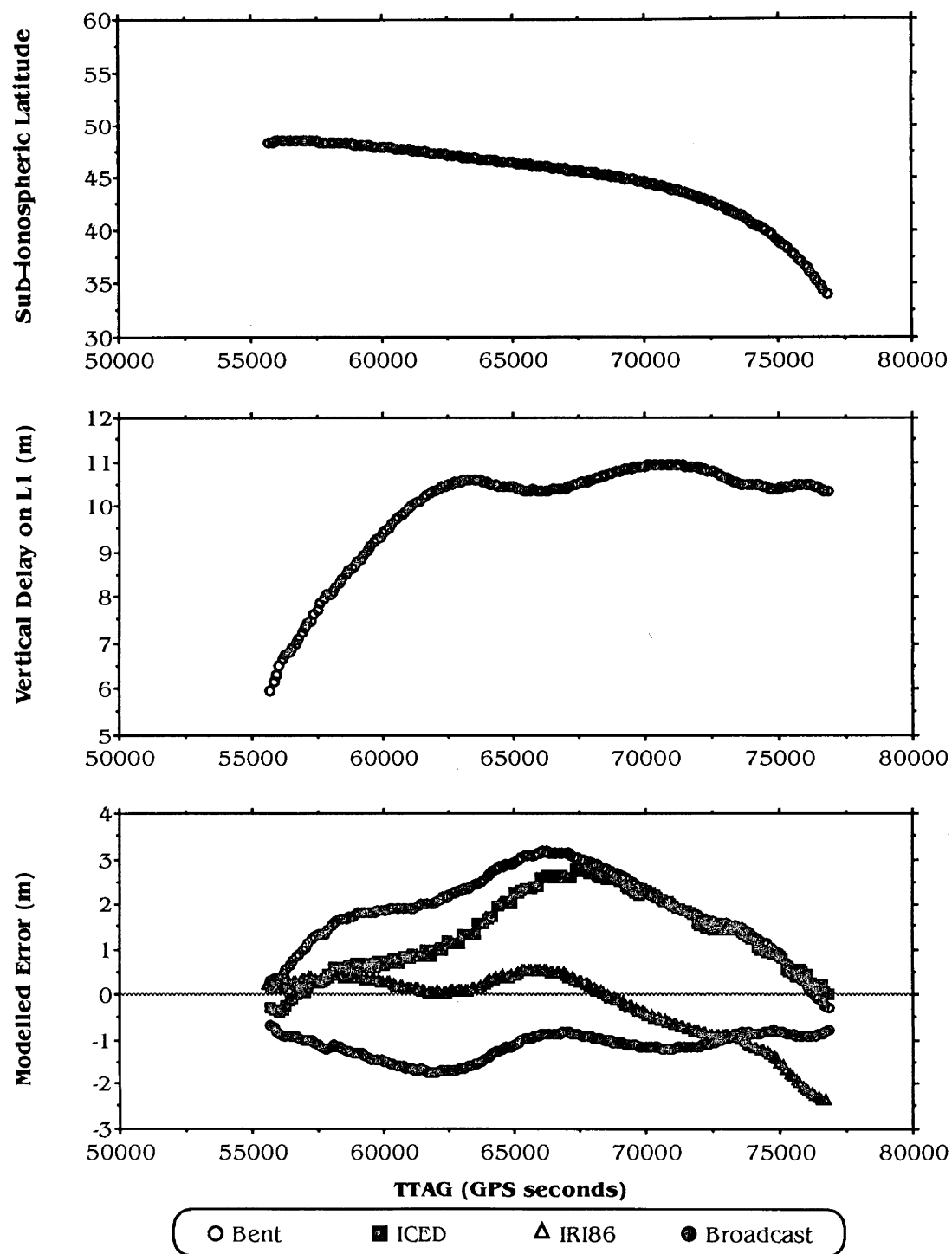


**Algonquin PRN# 20**  
**– Observed Delay and Modelled Errors**

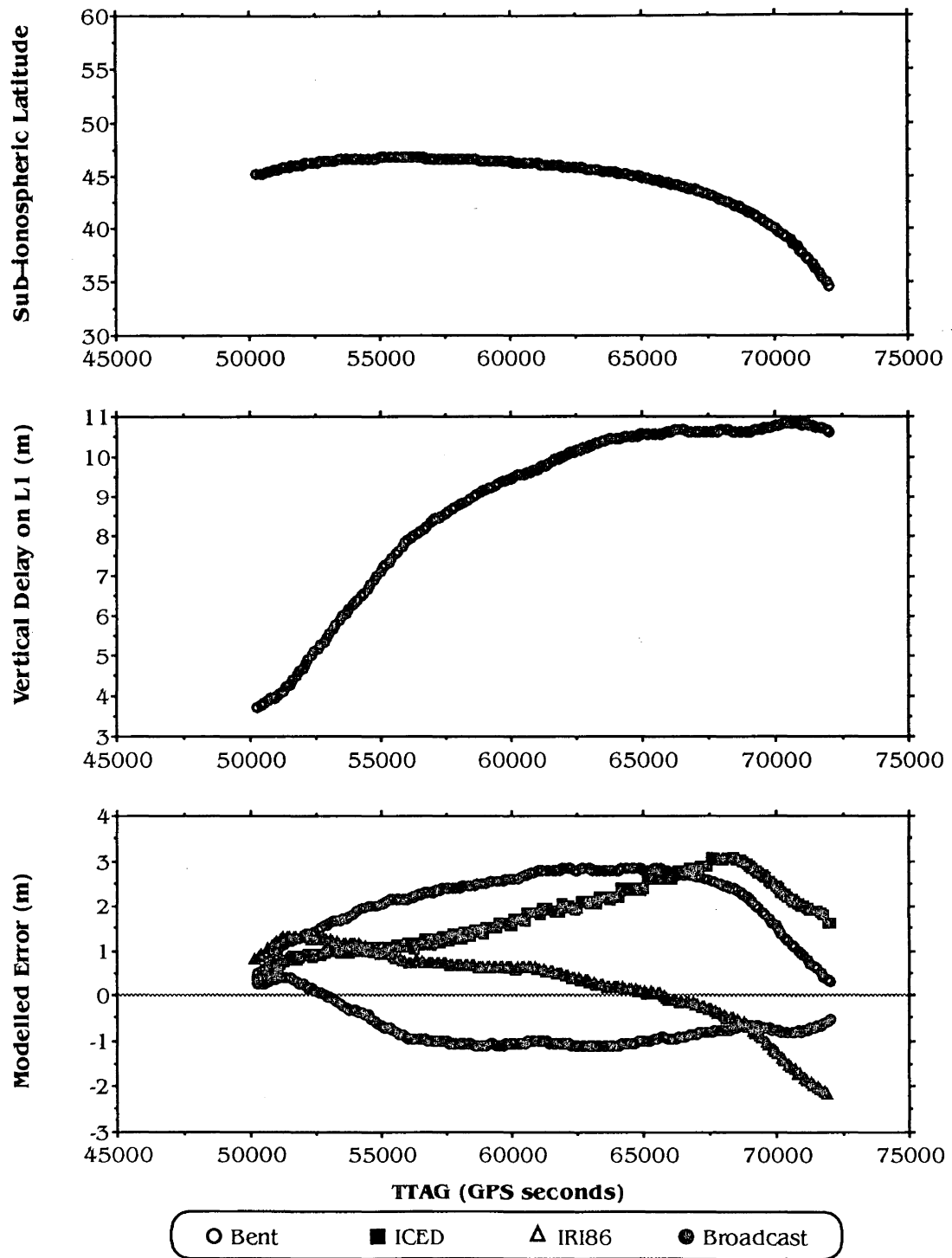




**Algonquin PRN# 21**  
**– Observed Delay and Modelled Errors**



**Algonquin PRN# 23**  
**– Observed Delay and Modelled Errors**

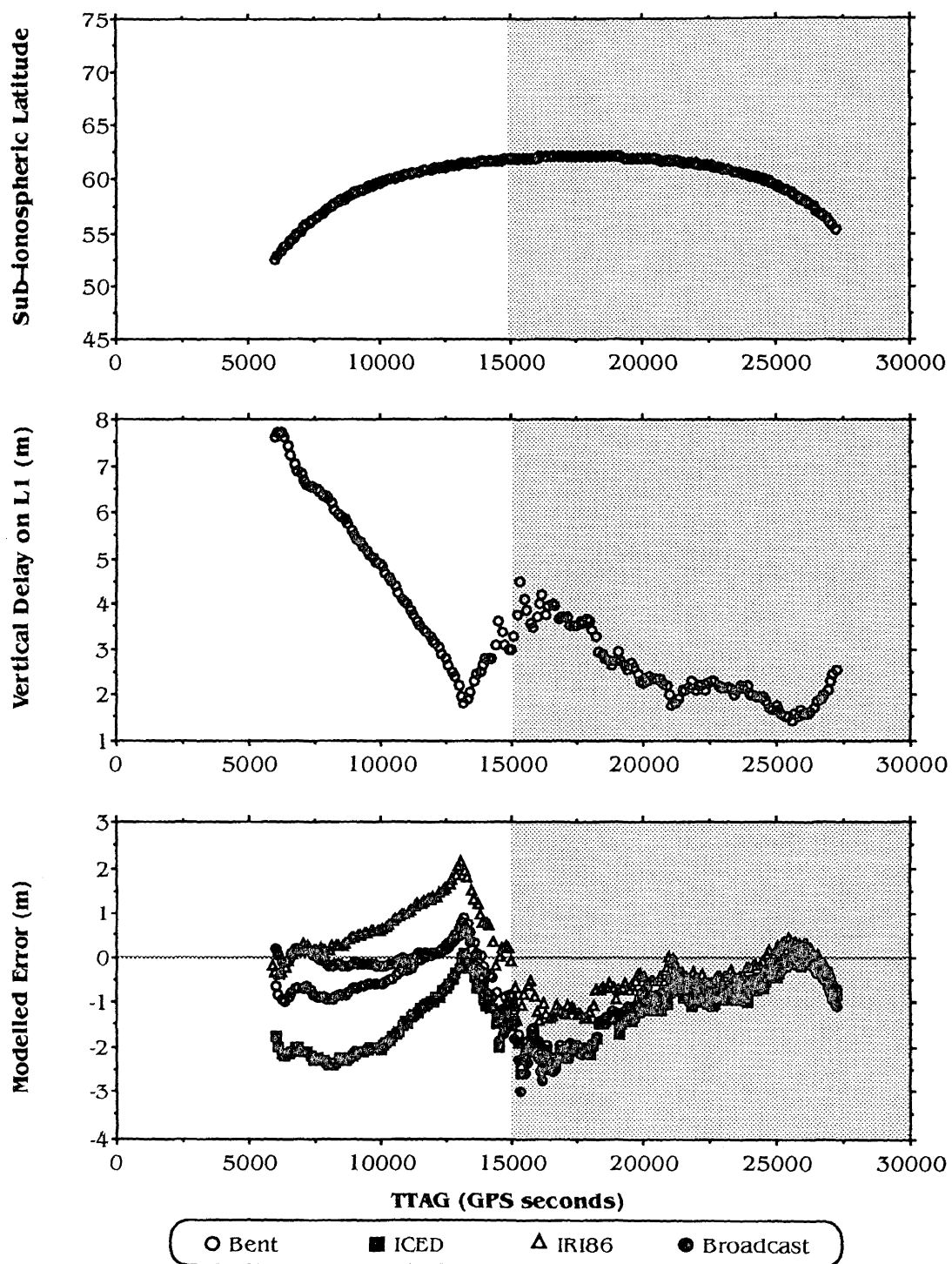


## ***APPENDIX V***

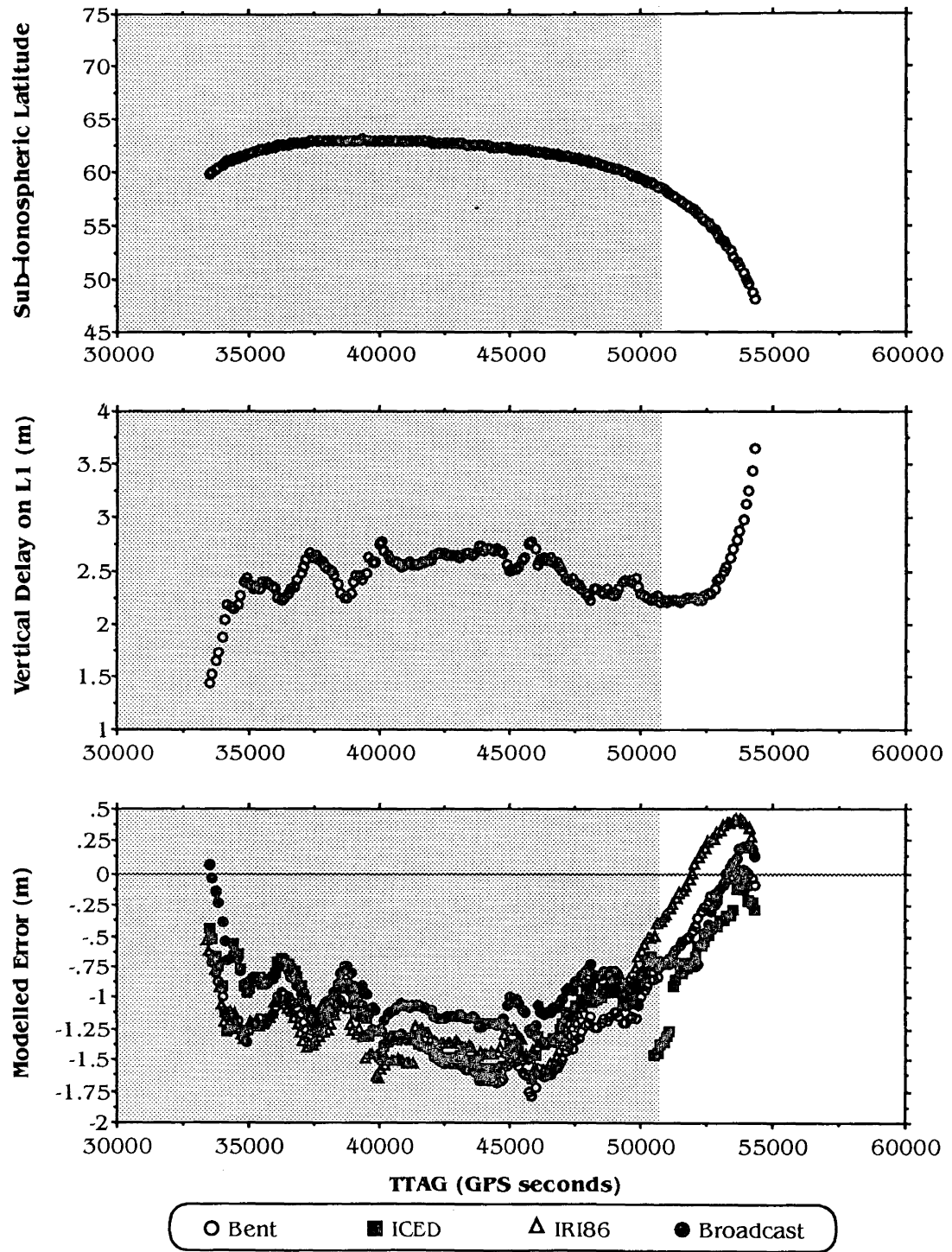
**Yellowknife** Plots Showing the Latitude of the Sub-Ionospheric Point, the Vertical Ionospheric Delay on L1, and the Modelled Errors from Each of Four Ionospheric Models.

**IMPORTANT NOTES** : The scales of the Y-axes in the plots of the L1 ionospheric delay and of the modelled errors are not equal. Also note that the apparent discontinuities which are occasionally evident in ICED's modelled errors are caused by sudden changes in the *Kp* index which is used by ICED.

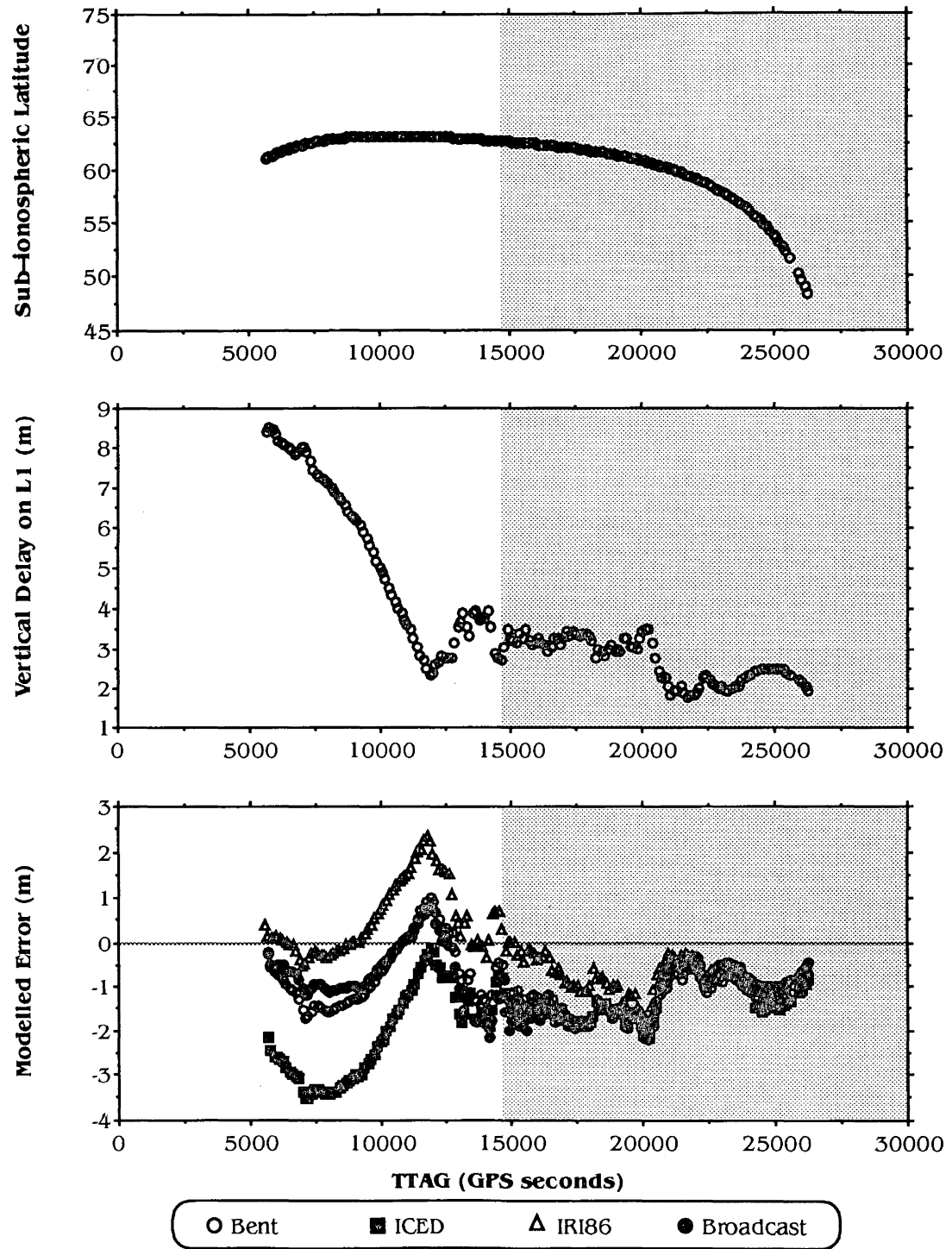
**Yellowknife PRN#02**  
**– Observed Delay and Modelled Errors**



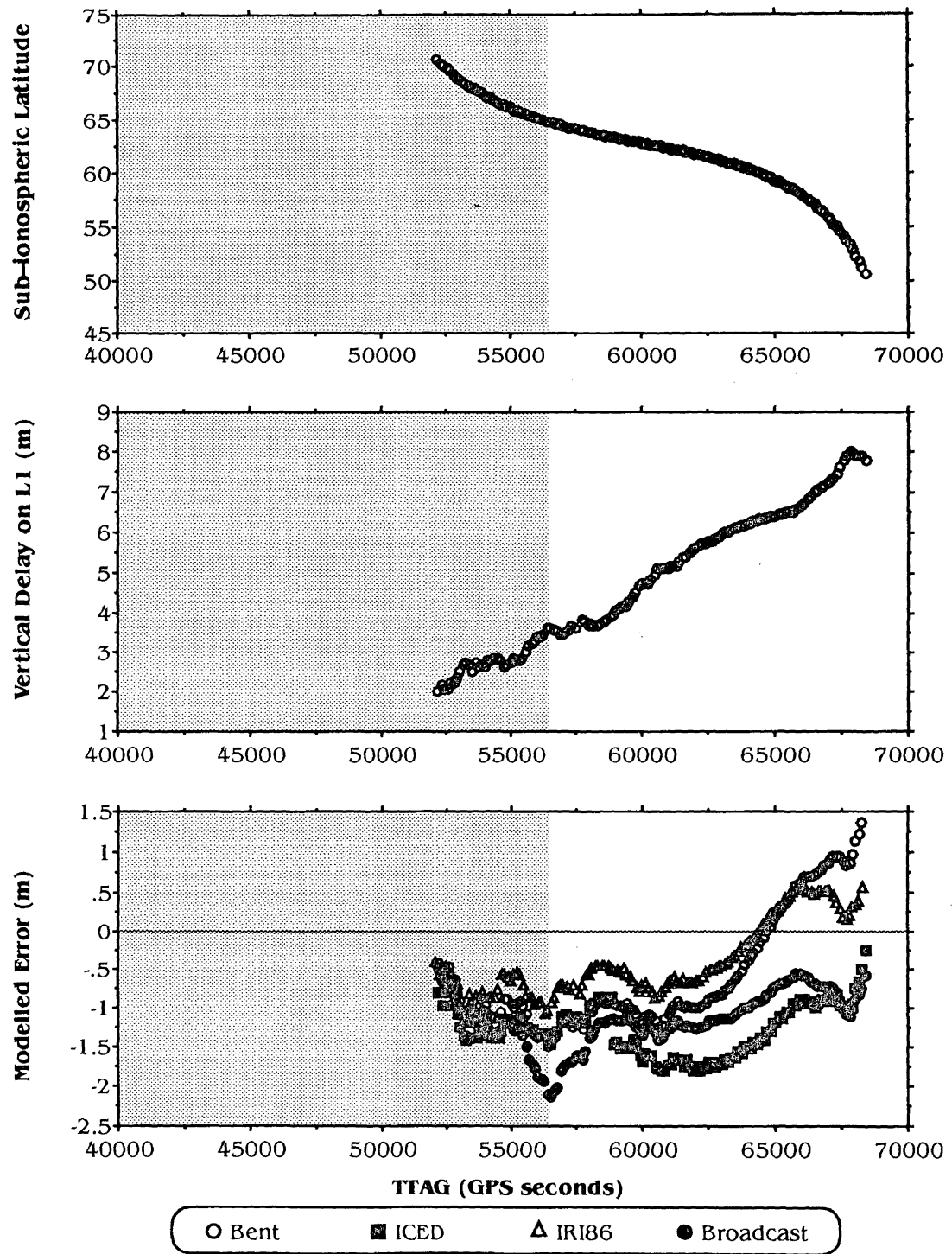
**Yellowknife PRN#03**  
**– Observed Delay and Modelled Errors**



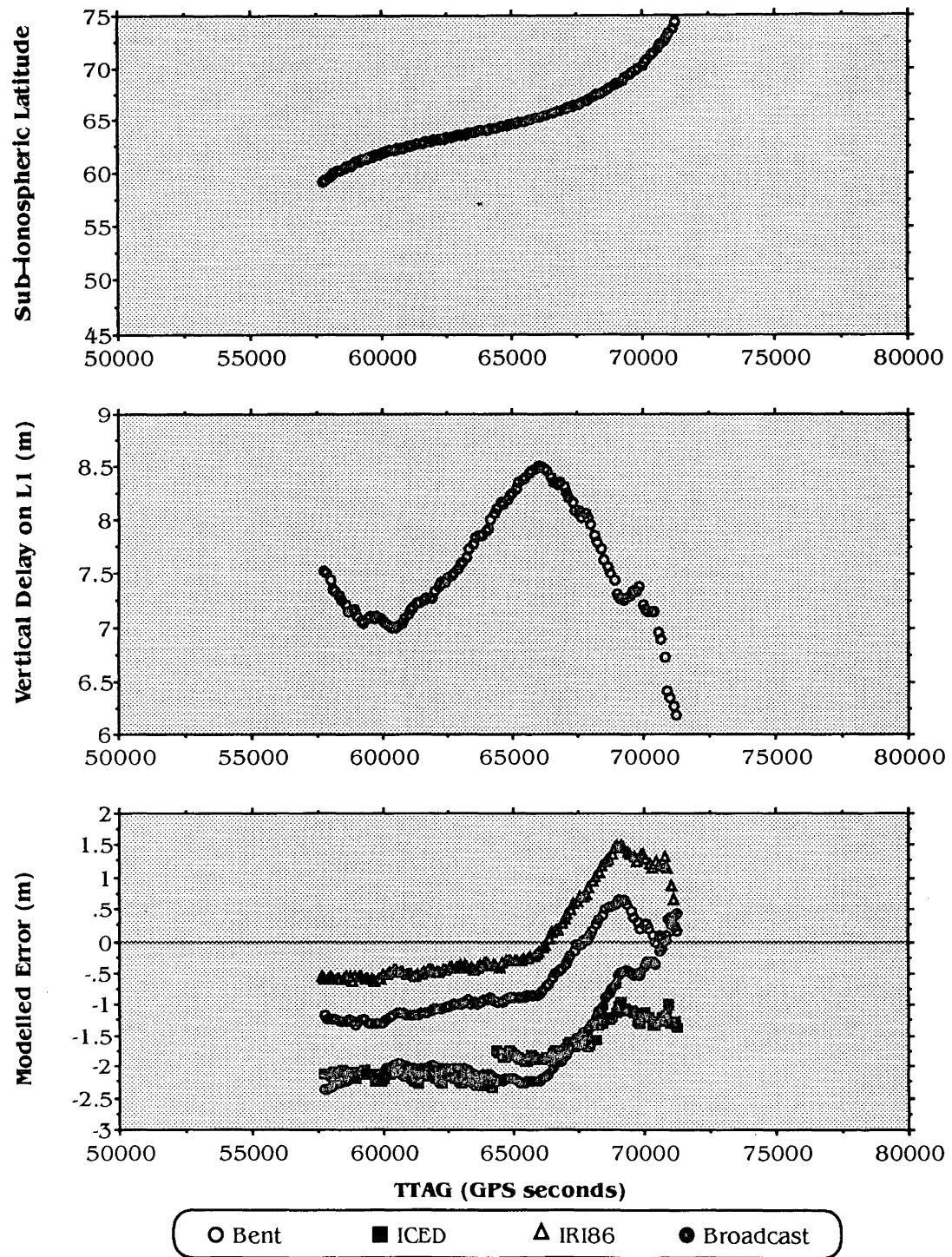
**Yellowknife PRN#06**  
**– Observed Delay and Modelled Errors**



**Yellowknife PRN# 11**  
**– Observed Delay and Modelled Errors**

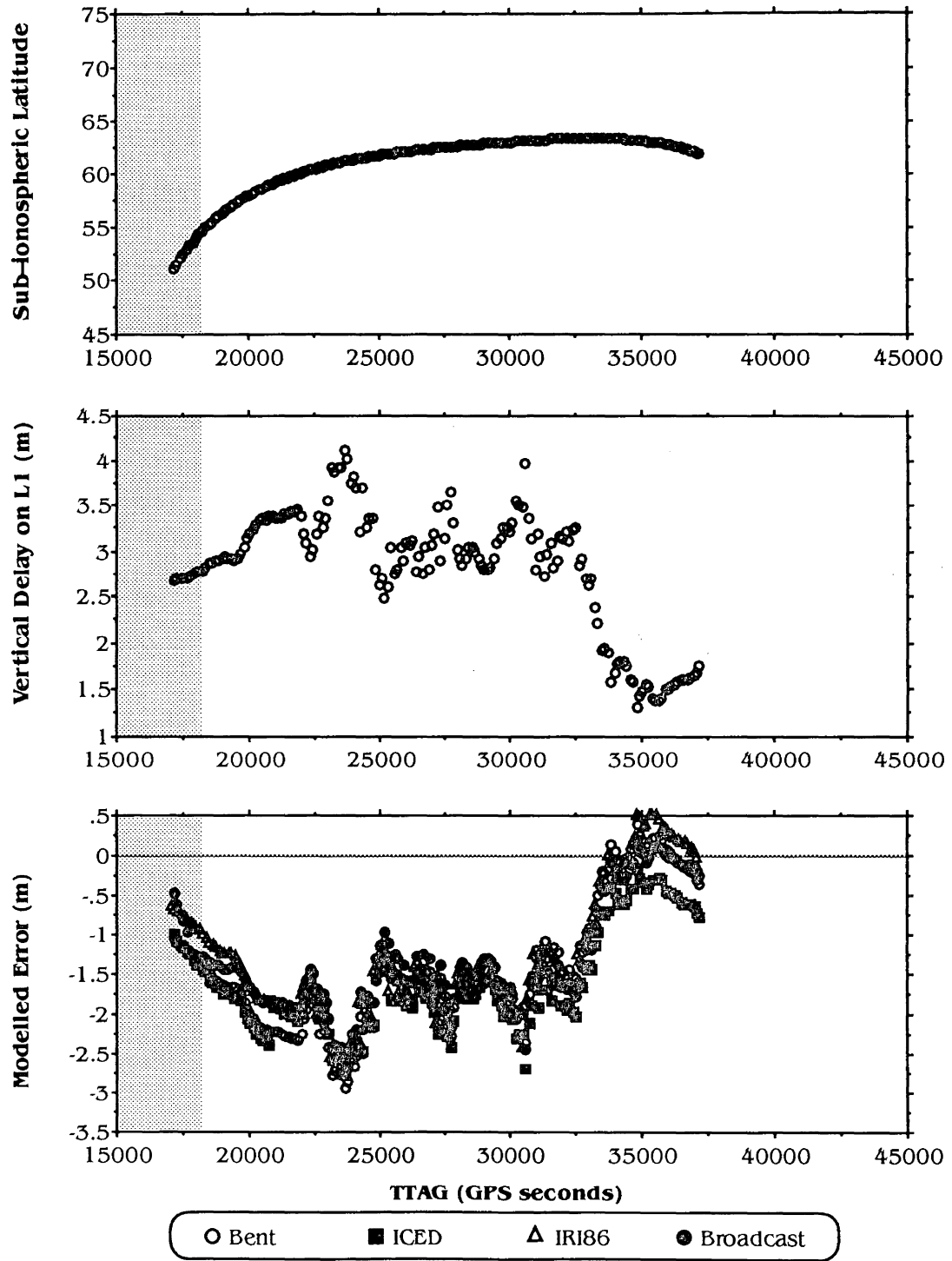


**Yellowknife PRN# 12**  
**– Observed Delay and Modelled Errors**

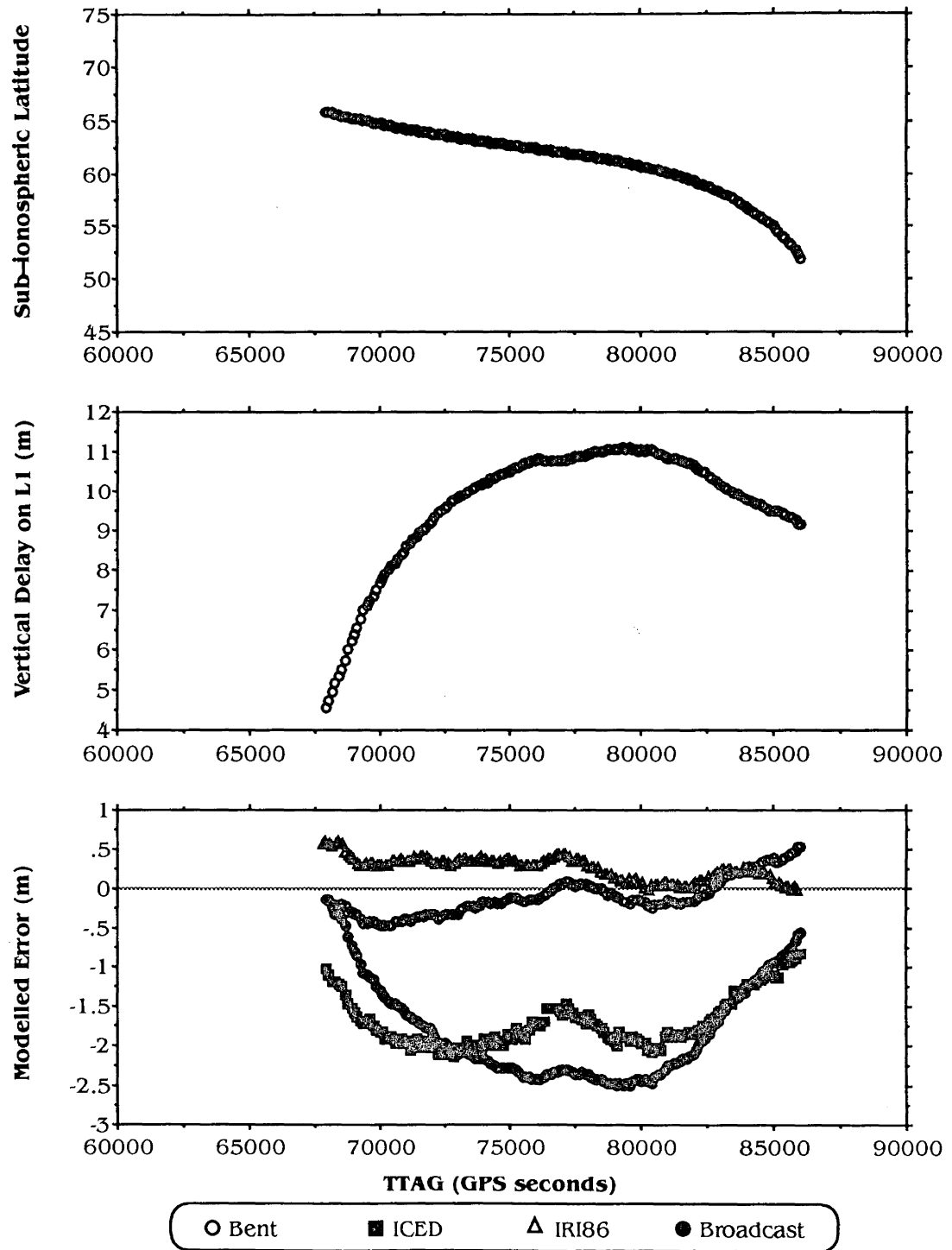




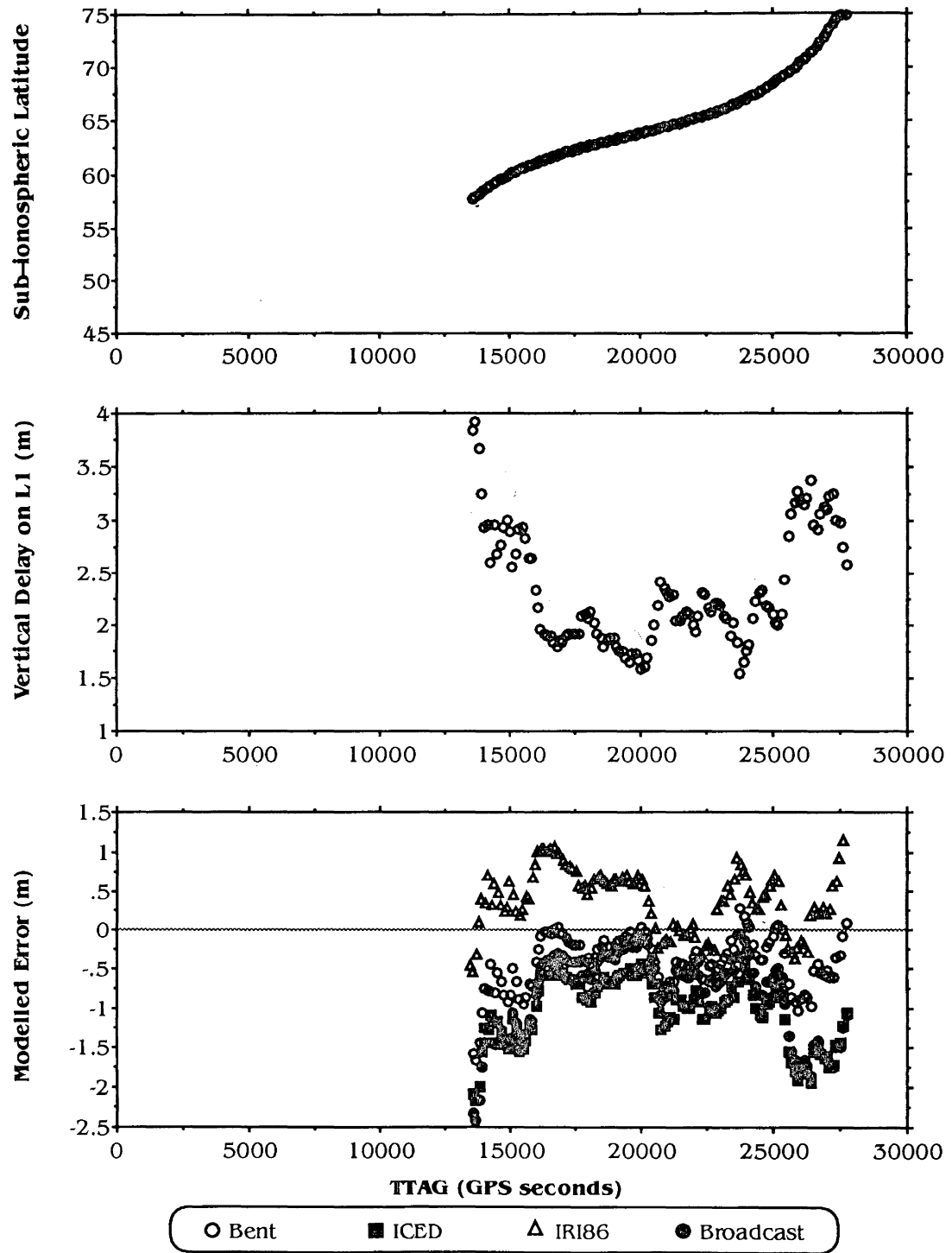
# **Yellowknife PRN# 13** **– Observed Delay and Modelled Errors**



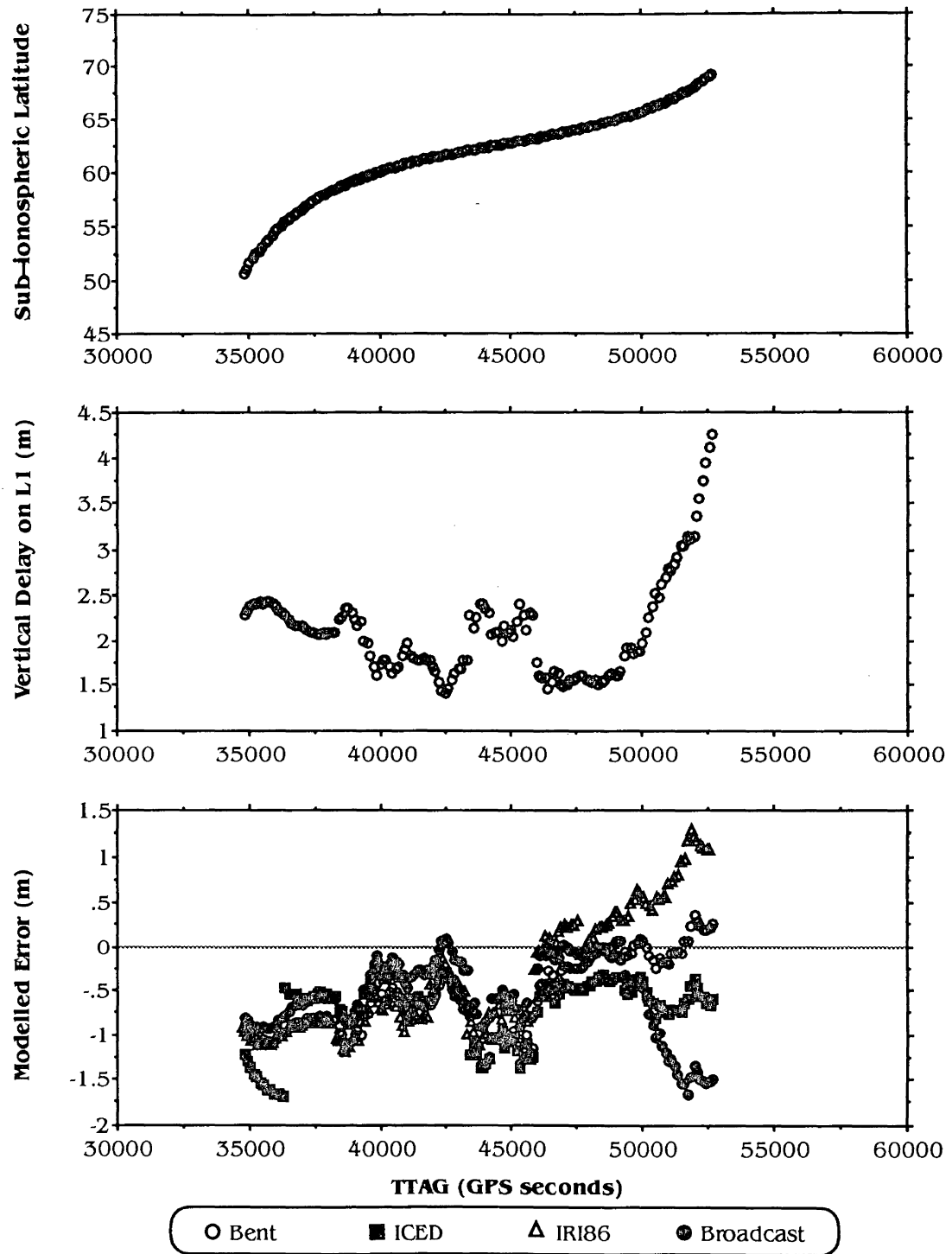
# **Yellowknife PRN#14** **- Observed Delay and Modelled Errors**



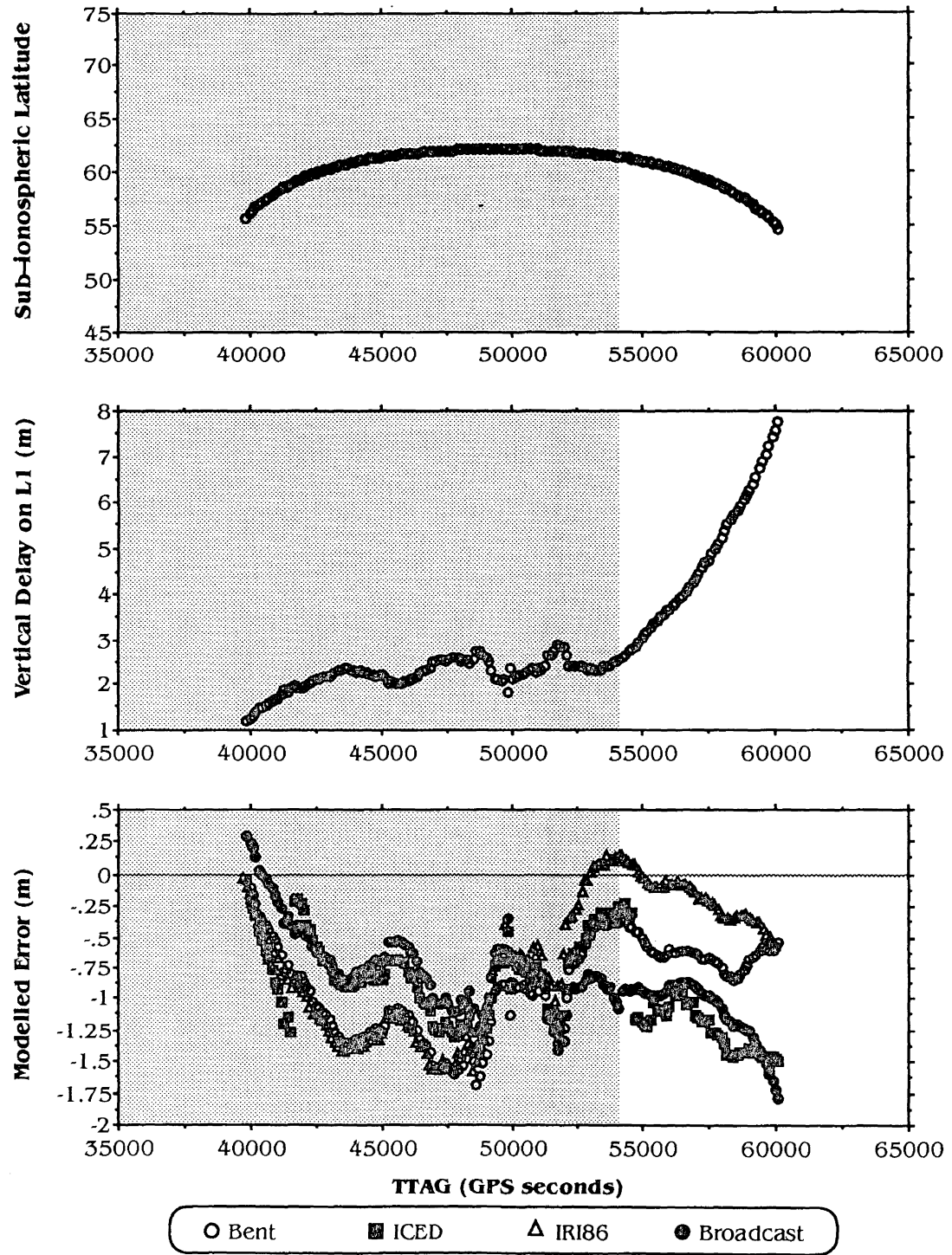
# **Yellowknife PRN# 15** **- Observed Delay and Modelled Errors**



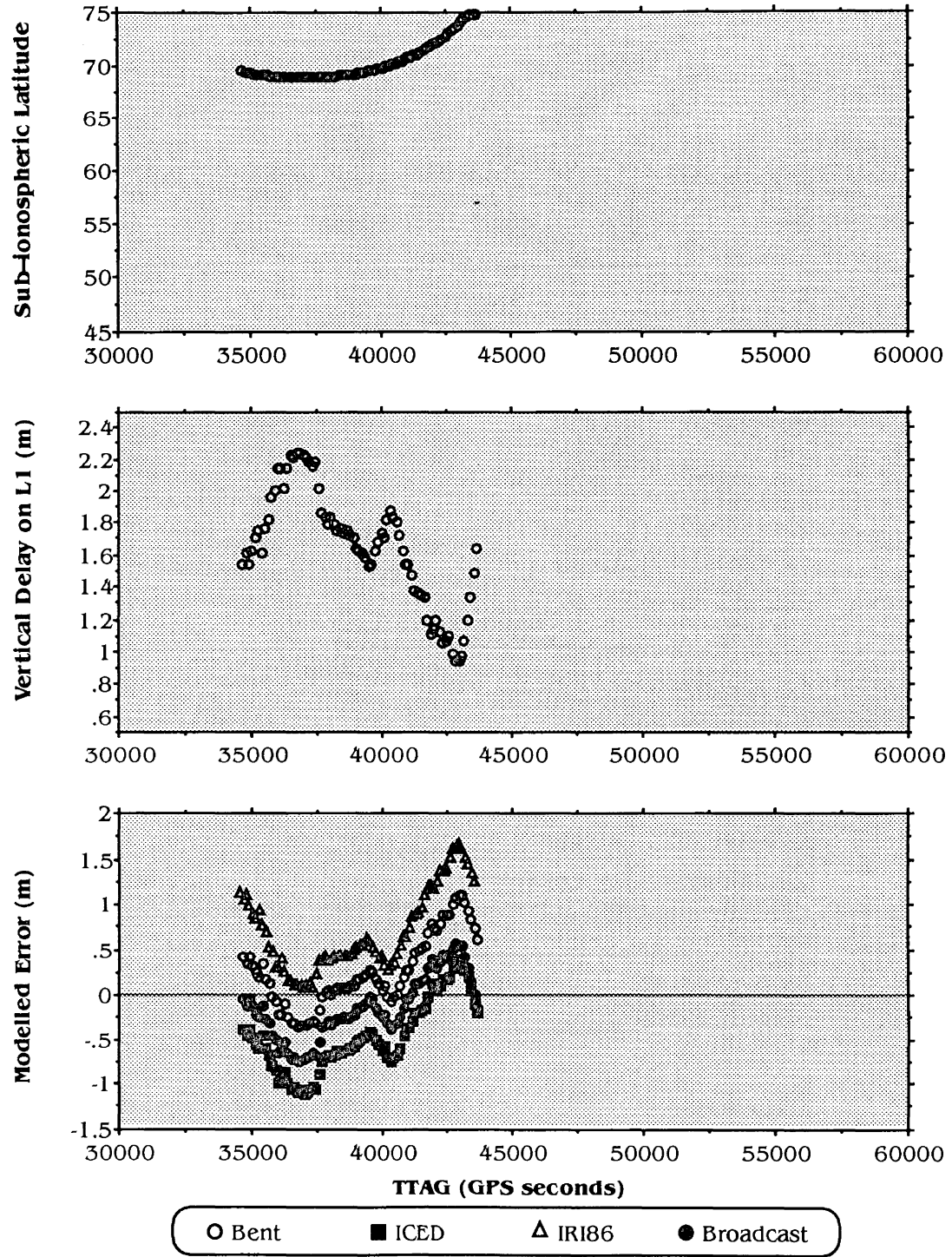
**Yellowknife PRN# 16**  
**– Observed Delay and Modelled Errors**



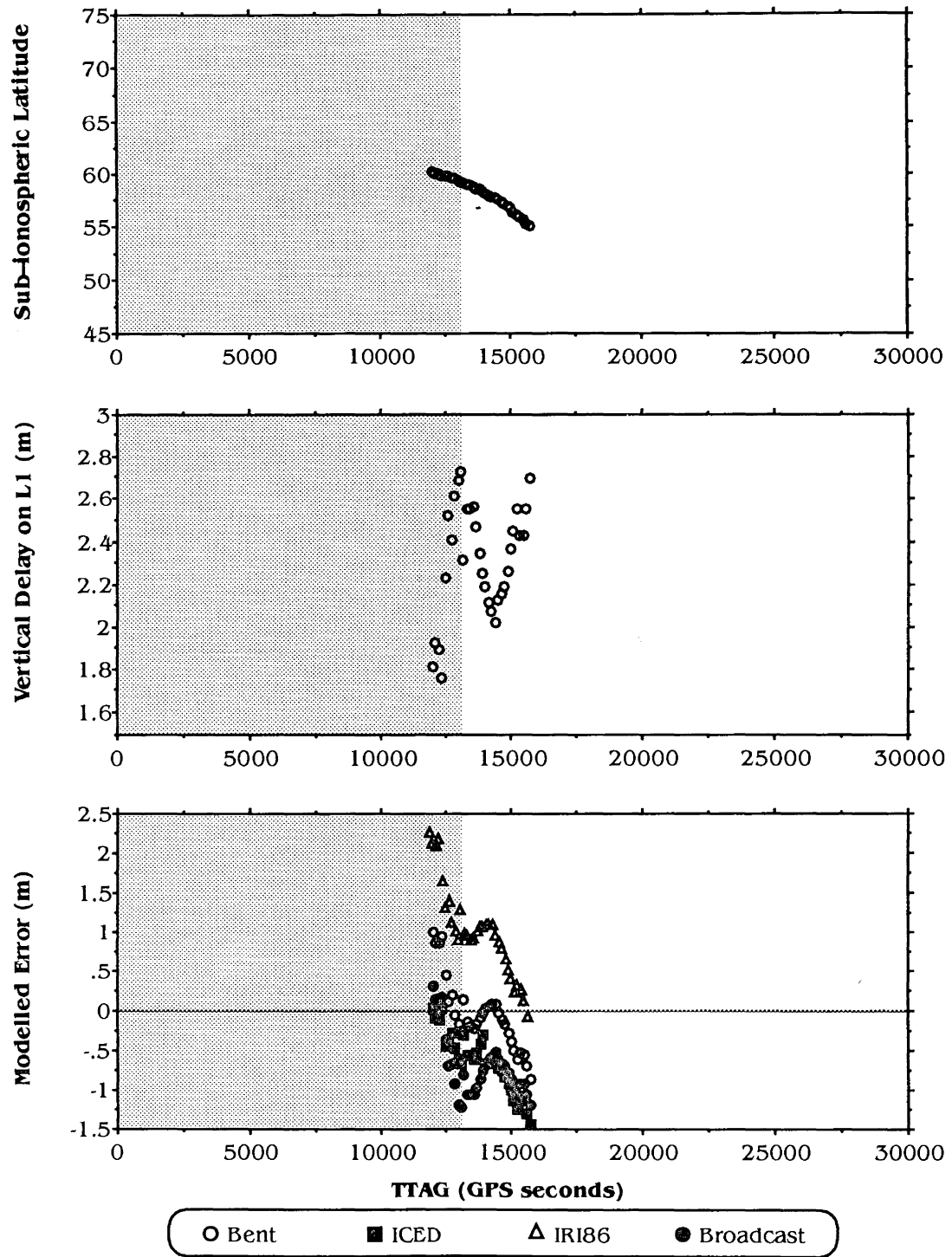
# **Yellowknife PRN# 17** **- Observed Delay and Modelled Errors**



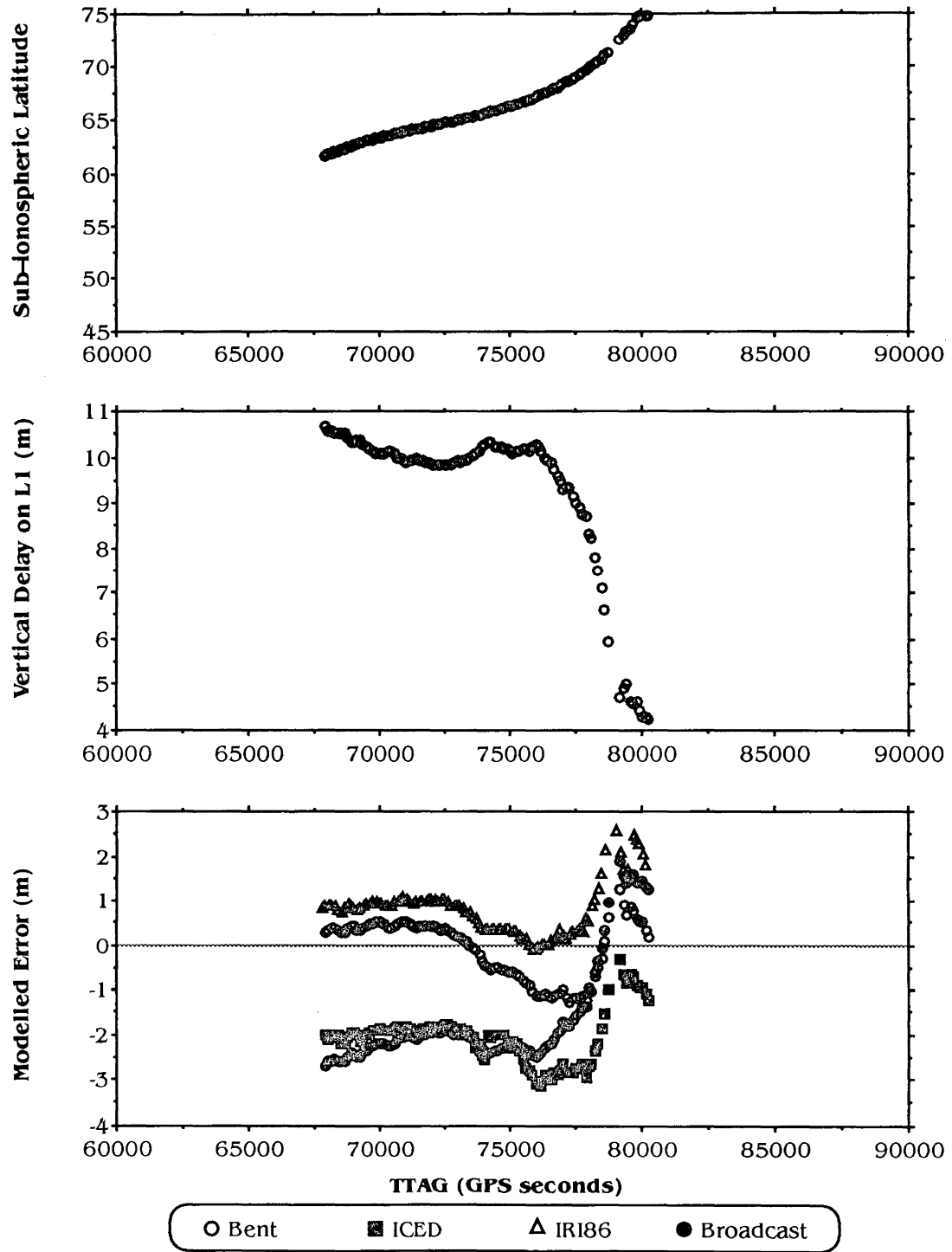
# **Yellowknife PRN# 18** **– Observed Delay and Modelled Errors**



**Yellowknife PRN# 19**  
**– Observed Delay and Modelled Errors**

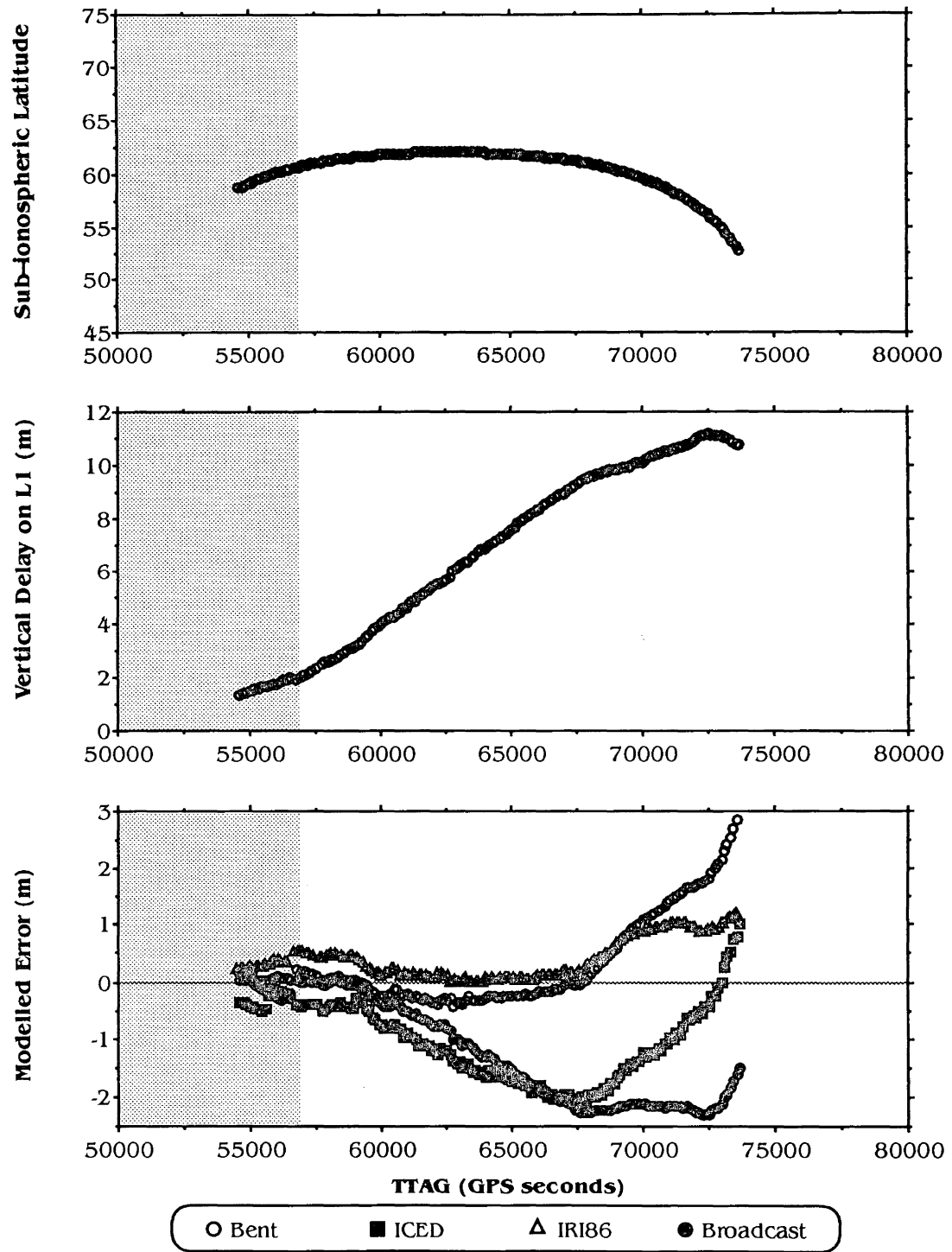


**Yellowknife PRN#20**  
**– Observed Delay and Modelled Errors**

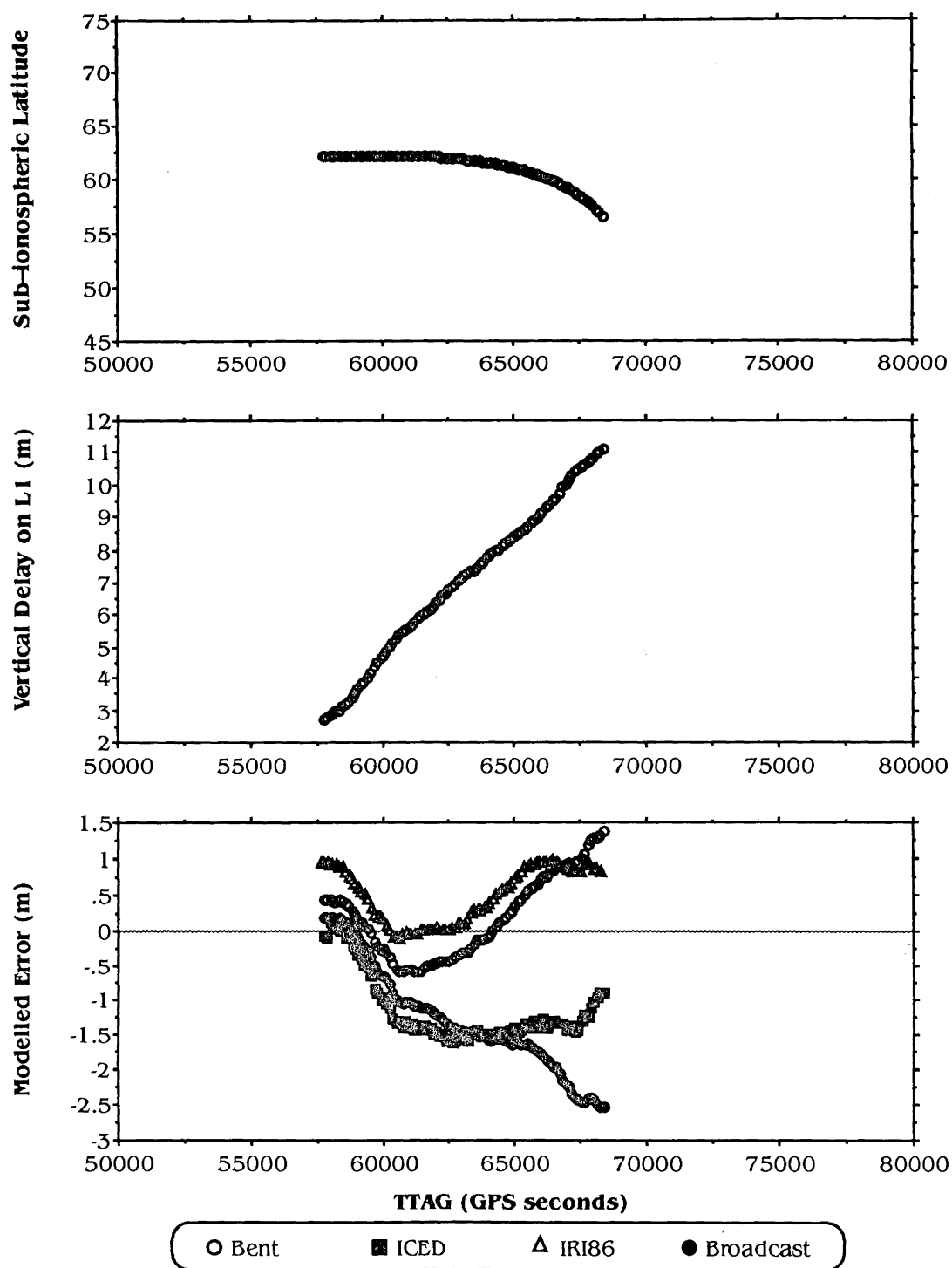




**Yellowknife PRN# 21**  
**- Observed Delay and Modelled Errors**



**Yellowknife PRN#23**  
**- Observed Delay and Modelled Errors**



## ***APPENDIX VI***

---

**Daily** Sets of **Daytime and Night-Time r.m.s. Statistics** Similar to the Whole Week Summaries Presented in **Tables 6.4** and **6.5**. There are Seven Sets of Daily Statistics for Algonquin and Seven Sets for Yellowknife.

ALGONQUIN – DAILY SUMMARY FOR FEBRUARY 3rd 1991								
PRN	DAYTIME				NIGHT-TIME			
	BENT	IRI86	ICED	B'cast	BENT	IRI86	ICED	B'cast
<b>2</b>	.78 (21)	.16 (4)	1.43 (38)	1.07 (30)	1.04 (54)	.83 (27)	1.48 (48)	1.57 (51)
<b>3</b>	1.01 (13)	.58 (11)	1.58 (22)	1.06 (15)	.88 (43)	.78 (37)	1.16 (56)	.54 (26)
<b>6</b>	1.52 (20)	.64 (8)	.74 (12)	1.74 (21)	1.08 (34)	.86 (28)	1.53 (49)	1.63 (52)
<b>9</b>	N/A	N/A	N/A	N/A	N/A	N/A	N/A	N/A
<b>11</b>	1.57 (25)	.99 (17)	1.70 (30)	2.08 (30)	1.22 (31)	.77 (19)	1.88 (54)	2.03 (55)
<b>12</b>	1.21 (11)	1.20 (10)	.80 (7)	2.69 (23)	.71 (26)	.62 (23)	1.36 (51)	1.18 (44)
<b>13</b>	.32 (13)	.19 (8)	.38 (15)	.36 (15)	1.17 (42)	1.09 (40)	1.60 (56)	1.36 (47)
<b>14</b>	1.33 (14)	.64 (7)	.94 (12)	1.11 (11)	.86 (32)	.75 (28)	1.26 (49)	1.16 (43)
<b>15</b>	3.20 (33)	.92 (12)	2.09 (23)	1.38 (18)	.82 (26)	.57 (18)	1.29 (46)	1.38 (46)
<b>16</b>	1.35 (18)	.71 (19)	.63 (8)	1.13 (13)	1.04 (43)	1.05 (43)	1.16 (49)	.82 (34)
<b>17</b>	.89 (11)	1.26 (18)	.72 (8)	1.82 (21)	.37 (22)	.70 (30)	.53 (27)	.90 (31)
<b>18</b>	1.41 (26)	1.06 (20)	2.06 (36)	1.39 (26)	.69 (34)	.58 (29)	.90 (44)	.52 (25)
<b>19</b>	1.36 (25)	.83 (14)	2.19 (39)	1.56 (31)	1.34 (39)	1.02 (30)	1.72 (49)	2.02 (57)
<b>20</b>	1.16 (11)	1.04 (9)	1.82 (19)	1.56 (15)	.81 (41)	.80 (40)	1.10 (54)	.56 (27)
<b>21</b>	2.08 (20)	.78 (8)	1.60 (15)	1.17 (12)	.33 (16)	.87 (41)	.13 (6)	.70 (32)
<b>23</b>	2.25 (25)	.89 (13)	1.93 (20)	.85 (9)	N/A	N/A	N/A	N/A

Daytime and Night-Time r.m.s. (m) Errors on L1 to Sixteen Satellites  
at Algonquin (the r.m.s. (%) errors are italicised and in parentheses)

ALGONQUIN – DAILY SUMMARY FOR FEBRUARY 4th 1991								
PRN	DAYTIME				NIGHT-TIME			
	BENT	IRI86	ICED	B'cast	BENT	IRI86	ICED	B'cast
<b>2</b>	.27 (9)	.37 (11)	1.66 (50)	.75 (24)	.73 (26)	.56 (20)	1.70 (61)	1.29 (46)
<b>3</b>	1.13 (15)	.40 (9)	2.53 (38)	.72 (11)	.23 (17)	.21 (14)	.71 (53)	.22 (18)
<b>6</b>	2.41 (35)	1.44 (21)	1.83 (24)	1.15 (15)	.72 (26)	.50 (18)	1.74 (61)	1.33 (47)
<b>9</b>	N/A	N/A	N/A	N/A	N/A	N/A	N/A	N/A
<b>11</b>	1.54 (24)	1.03 (18)	3.20 (47)	1.99 (29)	1.40 (35)	.94 (23)	2.59 (69)	2.27 (59)
<b>12</b>	2.56 (26)	.53 (5)	2.33 (22)	1.48 (14)	.19 (9)	.30 (15)	1.19 (56)	.64 (30)
<b>13</b>	.20 (9)	.21 (8)	.85 (35)	.29 (12)	.91 (36)	.86 (34)	1.68 (66)	1.07 (42)
<b>14</b>	1.42 (14)	.50 (5)	3.23 (36)	1.18 (12)	.59 (21)	.53 (18)	1.41 (59)	1.03 (37)
<b>15</b>	3.28 (33)	.97 (13)	2.15 (25)	1.35 (19)	.87 (25)	.68 (22)	1.73 (59)	1.42 (44)
<b>16</b>	2.14 (32)	1.22 (28)	.89 (18)	.40 (8)	.80 (37)	.82 (38)	1.25 (59)	.60 (27)
<b>17</b>	2.06 (26)	.75 (20)	1.31 (23)	.89 (17)	.27 (20)	.59 (35)	.77 (35)	1.00 (39)
<b>18</b>	.84 (17)	.51 (10)	3.05 (50)	.96 (18)	.57 (32)	.65 (43)	1.01 (54)	.39 (22)
<b>19</b>	.73 (16)	.34 (7)	2.78 (52)	1.08 (25)	1.30 (37)	1.00 (30)	2.28 (65)	2.02 (57)
<b>20</b>	2.20 (22)	.30 (3)	2.52 (28)	.82 (9)	.46 (34)	.45 (32)	.80 (55)	.19 (15)
<b>21</b>	2.68 (27)	.74 (8)	1.72 (19)	.76 (8)	.13 (6)	.66 (28)	.84 (35)	.91 (38)
<b>23</b>	3.21 (40)	1.31 (21)	.70 (9)	.24 (6)	N/A	N/A	N/A	N/A

Daytime and Night-Time r.m.s. (m) Errors on L1 to Sixteen Satellites  
 at Algonquin (the r.m.s. (%) errors are italicised and in parentheses)

ALGONQUIN – DAILY SUMMARY FOR FEBRUARY 5th 1991								
PRN	DAYTIME				NIGHT-TIME			
	BENT	IRI86	ICED	B'cast	BENT	IRI86	ICED	B'cast
<b>2</b>	.31 (9)	.29 (8)	2.00 (57)	.77 (23)	.77 (27)	.60 (21)	1.91 (67)	1.36 (47)
<b>3</b>	1.10 (14)	.47 (9)	3.19 (47)	.90 (14)	.41 (27)	.37 (24)	.98 (62)	.16 (9)
<b>6</b>	2.37 (33)	1.31 (18)	2.35 (34)	1.07 (17)	.80 (28)	.57 (20)	1.99 (68)	1.44 (49)
<b>9</b>	N/A	N/A	N/A	N/A	N/A	N/A	N/A	N/A
<b>11</b>	1.78 (25)	.75 (14)	3.27 (50)	1.66 (27)	1.25 (33)	.77 (20)	2.66 (73)	2.18 (59)
<b>12</b>	2.41 (24)	.48 (4)	3.47 (33)	1.85 (17)	.35 (15)	.31 (13)	1.51 (65)	.87 (37)
<b>13</b>	.12 (5)	.19 (8)	.89 (38)	.22 (10)	.81 (33)	.78 (32)	1.78 (70)	1.05 (40)
<b>14</b>	1.56 (15)	.39 (4)	3.97 (44)	1.19 (11)	.66 (23)	.60 (20)	1.65 (68)	1.09 (38)
<b>15</b>	3.77 (39)	1.11 (13)	2.85 (32)	1.19 (17)	.64 (21)	.44 (15)	1.77 (66)	1.26 (43)
<b>16</b>	2.20 (31)	1.09 (24)	1.52 (29)	.48 (7)	.74 (35)	.78 (37)	1.27 (61)	.57 (26)
<b>17</b>	1.92 (22)	.63 (14)	2.15 (33)	1.13 (18)	.56 (24)	.34 (23)	1.38 (52)	1.38 (35)
<b>18</b>	.87 (16)	.52 (10)	3.67 (57)	1.06 (18)	.52 (26)	.58 (34)	1.01 (55)	.42 (22)
<b>19</b>	.83 (18)	.37 (8)	3.29 (60)	1.22 (28)	1.15 (35)	.88 (27)	2.29 (68)	1.89 (56)
<b>20</b>	2.05 (20)	.46 (6)	3.51 (37)	1.08 (12)	.42 (26)	.41 (26)	.86 (57)	.17 (11)
<b>21</b>	2.89 (30)	.80 (8)	2.60 (28)	.80 (9)	.66 (19)	.37 (11)	1.69 (54)	1.63 (52)
<b>23</b>	3.15 (37)	1.11 (16)	1.72 (21)	.30 (5)	N/A	N/A	N/A	N/A

Daytime and Night-Time r.m.s. (m) Errors on L1 to Sixteen Satellites

at Algonquin (the r.m.s. (%) errors are italicised and in parentheses)

ALGONQUIN – DAILY SUMMARY FOR FEBRUARY 6th 1991								
PRN	DAYTIME				NIGHT-TIME			
	BENT	IRI86	ICED	B'cast	BENT	IRI86	ICED	B'cast
<b>2</b>	.20 (7)	.40 (12)	2.03 (62)	.76 (23)	1.00 (32)	.87 (28)	2.22 (72)	1.57 (51)
<b>3</b>	.88 (13)	.60 (11)	3.49 (53)	.48 (8)	.63 (35)	.53 (31)	1.26 (72)	.35 (17)
<b>6</b>	2.08 (28)	1.04 (15)	2.98 (44)	.65 (12)	.77 (26)	.62 (21)	2.01 (70)	1.36 (47)
<b>9</b>	N/A	N/A	N/A	N/A	N/A	N/A	N/A	N/A
<b>11</b>	1.87 (27)	.93 (17)	3.71 (57)	1.12 (21)	.89 (25)	.68 (25)	2.18 (70)	1.62 (48)
<b>12</b>	3.09 (31)	.77 (8)	3.68 (37)	.79 (8)	.41 (16)	.45 (19)	1.61 (68)	.88 (36)
<b>13</b>	.81 (30)	.73 (27)	1.68 (61)	.52 (19)	1.19 (41)	1.17 (40)	2.20 (76)	1.40 (48)
<b>14</b>	1.70 (16)	.42 (4)	4.56 (49)	.87 (9)	.63 (21)	.59 (20)	1.70 (69)	1.10 (38)
<b>15</b>	3.59 (38)	1.12 (17)	3.46 (44)	.87 (18)	.81 (31)	.69 (33)	1.87 (67)	1.32 (42)
<b>16</b>	1.69 (21)	.50 (10)	2.36 (44)	.50 (10)	1.07 (45)	1.10 (46)	1.71 (72)	.87 (36)
<b>17</b>	2.16 (28)	.68 (25)	2.42 (40)	.37 (8)	.59 (35)	.58 (32)	1.08 (65)	.25 (14)
<b>18</b>	.82 (13)	.46 (7)	3.82 (60)	.40 (6)	.80 (36)	.81 (41)	1.41 (66)	.64 (27)
<b>19</b>	.76 (17)	.36 (8)	3.51 (64)	.78 (20)	1.37 (39)	1.17 (33)	2.59 (74)	2.03 (58)
<b>20</b>	2.74 (28)	.45 (5)	3.75 (40)	.63 (12)	.64 (33)	.65 (34)	1.23 (68)	.34 (18)
<b>21</b>	3.47 (38)	1.20 (13)	2.95 (32)	.40 (4)	.55 (32)	1.02 (55)	.89 (39)	.69 (30)
<b>23</b>	3.92 (48)	1.55 (21)	1.82 (26)	1.00 (14)	N/A	N/A	N/A	N/A

Daytime and Night-Time r.m.s. (m) Errors on L1 to Sixteen Satellites

at Algonquin (the r.m.s. (%) errors are italicised and in parentheses)

ALGONQUIN – DAILY SUMMARY FOR FEBRUARY 7th 1991								
PRN	DAYTIME				NIGHT-TIME			
	BENT	IRI86	ICED	B'cast	BENT	IRI86	ICED	B'cast
<b>2</b>	.28 (10)	.81 (28)	1.61 (54)	.87 (27)	.59 (20)	.57 (20)	1.67 (65)	1.06 (40)
<b>3</b>	1.28 (26)	.81 (28)	2.98 (46)	.57 (20)	.90 (43)	.86 (40)	1.48 (73)	.52 (24)
<b>6</b>	2.92 (46)	1.97 (33)	1.84 (34)	.63 (13)	.46 (18)	.49 (20)	1.61 (65)	.99 (40)
<b>9</b>	N/A	N/A	N/A	N/A	N/A	N/A	N/A	N/A
<b>11</b>	1.90 (24)	.66 (10)	3.01 (54)	.58 (15)	.51 (20)	.53 (27)	1.71 (63)	1.18 (41)
<b>12</b>	3.30 (34)	.93 (10)	3.14 (32)	.48 (5)	.32 (16)	.47 (24)	1.29 (61)	.59 (27)
<b>13</b>	.70 (27)	.61 (24)	1.50 (58)	.42 (16)	.79 (32)	.78 (31)	1.74 (71)	.94 (38)
<b>14</b>	2.56 (27)	1.18 (12)	3.64 (42)	.53 (7)	.32 (14)	.32 (15)	1.31 (63)	.71 (28)
<b>15</b>	4.42 (48)	1.77 (19)	2.34 (35)	.78 (13)	.42 (24)	.53 (32)	1.22 (59)	.67 (27)
<b>16</b>	2.33 (38)	1.36 (30)	1.37 (31)	.72 (24)	1.02 (43)	1.07 (44)	1.64 (70)	.87 (35)
<b>17</b>	2.58 (34)	.92 (24)	1.69 (32)	.57 (20)	.44 (29)	.37 (25)	.89 (61)	.08 (6)
<b>18</b>	.95 (11)	.68 (10)	3.23 (54)	.57 (16)	.51 (26)	.52 (27)	1.14 (62)	.38 (18)
<b>19</b>	.43 (6)	.39 (9)	2.91 (57)	.41 (12)	.72 (25)	.58 (20)	1.86 (65)	1.36 (48)
<b>20</b>	2.84 (29)	.67 (8)	3.11 (35)	.32 (8)	.50 (28)	.52 (30)	1.19 (68)	.30 (16)
<b>21</b>	3.61 (40)	1.11 (14)	2.36 (27)	.53 (6)	1.11 (79)	1.65 (117)	.12 (8)	.12 (9)
<b>23</b>	3.96 (55)	1.83 (31)	1.52 (19)	1.20 (23)	N/A	N/A	N/A	N/A

Daytime and Night-Time r.m.s. (m) Errors on L1 to Sixteen Satellites

at Algonquin (the r.m.s. (%) errors are italicised and in parentheses)



ALGONQUIN – DAILY SUMMARY FOR FEBRUARY 8th 1991								
PRN	DAYTIME				NIGHT-TIME			
	BENT	IRI86	ICED	B'cast	BENT	IRI86	ICED	B'cast
<b>2</b>	.15 (5)	.49 (15)	1.91 (58)	.80 (23)	.63 (23)	.55 (20)	1.81 (67)	1.18 (44)
<b>3</b>	1.59 (53)	1.52 (62)	2.99 (43)	1.26 (53)	1.41 (55)	1.35 (53)	2.00 (78)	1.05 (41)
<b>6</b>	3.66 (68)	2.77 (54)	1.23 (28)	1.37 (27)	.52 (20)	.50 (19)	1.74 (67)	1.09 (42)
<b>9</b>	N/A	N/A	N/A	N/A	N/A	N/A	N/A	N/A
<b>11</b>	3.41 (56)	2.27 (38)	2.77 (50)	1.54 (28)	.62 (19)	.44 (18)	1.89 (64)	1.46 (47)
<b>12</b>	3.98 (45)	1.37 (15)	2.61 (28)	.42 (5)	.35 (19)	.36 (22)	1.16 (59)	.60 (26)
<b>13</b>	.75 (29)	.67 (26)	1.56 (59)	.44 (17)	.59 (25)	.56 (25)	1.49 (68)	.75 (31)
<b>14</b>	4.06 (53)	2.57 (34)	2.80 (36)	1.59 (21)	.59 (32)	.56 (32)	1.56 (67)	.93 (36)
<b>15</b>	6.04 (82)	3.43 (48)	1.32 (32)	2.16 (32)	.57 (33)	.54 (37)	1.54 (64)	.95 (36)
<b>16</b>	2.79 (50)	1.75 (38)	.95 (27)	.99 (27)	.82 (37)	.89 (41)	1.39 (63)	.73 (37)
<b>17</b>	2.92 (50)	1.51 (43)	1.31 (29)	.95 (25)	.88 (45)	.74 (38)	1.41 (72)	.50 (25)
<b>18</b>	1.62 (23)	1.25 (17)	3.24 (56)	.61 (9)	.63 (30)	.54 (26)	1.28 (64)	.58 (29)
<b>19</b>	1.08 (20)	.77 (12)	3.03 (60)	.91 (20)	.81 (27)	.57 (20)	1.97 (66)	1.50 (50)
<b>20</b>	2.94 (31)	.98 (15)	3.08 (36)	.47 (8)	.42 (24)	.46 (26)	1.06 (62)	.31 (22)
<b>21</b>	4.47 (66)	2.31 (40)	2.16 (21)	1.54 (30)	.48 (16)	.48 (20)	1.44 (50)	1.37 (47)
<b>23</b>	4.83 (88)	2.78 (62)	1.31 (15)	2.13 (51)	N/A	N/A	N/A	N/A

Daytime and Night-Time r.m.s. (m) Errors on L1 to Sixteen Satellites  
 at Algonquin (the r.m.s. (%) errors are italicised and in parentheses)

ALGONQUIN – DAILY SUMMARY FOR FEBRUARY 9th 1991								
PRN	DAYTIME				NIGHT-TIME			
	BENT	IRI86	ICED	B'cast	BENT	IRI86	ICED	B'cast
<b>2</b>	.43 (11)	.21 (6)	2.03 (53)	.90 (26)	.78 (53)	.98 (71)	1.12 (46)	.82 (33)
<b>3</b>	1.70 (40)	1.49 (44)	2.58 (34)	1.19 (29)	.43 (26)	.47 (29)	.88 (55)	.22 (15)
<b>6</b>	3.24 (55)	2.20 (39)	.82 (17)	.32 (8)	.70 (37)	.91 (52)	1.31 (52)	.95 (36)
<b>9</b>	N/A	N/A	N/A	N/A	N/A	N/A	N/A	N/A
<b>11</b>	2.20 (30)	1.14 (18)	2.67 (44)	1.39 (25)	.44 (21)	.74 (37)	1.37 (53)	.97 (37)
<b>12</b>	3.70 (43)	1.12 (14)	1.94 (18)	1.32 (13)	.54 (43)	.61 (46)	.83 (45)	.39 (23)
<b>13</b>	.24 (11)	.18 (8)	.92 (41)	.28 (12)	.67 (38)	.68 (39)	1.09 (52)	.61 (25)
<b>14</b>	1.66 (15)	.39 (5)	3.67 (38)	1.65 (15)	.89 (68)	.92 (73)	1.25 (50)	1.05 (45)
<b>15</b>	3.78 (39)	1.12 (16)	2.12 (30)	1.38 (22)	.89 (83)	.91 (92)	1.31 (51)	1.05 (50)
<b>16</b>	2.94 (53)	1.77 (44)	.44 (11)	.26 (11)	.67 (33)	.74 (37)	1.15 (56)	.58 (25)
<b>17</b>	3.06 (45)	1.24 (35)	.61 (13)	.32 (9)	.60 (49)	.93 (68)	.30 (26)	.68 (65)
<b>18</b>	1.30 (22)	.99 (18)	3.80 (54)	1.53 (23)	.29 (31)	.36 (35)	.58 (40)	.39 (44)
<b>19</b>	.84 (15)	.46 (8)	3.19 (54)	1.26 (26)	.92 (29)	.70 (22)	1.98 (62)	1.70 (53)
<b>20</b>	2.83 (38)	1.21 (34)	2.47 (25)	1.48 (26)	.44 (35)	.40 (31)	.73 (50)	.37 (42)
<b>21</b>	3.59 (42)	1.60 (19)	1.60 (15)	1.00 (9)	1.12 (84)	1.63 (120)	.41 (18)	.44 (20)
<b>23</b>	4.30 (63)	2.04 (36)	.49 (7)	.76 (15)	N/A	N/A	N/A	N/A

Daytime and Night-Time r.m.s. (m) Errors on L1 to Sixteen Satellites

at Algonquin (the r.m.s. (%) errors are italicised and in parentheses)

YELLOWKNIFE – DAILY SUMMARY FOR FEBRUARY 3rd 1991								
PRN	DAYTIME				NIGHT-TIME			
	BENT	IRI86	ICED	B'cast	BENT	IRI86	ICED	B'cast
<b>2</b>	.72 (24)	1.19 (46)	1.30 (26)	.42 (14)	1.23 (39)	.69 (22)	1.33 (44)	1.34 (41)
<b>3</b>	.57 (13)	1.39 (31)	1.36 (22)	1.21 (35)	1.27 (51)	1.23 (49)	1.18 (47)	.97 (39)
<b>6</b>	.84 (21)	1.09 (40)	1.72 (30)	.85 (23)	1.18 (41)	.85 (30)	1.25 (43)	1.39 (46)
<b>9</b>	N/A	N/A	N/A	N/A	N/A	N/A	N/A	N/A
<b>11</b>	1.03 (30)	1.26 (50)	1.44 (28)	1.13 (30)	1.02 (33)	.63 (22)	1.60 (52)	1.60 (51)
<b>12</b>	.88 (13)	.73 (12)	1.84 (25)	1.80 (25)	1.68 (57)	1.59 (54)	1.60 (54)	1.42 (47)
<b>13</b>	.86 (14)	.89 (16)	1.59 (20)	1.20 (15)	1.65 (51)	1.55 (48)	1.73 (55)	1.50 (47)
<b>14</b>	.26 (3)	.30 (4)	1.72 (18)	1.89 (19)	.47 (29)	.63 (44)	1.04 (44)	.83 (35)
<b>15</b>	1.29 (13)	.77 (8)	1.42 (18)	1.46 (18)	.56 (20)	.52 (26)	1.11 (43)	1.01 (36)
<b>16</b>	1.82 (23)	1.05 (16)	3.10 (42)	1.28 (20)	.74 (35)	.74 (35)	.81 (38)	.64 (27)
<b>17</b>	.69 (16)	.63 (16)	1.57 (36)	1.05 (23)	1.09 (47)	1.04 (46)	.86 (38)	.81 (34)
<b>18</b>	1.80 (20)	1.10 (12)	2.78 (33)	1.86 (20)	.48 (41)	.82 (67)	.63 (34)	.39 (25)
<b>19</b>	1.39 (21)	.97 (39)	1.45 (15)	1.21 (15)	.48 (34)	1.01 (68)	.75 (32)	.82 (36)
<b>20</b>	.67 (8)	.98 (17)	2.14 (23)	2.07 (23)	.95 (43)	.99 (44)	.90 (41)	.72 (30)
<b>21</b>	.91 (9)	.54 (9)	1.29 (18)	1.58 (18)	.98 (31)	1.04 (46)	1.37 (47)	1.19 (40)
<b>23</b>	.60 (8)	.62 (12)	1.26 (18)	1.51 (18)	.76 (25)	.75 (28)	1.41 (48)	1.43 (48)

Daytime and Night-Time r.m.s. (m) Errors on L1 to Sixteen Satellites

at Yellowknife (the r.m.s. (%) errors are italicised and in parentheses)

YELLOWKNIFE -- DAILY SUMMARY FOR FEBRUARY 4th 1991								
PRN	DAYTIME				NIGHT-TIME			
	BENT	IRI86	ICED	B'cast	BENT	IRI86	ICED	B'cast
<b>2</b>	.52 (10)	.82 (27)	2.57 (54)	.55 (16)	.48 (30)	.57 (46)	.79 (37)	.60 (32)
<b>3</b>	.81 (26)	1.59 (44)	2.39 (39)	1.14 (34)	.50 (31)	.50 (35)	.58 (35)	.37 (32)
<b>6</b>	.76 (28)	1.01 (47)	3.13 (45)	.36 (11)	.79 (41)	1.50 (75)	.66 (28)	.77 (53)
<b>9</b>	N/A	N/A	N/A	N/A	N/A	N/A	N/A	N/A
<b>11</b>	.67 (14)	.90 (24)	2.12 (44)	.92 (21)	.94 (24)	.89 (43)	1.77 (54)	1.46 (38)
<b>12</b>	.47 (8)	.97 (16)	2.57 (40)	.98 (16)	.82 (36)	.72 (33)	1.09 (51)	.65 (30)
<b>13</b>	.40 (9)	.89 (14)	2.92 (39)	.77 (12)	.70 (43)	.58 (40)	.83 (43)	.51 (33)
<b>14</b>	.87 (10)	1.02 (13)	3.31 (36)	1.33 (13)	.66 (46)	.99 (67)	.71 (45)	.18 (11)
<b>15</b>	2.16 (26)	1.65 (23)	2.20 (31)	.61 (9)	.82 (67)	1.12 (105)	1.13 (44)	.90 (53)
<b>16</b>	1.42 (22)	1.00 (23)	3.71 (55)	.69 (10)	.33 (24)	.57 (37)	.38 (30)	.37 (33)
<b>17</b>	.81 (28)	1.46 (53)	1.73 (42)	.91 (27)	.42 (32)	.52 (37)	.40 (27)	.35 (42)
<b>18</b>	1.37 (16)	1.03 (13)	3.76 (45)	1.27 (13)	N/A	N/A	N/A	N/A
<b>19</b>	1.49 (23)	1.53 (45)	2.79 (42)	.87 (16)	.30 (15)	.83 (45)	1.11 (52)	.63 (27)
<b>20</b>	.90 (11)	1.05 (19)	4.45 (46)	2.37 (26)	.34 (41)	.27 (33)	.27 (28)	.55 (64)
<b>21</b>	1.26 (18)	.95 (22)	2.60 (36)	1.16 (16)	.63 (87)	1.27 (131)	.42 (35)	.63 (119)
<b>23</b>	.98 (80)	1.45 (110)	.76 (25)	.70 (57)	.81 (643)	1.41 (769)	.76 (262)	1.01 (836)

Daytime and Night-Time r.m.s. (m) Errors on L1 to Sixteen Satellites

at Yellowknife (the r.m.s. (%) errors are italicised and in parentheses)

YELLOWKNIFE -- DAILY SUMMARY FOR FEBRUARY 5th 1991								
PRN	DAYTIME				NIGHT-TIME			
	BENT	IRI86	ICED	B'cast	BENT	IRI86	ICED	B'cast
<b>2</b>	.59 (15)	.59 (12)	2.96 (62)	.80 (20)	1.12 (40)	.64 (24)	1.71 (62)	1.25 (44)
<b>3</b>	2.97 (169)	3.37 (211)	2.93 (67)	3.21 (205)	1.95 (134)	1.84 (109)	2.14 (91)	1.71 (147)
<b>6</b>	.42 (9)	1.22 (31)	2.76 (57)	.53 (15)	.95 (35)	.66 (23)	1.43 (54)	1.12 (38)
<b>9</b>	N/A	N/A	N/A	N/A	N/A	N/A	N/A	N/A
<b>11</b>	1.20 (24)	.83 (21)	3.14 (62)	1.70 (34)	.97 (31)	.61 (22)	2.32 (73)	1.70 (52)
<b>12</b>	N/A	N/A	N/A	N/A	1.85 (57)	1.80 (55)	2.13 (67)	1.63 (51)
<b>13</b>	.87 (34)	.46 (18)	1.56 (62)	.51 (20)	1.14 (42)	1.05 (38)	1.67 (66)	1.03 (38)
<b>14</b>	N/A	N/A	N/A	N/A	.64 (35)	.78 (48)	1.41 (59)	.84 (30)
<b>15</b>	N/A	N/A	N/A	N/A	1.07 (38)	.80 (43)	1.91 (67)	1.34 (42)
<b>16</b>	1.27 (17)	.98 (18)	3.97 (60)	.90 (15)	1.44 (88)	1.48 (105)	1.80 (74)	1.35 (118)
<b>17</b>	.86 (24)	1.29 (41)	2.39 (60)	.86 (24)	1.07 (46)	1.09 (47)	1.17 (53)	.73 (32)
<b>18</b>	1.38 (17)	.82 (13)	4.20 (59)	1.19 (16)	.79 (28)	.48 (17)	2.02 (74)	1.24 (45)
<b>19</b>	1.14 (15)	1.14 (29)	3.65 (60)	1.00 (17)	.86 (29)	.38 (13)	2.08 (71)	1.44 (49)
<b>20</b>	N/A	N/A	N/A	N/A	.86 (38)	.90 (39)	1.09 (53)	.65 (28)
<b>21</b>	N/A	N/A	N/A	N/A	.11 (15)	.36 (48)	.28 (38)	.88 (119)
<b>23</b>	N/A	N/A	N/A	N/A	.38 (26)	.33 (24)	.80 (58)	.38 (44)

Daytime and Night-Time r.m.s. (m) Errors on L1 to Sixteen Satellites

at Yellowknife (the r.m.s. (%) errors are italicised and in parentheses)

YELLOWKNIFE – DAILY SUMMARY FOR FEBRUARY 6th 1991								
PRN	DAYTIME				NIGHT-TIME			
	BENT	IRI86	ICED	B'cast	BENT	IRI86	ICED	B'cast
<b>2</b>	.41 (16)	1.20 (43)	2.74 (60)	.89 (25)	.84 (33)	.56 (22)	1.51 (62)	.94 (37)
<b>3</b>	1.87 (45)	2.66 (63)	2.15 (46)	2.26 (56)	1.50 (52)	1.49 (52)	1.88 (67)	1.27 (44)
<b>6</b>	.75 (30)	1.51 (57)	2.89 (58)	.99 (37)	.72 (38)	.82 (44)	1.07 (51)	.64 (27)
<b>9</b>	N/A	N/A	N/A	N/A	N/A	N/A	N/A	N/A
<b>11</b>	1.04 (34)	1.28 (49)	2.62 (54)	1.18 (40)	.98 (31)	.93 (38)	2.11 (70)	1.54 (47)
<b>12</b>	1.26 (24)	1.49 (28)	2.85 (47)	.87 (17)	1.43 (50)	1.38 (48)	1.83 (67)	1.22 (42)
<b>13</b>	2.23 (45)	2.67 (52)	2.11 (41)	1.76 (36)	1.31 (45)	1.30 (43)	2.03 (73)	1.29 (44)
<b>14</b>	1.95 (24)	1.76 (23)	3.73 (45)	.62 (11)	.80 (26)	.63 (22)	2.25 (76)	1.44 (48)
<b>15</b>	2.38 (31)	1.81 (28)	2.87 (39)	.72 (14)	1.23 (39)	1.10 (48)	2.14 (70)	1.44 (45)
<b>16</b>	1.46 (22)	1.18 (25)	4.44 (64)	.87 (15)	.79 (38)	.92 (46)	1.12 (57)	.52 (24)
<b>17</b>	.54 (13)	.82 (22)	2.14 (53)	.53 (15)	1.24 (47)	1.24 (47)	1.45 (59)	1.01 (40)
<b>18</b>	1.57 (18)	1.25 (15)	4.56 (56)	.87 (12)	1.02 (31)	.88 (35)	2.06 (72)	1.37 (39)
<b>19</b>	1.66 (42)	1.75 (67)	3.86 (54)	1.31 (47)	.34 (21)	.99 (56)	1.20 (61)	.49 (23)
<b>20</b>	.55 (6)	1.06 (14)	4.91 (55)	1.62 (16)	.94 (38)	1.02 (41)	1.34 (60)	.82 (35)
<b>21</b>	2.09 (27)	1.57 (22)	2.73 (46)	.53 (9)	.40 (45)	1.03 (72)	.78 (45)	.69 (92)
<b>23</b>	1.44 (26)	1.44 (32)	2.38 (36)	.74 (18)	.58 (47)	.49 (53)	1.01 (54)	.78 (128)

Daytime and Night-Time r.m.s. (m) Errors on L1 to Sixteen Satellites

at Yellowknife (the r.m.s. (%) errors are italicised and in parentheses)



YELLOWKNIFE - DAILY SUMMARY FOR FEBRUARY 7th 1991								
PRN	DAYTIME				NIGHT-TIME			
	BENT	IRI86	ICED	B'cast	BENT	IRI86	ICED	B'cast
2	.22 (6)	.91 (30)	2.91 (60)	.63 (13)	.53 (25)	.25 (12)	1.12 (53)	.66 (27)
3	1.60 (37)	2.50 (57)	2.09 (45)	2.08 (50)	1.08 (46)	1.05 (46)	1.36 (59)	.79 (33)
6	.69 (29)	1.58 (62)	2.63 (54)	.96 (33)	.70 (35)	.81 (41)	1.16 (50)	.81 (31)
9	N/A	N/A	N/A	N/A	N/A	N/A	N/A	N/A
11	1.23 (40)	3.39 (79)	2.00 (45)	1.14 (43)	.30 (14)	1.71 (76)	1.35 (59)	.80 (32)
12	1.91 (40)	2.27 (47)	1.77 (36)	1.26 (27)	1.48 (53)	1.40 (50)	1.83 (67)	1.24 (44)
13	2.29 (45)	2.79 (54)	1.55 (35)	1.90 (40)	1.22 (43)	1.18 (41)	1.84 (69)	1.16 (40)
14	2.75 (37)	2.59 (36)	2.70 (36)	1.07 (16)	.67 (25)	.58 (27)	1.99 (73)	1.23 (44)
15	3.36 (50)	2.75 (45)	1.69 (29)	1.36 (24)	.56 (29)	.99 (64)	1.33 (59)	.81 (30)
16	1.13 (19)	.92 (23)	4.21 (62)	.79 (14)	.61 (32)	.72 (39)	.99 (53)	.41 (20)
17	.53 (13)	.91 (25)	1.83 (47)	.54 (16)	1.12 (44)	1.06 (44)	1.31 (52)	.99 (38)
18	2.20 (32)	2.08 (31)	3.63 (49)	1.29 (22)	1.11 (76)	1.08 (95)	1.99 (67)	1.32 (54)
19	1.85 (32)	1.74 (51)	3.22 (52)	1.04 (28)	.62 (22)	.49 (19)	1.84 (70)	1.14 (43)
20	N/A	N/A	N/A	N/A	N/A	N/A	N/A	N/A
21	2.53 (34)	1.99 (29)	2.05 (36)	.63 (13)	.46 (27)	1.01 (60)	1.01 (61)	.43 (40)
23	1.84 (43)	1.86 (54)	1.76 (28)	.85 (34)	.33 (23)	.34 (24)	.56 (44)	.38 (48)

Daytime and Night-Time r.m.s. (m) Errors on L1 to Sixteen Satellites

at Yellowknife (the r.m.s. (%) errors are italicised and in parentheses)

YELLOWKNIFE – DAILY SUMMARY FOR FEBRUARY 8th 1991								
PRN	DAYTIME				NIGHT-TIME			
	BENT	IRI86	ICED	B'cast	BENT	IRI86	ICED	B'cast
2	.86 (18)	.69 (29)	3.53 (62)	.39 (10)	.64 (63)	1.11 (106)	.62 (35)	.59 (58)
3	2.22 (53)	3.03 (72)	2.03 (44)	2.49 (62)	1.95 (59)	1.96 (59)	2.26 (69)	1.71 (49)
6	1.13 (45)	2.06 (80)	2.06 (46)	1.46 (50)	1.55 (69)	1.43 (82)	1.75 (58)	1.34 (43)
9	N/A	N/A	N/A	N/A	N/A	N/A	N/A	N/A
11	1.30 (70)	1.62 (92)	2.51 (51)	1.44 (81)	.59 (23)	.65 (27)	1.77 (63)	1.19 (41)
12	1.75 (40)	2.05 (45)	2.09 (39)	1.10 (26)	.98 (43)	.93 (41)	1.30 (58)	.73 (31)
13	3.30 (89)	3.70 (98)	1.88 (37)	2.88 (77)	.84 (34)	.77 (31)	1.45 (63)	.80 (33)
14	N/A	N/A	N/A	N/A	1.09 (46)	.87 (35)	1.33 (58)	.82 (33)
15	3.30 (93)	2.79 (100)	2.01 (41)	1.65 (83)	.36 (21)	1.01 (60)	1.10 (54)	.60 (25)
16	1.53 (91)	1.92 (106)	3.77 (67)	1.98 (123)	1.25 (65)	1.41 (85)	1.42 (55)	1.03 (44)
17	1.74 (34)	1.56 (35)	2.91 (59)	1.74 (35)	2.28 (57)	2.20 (57)	2.46 (61)	2.20 (52)
18	1.90 (26)	1.81 (25)	3.74 (50)	1.09 (18)	1.18 (48)	1.08 (57)	2.18 (71)	1.48 (44)
19	1.86 (36)	1.59 (51)	3.90 (55)	1.23 (37)	.48 (28)	.74 (50)	1.45 (64)	.77 (33)
20	2.51 (37)	2.90 (44)	3.20 (42)	1.56 (24)	.95 (41)	1.02 (44)	1.29 (58)	.74 (33)
21	2.39 (34)	1.66 (26)	2.63 (46)	.98 (22)	2.05 (56)	2.02 (57)	2.79 (81)	1.97 (54)
23	2.33 (51)	2.26 (58)	1.36 (29)	1.14 (40)	1.87 (58)	1.79 (56)	2.11 (67)	1.54 (47)

Daytime and Night-Time r.m.s. (m) Errors on L1 to Sixteen Satellites

at Yellowknife (the r.m.s. (%) errors are italicised and in parentheses)



YELLOWKNIFE – DAILY SUMMARY FOR FEBRUARY 9th 1991								
PRN	DAYTIME				NIGHT-TIME			
	BENT	IRI86	ICED	B'cast	BENT	IRI86	ICED	B'cast
<b>2</b>	1.43 (69)	2.23 (103)	2.12 (39)	1.26 (60)	.69 (33)	.99 (49)	1.05 (47)	.73 (32)
<b>3</b>	2.87 (115)	3.76 (149)	.94 (38)	3.27 (164)	.71 (70)	.61 (57)	.79 (56)	.60 (74)
<b>6</b>	1.59 (60)	2.47 (94)	1.90 (37)	1.32 (48)	.53 (21)	.66 (33)	1.00 (41)	.86 (28)
<b>9</b>	N/A	N/A	N/A	N/A	N/A	N/A	N/A	N/A
<b>11</b>	1.75 (61)	2.19 (83)	.83 (24)	1.31 (50)	.46 (22)	1.29 (63)	.95 (46)	.66 (28)
<b>12</b>	3.80 (204)	4.02 (214)	1.96 (87)	2.79 (147)	.58 (30)	.52 (27)	.87 (46)	.44 (20)
<b>13</b>	4.19 (136)	4.56 (147)	1.18 (43)	3.21 (103)	.54 (36)	.40 (29)	.85 (45)	.44 (29)
<b>14</b>	3.32 (80)	3.15 (82)	2.69 (31)	1.96 (50)	1.46 (241)	1.74 (281)	.30 (43)	.80 (141)
<b>15</b>	4.66 (205)	4.07 (207)	1.30 (98)	2.26 (141)	.80 (86)	1.45 (137)	.60 (34)	.50 (43)
<b>16</b>	2.18 (63)	2.96 (84)	1.74 (33)	2.61 (75)	.60 (74)	.80 (83)	.53 (52)	.69 (87)
<b>17</b>	.96 (28)	1.21 (44)	1.65 (37)	.87 (28)	.56 (29)	.56 (31)	.68 (35)	.56 (26)
<b>18</b>	2.50 (43)	2.52 (45)	2.76 (35)	1.71 (29)	.84 (72)	1.13 (95)	.44 (34)	.32 (29)
<b>19</b>	2.33 (56)	2.45 (81)	2.26 (30)	1.61 (42)	.98 (104)	1.34 (149)	1.31 (44)	1.15 (71)
<b>20</b>	3.41 (87)	3.86 (101)	2.58 (33)	2.92 (80)	1.10 (1659)	1.03 (1490)	.93 (1245)	1.20 (1825)
<b>21</b>	2.88 (60)	2.42 (58)	1.67 (20)	1.30 (28)	.50 (27)	.86 (44)	.90 (50)	.53 (27)
<b>23</b>	2.30 (59)	2.29 (65)	1.58 (19)	1.14 (26)	.70 (42)	.85 (51)	.83 (47)	.37 (18)

Daytime and Night-Time r.m.s. (m) Errors on L1 to Sixteen Satellites  
 at Yellowknife (the r.m.s. (%) errors are italicised and in parentheses)

## ***APPENDIX VII***

---

Two Tables Showing the "Whole Week" Summaries of the Daytime and Night-time **Mean Statistics** for Algonquin and Yellowknife (these tables correspond with Tables 6.4 and 6.5 which showed the r.m.s. statistics).

ALGONQUIN – WHOLE WEEK SUMMARY OF AVERAGES								
PRN	DAYTIME				NIGHT-TIME			
	BENT	IRI86	ICED	B'cast	BENT	IRI86	ICED	B'cast
2	0.19 (-5)	-0.35 (11)	1.79 (-53)	0.17 (-6)	0.62 (-19)	0.41 (-10)	1.66 (-60)	1.21 (-42)
3	-0.41 (9)	-0.19 (9)	2.36 (-37)	0.33 (-2)	0.60 (-30)	0.49 (-23)	1.14 (-61)	0.31 (-13)
6	-2.41 (38)	-1.56 (26)	1.45 (-23)	0.34 (-4)	0.61 (-20)	0.31 (-9)	1.67 (-61)	1.22 (-43)
9	N/A	N/A	N/A	N/A	N/A	N/A	N/A	N/A
11	-0.32 (0)	0.24 (-5)	2.73 (-43)	1.07 (-17)	0.69 (-17)	0.21 (-1)	1.99 (-63)	1.61 (-49)
12	-2.78 (29)	-0.34 (4)	2.33 (-23)	1.13 (-11)	0.13 (-2)	0.02 (3)	1.24 (-56)	0.68 (-29)
13	0.43 (-16)	0.30 (-11)	1.12 (-44)	0.12 (-5)	0.72 (-26)	0.67 (-24)	1.61 (-65)	0.95 (-36)
14	-1.65 (18)	-0.50 (6)	3.16 (-35)	0.37 (-3)	0.38 (-10)	0.30 (-6)	1.57 (-59)	0.78 (-27)
15	-3.44 (34)	-1.10 (10)	1.76 (-23)	0.45 (-6)	0.28 (-2)	0.03 (9)	1.44 (-57)	0.96 (-32)
16	-1.69 (30)	-1.08 (25)	0.95 (-22)	-0.03 (6)	0.75 (-33)	0.75 (-32)	1.28 (-59)	0.60 (-25)
17	-1.85 (27)	-0.50 (15)	1.24 (-22)	0.33 (-2)	0.15 (-5)	-0.16 (10)	0.74 (-39)	0.30 (-1)
18	0.32 (-9)	0.18 (-5)	3.15 (-51)	0.60 (-9)	0.37 (-16)	0.22 (-7)	0.96 (-53)	0.22 (-7)
19	0.49 (-11)	0.13 (-3)	2.92 (-55)	0.69 (-15)	1.09 (-33)	0.81 (-25)	2.08 (-63)	1.79 (-54)
20	-2.10 (20)	-0.04 (1)	2.39 (-26)	0.52 (-4)	0.30 (-14)	0.33 (-16)	0.93 (-56)	0.13 (-4)
21	-3.03 (35)	-0.47 (8)	1.58 (-17)	0.20 (-1)	-0.27 (22)	-0.80 (48)	0.70 (-26)	0.73 (-27)
23	-3.44 (48)	-1.23 (22)	0.63 (-8)	-0.53 (11)	N/A	N/A	N/A	N/A
AV.	-1.45 (16)	-0.43 (8)	1.97 (-32)	0.38 (-5)	0.46 (-15)	0.26 (-6)	1.34 (-56)	0.82 (-28)

The Daytime and Night-time Average (m) Errors on L1 to Sixteen Satellites  
at Algonquin (the average (%) errors are italicised and in parentheses)

YELLOWKNIFE – WHOLE WEEK SUMMARY OF AVERAGES								
PRN	DAYTIME				NIGHT-TIME			
	BENT	IRI86	ICED	B'cast	BENT	IRI86	ICED	B'cast
<b>2</b>	0.04 (5)	-0.89 (31)	2.23 (-47)	-0.12 (4)	0.44 (-11)	-0.08 (14)	1.05 (-44)	0.62 (-19)
<b>3</b>	-1.16 (36)	-2.09 (59)	1.52 (-29)	-1.70 (53)	1.02 (-30)	1.00 (-31)	1.27 (-45)	0.74 (-15)
<b>6</b>	-0.39 (17)	-1.37 (46)	1.94 (-42)	-0.29 (9)	0.52 (-17)	-0.04 (7)	1.13 (-46)	0.84 (-31)
<b>9</b>	N/A	N/A	N/A	N/A	N/A	N/A	N/A	N/A
<b>11</b>	-0.21 (11)	-0.10 (11)	1.82 (-39)	0.15 (3)	0.44 (-12)	0.00 (2)	1.53 (-57)	1.08 (-37)
<b>12</b>	-0.93 (31)	-1.45 (42)	1.78 (-26)	-0.09 (14)	1.16 (-44)	1.05 (-39)	1.44 (-57)	0.90 (-31)
<b>13</b>	-1.57 (39)	-2.15 (51)	1.31 (-21)	-1.17 (33)	0.80 (-27)	0.72 (-23)	1.39 (-58)	0.76 (-26)
<b>14</b>	-1.64 (26)	-1.59 (26)	2.58 (-29)	0.20 (3)	-0.15 (-40)	-0.44 (58)	1.17 (-45)	0.53 (-3)
<b>15</b>	-2.44 (56)	-2.09 (54)	1.38 (-12)	-0.54 (25)	0.08 (11)	-0.65 (50)	1.13 (-49)	0.58 (-16)
<b>16</b>	0.51 (0)	-0.45 (17)	3.34 (-50)	-0.24 (12)	0.33 (-3)	0.19 (7)	0.84 (-37)	0.30 (2)
<b>17</b>	0.11 (0)	-0.62 (20)	1.84 (-44)	0.38 (-7)	0.90 (-35)	0.85 (-33)	1.03 (-43)	0.64 (-19)
<b>18</b>	-0.26 (5)	-0.75 (12)	3.32 (-43)	0.19 (1)	0.17 (11)	-0.17 (30)	1.35 (-54)	0.65 (-17)
<b>19</b>	-0.50 (16)	-1.07 (35)	2.72 (-44)	-0.10 (9)	0.11 (8)	-0.62 (44)	1.25 (-50)	0.70 (-21)
<b>20</b>	-1.01 (19)	-1.60 (28)	3.18 (-36)	0.49 (4)	0.37 (-66)	0.42 (-64)	0.65 (-73)	0.09 (-48)
<b>21</b>	-1.31 (19)	-1.13 (20)	1.88 (-31)	0.29 (-2)	0.22 (8)	-0.34 (40)	0.97 (-41)	0.39 (9)
<b>23</b>	-1.36 (35)	-1.53 (43)	1.16 (-18)	-0.26 (15)	0.22 (56)	-0.12 (86)	0.74 (-11)	0.17 (93)
<b>AV.</b>	-0.81 (21)	-1.26 (33)	2.13 (-34)	-0.19 (12)	0.44 (-13)	0.12 (10)	1.13 (-47)	0.60 (-12)

The Daytime and Night-time Average (m) Errors on L1 to Sixteen Satellites  
at Yellowknife (the average (%) errors are italicised and in parentheses)

## VITA

**Candidate's Full Name** : Simon Peter Newby.

**Place and Date of Birth** : Corby, Northamptonshire, England. 29th September 1963.

**Permanent Address** : 23 Brunswick Gardens,  
Corby.  
Northants NN18 9ER.  
ENGLAND.

**Schools Attended** : Beanfield Comprehensive School, Corby, Northants.

**Universities Attended** : Department of Land Surveying,  
North East London Polytechnic,  
Longbridge Road,  
Dagenham. Essex RM8 2AS.  
ENGLAND.  
1984 –1987, B.Sc. (Hons) Surveying & Mapping Sciences.

**Publications** :

- S. Newby, and R. Langley. "Three alternative empirical ionospheric models — Are they better than the GPS Broadcast model?" *Proceedings of the 6th International Geodetic Symposium on Satellite Positioning*, Columbus, Ohio March 1992 (in press).
- S. Newby, and R. Langley. "Ionospheric models and the Global Positioning System." Presented at IUGG XX General Assembly, Vienna, 11–24 August 1991.
- H. Janes, R. Langley, and S. Newby. "Analysis of tropospheric delay prediction models: comparisons with ray-tracing and implications for GPS relative positioning." *Bulletin Géodésique*, Volume 65, Number 3, 1991, pp. 151–161.
- S. Newby, R. Langley, and H. Janes. "Ionospheric modelling for single frequency users of the Global Positioning System: A status report." *Proceedings of GPS '90*, Ottawa, Canada, 3–7 September 1990, pp. 429–443.
- H. Janes, R. Langley, and S. Newby. "Analysis of tropospheric delay prediction models: comparisons with ray-tracing and implications for GPS relative positioning (a summary)." *Proceedings of GPS '90*, Ottawa, Canada, 3–7 September 1990, pp. 444–450.

- S. Newby, and R. Langley. "The potential use of global ionospheric models for making reliable, accurate predictions of ionospheric delay corrections." Presented at 125th anniversary General Meeting of the International Association of Geodesy, Edinburgh, 3–12 August 1989.
- S. Newby, R. Langley, and H. Janes. "The spatial correlation of meteorological measurements in tropospheric delay modelling." *Proceedings of the 5th International Geodetic Symposium on Satellite Positioning*, Las Cruces, New Mexico, March 1989, pp. 757–766.
- H. Janes, R. Langley, and S. Newby. "A comparison of several models for the prediction of tropospheric propagation delay." *Proceedings of the 5th International Geodetic Symposium on Satellite Positioning*, Las Cruces, New Mexico, March 1989, pp. 777–788.
- R. Langley, S. Newby, and H. Janes. "Tropospheric propagation delay: balloon profiling vs. surface-driven models." Presented at the Chapman Conference on GPS Measurements for Geodynamics, Ft. Lauderdale, Florida. September 1988.